

Nanocrystalline Diamond for Nano-Electro-Mechanical Systems



Evan Lloyd Hunter Thomas

Submitted in partial fulfilment of the requirements for the degree of
Doctor of Philosophy

School of Physics and Astronomy
Cardiff University

2017

Acknowledgements

First and foremost I would like to thank my Supervisor, Prof. Oliver ‘Ollie’ Williams. Starting with just the two of us in the singular ‘lab’ to the current group spread across multiple ‘labs’ he has always been available for scientific discussion, advice, and guidance. Unfathomably enthusiastic and perpetually laid-back, he has helped to ensure that I can only look back on my time within the group with fondness, from having one beer too many in the City Arms after my PhD interview right up to the day before I started writing this thesis. I will forever be thankful to him for taking me on and putting up with me for the past four years.

For his everyday assistance and company within the lab I wish to thank Dr Soumen Mandal. Much of the work on the construction of NEMS within this thesis was based on resonators constructed during his stint at Grenoble and without him showing me the ways of the nano-fabrication of diamond, both conventional and not-so-conventional, construction of the devices within this thesis would not have been possible. In addition, I wish to thank Dr Georgina Klemencic for her helpful discussions on the characterisation of the devices, assistance with ICP, and for working with Soumen during HF etching; The latter of which I was not allowed near and relieved for it.

For their leading of the X-ray scattering measurements performed within this thesis I wish to say thanks to Prof. Emyr Macdonald of Cardiff University, Dr Thomas Dane, formerly of Bristol University, and the staff at Beamline I07 of Diamond Light Source: Dr Chris Nicklin, Dr Jonathan Rawle, and Dr Tom Arnold. For assistance with AFM thanks are owed to Dr Sam Ladak and Dr Emmanuel Brousseau here at Cardiff, while the Raman measurements of the initial stages of NCD growth were kindly performed by Ashek Ahmed under the supervision of Prof. Chia-Liang Cheng at National Dong Hwa University in Taiwan.

To the technical staff within the department, in particular Hugh Lang, I wish to say

thank you for assistance with installing equipment within the lab and helping to keep it running. Similarly, thanks are also owed to Scott Cook and Dave Melhuish within the workshop for humouring me when handing them my attempt at engineering drawings and machining many of the items used within this thesis.

For the non-scientific discussions and their valiant attempts, even when it seemed futile, at cheering me up during the later stages of the PhD I wish to express my gratitude towards Jess Werrell and Laia Ginés. The lab would be a duller place without them and when the time comes to to return the favour I can only hope to be half as determined.

Finally, I would like to thank my mother and brother for their unwavering support both before, and during the course of this PhD. I am truly grateful for everything my mother has done for my brother and I and without her sacrifices I wouldn't be where I am today.

To my mother...

Abstract

Micro and Nano-Electro-Mechanical Systems (MEMS/NEMS) incorporating micro- and nano-scale mechanical elements into electronic circuits are of increasing interest in both fundamental physics and technological applications, with uses ranging from atomic-resolution mass spectrometers to low cost gravimeters and RF filtering. For applications reliant on the perturbation of mechanical elements, a high resonant frequency (f) with minimal dissipation (Q^{-1}) is desired to increase device response, while for filtering within the RF high Q enables the selection of individual channels. With the resonant frequency of devices proportional to the acoustic value of the material, diamond's unrivalled value of $18\,000\text{ m s}^{-1}$ makes it ideal for high frequency devices with minimal dissipation from scaling induced loss.

However, the use of Nanocrystalline Diamond (NCD) for smaller scale NEMS is inhibited by the quality of the resulting films, in particular the non-diamond carbon content, and the considerable surface roughness resulting from the competitive growth of randomly orientated crystallites. Within Chapter 4 spectroscopy ellipsometry, a powerful technique capable of probing the variation in the optical properties with depth, and hence microstructure, of thin films is therefore applied to the characterisation of 25–75 nm thick NCD films. The model developed is able to discern the point of coalescence of the film, with the indicated surface roughness and composition verified by AFM and Raman spectroscopy.

Chapter 5 then details the adaption of chemical mechanical polishing, a technique routinely used within the IC fabrication industry, to the polishing of diamond. Using a soft polymer polishing pad and an alkaline colloidal silica polishing fluid a reduction in roughness is observed for NCD films from 18.3 to 1.7 nm RMS over $25\text{ }\mu\text{m}^2$ after 4 hours. Finally, the polishing technique is used to aid in the construction of NEMS devices within Chapter 6 with the aim of improving the Q factor.

Publications and Conference Proceedings

- ¹E. L. H. Thomas, G. W. Nelson, S. Mandal, J. S. Foord, and O. A. Williams, “Chemical mechanical polishing of thin film diamond”, *Carbon* **68**, 473–479 (2014).
- ²E. L. H. Thomas, S. Mandal, E. B. Brousseau, and O. A. Williams, “Silica based polishing of {100} and {111} single crystal diamond”, *Science and Technology of Advanced Materials* **15**, 035013 (2014).
- ³J. A. Cuenca, E. Thomas, S. Mandal, O. Williams, and A. Porch, “Broadband microwave measurements of nanodiamond”, in *2014 asia-pacific microwave conference* (2014), pp. 441–443.
- ⁴I. Pope, L. Payne, G. Zorinants, E. Thomas, O. Williams, P. Watson, W. Langbein, and P. Borri, “Coherent anti-stokes Raman scattering microscopy of single nanodiamonds”, *Nat Nano* **9**, 940–946 (2014).
- ⁵J. A. Cuenca, E. Thomas, S. Mandal, O. Williams, and A. Porch, “Microwave determination of sp^2 carbon fraction in nanodiamond powders”, *Carbon* **81**, 174–178 (2015).
- ⁶J. A. Cuenca, E. Thomas, S. Mandal, O. Williams, and A. Porch, “Investigating the broadband microwave absorption of nanodiamond impurities”, *IEEE Transactions on Microwave Theory and Techniques* **63**, 4110–4118 (2015).
- ⁷S. Mandal, E. L. H. Thomas, T. A. Jenny, and O. A. Williams, “Chemical nucleation of diamond films”, *ACS Applied Materials & Interfaces* **8**, 26220–26225 (2016).

Contents

1	Introduction	1
2	Structure and Properties of Diamond	5
2.1	Structure of Diamond and Graphite	5
2.2	Synthesis of Diamond	8
2.2.1	High Pressure High Temperature	8
2.2.2	Detonation	10
2.2.3	Chemical Vapour Deposition	13
2.3	Properties of Diamond	15
3	Experimental Methods	18
3.1	Scanning Electron Microscopy	18
3.2	Atomic Force Microscopy	21
3.3	Raman Scattering	23
3.4	X-ray Diffraction	26
3.5	Spectroscopic Ellipsometry	27
3.6	Spectral Reflectance	30
3.7	X-ray Photoelectron Spectroscopy	31
3.8	Chemical Vapour Deposition	33
4	Spectroscopic Ellipsometry of Thin Film Diamond Growth	36
4.1	Spectroscopic Ellipsometry of Amorphous Carbon	37
4.2	Previous Spectroscopic Ellipsometry Studies of Polycrystalline Diamond	45
4.2.1	Bulk Layer	45
4.2.2	Seed Layer	50
4.2.3	Microcrystalline Films	53

4.2.4	<i>In-Situ</i> Spectroscopic Ellipsometry	57
4.3	Spectroscopic Ellipsometry of Nanocrystalline Diamond Growth	63
4.3.1	Experimental Methods	63
4.3.2	Morphology	68
4.3.3	Raman	69
4.3.4	X-ray Scattering	77
4.3.5	Spectroscopic Ellipsometry	84
4.3.6	Discussion	91
4.4	Conclusion	96
5	Chemical Mechanical Polishing of Diamond	97
5.1	Why Polish?	98
5.2	Mechanical Polishing	101
5.2.1	Polishing Process	101
5.2.2	Removal Mechanism	104
5.2.3	Surface Finish	106
5.2.4	Mechanical Polishing of Nanocrystalline Diamond	109
5.3	Chemically Assisted Mechanical Polishing	110
5.3.1	Polishing Process and Removal Mechanism	111
5.3.2	Single Crystal Diamond CAMPP	112
5.3.3	Polycrystalline Diamond CAMPP	113
5.4	Chemical Mechanical Polishing	118
5.4.1	Polishing Process and Removal Mechanism	118
5.4.2	Removal Rate	119
5.4.3	Previous Attempts at CMP of Diamond	122
5.5	CMP of Nanocrystalline Diamond	123
5.5.1	Experimental Methods	123
5.5.2	Morphology	126
5.5.3	X-ray Photoelectron Spectroscopy	129
5.5.4	Discussion	135
5.6	CMP of Single Crystal Diamond	140
5.6.1	Experimental Methods	140

5.6.2	AFM of Polished {100} and {111} Single Crystal Samples	141
5.6.3	Polishing Pad	143
5.6.4	Discussion	147
5.7	Further Polishing Experiments	148
5.8	Conclusion	150
6	Nanocrystalline Diamond Nano-Electro-Mechanical Systems	151
6.1	Micro and Nano-Electro-Mechanical Systems	152
6.2	NEMS Fabrication	158
6.2.1	Surface Termination	160
6.2.2	E-beam Processing	164
6.2.3	ICP	167
6.2.4	HF	173
6.2.5	Condensed Recipe	176
6.3	NEMS Testing	177
6.4	Conclusion	181
7	Conclusions and Future Work	183

List of Figures

1.1	Diamond doubly clamped resonator	2
2.1	Carbon electron configuration	6
2.2	sp^3 orbitals	7
2.3	Lattice of diamond and graphite	7
2.4	Carbon phase diagram	9
2.5	Detonation nano-diamond	11
2.6	Chemical vapour deposition model	14
2.7	Electronic diagrams of diamond and graphite	16
3.1	Scanning electron microscope schematic	20
3.2	Atomic force microscope schematic	21
3.3	Raman spectroscopy	24
3.4	X-ray diffraction	25
3.5	Spectroscopic ellipsometry	27
3.6	X-ray photoelectron spectroscopy	32
3.7	Seki AX6500 MWPECVD reactor	34
4.1	Cauchy modelling of DLC films	39
4.2	Idealised electronic band structure of a solid	42
4.3	$\epsilon_2(\omega)$ of sputtered and tetrahedral amorphous carbon films	44
4.4	SE modelling of nanocrystalline diamond films	48
4.5	P_{RSA} and P_{SCRA} obtained depolarisation and ellipsometry spectra for a 200 nm thick NCD	55
4.6	Reflectance intensity for R_p and R_s polarised light with increasing growth duration	56

4.7	<i>In-situ</i> SE of NCD film growth	60
4.8	X-ray scattering setup	65
4.9	Details of x-ray scattering sample chamber	66
4.10	AFM image and trace of seeded silicon wafer	69
4.11	AFM images of the initial stages of NCD growth	70
4.12	SEM images of the initial stages of NCD growth	71
4.13	Roughness against growth duration of the initial stages of NCD growth .	72
4.14	Particle size against growth duration of the initial stages of NCD growth	73
4.15	Raman spectra of the initial stages of NCD growth	75
4.16	Magnified Raman spectra of the initial stages of NCD growth	76
4.17	X-ray diffraction of the initial stages of NCD growth	79
4.18	Fitting to X-ray diffraction of the initial stages of NCD growth	80
4.19	X-ray reflectivity of the initial stages of NCD growth	83
4.20	Progression of SE model fitted to the 13 min. early growth sample . . .	85
4.21	Modelled and acquired Ψ and Δ spectra for the 13 min. early growth sample	88
4.22	Fitting parameter trends with increasing growth duration of the initial stages of NCD growth	90
5.1	UNCD and polycrystalline surface acoustic wave devices	100
5.2	Polishing directions of diamond plane groups	103
5.3	Mechanical polishing wear surface	105
5.4	AFM of mechanically polished single crystal samples	108
5.5	Exaggerated schematic of wafer bow due to high stress	110
5.6	Chemically assisted mechanical polishing of single crystal diamond and subsequent homoepitaxial growth	114
5.7	Reduction in roughness with time for mechanical polishing and CAMPP	115
5.8	Chemically assisted mechanical polishing of polycrystalline diamond . .	117
5.9	CMP model of SiO_2	119
5.10	Polishing puck with NCD wafer	125
5.11	Schematic of chemical mechanical polishing system	125
5.12	SEM images of as the grown to 4 hour polished NCD films	127

5.13	AFM images of the as-grown to 4 hour polished NCD films	128
5.14	XPS of the as-grown to 4 hour polished NCD films	131
5.15	XPS elemental ratios for as-grown to 4 hour polished NCD films	132
5.16	De-convoluted C1s elemental ratios for as-grown to 4 hour polished NCD films	133
5.17	Magnified SEM image of CMP film	136
5.18	Proposed mechanism for CMP of diamond	138
5.19	Single crystal polishing holder	141
5.20	CMP of {100} single crystal diamond	142
5.21	CMP of {111} single crystal diamond	144
5.22	Polishing directions of diamond plane groups	146
5.23	NCD film polished with recycled SF-1	149
6.1	SiC doubly clamped NEMS resonators	153
6.2	Free-free and paddle NEMS geometries	155
6.3	NEMS fabrication process	159
6.4	Metal deposition with and without piranha surface modification	162
6.5	E-beam lithography dose test	165
6.6	Metallised e-beam lithography dose test	166
6.7	NEMS e-beam pattern	168
6.8	NEMS ICP-RIE etching trials	172
6.9	NEMS nickel etch mask removal	173
6.10	NEMS hydrofluoric acid release	174
6.11	Tested resonator and NEMS sample holder	178
6.12	NEMS magneto-motive testing setup	179

List of Tables

4.1	Correlation matrix of fitting parameters for the 13 min. growth duration sample	87
5.1	Polishing rates and roughness values for the as-grown to 4 hour polished NCD films	126

Chapter 1

Introduction

Micro and Nano-Electro-Mechanical Systems (MEMS/NEMS) incorporating the actuation, perturbation, and sensing of micro- and nano-scale mechanical elements within electronic circuits are becoming more frequently used in applications as diverse as single virus detectors, RF filtering, and gyroscopes for optical image stabilisation within consumer electronics [1–3]. For applications dependant on the perturbation of an oscillating object increases in frequency (f) and reductions in dissipation (Q^{-1}) are desired to maximise sensitivity, while high Q at RF frequencies allows for individual channel filtering with minimal power consumption within communications applications [4, 5].

Shown within Figure 1.1 is one such simple doubly clamped NEMS structure constructed from 300 nm thick diamond with width W of 480 nm, length L of 5 μm , and designed to resonate in the plane of the sample at frequencies of ~ 320 MHz. The resonant frequency of the device is a product of the geometry, W/L^2 , and the acoustic velocity of the material, $\sqrt{E/\rho}$, where E is the Young's modulus and ρ is the mass density. Increases in the resonant frequency can therefore be gained through reducing the length of the device, pushing the dimensions further into the nano-scale, or through the selection of a material with a high acoustic velocity. However, reducing the dimensions of a device leads to an increase in loss from both intrinsic properties of the material and extrinsic sources such as circuit design and the medium in which the device is oscillating, with Q scaling with device volume (V) as $Q \propto V^{1/3}$ [6]. Therefore, the use of diamond with an unrivalled sound velocity of 18 000 m s^{-1} in comparison to values of 7500 and 11 400 m s^{-1} for Si and SiC respectively allows comparatively large diamond structures to reach GHz resonant frequencies, placing less stress on the nano-fabrication

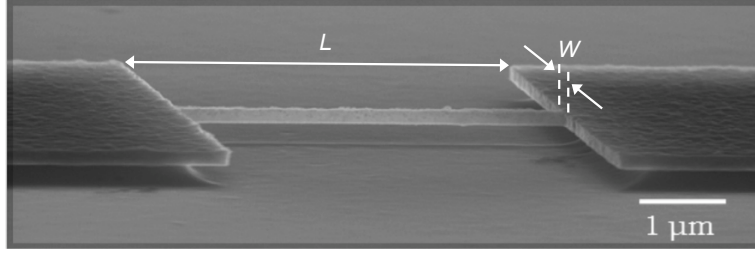


Figure 1.1: Doubly clamped resonator constructed from nanocrystalline diamond, with the high acoustic velocity of diamond allowing for relatively simple and large structures to achieve fQ products rivalling those of more complex Si geometries. Reprinted from Carbon, **72**, T. Bautze *et al.*, "Superconducting nano-mechanical diamond resonators", 100–105, Copyright (2014), with permission from Elsevier.

process and minimising scaling induced losses [7]. As a result, existing relatively large structures constructed from diamond offer fQ products that rival values from more complicated geometries constructed from Si [8].

To create devices from single crystal diamond, FIB milling, selective etching of a ion irradiated damaged layer, and angled anisotropic etching can be used to create free-standing structures [9–11]. Alternatively, thinned micron diamond plates (10–40 μm) can be ‘sandwiched’ between two quartz carriers or bonded to a Si substrate [10, 11]. However, high energy ion irradiation (MeV) typically results in the formation of defects acting to reduce the performance of devices, while the extensive polishing required to remove thickness non-uniformities within the plate in preparation for carrier attachment and the careful monitoring required during plasma thinning significantly complicate fabrication [10, 11]. In addition, the significant undercuts resulting from both methods are expected to radiate strain away from the resonator and into the anchors, resulting in low fQ product devices [6].

Therefore, for the purposes of device construction and ease of integration with current processing techniques, wafer-scale thin film diamond is preferred over mm^2 sized bulk single crystals. With single crystal heteroepitaxy limited to growth on iridium due to its unique ability to dissolve and then expel carbon at a sufficiently fast rate, attempts at deposition on foreign substrates typically result in Volmer-Weber type island growth due to the high surface energy difference between diamond and commonly used

substrates [12, 13]. Before coalescence of these islands a critical nucleation period will therefore be observed with varying carbide, non-diamond, and void contents dependant on the growth and seeding conditions. Upon the formation of a complete Nanocrystalline Diamond (NCD) film, overgrowth of the randomly orientated crystallites will then lead to a substantial roughness that increases with growth durations [14]. With the correlation between the Young's Modulus and the surface/volume ratio of crystallites, and hence non-diamond content within grain boundaries, the initial stages of film growth are critical to the retention of the properties of bulk diamond for the production of NCD MEMS, and more so for reduced volume NCD NEMS [15]. The considerable surface roughness meanwhile is expected to increase dissipation due to the increase in adsorbates, dangling bonds and defects, with SiC resonators possessing a roughness of 6.1 nm RMS previously reported to only be operational to VHF frequencies while smoother < 2 nm RMS beams were able to operate within the UHF/microwave regime [6, 16–18]. This thesis therefore concerns itself with the characterisation of the initial stages of growth to realise high quality films, processing of the surface roughness, and finally the construction of high fQ product NEMS from smooth NCD films.

After the obligatory chapters detailing the structure and properties of diamond as well as the experimental methods used within this thesis, Chapter 4 details the work performed on the characterisation of the initial stages of NCD film growth. Within the chapter the technique of Spectroscopic Ellipsometry (SE) has been applied to the modelling of the point of coalescence and structural parameters of 25–75 nm thick NCD films. The resulting presence of an interfacial carbide and trend in non-diamond carbon content are correlated with Raman spectroscopy, while the surface roughness is in observance with values provided by atomic force microscopy. As such SE is demonstrated to be a powerful technique for the characterisation of the initial stages of growth, and hence the optimisation of the non-diamond contents within films to yield high quality NCD.

Chapter 5 then moves onto the post growth processing of NCD films to remove the significant roughness resulting from the columnar nature of film growth. Through the adaption of Chemical Mechanical Polishing (CMP), a technique heavily utilised within the IC fabrication industry, polishing of highly bowed thin film diamond is demonstrated with a reduction in roughness from ~ 20 nm RMS to under 2 nm RMS over an area of

25 μm^2 . To explain the polishing observed with the comparatively softer colloidal silica polishing fluid, X-ray photoelectron spectroscopy was performed with the polishing mechanism proposed supported by recent density functional theory calculations [19]. Finally, polishing was performed on single crystal samples demonstrating the removal of mechanical polishing introduced damage to both the $\{100\}$ and the highly wear resistant $\{111\}$ diamond planes.

The construction of doubly clamped resonant beams from smooth NCD stock is then presented within Chapter 6. With the aim to study the effect of surface roughness on the dissipation the steps involved in the fabrication from surface oxidation to HF vapour release of freestanding structures are discussed along with initial attempts at the testing of the resulting devices. Chapter 7 then concludes the thesis, detailing the pertinent findings and briefly discussing the continuation of the work performed.

Chapter 2

Structure and Properties of Diamond

One of several of the allotropes of carbon including graphite, amorphous carbon and the more exotic buckminsterfullerene and lonsdaleite, diamond exhibits many unique properties as a result of its crystal structure. Within this chapter a brief overview is given of the structure in explanation of these properties, followed by a succinct description of the more commonly used synthesis methods. Finally, the more significant properties of diamond are briefly discussed.

2.1 Structure of Diamond and Graphite

In the ground state each lone carbon atom possesses six electrons with a configuration $1s^2 2s^2 2p^2$. With the requirement that each electron possess a unique set of quantum numbers as per the Pauli exclusion principle, the 1s K shell and 2s orbital within the L shell are full with two electrons of opposite spin. The remaining electrons are situated within two singly occupied 2p orbitals to provide the lowest possible energy, with the full configuration represented graphically within Figure 2.1. Upon the formation of diamond carbon expends 230 kJ mol^{-1} to create four spin-uncoupled valence electrons through the promotion of an electron from the 2s to the 2p sub-shell to maximise the energy decrease that comes with the formation of bonds [20]. The electron density is then distributed equally resulting in the formation of four sp^3 hybridised states of equal energy as shown to the right of Figure 2.1. As a result of the combination

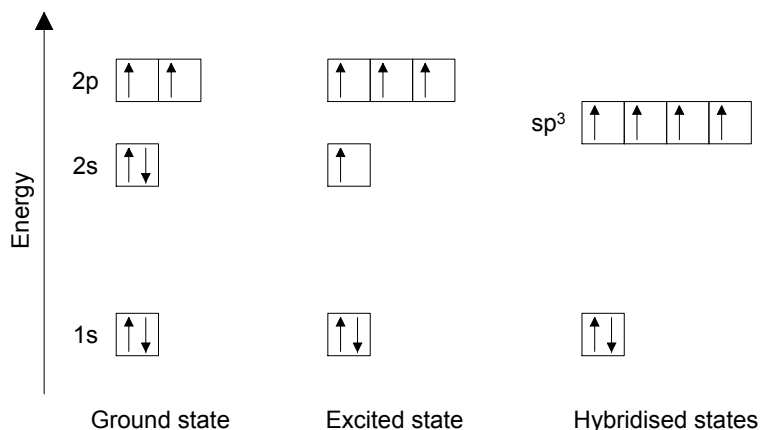


Figure 2.1: Electronic configuration of a lone carbon atom in the ground state and within the diamond lattice. To maximise the energy decrease upon the formation of bonds an electron is promoted from the 2s to the 2p sub-shell to form four spin-uncoupled sp^3 valence electrons of equal energy.

of the 2s and 2p atomic orbitals with the wave functions towards the top of Figure 2.2, four ‘dumb-bell’ shaped orbitals are then formed with enlarged positive lobes due to the spherically symmetric positive 2s orbital. These four sp^3 orbitals then point symmetrically along four tetrahedral directions with an angle between the orbitals of 109° to minimise repulsion between the lobes, resulting in the recognisable geometry shown to the bottom of Figure 2.2.

The resulting covalent structure of diamond is shown within panel A of Figure 2.3. The lattice is best described as two interpenetrating Face Centred Cubic (FCC) lattices shifted along the diagonal by $(1/4, 1/4, 1/4)a$ where a is the lattice constant of the cubic cell, equal to 3.57 \AA at room temperature [22, 23]. Such a compact structure with large overlaps between lobes while utilising 4 of the 6 constituent electrons then leads to strong sp^3 , or σ , bonds with lengths of 1.54 \AA [20, 24]. In combination with the three-dimensional structure these strong bonds with a binding energy of 717 kJ/mol are responsible for many of the superlative properties of diamond from thermal conductivity to hardness [24, 25].

In comparison, graphite displays sp^2 hybridisation in which the 2s sub-shell is hybridised with only two 2 p sub-shells. The resulting electron densities of the hybridised bonds are then similar to that of the sp^3 orbitals shown to the middle of Figure 2.2, and lie in a single plane with trigonal symmetry and a separation angle of 120° . Within

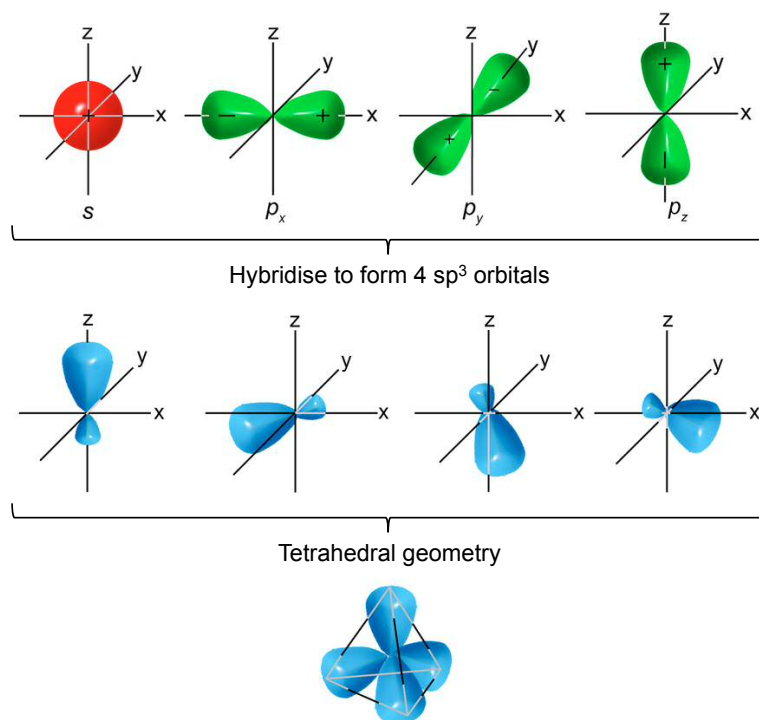


Figure 2.2: Spherically symmetric s and ‘dumb-bell’ shaped p type orbitals combining to form the four sp^3 hybridised bonds responsible for the tetrahedral structure of diamond. Adapted from [21].

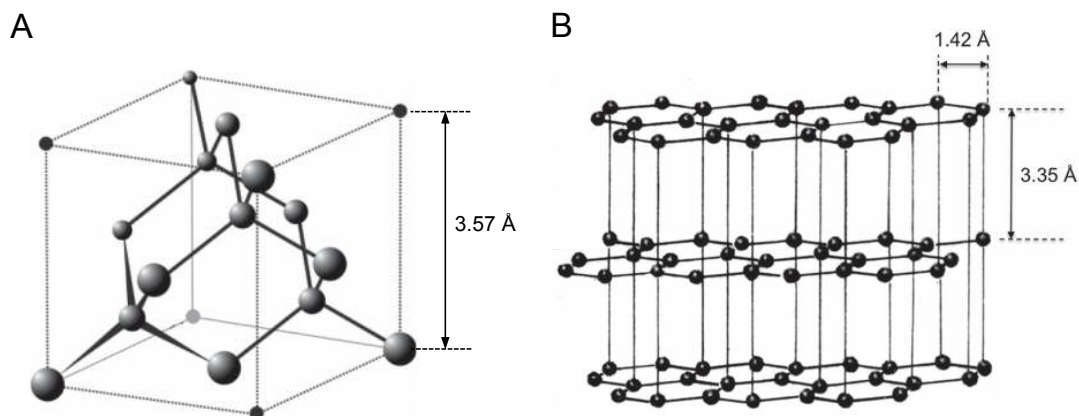


Figure 2.3: Lattices of (A) diamond and (B) graphite. The tetrahedral sp^3 bonding configuration results in the compact and strong diamond lattice, in stark contrast to the hexagonal planar structures provided by sp^2 bonds within graphite held weakly together by the unhybridised p_z orbitals and van der Waals forces. Reprinted from [24], Copyright © 2011 by John Wiley & Sons, Inc. all rights reserved, with permission by John Wiley & Sons, Inc.

the graphite structure shown within panel B of Figure 2.3 the trigonal σ bonds produce laminar hexagonal rings with a bond length of 1.42 Å [24]. The un-hybridised and symmetrical ‘dumb-bell’ $2p_z$ orbital is meanwhile orientated perpendicular to the plane of the sp^2 orbitals. The $2p_z$ orbital then forms π bonds with those of neighbouring carbon atoms allowing the electrons to migrate parallel to the hexagonal planes, and in contribution with weak van der Waals forces ‘glues’ the laminar structure together [24]. With an alternating stacking structure the lattice constant in the basal plane between repeating layers is 6.707 Å [26].

2.2 Synthesis of Diamond

Shown within Figure 2.4 is the phase diagram of carbon highlighting the regions in which diamond and graphite are the thermodynamically favoured allotropes of carbon, separated by the solid Berman-Simon equilibrium line [20, 28]. As visible, graphite is the thermodynamically favoured allotrope of carbon at standard temperature and pressure with an energy of 0.02 eV per atom less than that of diamond [29]. While the difference in enthalpy is relatively minor between the two phases, a significant activation barrier (~ 0.4 eV per atom) must be overcome to observe a considerable conversion from graphite to the denser diamond, requiring temperatures of 3000 K and pressures above 125 kbar [20, 30]. Similarly, this large activation energy requires temperatures of 1800 °C to break the large binding energy of bonds within the diamond lattice and considerably reverse the process at atmospheric pressure, hence making diamond metastable with kinetics limiting the thermodynamically favoured transition to graphite [28].

2.2.1 High Pressure High Temperature

While replication of these pressures and temperatures used to produce natural diamonds are unfeasible, work performed by General Electric, Allmänna Svenska Elektriska Aktieföretaget in Sweden, and the former Soviet Union in the early 1950’s resulted in the creation of the catalyst aided High Pressure High Temperature (HPHT) technique [31]. With the technique a catalytic solvent, typically a transition metal such as Fe, Co, Cr, Ni, Pt, Pd or mix thereof, is used to reduce the activation energy and hasten the rate of diamond formation. A graphitic carbon source, seed diamond, and catalytic solvent

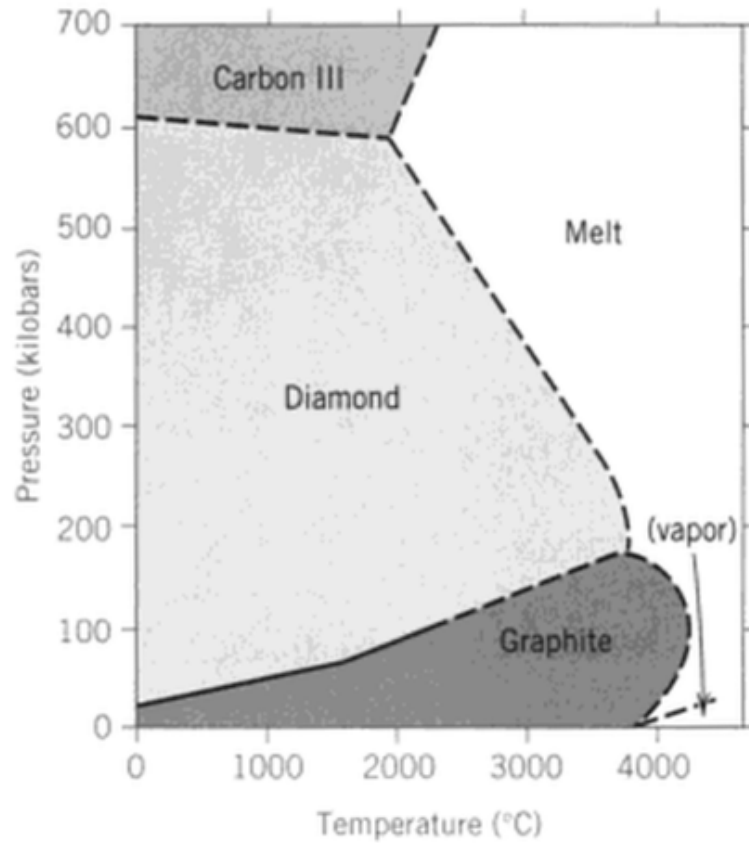


Figure 2.4: Carbon phase diagram detailing regions in which graphite and diamond are the thermodynamically favoured allotropes of carbon. The intense pressures and temperatures required to replicate the production of natural diamonds are unfeasible for the commercial production of diamond, resulting in the catalyst-assisted HPHT method. TNT/RDX detonation meanwhile results in a shock wave of pressure and temperature above the solid Berman-Simon equilibrium line, while CVD circumvents thermodynamics and grows diamond kinetically at less than atmospheric pressures. Reprinted from [27], Copyright 2008 © John Wiley & Sons, Inc. all rights reserved, with permission by John Wiley & Sons, Inc.

can then be compressed at reduced pressures and temperatures of the order of 5 GPa and 1500 K respectively to produce diamond at a rate of mg h^{-1} [31, 32]. During compression the catalytic solvent acts to break apart the C–C bonds within the graphitic carbon to saturate the molten metal at pressures and temperatures conducive to the formation of diamond, resulting in the transport of carbon and growth of the diamond seed. However during the process nitrogen within the solvent metal, the carbon source, and the compression chamber is incorporated into the lattice at levels of between tens and 200 ppm dependant on the solvent used [32]. Metallic inclusions from the solvent metal and getters added to minimise the impact of nitrogen on the crystal are meanwhile preferentially trapped near the seed. Coupled with the fact that crystal sizes are limited to the order of millimetres, the process products are then predominantly used for industrial applications [30].

2.2.2 Detonation

The conditions conducive to diamond growth can also be produced through the detonation of CHNO based explosives, with or without a carbon source, within an oxygen deficient environment [33, 34]. While working on the production of diamond through shock compression of graphite and carbon black in the 1960's, researchers within the former Soviet Union observed a sharp increase in yield upon placing the carbon source directly within the charge [35]. Subsequent control experiments without graphite in 1963 demonstrated the synthesis of diamond directly from carbon contained in the explosive, termed Detonation Nano-Diamond (DND) [35].

During the process 2,4,6-TriNitroToluene (TNT) is typically mixed with Royal Demolition eXplosive (RDX, chemically termed 1,3,5-trinitro-1,3,5-triazin) in the ratio 3:2, with the highly under-oxygenated TNT the source of carbon and the RDX used to reach the conditions necessary for diamond formation [33, 34]. Upon detonation of the charge within a negative oxygen balanced environment the passing shock wave leads to incomplete combustion of the explosive, and the formation of elemental carbon along with CO, CO₂, H₂O, and N₂ [34, 36]. Decomposition then continues along the line AB within the phase diagram of Figure 2.5, raising the pressure and temperature above the M_1 equilibrium line where liquid carbon clusters containing 10^3 – 10^4 atoms are able to form [35, 37]. The Jouguet point, B , marks the end of decomposition with a maximum in

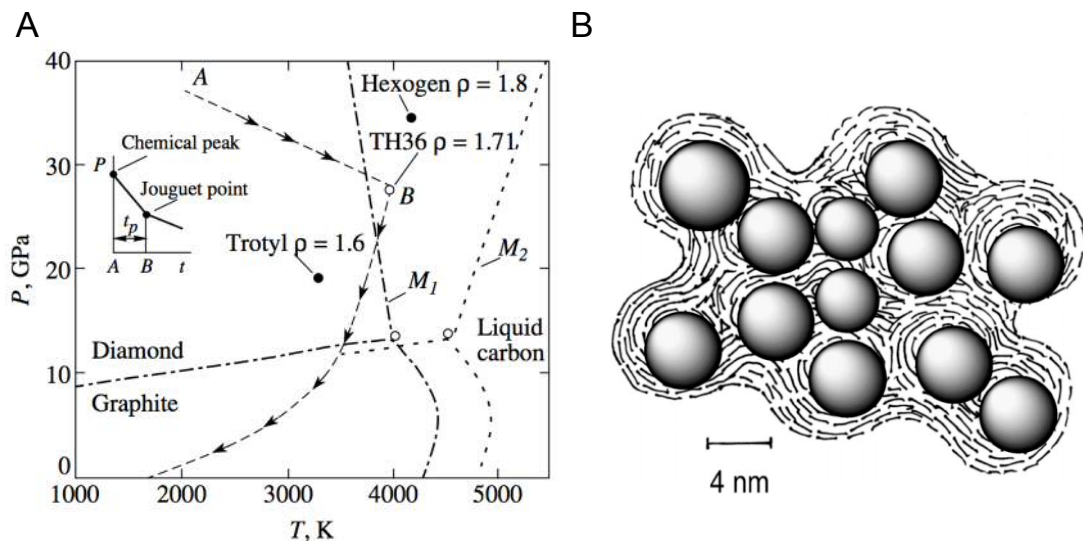


Figure 2.5: (A) Synthesis of detonation nano-diamond overlaid atop of the phase diagram of carbon, and (B) resulting core aggregate produced. Decomposition of the carbon containing explosives occurs along the line AB to produce liquid carbon clusters which subsequently condense to form spherical nano-diamond particles. Elevated temperatures upon cooling from the Jouguet point, B , leads to the creation of onion like shells to the nano-diamond as a result of phase conversion, while graphitic carbon binds particles together to form tightly bound core aggregates. Panel A reprinted from *Physics of the Solid State*, "On the history of the discovery of nanodiamond synthesis", **46**, 2004, 595–599, V. V. Danilenko, original Russian text copyright © 2004 by Danilenko with permission of Springer. Panel B reprinted from *Carbon*, **43**, A. Krüger *et al.*, "Unusually tight aggregation in detonation nanodiamond: identification and disintegration", 1722–1730, Copyright (2014), with permission from Elsevier.

temperature of 3000–4000 K reached at pressures of 20–30 GPa [33, 35]. Condensation within these clusters then yields rounded nano-diamond particles of ~ 5 nm diameter with a narrow size distribution due to the microsecond formation time [33–35, 38]. As the pressure begins to rapidly drop the sustained high temperature leads to formation of graphitic onion like shells around the nano-diamond as a result of phase conversion, with graphitic structures binding the particles together to form core aggregates of 100–200 nm in size as shown within Figure 2.5B [33, 38]. Therefore, detonation usually occurs in an inert gas or water to accelerate cooling and minimise the conversion to, and formation of graphitic structures [29]. These core aggregates are then in turn weakly bound through electrostatic attraction to create large aggregates ranging in size from hundreds of nm to μm [34]. As a result, also present with nano-diamond is 25–85% graphitic carbon and 1–8% incombustible material [29].

After detonation the resulting soot is collected and filtered with sieves and magnets to remove large foreign debris arising from the chamber walls, metal from the detonator, and polyethylene should a water container surrounding the charge be used [33, 34]. The remaining material is then acid treated to remove any remaining metallic contamination and to selectively etch the sp^2 content of the soot [33, 34]. While ultrasonic treatment of the material within a solution can be used to easily break apart the large agglomerates electrostatically attracted to each other, tightly bound core aggregates remain more difficult to separate [34]. As such, techniques utilising zirconia or silicon dioxide ceramic beads to impart shear on the aggregates either through milling or cavitation upon the use of a strong ultrasound have been demonstrated, however their use results in contamination of the material of the order of 5% [34, 38]. For DND used within this thesis hydrogen annealing, ultrasonic dispersion, and subsequent centrifugation to remove remaining aggregated materials has been used to produce stable mono-dispersed hydrogen terminated H_2O colloids. The resulting large positive zeta potential then renders the colloids suitable for electrostatic seeding of the predominantly negatively charged silicon substrates, which as described later is required in the production of nanocrystalline diamond films [15, 39].

2.2.3 Chemical Vapour Deposition

Diamond growth by Chemical Vapour Deposition (CVD) was first pioneered in the early 1950's by Eversole and independently by groups within the United States and the former Soviet Union [40]. Through thermal decomposition of CO under less than atmospheric pressure Eversole observed growth on natural diamond samples heated to 960 °C, with subsequent experiments with ^{13}C enriched CO_2 showing an increase in the abundance of ^{13}C within the diamonds, conclusively demonstrating the metastable growth of diamond [30, 41]. The subsequent addition of atomic hydrogen to preferentially etch the co-deposited graphitic component in the 1960's and the developments in reactor design by Japanese groups in the 1980's facilitated the routine CVD of diamond [40, 42]. Through use of the technique diamond is grown kinetically rather than thermodynamically with the associated high pressures and temperatures, simplifying the equipment and running costs significantly while growth from the gas phase minimises the impurity content and allows conformal growth on a range of substrates [30, 42].

During growth the process gasses, typically methane diluted in an excess of hydrogen ($\sim 1\%$ vol. CH_4), are fed into the reactor while maintaining pressures of the order of 20–100 Torr [30, 40]. As the feed gas passes through an activation region the diatomic hydrogen is then decomposed thermally through the use of filament or in combination with electron collision induced disassociation upon the use of plasma activation [30, 43, 44]. The atomic hydrogen is then able to abstract hydrogen from the feed methane to form the methyl radical (CH_3), demonstrated through *in-situ* spectrometry to be the dominant species for diamond growth [45]. Laminar, convective, or diffusive flow mechanisms transport the radicals towards the substrate, typically held at temperatures exceeding 700 °C, before either reacting or diffusing across or through the surface [30]. Upon reaching a nucleation site the atomic hydrogen can then remove a hydrogen atom terminating the diamond surface to form H_2 , leaving a reactive surface site as shown within the first and second panels of Figure 2.6. While this dangling bond will typically be saturated by another H atom, occasionally a methyl CH_3 radical will take its place. This detachment of hydrogen and addition of methyl radicals continues until the carbon atoms become incorporated into the tetrahedral lattice resulting in the atom by atom growth of diamond, with approximately 10^4 H_2 recombinations for each carbon atom left on the growing surface [40]. The hydrogen content is therefore critical for the

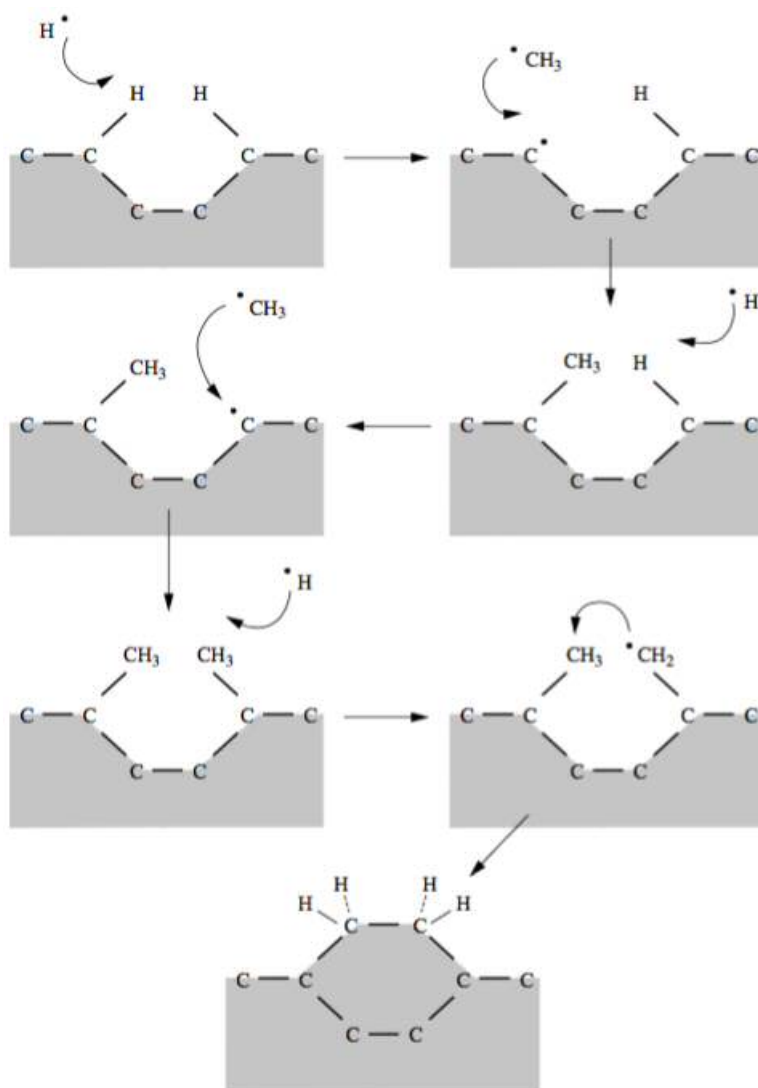


Figure 2.6: Model of chemical vapour deposition diamond growth. Activated atomic hydrogen removes the sp^3 stabilising hydrogen atoms bonded to the diamond surface, forming the diatomic H_2 and leaving a reactive surface site. While typically terminated by another hydrogen atom a methyl radical can alternatively react with the site, adding a lone carbon atom to the surface. Further H abstraction and methyl deposition can then occur until the carbon atoms are locked within the tetrahedral lattice, growing the diamond surface atom by atom. Reprinted from P. W. May, "Diamond thin films: a 21st-century material", *Philosophical Transactions of the Royal Society of London A: Mathematical, Physical and Engineering Sciences*, (2000), **358**, 473–495, by permission of the Royal Society.

production of high quality diamond, aiding in the fracturing of methane, keeping the sp^3 hybridisation of the surface intact through preventing surface reconstruction to the thermodynamically favoured allotrope graphite, and preferentially etching away sp^2 sites at a rate exceeding that of their growth [45].

With the use of a Ta or W filament heated to 2200 °C however metallic impurities at ppm levels limit the resulting quality of films and prevent the use of highly corrosive and oxidising gas mixtures, while the process is inherently limited by the reduced density of gas phase ions available upon thermal cracking [30]. Although more complex and limited in deposition area, the high gas temperatures attainable upon using an electrical discharge result in more efficient thermal disassociation of H_2 [30]. In addition, the high power densities available to be coupled to the plasma makes MicroWave Plasma Enhanced Chemical Vapour Deposition (MWPECVD) the favoured technique for the deposition of high quality, electronic grade diamond samples [44].

2.3 Properties of Diamond

As mentioned previously, the dense packing and tetrahedral arrangement of strong bonds result in diamond exhibiting unique mechanical properties. With removal of atoms difficult from the lattice diamond is the hardest know substance with a Vickers hardness of ~ 100 GPa dependant on the crystallographic plane, while also being the least compressible with Young's modulus of up to 1200 GPa [15, 46, 47]. In addition, diamond possess a scratch resistance of 10 on the Mohs scale and a coefficient of friction of 0.1, making it a suitable material for cutting and polishing applications, scratch resistant coatings, and sliding components [47].

The combination of light atomic mass and stiff chemical bonds within the diamond lattice also result in superior values for properties dependant on the propagation of phonons through the lattice. As a result sound is able to pass through diamond at speeds of $18\,000\text{ m s}^{-1}$, a crux of the use of NCD for high frequency MEMS/NEMS devices and exceeding that of all solid materials with AlN, Si, and SiC offering values of 5500, 7500, and $11\,400\text{ m s}^{-1}$ respectively [7]. In addition, while for many high thermal conductivity materials heat is conducted by electrons and hence linked to electrical conductivity, within diamond these phonons provide the main mechanism of thermal conduction [42].

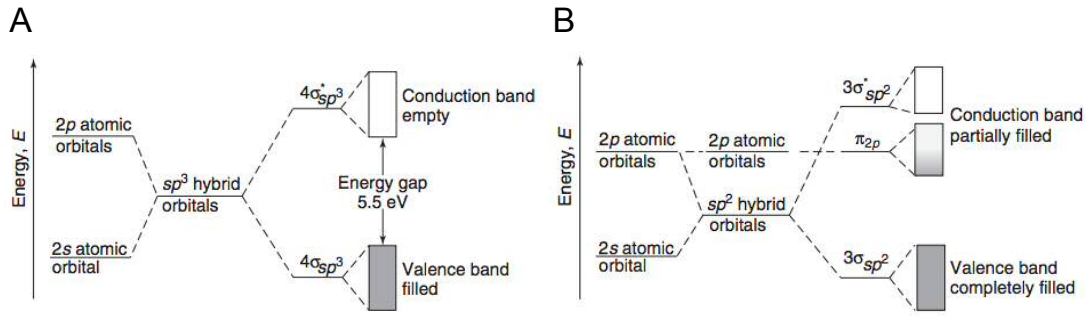


Figure 2.7: Electronic diagrams of (A) diamond and (B) graphite. As a result of the strong sp^3 bonding a large energy gap is observed between the σ and σ^* states forming the valence and conduction bands separated by 5.5 eV, while the π bonds within graphite create a partially filled conduction band allowing conduction along the sheets of hexagonal rings. Reprinted from [24], Copyright © 2011 by John Wiley & Sons, Inc. all rights reserved, with permission by John Wiley & Sons, Inc.

Resulting thermal conductivity values then peak at $\sim 15\,000\text{ W m}^{-1}\text{ K}^{-1}$ for high quality natural type IIa diamond at temperatures of 70 K while decreasing to $2000\text{ W m}^{-1}\text{ K}^{-1}$ at room temperature as a result of impurity or defect scattering, exceeding that of all solids in the range 90 to 1200 K [22, 42, 47]. Such values exceed that of copper and competitive ceramics by factors of 5 and 4–6 respectively [42].

Upon the formation of diamond, the potential wells surrounding each atom and the wave functions of attracted electrons will begin to interact. Assuming the electrons are tightly bound to their respective atoms and possessing wave functions similar to an atomic orbital of a free electron, the solution to the Schrödinger equation of the lattice can then be approximated by the superposition of the constituent electrons' wave functions [48]. The symmetric and anti-symmetric additions of the wave functions then result in bonding and anti-bonding energy levels, termed σ and σ^* respectively, with the two electrons within two electrons within each bond filling the higher value wave function σ state. Over the lattice the two discrete states become continuous due to the differing quantum states required for each electron, resulting in the formation of valence and conduction bands separated by a large indirect band gap of 5.5 eV as shown within panel A of Figure 2.7. In stark contrast, the π bonds formed from p_z orbitals in graphite meanwhile lead to the presence of a π band partially filled due to

the delocalised electrons situated between the two σ states. Electrons are then able to move within the resulting conduction band allowing conduction along the hexagonal planes of approximately $3 \times 10^4 \text{ S cm}^{-1}$, in comparison to the 10^{14} – $10^{16} \text{ } \Omega \text{ cm}$ resistivity for high purity undoped diamond [24, 47]. Combined with diamond’s relatively low permittivity (5.5), this large band gap then leads to a breakdown field of 10 MV cm^{-1} [49, 50]. Additionally, the growth of high quality single crystal diamond with low dislocation densities of $<10^6 \text{ cm}^{-2}$ permits electron and hole mobilities of 4500 and $3800 \text{ cm}^2 \text{ V}^{-1} \text{ s}^{-1}$ respectively [51]. However, the range of dopants is limited due to the lattice spacing of diamond while the commonly used P-type dopant boron displays an activation energy of 0.37 eV, requiring doping levels exceeding 10^{20} cm^{-3} to enable sufficient activation of carriers at room temperature and leading to an alteration in the conduction mechanism [42, 50, 51].

With a band gap of 5.5 eV, absorption as a result of electronic transitions within the UV region of the spectrum begin below a wavelength of 226 nm [42]. Meanwhile, the highest fundamental phonon frequency of any material of diamond at 1332 cm^{-1} extends transparency into the far infra-red with the symmetric lattice preventing one phonon absorption at $7.5 \text{ } \mu\text{m}$ [52]. Two and three phonon processes lead to minor absorption between 2.6 and $6.2 \text{ } \mu\text{m}$ before decreasing to as low as 0.03 cm^{-1} within the 8– $12 \text{ } \mu\text{m}$ IR atmospheric window, with the resulting wide ranging transparency in comparison to ZnS and ZnSe making diamond an attractive material for optical applications [52].

However, as will be discussed within the coming chapters the use of diamond and its superlative properties are often limited by the difficulty in nucleation and the resulting nature of diamond growth. This thesis then concerns itself with the improvements in the production of diamond films through the characterisation of the initial stages of growth atop a foreign substrate with spectroscopic ellipsometry, and processing of the considerable roughness typical with diamond film growth to make the resulting films more amenable to use. Within the last experimental chapter the latter is then utilised to more easily facilitate the construction of NEMS devices and take advantage of the superior speed of sound within diamond.

Chapter 3

Experimental Methods

Within this chapter the principles of the characterisation and growth techniques used later within the thesis are presented along with the nuances of their use on diamond. The techniques of chemical mechanical polishing, which forms a key component of its respective chapter, as well as reactive ion etching and hydrofluoric acid vapour etching, used in the construction of NCD NEMS devices and best described with reference to the resulting structures, are instead discussed within the relevant chapters.

3.1 Scanning Electron Microscopy

Scanning Electron Microscopy (SEM) involves the rastering of a ‘primary’ electron beam across a sample under vacuum. Upon the electrons penetrating the sample, inelastic and elastic collisions result in a range of signals that can be used for obtaining topographical and compositional high magnification images of a sample: Electrons scattered from the sample with energy > 50 eV and largely close to that of the ‘primary’ beam are typically Auger electrons or the result of elastic scattering events with the nucleus, termed ‘Backscattered Electrons’ or ‘BSE’. Due to changes in the cross-sectional area of the atom, the number of BSE is expected to increase monotonically with atomic number, Z , from ~ 0.05 for carbon to ~ 0.5 for gold [53]. As such, BSE images are able to provide contrast between different materials, with higher Z areas appearing brighter than those of lower Z [53]. In addition, the high energy of BSE lead to a large interaction volume of the order of a fraction of a micrometer in breadth and depth. This sampling depth then allows for the imaging of the sub-surface region, albeit it at

the expense of spatial resolution, and changes in contrast linked to the orientation of the ‘primary’ beam with respect to the crystallographic planes of the sample.

Lower energy electrons (< 50 eV) scattered from the sample meanwhile are the result of inelastic collisions between atomic electrons and ‘primary’ beam electrons traversing the sample or backscattered electrons leaving the sample, and termed ‘Secondary Electrons’ or ‘SE’. With energy required to surmount the work function of the material, SE created from the ‘primary’ beam deeper than a few nm from the surface are typically trapped within the material with further inelastic collisions: Typical mean free paths of SE within metals and insulators are 1 nm and 20 nm respectively, providing high resolution information of the sample surface [54]. However SE created through scattering with higher energy, and hence more penetrating, backscattered electrons typically can come from a larger interaction volume of diameter up to 1 μm , reducing the resolution achievable [53]. Therefore, as the penetration depth of the incident beam increases upon shallower angles of incidence to the surface, changes in topography will then be reflected in a change in brightness with slopes facing towards the detector brighter than those facing away. With ease of interpretation, spatial resolution of down to ~ 1 nm, and ease of collection due to their low energy, SEM images are largely produced through the use of SE emission [53].

As the ‘primary’ beam interacts with the sample the resulting alteration in the number of electrons within the sample can cause a build up of electrostatic charge, modifying the local electric field and leading to a reduction in the achievable resolution for insulating samples. To work around such an effect the sample can be coated in a thin (~ 10 nm) conductive film of carbon or gold, or through imaging at high pressures with water vapour while differentially pumping the electron source. Alternatively, the acceleration voltage can be chosen such that the electron yield is equal to 1, typically less than 2 keV, requiring the use of field emission electron source due to their capability to produce the sufficient brightness at low voltages.

Figure 3.1 shows a simplified cross-sectional schematic of a typical SEM. A gun is first used to emit electrons either through thermionic emission from a tungsten or LaB_6 filament, or from a sharpened field emission tip and then accelerates the charged particles to an energy of 0.5–30 keV [53]. The beam then passes through a series of electromagnetic Condenser Lenses (CL) to demagnify and then focus the beam to 1–2 nm in

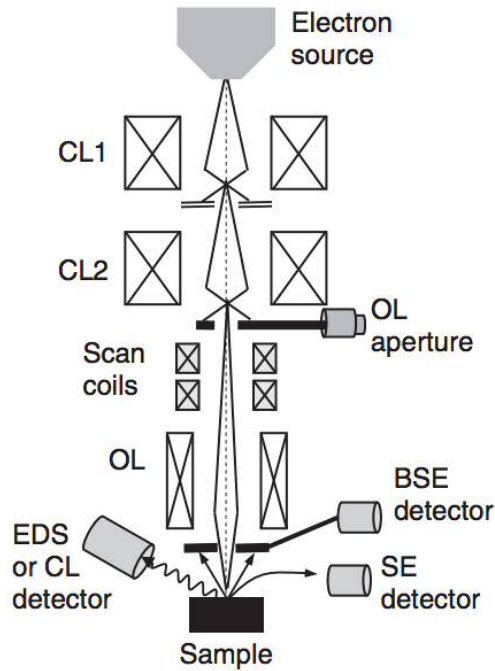


Figure 3.1: Schematic of scanning electron microscope detailing the arrangement of electron source, lenses, and detectors. Reprinted from [54], © 2013 by John Wiley & Sons, Inc., with permission by John Wiley & Sons, Inc.

diameter before being rastered across the sample by the scan coils to produce an image or alter the solubility of a resist, with final focusing on the sample performed by the Objective Lens (OL) [55]. A Everhart-Thornley scintillator/photomultiplier detector is then used to count SE, while semiconductor or scintillators and photomultipliers can be then be used to count BSE above the sample, with additional detectors to measure florescent X-rays as part of Energy-Dispersive X-ray Spectroscopy (EDS) or Cathodo-Luminescence (CL) emitted from the sample dependant on SEM configuration [53, 55]. The Raith eLine columns used throughout this thesis for imaging and electron beam exposure utilise field emission tips due to their superior brightness and sharper energy profile in comparison to filament sources, with the achievable resolution then limited by lens introduced aberration and sample interaction volume rather than the electron gun [53, 55].

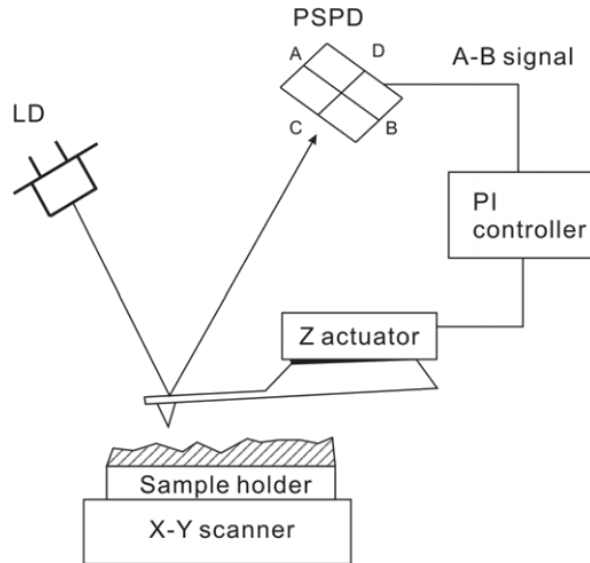


Figure 3.2: Schematic of atomic force microscope detailing rastering of the nanoscale probe across the sample surface through the use of stepper motors, with the resulting deflection maintained through the use of a laser reflected off the cantilever and quadrant photodetector. Reprinted from [58], © IOP Publishing. Reproduced with permission. All rights reserved.

3.2 Atomic Force Microscopy

Atomic Force Microscopy (AFM) involves the rastering of a nano-sized probe to trace the topography of a surface at atomic scale resolutions both laterally and vertically. As laid out in Figure 3.2, the pyramidal tip, typically constructed from Si, SiO₂, or Si₃N₄, is scanned across the sample while either in contact or in close proximity to the surface with the resulting interaction between tip and sample causing deflection of the reflective cantilever [56]. Using the optical lever technique this deflection then causes an amplified shift in the position of a laser beam reflected from the probe upon a quadrant detector, allowing the measurement of the deflection, amplitude of oscillation and torsion of the cantilever. Feedback is then used to maintain the separation between tip and cantilever through driving a series of piezoelectric scanners. As a result of the sensitivity of the photodiode sub Å vertical resolutions are achievable, limited by thermal vibrations of the cantilever [56, 57]. As such scans can be taken of the surface of insulators, semi-conductors, and conductors under ambient, liquid, or ultrahigh vacuum conditions, while being insensitive to the optical properties of the sample.

As the tip approaches the sample surface and reaches a separation of several nm, weak van der Waals, capillary, and electrostatic attractive forces act to bring the two together with increasing force as the distance decreases. Upon reaching a separation of 0.5 nm from the surface the electron clouds of atoms within the tip and surface begin to interact and repel each other. AFM is therefore able to operate in repulsion mode with tip and sample in direct contact while maintaining a constant force, or non-contact mode at 2–10 nm separation with the weak attractive forces perturbing the amplitude, frequency, and phase of the oscillations of the resonating cantilever [56]. An attractive tip-sample force lowers the frequency of resonance, while a repulsive force increases the frequency. However, when operating in non-contact mode the comparatively weak van der Waals forces lead to a reduction in the lateral resolution of the AFM to nm levels, leading to the development of ‘tapping mode’ in which the tip is oscillated at high amplitudes between 10–100 nm and intermittently brought into contact with the sample causing dampening in the amplitude of oscillation as energy is lost [59]. With a static cantilever being dragged across the sample at forces of 1–100 nN in contact mode the resulting GPa contact pressure leads to damage of soft surfaces and contamination of the tip [59]. In comparison the dynamic non-contact ‘tapping’ mode applies forces of ~ 0.1 nN making it equally suitable for soft materials in which sample damage could occur and, conversely, hard materials where tip damage is likely to occur while minimising reductions in resolution and stiction issues of non-contact AFM [56].

Due to the use of a probe to effectively trace the sample, the data obtained consists of the convolution of the shape of the tip and the sample topography. Should the sample consist of features of the same scale as the tip with steep sidewalls the lateral width of the imaged feature will be dominated by the dimensions of the tip. Throughout this thesis tapping or non-contact mode is therefore used to minimise tip wear and the resulting increase in ‘tip imaging’ with a dull probe, while feature sizes of dispersed nano-diamond of similar scale to the tip radius are estimated by the vertical displacement rather than lateral width.

3.3 Raman Scattering

When a sample is irradiated by light the electric field causes a distortion of the electron cloud of chemical bonds within the first few microns from the surface [60]. Upon the field reversing the dipole will then relax, typically to the ground state, and radiate photons at an identical energy to the probing light through elastic Rayleigh scattering as shown in panel A of Figure 3.3. However, a small portion of the scattered photons will be the result of relaxation to an excited state, causing a downward shift in the radiated energy through Stokes Raman scattering, also shown within panel A of Figure 3.3. The energy difference between the exciting light and radiated light is then equal to a vibrational energy of the molecule or crystal. Alternatively, excitation and subsequent relaxation to the ground state of thermally activated vibrational modes can lead to an increase in the energy of scattered radiation through anti-Stokes Raman Scattering. Due to the extremely weak nature of Raman scattering however, intensities of 10^{-3} – 10^{-6} of the Rayleigh line are observed which in turn is 10^{-3} – 10^{-5} of the intensity of the exciting line, requiring intense monochromatic laser light sources to observe such Raman scattering [60]. Shown in panel B of Figure 3.3 is the Raman spectra of the mineral realgar (As_4S_4) showing such symmetric inelastic scattering bands centred around the central Rayleigh line, suppressed by a holographic filter [61]. With the temperature dependance due to the requirement of existing thermally activated vibrations the anti-Stokes Raman lines are typically of lower intensity than temperature independent Stokes scattering.

As the resonant frequency of chemical bonds are dependant on the mass of the atomic constituents and the bond force constant, this vibrational energy can then be used to identify the constituent atomic bonding within the sample. Considering a diatomic molecule composed of two atoms as a simple harmonic oscillator, a single mode of vibration will be observed with a similar single resonant frequency for diatomic crystals. Extending to more complex structures to include stretching and bending, the number of possible vibrational modes for non-linear and linear molecules, and crystals are $3n - 6$, $3n - 5$, and $3n - 3$ respectively where n is the number of atoms within the molecule or primitive cell [60]. As a result, diamond exhibits a single Raman active vibrational mode at 1332 cm^{-1} [62]. Graphite predominantly exhibits peaks at 1580

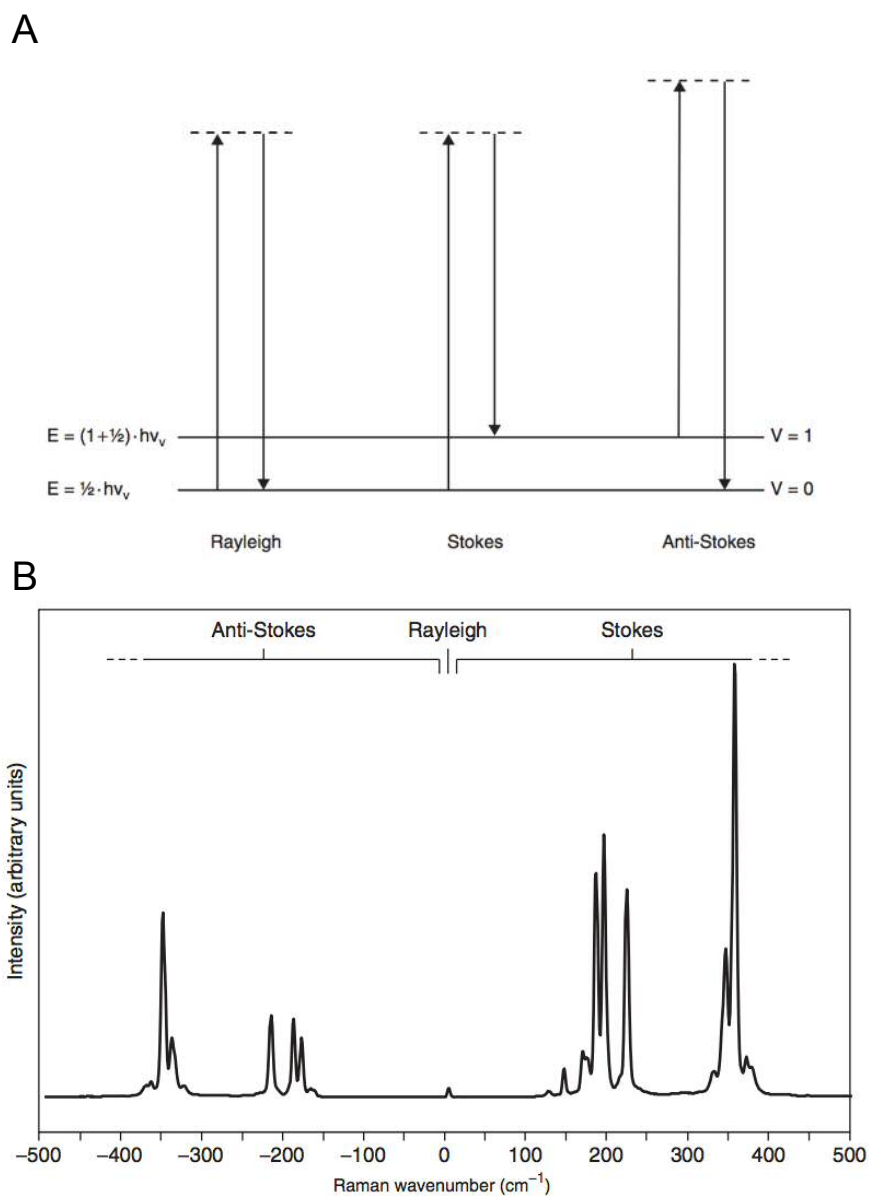


Figure 3.3: Raman scattering spectroscopy. (A) Rayleigh, Stokes, and anti-Stokes scattering detailing the excitation to a virtual energy level and subsequent relaxation to either the ground state or a vibrational state, and (B) formation of scattering lines centred around the suppressed Rayleigh line of the mineral realgar (As_4S_4). Reprinted from [61], © 2013 by John Wiley & Sons, Inc., with permission by John Wiley & Sons, Inc.

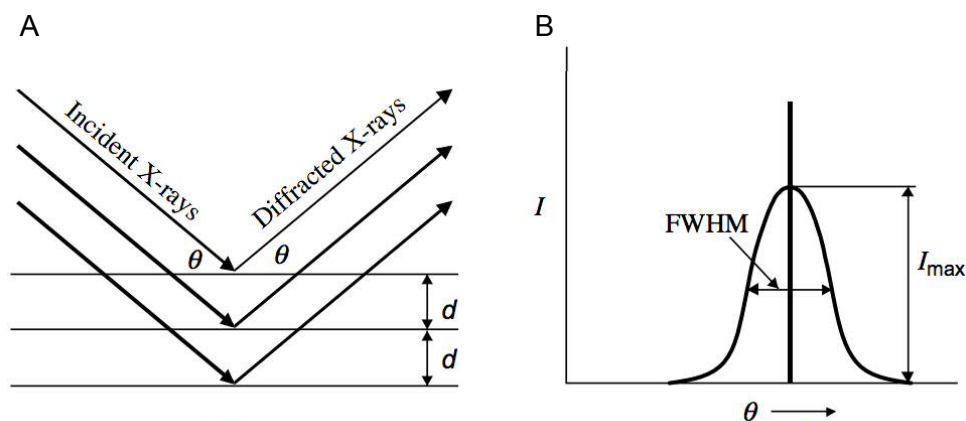


Figure 3.4: X-ray diffraction. (A) Thomson scattering of incident x-rays leads to the interference of radiation emitted from electrons within crystal planes, with the formation of a peak in diffracted intensity (B) upon the incident angle and the separation between atomic planes satisfying Bragg's law. Reprinted from [64], Copyright © 2009 by John Wiley & Sons, Inc. all rights reserved, with permission by John Wiley & Sons, Inc.

and 1350 cm^{-1} , termed the G and D peaks, attributed to bond stretching of all pairs of sp^2 atoms in chains and rings, and the breathing modes of sp^2 rings respectively [62, 63]. Amorphous materials are meanwhile expected to cause changes in bond force constant and a corresponding shift in the vibrational energy, with the transition from nanocrystalline graphite to amorphous carbons shown to shift the position of the G peak from ~ 1600 to $\sim 1510\text{ cm}^{-1}$ [61, 62]. Through irradiating a sample with an intense laser, typically continuous gas Ar, He-Ne, Kr in the visible, or He-Cd in the UV, holographic filtering and collection with a CCD detector inferences can then be made to the bonding present within the sample [60].

Thus with the ability to discern hybridisations of carbon, and speed and simplicity of measurement, Raman scattering is extensively used within the diamond community for the characterisation of films and particles. Further discussion of the relevant peaks and idiosyncrasies upon application of the technique to diamond is presented within the next chapter.

3.4 X-ray Diffraction

Upon a material being irradiated with x-rays, the electric field will cause an acceleration of the constituent electrons resulting in the spherical radiation of elastic scattered waves, termed Thomson scattering. Super-positioning of the wavefronts from each electron within an array of atoms with interatomic spacing comparable to the incident wavelength will then lead to interference of the scattered radiation. Considering the regular array of atoms within panel A of Figure 3.4, should the path length difference between scattering from successive layers be equal to an integer multiple of the wavelength constructive interference will occur in accordance with Bragg's law [64]:

$$2d \sin \theta = m\lambda \quad (3.1)$$

Where: d is the separation between diffracting planes, linked to the Miller indices and lattice constant of the crystal; θ is the angle of incidence and diffraction; m is an integer, termed the order of reflection; and λ is the wavelength of the probing x-rays. For polycrystalline films and powder with an isotropic distribution of grain orientations, constructive interference will then lead to Debye-Scherrer cones of high intensity for each Bragg reflection from planes lying parallel to the sample with varying θ , with a typical cross section shown within panel B of Figure 3.4. For perfect crystals and instrumentation the peak will present as a delta function, with crystal imperfections, thermal vibrations, and instrumental limitations from beam size to divergence causing peak broadening: should the sample be uniformly strained the changing unit size will be reflected in the position of the peak, while in-homogenous strain from crystal to crystal and crystallite size will cause a broadening of the peak distinguishable by the variation with $\sin \theta$.

As the absorption length for x-rays of 1.54 Å wavelength increases from $\sim 66 \mu\text{m}$ to $\sim 1 \text{ mm}$ for carbon and silicon respectively due to the increase in Z , XRD performed on thin film diamond on silicon will result in a large signal originating from the substrate [65]. Rather than using the conventional Bragg-Brentano geometry in which the sample is rotated at one half the angular velocity of the detector along the scattering plane, grazing incidences ($\sim 0.5^\circ$) are used within this thesis while sweeping the detector in the plane of the sample to maximise the signal from the thin film. In addition, the less than

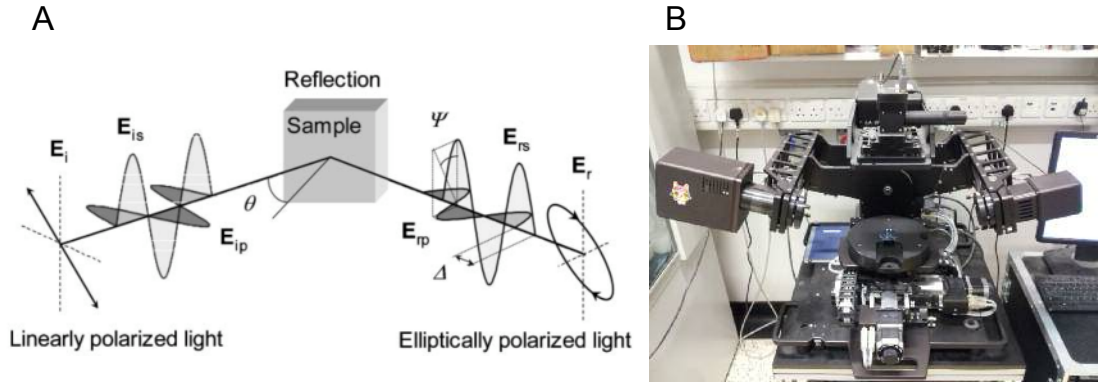


Figure 3.5: Spectroscopic ellipsometry. (A) Schematic of spectroscopic ellipsometry demonstrating incident linearly polarised light becoming elliptically polarised upon reflection from the sample surface due to the differing reflectivity for the two orthogonal electric field components, with the resulting phase shift ψ and amplitude ratio Δ dependant on the properties of the material stack. (B) J. A. Woollam M-2000D PSC_{RA} type SE used within this thesis for performing spectroscopic ellipsometry measurements. Panel A reproduced from [67] with permission of The Royal Society of Chemistry.

unity refractive index of materials at x-ray wavelengths are exploited through varying the incidence angle around the critical angle of the material, causing total external reflection and a varying penetration depths from $\sim 50 \text{ \AA}$ to several μm [65]. Thus through irradiating a sample with X-rays while varying θ and studying the reflected intensity, X-ray Diffraction (XRD) is a powerful non-destructive technique capable of identifying crystalline phases and imperfections present within thin film samples.

3.5 Spectroscopic Ellipsometry

Spectroscopic Ellipsometry (SE) involves illuminating a sample with a collimated beam of polarised light at oblique angles and measuring the change in polarisation upon reflectance to determine the film thicknesses, optical constants, and microstructure of a layered sample. Upon probing a sample with polarised light as shown within panel A of Figure 3.5, the reflection coefficients for components of light oscillating perpendicular and parallel to the plane of incidence, labelled s and p respectively, are provided by the Maxwell equation derived Fresnel relations and Snell's law [66]:

$$r_s \equiv \frac{E_{rs}}{E_{is}} = \frac{\cos \theta_i - (N_{ti}^2 - \sin^2 \theta_i)^{\frac{1}{2}}}{\cos \theta_i + (N_{ti}^2 - \sin^2 \theta_i)^{\frac{1}{2}}} = |r_s| e^{i\delta_{rs}} \quad (3.2)$$

$$r_p \equiv \frac{E_{rp}}{E_{ip}} = \frac{N_{ti}^2 \cos \theta_i - (N_{ti}^2 - \sin^2 \theta_i)^{\frac{1}{2}}}{N_{ti}^2 \cos \theta_i + (N_{ti}^2 - \sin^2 \theta_i)^{\frac{1}{2}}} = |r_p| e^{i\delta_{rp}} \quad (3.3)$$

Where: E_{is} and E_{ip} are the electric fields for the s and p incident components; E_{rs} and E_{rp} are the electric fields for the s and p reflected components; N_{ti} is the ratio of the complex refractive indices of the sublayer N_t and incident N_i materials; and θ_i is the angle of incidence with respect to the normal [66]. Ellipsometry then measures the ratio of the reflection coefficients, with incident angles set close to the Brewster angle of the sample in which the oscillatory direction of the radiating dipoles within the material maximise the difference between r_s and r_p [68]:

$$\rho \equiv \frac{r_p}{r_s} \equiv \tan \quad e^{i\Delta} \quad (3.4)$$

Where $\tan \quad$ is the amplitude ratio equal to $|r_p|/|r_s|$ and \quad is the phase shift between the two orthogonal components, equal to $\delta_{rp} - \delta_{rs}$ [66]. For simple two-layer structures assuming a lack of surface and interfacial roughness or oxide layer the above Fresnel equations can be used to calculate the physical parameters, with the amplitude ratio dependant on the real part of the complex refractive indices, n , and the phase dependant on the extinction coefficients, k . However, for more complicated structures spectra are compared to modelled \quad and \quad curves generated with computationally intense regression analysis to obtain the best fit with the measured \quad and \quad . As ellipsometry measures relative light intensities rather than absolute values of the orthogonal components ellipsometry film properties can be determined precisely with little noise from imperfections in the instrument or environmental sources. The interferometry of the phase meanwhile makes ellipsometry sensitivity to films of sub-nanometre thickness, with \quad able to track oxygen absorption processes on (111) silicon to a sensitivity of ± 0.02 of a monolayer [69].

While the schematic within Figure 3.5A shows the light reflected from the sample as being perfectly elliptically polarised, non-isotropic and non-perfect samples along with instrument imperfections will introduce depolarisation. To fully characterise the light

the Stokes parameters can be used to describe all degrees of polarisation present from fully polarised to totally unpolarised light, often represented in vector form to allow for the simple mathematical description and calculation of the polarisation state during measurement and known as the Stokes vector:

$$S = \begin{bmatrix} S_0 \\ S_1 \\ S_2 \\ S_3 \end{bmatrix} = \begin{bmatrix} 1 \\ -p \cos 2 \\ p \sin 2 \cos \\ -p \sin 2 \sin \end{bmatrix} \quad (3.5)$$

Where: S_0 represents the total light intensity; S_1 the difference in intensity of light linearly polarised along the x and y axis; S_2 the difference in intensity of light linearly polarised at $+45^\circ$ and -45° ; S_3 the difference in intensity of right hand and left hand circularly polarised light; and finally, p represents the degree of polarisation equal to $(S_1^2 + S_2^2 + S_3^2)^{1/2} / S_0$ [70]. While beyond the scope of this thesis, ellipsometry essentially measures 3 or all 4 of these Stokes parameters depending on the configuration of optical elements used. For a more detailed description of the mathematics behind the technique the reader is referred to the comprehensive textbook by Fujiwara [70]. With the use of light to probe the sample highly precise measurements can therefore be taken in atmosphere, vacuum, liquid, or hostile environments, making SE particularly suitable for *in-situ* studies of thin film growth.

To perform such a measurement modern spectroscopic ellipsometry instruments capable of real-time monitoring typically utilise a Xe arc lamp to produce unpolarised, visible white light. For thin film applications and the studying of free carriers within conductive films the spectrum can be extended into the UV and near-IR regions of the electromagnetic spectrum respectively. The beam is then collimated and 45° linearly polarised with a Polariser (P) such that $E_{ip} = E_{is}$, before impinging upon the Sample (S) and altering Ψ and Δ . The specular reflected beam then passes through an optional Compensator (C) and Analyser (A), with either rotating, before being separated by wavelength with a holographic grating or spectrograph and subsequently measured simultaneously with a CCD detector. Through taking Ψ and Δ spectra at multiple wavelengths and incident angles the analysis can be over-determined such as the number of measurement points exceed the number of unknown parameters, resulting in a

unique result to the fit. The J.A. Woollam M2000-D ellipsometer used within this thesis, pictured within Figure 3.5B, is of the PSC_RA configuration, with the ordering of the letters denoting the components used while the subscript R indicates the rotating optical element. As will be discussed fully with reference to diamond within the next chapter, the optical configuration used limits both the Stokes parameters and the range of ψ and χ measurable, significantly affecting the analysis.

3.6 Spectral Reflectance

Using a similar, albeit simpler, technique to SE, spectral reflectance (SR) involves the shining of non-polarised white light normal to a sample to model film thicknesses and indices of stacked films. As light reflects off the interfaces between layers within the stack and the surface, constructive and destructive interference occurs leading to oscillating intensity with probing wavelength with peaks occurring within the spectrum at:

$$2nt = m\lambda \quad (3.6)$$

Where t is the thickness of the film, m is an integer, λ is the wavelength of light, and n is the real part of the complex refractive index (2.4 for diamond within the visible region of the electromagnetic spectrum) [71]. At normal incidences the distinction between p and s polarised light is lost, leading to the reflection coefficients provided by the Fresnel relations within Equations 3.2 and 3.3 converging and defining the amplitude of oscillations:

$$r = \frac{N_t - N_i}{N_t + N_i} \quad (3.7)$$

With the lack of precise rotating optical elements the measurement and analysis is simpler and less costly, however the loss of phase information limits the intensity only technique to measuring films with thickness exceeding 20 nm. This is further limited by the 380–1050 nm spectral range of the Filmetrics F20 spectral reflectance used in comparison to the wider 193–1000 nm range of the J.A. Woollam M2000-D SE. Within this thesis SR is therefore used for confirmation of the *in-situ* laser and pyrometer interferometry predicted thicknesses and during the processing of comparatively thick

nanocrystalline diamond films.

3.7 X-ray Photoelectron Spectroscopy

During X-ray Photoelectron Spectroscopy (XPS) x-rays are used to probe and quantify the compositional and chemical state of a sample surface. When irradiating a sample with x-rays of sufficient energy, ejection of an electron and ionisation of the constituent atoms can occur as shown in panel A of Figure 3.6. The kinetic energy (KE) of the photoelectron is then related to the energy of the impinging photon and the binding energy (BE) of the particle within the atom through Einstein's photoelectric equation:

$$KE = h\nu - BE \quad (3.8)$$

Where h is the Planck constant and ν is the frequency of the photon, typically fixed at either 1486.6 eV or 1256.6 eV when using the $K\alpha$ radiation lines of either Al or Mg respectively as radiation sources [72]. As the electrons are located within discrete orbits surrounding the nucleus by electrostatic attraction, the binding energy of the particles therefore depends on the number of protons, and hence atomic number of the element. Neglecting the relaxation of the remaining electrons within the atom, termed 'final state effects', measuring the kinetic energy of resulting photoelectrons then permits the identification of elements within a sample with the number of peaks in the spectrum corresponding to the number of occupied levels. Furthermore, electron shells can be divided into two broad categories, core levels that remain tightly bound to the nucleus and valence level electrons that interact with other atoms to form compounds. Upon the formation of a compound the bonds formed will possess distinctive binding energies. Meanwhile, the change in charge on the surface of the atom will cause subtle electrostatic shifts in the binding energies of the core electrons with higher oxidation states increasing the binding energy, additionally allowing chemical state analysis [72]. Panel B of Figure 3.6 shows a XPS spectra of lead superimposed on a schematic of the band structure, detailing the characteristic peaks of the 4th and 5th quantum numbers with the staggered background due to inelastic scattering of photoelectrons. Calculating the intensities of the peaks and accounting for the differing photoionisation cross sections of the elements then allows compositional analysis with accuracy of between a few percent

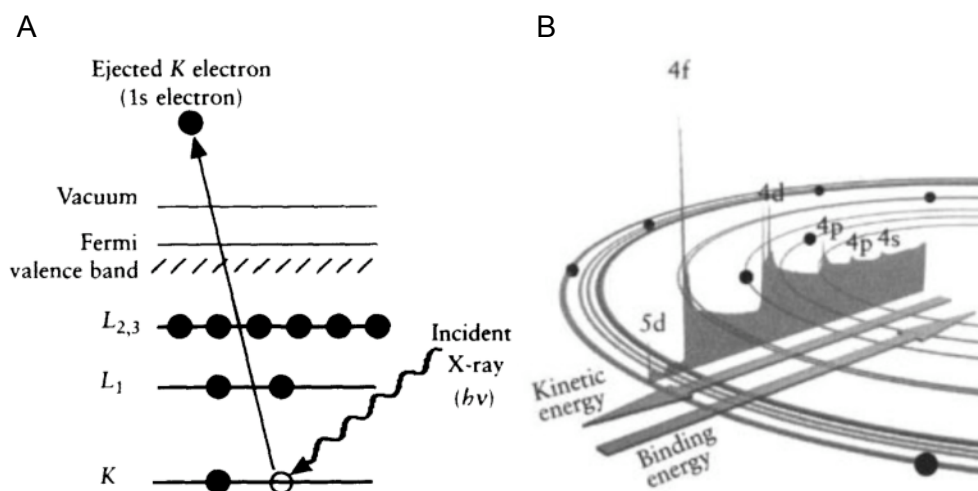


Figure 3.6: X-ray photoelectron spectroscopy. (A) X-ray irradiation with sufficient energy leads to the emission of a photoelectron with characteristic kinetic energy dependant on the binding energy of the shell, and subsequent ionisation of the atom. (B) XPS spectra of lead with atomic number 82 overlaid on a schematic of the electron orbits, highlighting the characteristic peaks and staggered background from inelastic scattering. Reprinted from [73], Copyright © 2003 by John Wiley & Sons Ltd, The Atrium, Southern Gate, Chichester, West Sussex PO19 8SQ, England, with permission by John Wiley & Sons, Inc.

and 30% dependant on instrumental effects and the accuracy of the determination of peak areas [72].

As typical for electron beam techniques, the distance liberated electrons can travel within a material is limited by inelastic scattering, termed the ‘inelastic mean free path’. Thus to retain the characteristic energy of the binding energy and contribute to peaks in the spectrum the electron must typically be created within the first $\sim 25 \text{ \AA}$ and $\sim 60 \text{ \AA}$ for kinetic energies of 200 eV and 1400 eV respectively [72]. To reduce the sampling depth further grazing incidences can be used, making XPS a highly surface sensitivity technique capable of qualitative analysis of elemental and chemical composition.

During XPS measurements an anode, often Al for laboratory sources due to its high intensity and line-width, is first struck with electrons from a high voltage source to create a beam of x-rays at 1486.6 eV with widths of $\sim 1 \text{ eV}$ [74]. Improvements in beam width to between 0.25–0.5 eV can be gained through utilising the Bragg reflection of a quartz single crystal, before directing the 100 μm diameter x-ray beam toward the sample [72,

74]. The resulting emitted photoelectrons are then slowed and focused before passing through a concentric hemispherical analyser while varying the applied voltage to select the energy of electrons passing through an exit aperture. Amplification and counting of the photoelectrons then results in XPS spectra similar to that within Figure 3.6B. To prevent collisions when traversing between sample and detector pressures of at least 1×10^{-6} Torr are however required necessitating vacuum pumps and suitable chambers [74]. Discussion of the analysis of XPS spectra will occur with reference to diamond within Chapter 5 while applying the technique to the characterisation of the polishing of NCD.

3.8 Chemical Vapour Deposition

Within this thesis a Seki, formerly ASTEX, AX6500 series reactor shown within panel A of Figure 3.7 has been used to produce the NCD samples characterised and processed using the microwave assisted chemical vapour deposition technique described within Subsection 2.2.3. The reactor consists of the ‘clam-shell’ water-cooled removable lid shown within the schematic of Figure 3.7B, with a dielectric window sealed between a water-cooled copper electrode and base plate through a tensioned spring to complete the vacuum chamber. The sample is held within a molybdenum holder placed at the centre of the copper electrode above a plenum chamber to control the temperature of the sample and keep the holder in place. Magnetron produced 2.45 GHz microwaves are then fed into a fundamental mode waveguide and radiated into the chamber through a coaxial conductor connected to the electrode and the waveguide connected to the chamber. The field then decreases radially outwards along the microwave-receiving underside of the electrode before travelling to the microwave radiating top of the electrode and converging and reaching maximum field strength above the sample. To prevent discharges as a result of standing waves from forming close to the dielectric window the separation between the underside of the electrode and the chamber walls, labelled 2 in Figure 3.7, is designed to be close to quarter of a wavelength. The separation between electrode and top of the chamber then gradually increases to keep a uniform electric field strength with decreasing electrode radius before culminating in a dome, with the distance 1 designed to be close to half of a wavelength to create a standing wave and

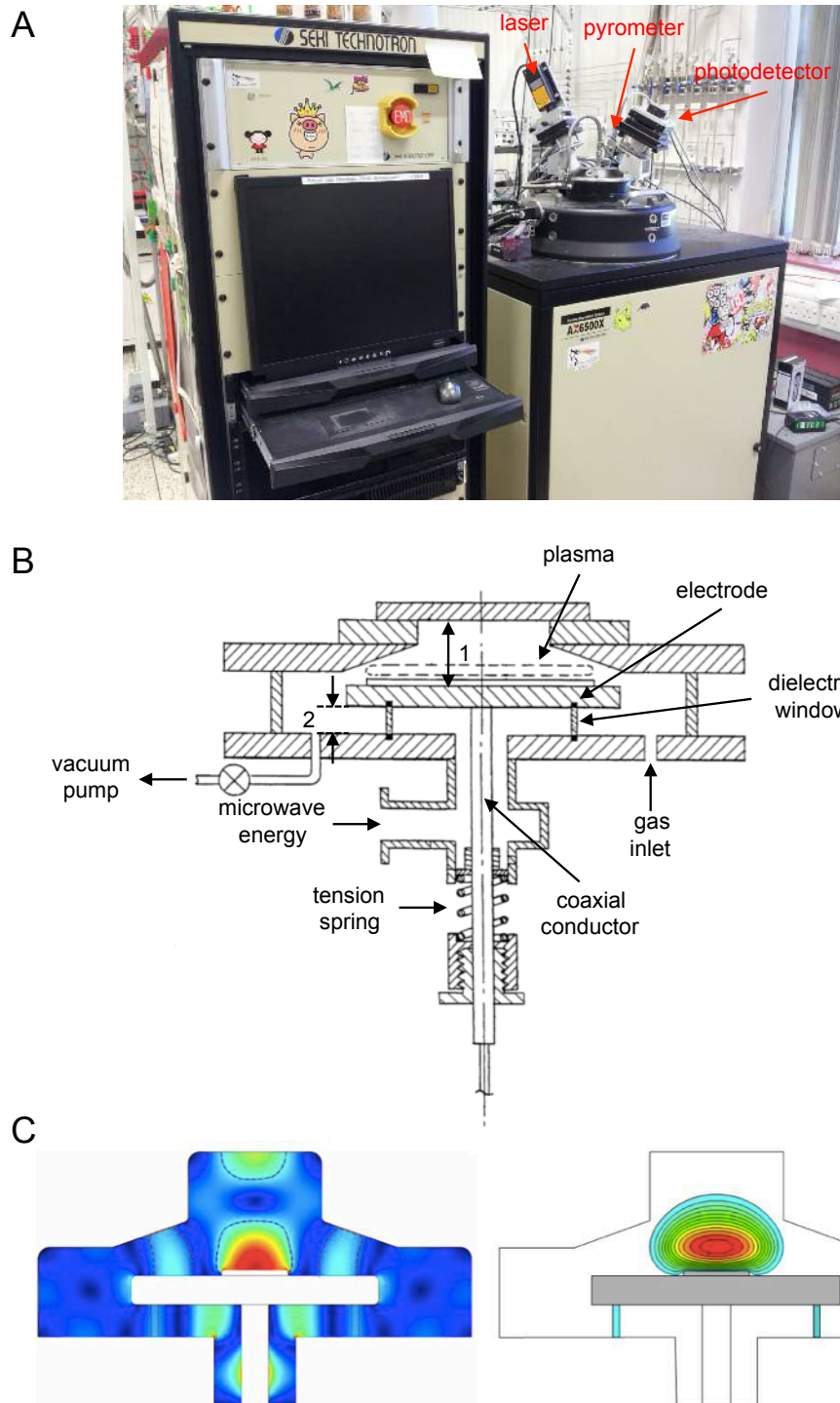


Figure 3.7: Seki AX6500 MWPECVD over-moded reactor. (A) Reactor at Cardiff Diamond Foundry equipped with 475 nm laser and photodetector, and pyrometer for *in-situ* monitoring. (B) Schematic of ‘clam-shell’ reactor design. (C) Electric field distribution and resulting 200 mbar plasma within the AX6500 reactor. Panel B reprinted from [75]. Panel C reprinted from [44], © IOP Publishing. Reproduced with permission. All rights reserved.

further enhance the electric field strength above the sample. As a result of the shape, the cylindrical component to the cavity excites the TM_{011} (blue dashes) mode with the addition of lobes from the TM_{021} (red dashes) mode as shown in panel B of Figure 3.7, producing the flat and extended plasma discharge modelled at 200 mbar shown to the right [44]. Unlike the more commonly used NIRIM tube and Seki TM_{013} mode reactors the dielectric window separating waveguide and process gas is placed at a minimum in the electric field, far away from and out of site of the plasma preventing etching and coating with amorphous material [75]. Such a design then allows large plasmas with uniform plasma density, allowing uniform deposition over a wide area [76].

The reactor at Cardiff Diamond Foundry is fully automated allowing for reproducible and long duration growth runs and equipped with rotary and turbo-molecular pumps to attain base pressures of the order 10^{-6} Torr between growth runs. In addition, the reactor is equipped with a Williamson dual wavelength pyrometer allowing the ratio measurement of temperatures between 475–1475 °C, with interferometry of the signal allowing tracking of the film thickness with a period of oscillation of ~ 360 nm. Enhanced monitoring of the film thickness is provided by a 445 nm laser and photodetector at an angle of incidence of 28° providing an interferometry period of 95 nm when assuming a refractive index of diamond of 2.4.

Chapter 4

Spectroscopic Ellipsometry of Thin Film Diamond Growth

With the applications of thin film diamond becoming both more numerous and demanding, characterisation of nucleation and the initial stages of growth are required to improve the quality of the resulting polycrystalline films. However, quantitative estimation of the impurity content is ruled out with Raman scattering due to its dependency on the distribution of non-diamond carbon, while techniques reliant on electrons are relatively insensitive to the differing carbon species present and constrained to surface studies by the electron mean free path. Therefore, spectroscopic ellipsometry with its ability to probe the depth variation while being equally sensitive to the diamond, non-diamond and void content within films as thin as 4 nm becomes a powerful alternative in the characterisation of the initial stages of thin film diamond growth. Within this chapter the methods of modelling ellipsometry spectra are first laid out within the context of the comparatively simpler amorphous carbon films, and then extended to give a brief overview of the ellipsometry of polycrystalline diamond to date. The method is then applied to the characterisation of the initial stages of growth on nano-diamond seeded silicon, with the results corroborated with Raman, AFM, SEM, and XRD.

4.1 Spectroscopic Ellipsometry of Amorphous Carbon

With the demonstration that amorphous carbon (a-C) films can exhibit diamond-like properties such as high mechanical hardness, chemical inertness, and low friction coefficient at a fraction of the cost of thin film diamond, research into the characterisation of such films has greatly expanded over the last half a century [77]. a-C films are typically produced through the ionisation of a carbon containing gas or the sputtering, ablation, or evaporation of a pure carbon target, resulting in a beam of medium energy carbon or hydrocarbon ions ($\sim 10\text{--}100$ eV) impinging upon the substrate. Upon passing through the surface sp^2 layer the ions will become trapped within the subsurface region in a process dubbed ‘sub-plantation’, leading to a local increase in the compressive stress and density, driving a phase transformation to sp^3 hybridised material [62, 78]. As a result, such films are typically composed of a mix of diamond like (sp^3), graphitic (sp^2), and linear (sp^1) hybridisations, while techniques utilising a hydrogen precursor can result in hydrogen incorporation of up to 60 at.% hydrogen in the carbon matrix [79, 80]. Films rich in sp^2 are typically denoted as glassy carbon (glassy-C), while those with a dominant sp^3 fraction are referred to as tetrahedral amorphous carbon (ta-C) or diamond-like carbon (DLC) [62]. As would be expected, the properties of such films vary with the differing hybridisations and amount of hydrogen present; the Vicker’s hardness has been seen to linearly increase from 12 GPa to 30 GPa upon an increase in the sp^3/sp^2 fraction from 3 to 6.14, while the thermal conductivity has been seen to linearly increase from ~ 0.3 to ~ 3.5 W/mK with an increase in density from 1.55 to 3.26 g/cm³ [81, 82]. The incorporation of hydrogen meanwhile has been seen to affect the lifetime and field emission stability of high sp^3 amorphous carbon films [83].

As a result of this peculiar combination of atomic sites, the dielectric function of amorphous carbon is dependant on the ratio and spatial correlation of the \rightarrow^* transitions of sp^2 and sp^3 sites in the ultraviolet with that of the \rightarrow^* electronic transition of the sp^2 clusters in the near infra-red–visible energy range [80, 84, 85]. In crystalline graphite the \rightarrow^* electronic transitions occur at ~ 4.5 eV, with strong absorption arising from the \rightarrow^* at 14.5–20 eV [86]. Meanwhile, in crystalline diamond the indirect band gap lies at ~ 5.45 eV, the first direct gap at ~ 7.2 eV, and the strong absorption peak at ~ 11.5 eV [87, 88]. Drawing parallels to the changes

in dispersion observed with silicon upon a transition from crystalline to amorphous ordering the loss of long range order leads to a reduction in the magnitude, an increase in the broadening, and a reduction in the peak energy of the strong absorption peaks and the electronic transitions attributable to sp^2 bonding; such a drop to ~ 9 eV has been observed for the $\sigma \rightarrow \sigma^*$ transition of a fully amorphous sp^3 material [77, 86, 87]. Meanwhile, the sp^2 sites present within ta-C films tend to form olefinic clusters distorted by strain from the sp^3 network while for films with reduced sp^3 content the larger sp^2 clusters contain aromatic rings [62, 89]. Therefore, for composite sp^2/sp^3 films, a strong absorption of 11.5–14.5 eV will result, while the $\sigma \rightarrow \sigma^*$ transitions of the amorphous sp^2 phase will lie below 4.5 eV with the size of the clusters and degree of distortion of the σ bonds controlling the band gap [62, 77, 79].

The simplest method to describe the resulting dispersion from the combination of sp^3 and sp^2 sites is through the use of the empirical Cauchy equation, derived to model the normal dispersion of materials observed within the transparent region away from resonant frequency peaks:

$$n(\lambda) = A + \frac{B}{\lambda^2} + \frac{C}{\lambda^4} \quad (4.1)$$

Where A – C are constants, and λ is the wavelength of impinging light. To account for the non-zero extinction coefficient observed when moving into weakly absorbing regions, a second separate formulation for $k(\lambda)$ was later developed:

$$k(\lambda) = D + \frac{E}{\lambda^2} + \frac{F}{\lambda^4} \quad (4.2)$$

Where D – F are constants left to vary during fitting. Using the model, Fedosenko *et al.* modelled the dielectric properties of DLC films produced with plasma enhanced chemical vapour deposition (PECVD) through the use of a two layer model of surface roughness/bulk [80]. During growth, methane diluted in helium was used as a carbon source while a varying bias voltage was applied to the holder between -250 and -500 V, resulting in film thicknesses of 1.01 – 1.65 μm . Upon performing SE between the range 1.3 – 5.4 eV the $n(\lambda)$ and $k(\lambda)$ values obtained can be converted to the imaginary part of the dielectric function through the knowledge that $\epsilon''(\lambda) = 2nk$, with the results being shown in panel A of Figure 4.1. As visible from the plot, all 4 samples demonstrate a

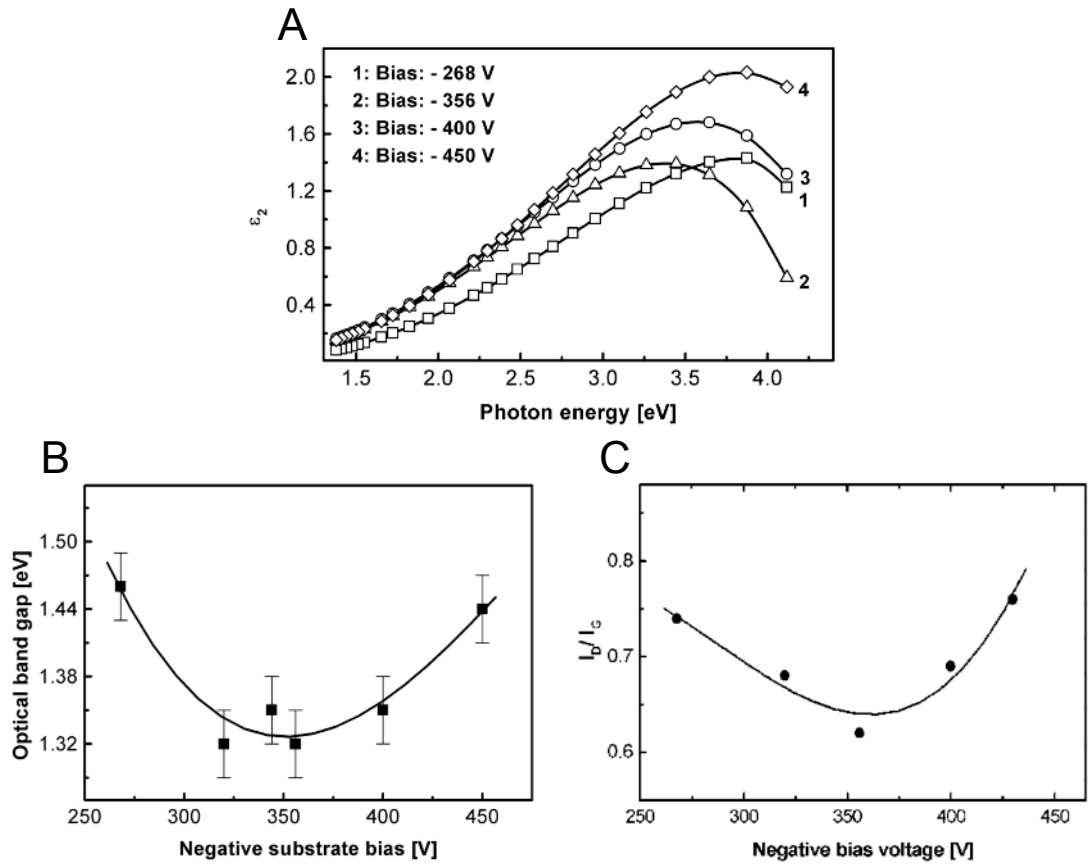


Figure 4.1: (A) $\epsilon_2(E)$ obtained from Cauchy based SE of PECVD produced DLC films with varying bias voltage, (B) resulting Tauc plot obtained optical band gaps, and (C) ratio of the integrated areas under the Raman D and G peaks. Upon an increase in the magnitude of the bias voltage, energetic ions cause sputtering of sp^3 stabilising hydrogen atoms, leading to a reduction in the sp^3 content within the film and an associated decrease in the optical band gap. Further increases in the bias voltage lead to helium ion bombardment, acting to reduce the size of the sp^2 clusters within the film, increasing the optical band gap. Micro-Raman studies corroborate such a model with the I_D/I_G ratio being inversely proportional to the sp^3 content with values of 0.7 suggesting a sp^3 fraction of 45–50% present within the film. Reprinted from Thin Solid Films, **406**, G. Fedosenko *et al.*, "Investigation of diamond-like carbon films synthesized by multi-jet hollow cathode rf plasma source", 275–281, Copyright (2002), with permission from Elsevier.

similar variation in α_2 with photon energy with a single peak at 3.4–3.8 eV attributable to the π transitions from sp^2 sites with slight variations in peak position and height dependant on the deposition conditions; an increase in the bias voltage from –268 V to –356 V results in the reduction of the peak position from 3.8 eV to 3.4 eV, with further increases to –450 V bringing about a gradual increase in the peak amplitude and position to 3.8 eV. Using the Tauc relation such a shift in peak transition can be correlated to the optical band gap:

$$\alpha_2(E) = B \frac{E - E_g}{E_2} \quad (4.3)$$

Where: E is the photon energy, B is a constant proportional to the joint density of states, and E_g is the optical band gap. Through plotting $(\alpha_2(E)E^2)^{0.5}$ vs. photon energy and approximating with a straight line, extrapolation to the x-axis intercept will then provide the optical band gap with the results of which plotted in panel B of Figure 4.1. Upon an increase in the bias voltage from –260 to –356 V the optical band gap can be seen to decrease due to preferential sputtering of hydrogen from the film due to the weak strength of the C–H bonds in comparison to that of the C–C bonds, supported by a reduction in FTIR absorption bands attributable to C–H stretching vibrations. The loss of tetrahedral stabilising hydrogen then causes a relaxation of the sp^3 sites into more stable sp^2 hybridised groups and a corresponding reduction in the optical band gap. Further increases in the bias voltage to –370 V and –450 V cause ion bombardment with the helium carrier gas, reducing the size of the sp^2 clusters within the film and thus increasing the band gap. Micro-Raman studies support the reduction in size of sp^2 inclusions with the ratio of the integrated area under the D peak to the G peak, shown to loosely correlate with sp^3 content, reaching a minimum value of 0.62 at –356 V as visible within panel C of Figure 4.1. Such an I_D/I_G value suggests a cluster size of ~1 nm while values of 0.7 correlate with a 45–50% sp^3 fraction within the film [80].

In a more rigorous approach, models reliant on the transformation from α_2 to α_1 through the use of the Kramers-Kronig dispersion relations can be used such as the Forouhi-Bloomer and Tauc-Lorentz formulations routinely used in the characterisation of amorphous materials [90, 91]. Paying consideration to the electronic states within covalent materials, the linear combination of atomic orbitals will lead to bonding and

anti bonding molecular orbital states, σ and σ^* respectively, which upon forming a solid broaden to create valence and conduction bands. Assuming zero absorption below the band gap, e.g. no Urbach tail due to disorder induced defect states lying within the band gap and parabolic edges to the conduction and valence band, the band structure can then be depicted as in Figure 4.2 [89, 91]. Given the maximum density of states occurs at E_σ and E_{σ^*} it can therefore be seen that the point of maximum absorption will occur when $\hbar\omega = E_{\sigma^*} - E_\sigma$, while the absorption will reach zero when the energy of impinging photons is below that of the difference between the bottom of the conduction band and top of the valence band, termed the band gap E_g . To model such a band structure Jellison and Modine combined the Tauc joint density of states with a classical Lorentzian oscillator, resulting in the aforementioned Tauc-Lorentz (TL) model. Through considering a charged electron bound to a positively charged atomic nucleus by a spring moving in a viscous fluid, the Lorentz oscillator models the resulting dielectric function as [69]:

$$\chi_{2L}(E) = 2nk = \frac{A_L E_0 C E}{[(E^2 - E_0^2)^2 + C^2 E^2]} \quad (4.4)$$

Multiplying by the Tauc relation of Equation 4.3 to account for the lack of absorption below the band gap then yields the Tauc-Lorentz model:

$$\chi_{2TL}(E) = \begin{cases} \frac{1}{E} \cdot \frac{A_L E_0 C (E - E_g)^2}{[(E^2 - E_0^2)^2 + C^2 E^2]}, & E > E_g \\ 0, & E \leq E_g \end{cases} \quad (4.5)$$

Where: A is the amplitude factor, proportional to the density of the material; E_0 is the peak transition energy or Penn gap; and C is the broadening parameter, inversely related to short-range order and crystallite size [89]. Given that a signal cannot be transmitted through a medium at a speed greater than that of light in vacuum, causality can be applied allowing $\chi_1(E)$ to be gained analytically through the Kramers-Kronig relations as:

$$\chi_1(E) = \chi_1(\infty) + \frac{2}{P} \int_{E_g}^{\infty} \frac{\xi \chi_2(\xi)}{\xi^2 - E^2} d\xi \quad (4.6)$$

Where P represents the Cauchy principal part of the integral while the parameter $\chi_1(\infty)$ accounts for modifications to $\chi_1(\omega)$ from electronic transitions occurring at high

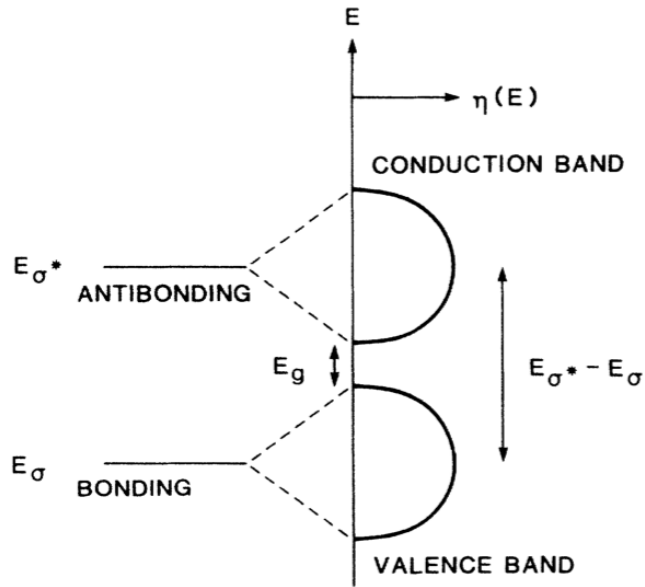


Figure 4.2: Idealised electronic band structure of a solid. Upon forming a solid the molecular states at E_{σ} and E_{σ}^* broaden into valence and conduction bands. With the parabolic density of states, $\eta(E)$, the point of maximum absorption will occur at $\hbar\omega = E_{\sigma}^* - E_{\sigma}$ while being zero when $\hbar\omega$ is less than the energy difference between the bottom of the conduction band and top of the valence band, termed the band gap E_g . Reprinted with permission from A. R. Forouhi and I. Bloomer, *Physical Review B*, **34**, 7018–7026, 1986. Copyright 1986 by the American Physical Society.

energies outside the spectral range used [86].

Gioti *et al.* successfully studied the dielectric dispersion of three a-C films produced with RF magnetron sputtering on silicon between 1.5–9.5 eV through the use of 2 or 3 TL oscillators [87]. During growth the bias voltage was varied, acting to enhance the sp^3 content through Ar^+ or N^+ bombardment [62, 87]. Also shown is a ta-C film grown through filtered cathodic vacuum arc deposition (FCVA), a technique utilising a toroidal magnetic filter to prevent larger atomic clusters from impinging upon the sample and increase the plasma ionisation to almost 100%, in turn producing a film with $\sim 80\%$ sp^3 content [62, 78, 87]. In the film grown with no external biasing, $0 \leq V_b \leq +10$ V, peaks at ~ 4.2 eV and ~ 13.7 eV attributable to the $\sigma \rightarrow \sigma^*$ and $\pi \rightarrow \pi^*$ transitions respectively are visible, close to the positions seen in c-G. Meanwhile the non zero value of $\epsilon_2(0)$ indicates the lack of a fundamental optical band gap. For low bias voltages the low energy ions will lack the energy required to penetrate the surface in the process of ‘sub-plantation’, preventing them from entering into an interstitial site as required to densify the subsurface region [62]. Upon an increase in the bias a downward shift of ~ 1 eV in the strong absorption peak is seen indicating an increased sp^3 /reduced sp^2 component due to the increased density and reformation with a larger sp^3 content, while the $\pi \rightarrow \pi^*$ shifts above that seen in c-G [62]. Coupled with the presence of an optical band gap the film contains significantly more diamond-like bonding with estimates of 25 and 50% sp^3/sp^2 for the zero bias and $-100 \leq V_b \leq 0$ V samples respectively [87]. Further increases in the bias energy lead to incident ions of high energy deeply penetrating the solid and losing significant energy in the form of phonons, allowing the excess density to relax to zero and preventing an increase in the sp^3 content [62]. As such the formation of a peak at ~ 1.4 eV is observed attributable to inter-band state transitions caused by interaction of p orbitals between neighbouring graphene layers [87, 92, 93]. In the case of the ta-C film with substantial sp^3 content ($\sim 80\%$), the $\pi \rightarrow \pi^*$ electronic transition contributes less resulting in a dielectric function dominated by a strong absorption peak at ~ 9.4 eV, approaching the position of ~ 9 eV observed in the case of a fully amorphous sp^3 film [86, 87].

As demonstrated, SE has shown to be a powerful technique in the characterisation of amorphous carbon films using both Kramers-Kronig and empirical modelling based techniques. From the reverse trends observed with varying bias energy between sput-

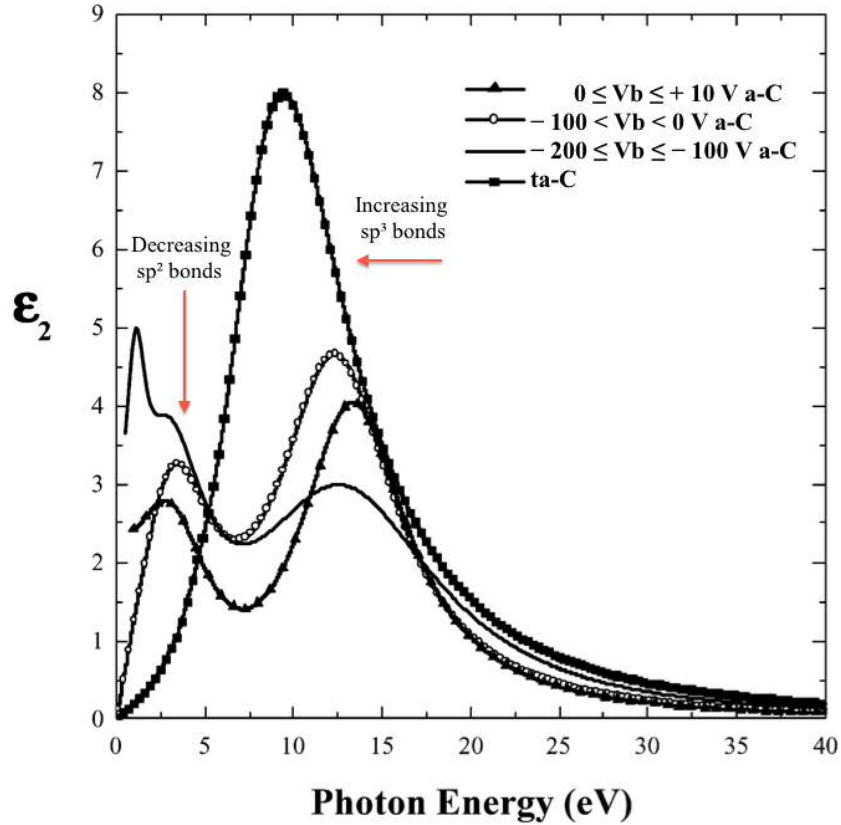


Figure 4.3: $\epsilon_2(\omega)$ of sputtered and tetrahedral amorphous carbon films. Upon an increase in the bias voltage of the magnetron sputtered a-C films a reduction in the position of the strong absorption peak and the magnitude of the sp^2 attributable \rightarrow^* peak is observed. Concurrently, the value of $\epsilon_2(0)$ drops to zero indicative of the formation of a fundamental optical band gap. Such a behaviour is attributable to the impinging carbon ions possessing enough energy to implant into interstitial sites, increase the density, and drive a phase conversion to sp^3 hybridised sites. Larger bias voltages lead to phonon induced relaxation reducing the sp^3 content and the addition of a third peak at ~ 1.4 eV attributable to inter-band transitions due to the interaction of neighbouring graphite planes. Lastly, further increases in the sp^3 content, as is the case of the ta-C film, lead to swamping of the \rightarrow^* electronic transition peak and a move of the strong absorption peak close to that of fully amorphous sp^3 at ~ 9 eV. Adapted from [87]. Reprinted from Diamond and Related Materials, **12**, M. Gioti and S. Logothetidis, "Dielectric function, electronic properties and optical constants of amorphous carbon and carbon nitride films", 957–962, Copyright (2003), with permission from Elsevier.

tering and PECVD produced films it can be seen that the dielectric function heavily depends on the deposition conditions, the resulting co-ordination, and relative amounts of sp^2 and sp^3 hybridised material. Combined with the fact that it is often difficult to probe the UV region where strong absorption peaks are expected to occur with available lamp based light sources, the study of carbon based materials is far from trivial [86, 87]. The application of the models discussed above will now be extended to polycrystalline diamond films, culminating in the studies performed on the initial stages of growth of nanocrystalline diamond at Cardiff Diamond Foundry.

4.2 Previous Spectroscopic Ellipsometry Studies of Polycrystalline Diamond

4.2.1 Bulk Layer

As the potential applications for diamond films become both more numerous and demanding, characterisation techniques capable of resolving the differing carbon containing phases present on the substrate and within the resulting growth with equal sensitivity are required to optimise film growth. While Raman is commonly used for such characterisation, the relative strengths of the spectral features are sensitive to the distribution of non-diamond carbon while being insensitive to the void content [94, 95]. Techniques utilising electrons meanwhile such as AES, RHEED, and XPS are limited in their sensitivity to different carbon environments while the short mean free path of electrons prevents all but characterisation of the surface [95]. Thus with its ability to non-destructively probe the depth variation in the optical constants with equal sensitivity to diamond, non-diamond, and void content in films as thin as 4 nm, SE is a powerful technique for the characterisation of diamond growth [96, 97]. With the requirement of a refractive index contrast between substrate and film however, SE characterisation of diamond films is typically only possible for heavily B doped homoepitaxial growth, or heteroepitaxial growth [98]. Furthermore, single crystal heteroepitaxy is limited to growth on iridium substrates due to its unique ability to dissolve and then expel carbon sufficiently fast for efficient nucleation [12]. Thus, ellipsometry of growth on foreign substrates is predominantly performed on polycrystalline films with grains of varied size and orientation, and interfacial grain boundaries.

At the point of coalescence of individual grains within this polycrystalline material the termination of growth will result in the presence of dangling bonds and a variety of hydrogenated sp^3 , sp^2 , and sp^1 hybridised impurities [99, 100]. For films grown with minimal hydrogen content within the plasma the lack of significant sp^2 etching will then result in these groups forming non-epitaxial nucleation sites on crystal facets, terminating existing growth and placing a limit on the maximum size of grains [97, 101, 102]. As a result of the significant surface/volume ratio of the grains as much as 10 at.% of the carbon can be present within the grain boundaries for NCD films with grain sizes of less than 100 nm. In combination with the increased non-diamond content a gentle transition from graphitic like to hydrogenated sp^3 sites have been observed to occur upon a reduction in the diamond grain size from 60 nm to 9 nm [103]. Growth temperatures are also expected to influence the hybridisations present with temperatures exceeding 500 °C causing a relaxation from sp^3 to sp^2 sites present within amorphous carbon films, while temperatures below 500 °C result in quenching in of sp^3 sites with an appropriate choice of precursor energy [96]. As such the nature of the grain boundaries within NCD films are expected to vary significantly with not only deposition conditions but also grain size and hence film thickness.

Should the grains and interfacial regions remain large enough that they retain the optical constants of the bulk, characterisation with ellipsometry can then be carried out on the films through the mixing of the dielectric functions of the diamond and grain boundary regions with the use of an effective medium approximation (EMA) [88, 104]. Assuming that the mixing is homogenous at scales close to the wavelength of the probing light and spherical inclusions of dielectric function $\epsilon_1, \epsilon_2, \dots$ inside of a host matrix of dielectric function ϵ_h , the effective medium can be represented by [104]:

$$\frac{\langle \epsilon \rangle - \epsilon_h}{\langle \epsilon \rangle + 2\epsilon_h} = f_1 \frac{\epsilon_1 - \epsilon_h}{\epsilon_1 + 2\epsilon_h} + f_2 \frac{\epsilon_2 - \epsilon_h}{\epsilon_2 + 2\epsilon_h} + \dots \quad (4.7)$$

Where: f_1 and f_2 are the volume fraction of the component materials with dielectric functions ϵ_1 and ϵ_2 respectively, $\langle \epsilon \rangle$ is the dielectric function of the effective medium, and ϵ_h is the dielectric function of the host medium [104, 105]. However, while such assumption is valid in the case of coated sphere microstructures and ceramic-metallic composites, in cases such as surface roughness and interface layers where the role of host

and inclusion is not clear, it can be seen that the effective medium approximation will yield a result dependant on this assignation even if the volume fractions remain constant [88, 106]. To remove this ambiguity the widely used Bruggeman effective medium approximation was created in which self consistency is achieved through allowing the effective medium to act as its own host by setting n_h equal to $\langle n \rangle$ [69, 104].

With such an approach Hong *et al.* measured the pseudo optical constants of a 200 nm thick diamond film grown at 800 °C through the use of the optical constants of bulk diamond, enabling the dispersion in the dielectric function of the grain boundary content to be measured [96]. With increasing photon energy the authors observed an increase in absorption with photon energy suggestive of the opening of a fundamental gap, with the Tauc relation suggesting an optical gap of 0.77 eV indicative of 60 at.% sp² content or nanocrystalline graphite planes of ~ 2 nm in size [96]. While the shape of the dielectric function of glassy C shows the inverse behaviour with rising extinction coefficient as E tends to 0, the authors note that the average magnitude are similar between the measured constants and glassy carbon [96]. Mistik *et al.* obtained a similar increase in absorption with photon energy for films grown between 520 and 600 °C, but conversely found the impurity content best modelled by the dielectric function of amorphous carbon with a single strong absorption peak outside of the 0.7–5.5 eV spectral range used [97]. However, parameter correlation with the complicated microstructure often prevents the direct measurement of the optical constants of the impurities for thin films. For this reason, the optical constants of glassy carbon, graphite, or amorphous carbon are commonly used as a substitute [71, 88, 94, 97]. Through assuming the dielectric functions of the component materials the photon energy independent parameters, i.e. the volume fractions and thicknesses, can then be uniquely determined through linear regression analysis.

Through the use of the optical constants of bulk diamond and glassy carbon Cong *et al.* performed SE on MPCVD produced films between the spectral range 1.6–4.2 eV, with the results and mean square error, χ^2 , of the fitting procedure plotted in Figure 4.4 [94]. To enhance the nucleation density the Si substrates were first polished with a 1 μ m diamond powder while the ensuing growth was carried out at 800 °C with a 0.7% flow of CH₄ diluted in H₂. A poor fit is initially observed when fitting with the optical constants of bulk diamond due to the increased absorption from grain boundary material

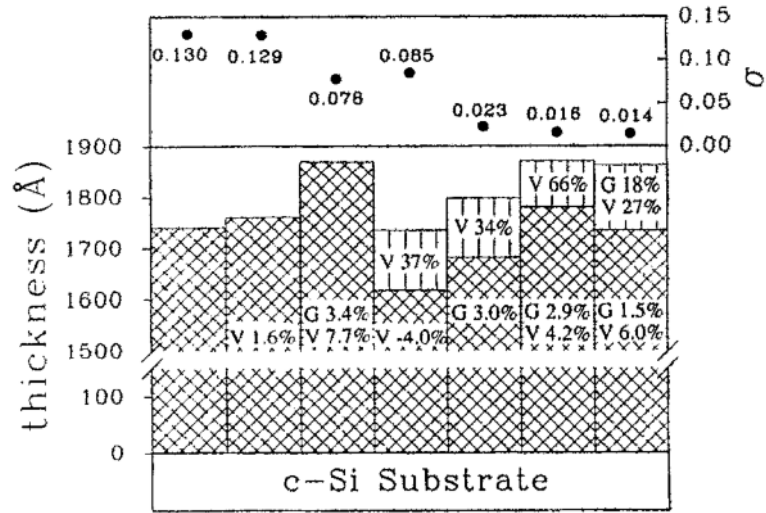


Figure 4.4: SE modelling of nanocrystalline diamond films. The initial large unbiased estimator of the mean square deviation, σ , obtained when fitting the film with the optical constants of diamond improves with successive fits incorporating volume fractions to account for the void in the bulk and surface, and grain boundary non-diamond through the optical constants of glassy carbon. Corresponding increases in bulk thickness is observed when the refractive index of the effective medium of the bulk decreases. The addition of glassy carbon to the surface roughness is unjustified with little reduction in σ while also being highly correlated to that in the bulk, supporting the residence of non-diamond within the grain boundary interfaces. Reprinted from [94], with the permission of AIP Publishing.

and the roughness induced scattering arising from the competitive nature of growth. The inclusion of glassy carbon and void with fractions of 7.7% and 3.4% respectively reduce the value of n_2 by 40% along with an increased thickness due to the reduction in the effective refractive index of the effective medium. Further improvements to the fit to a n_2 value of 12% of that when fitting with the optical constants of bulk diamond is obtained with the incorporation of a second EMA to represent the surface roughness, with thickness of 8.9 nm and void fraction of 66% on top of the 178 nm bulk layer. The inclusion of sp^2 to the surface roughness does little to the value of n_2 while being highly correlated with the sp^2 content within the bulk indicating the additional parameter is unjustified. With the non-diamond content expected to reside within grain boundaries it is to be expected that the content within the surface roughness would be lower than that in the bulk [94].

Alternatively, the optical constants of the film can be directly modelled through the use of the Lorentz oscillator and its derivatives or through other Kramers-Kronig consistent models such as the Forouhi-Bloomer dispersion model for amorphous semiconductors [90, 107–111]. Using a Lorentz oscillator Hu *et al.* used a tri-layer model consisting of surface roughness/NCD film/Si substrate to model spectra obtained on intrinsic NCD grown with varied oxygen content and growth temperature [108]. As the first direct optical gap and the resulting beginning in absorption of single crystal diamond occurs at 7.2 eV, within the 0.1–4.7 eV spectral range used the expected high purity of the NCD films will result in a n_2 value of zero. With this assumption the Lorentz oscillator of Equation 4.4 reduces to the KK satisfying Sellmeier dispersion model:

$$n^2 - 1 = \frac{E_0 A}{E_0^2 - E^2} \quad (4.8)$$

Where: n is the refractive index, E_0 is the peak transition energy, A is a constant chosen to match the experimental data, and E is the photon energy. Using the dielectric dispersion provided by the Lorentz oscillator the authors used the Sellmeier model to obtain an average value of E_0 of 10.3 eV, lying between the strong absorption peak of crystalline and fully amorphous sp^3 with locations of 11.5 and 9 eV respectively [86, 87]. Meanwhile, through the use of Wemple’s approximation an estimated band gap

of 6.9 eV was found, close to that of bulk diamond [108]. Using a similar approach, Zimmer *et al.* modelled the dielectric function of heavily boron doped nanocrystalline films between the spectral range 0.03–4.3 eV. In a similar fashion the best fit within the UV-visible part of the spectrum was obtained through the use of a Lorentz oscillator with the fit procedure suggesting a Penn gap of 10.5 eV, while the use of a Tauc-Lorentz oscillator with a term to account for the E_g suggested a band gap of 7 eV. A second Lorentz oscillator positioned at 0.2 eV was seen to be effective at modelling the increased absorption in the mid infrared from boron acceptors, close to the known level of 0.37 eV from the top of the valence band [109].

For composite NCD/amorphous carbon films with a larger non-diamond component, the substantial absorption from π states with the spectral range commonly used with lab based light sources tend to dominate the dielectric function [86, 112]. Boycheva *et al.* modelled such a NCD/a-C film prepared under 17% CH₄/N₂ conditions within the spectral range 1.4–4 eV in combination with reflectometry between 1.2–6.2 eV [107]. Without the presence of atomic hydrogen to suppress ‘re-nucleation’, the resulting film consisted of 3–5 nm diamond grains embedded within an amorphous matrix with an estimated crystalline/matrix volume ratio of 1/1. Upon fitting a peak in the extinction coefficient was observed at 3.1 eV, as to be expected with the amorphous nature of the sp² sites, while a Tauc plot provided an optical band gap of 1.4 eV close to that observed for the a-C films within Figure 4.1 [107].

4.2.2 Seed Layer

Due to the high surface energy of diamond relative to silicon (6 to 1.5 J m⁻² for the {111} Si face) in combination with the low sticking probability of carbon containing precursors, attempts at polycrystalline diamond growth on mirror polished silicon typically result in nucleation densities of 10⁴–10⁵ cm⁻² [14, 113]. To increase this density and facilitate the production of coalesced thin films a pretreatment step is therefore required. The most common methods of which involve coating the substrate with small diamond particles suitable for homoepitaxial growth, be it through mechanically embedding with a diamond paste or tailoring of the electrostatic attraction between substrate and a nano-diamond colloid [14, 39, 114, 115]. Upon being subjected to CVD, growth of these relatively stable nuclei occur from impinging methyl radicals from within the gas phase,

or from the diffusion of ad-atoms on the silicon surface due to their preference to bond to existing nuclei [113, 116]. As a result, isolated three-dimensional islands will form in accordance with the Volmer-Weber growth model in which the free surface energy of the film is substantially larger than that of the substrate [13]. Should the size of these nuclei be larger than the critical size of 3 nm, the isolated islands will continue to grow both laterally and vertically until coalescence, at which point growth transitions to the van der Drift model of competing columnar crystals [14, 97, 113]. During the nucleation phase the inevitable surface oxide on the silicon substrate will be chemically etched by the hydrogen plasma and replaced with a continuous amorphous/ β SiC, with an estimated critical thickness of 9 nm found with BEN studies and kinetically limited by silicon diffusion through the existing carbide layer [116–123]. After plateauing in thickness such a SiC layer then acts as a diffusion barrier to further carbon atoms, enabling the formation of critical clusters of carbon favourable for diamond nucleation [119, 124]. As a result, it is to be expected that the amorphous carbon content will peak at this interface due to the the large surface/volume ratio of the diamond nuclei with a contribution from these carbon clusters [119]. Meanwhile it is also expected that the entirety of the void content will occur during this period of Volmer-Weber growth and remain within the film once overgrown by crystals of higher growth rate [97].

Expanding upon the models discussed previously, other authors have more comprehensively taken into account the initial stages of growth observed during heteroepitaxial growth and the gradients expected in the void and non-diamond content [71, 95, 97]. Comparing the fits with and without such a seed layer, Mistrik *et al.* modelled the SE spectra between 0.7–5.5 eV obtained on NCD films grown at 520–600 °C, with a H₂ rich plasma on top of nano-diamond seeded silicon [97]. Through linear regression analysis with the optical constants of diamond and amorphous carbon from the literature, a thin seed layer (15–32 nm) was suggested of reduced refractive index due to the presence of voids and a larger extinction coefficient due to an enhanced a-C content. For one such film grown at 600 °C the fitting procedure indicated a seed layer of 26 nm buried under 175 nm of bulk in which the a-C content was 4 times higher than that in the bulk at 19.8%, with all of the void content within the film constituting 5.1% of this seed layer. While the addition of this layer did little to change the mass thickness of the a-C constituent of the film, over the entire sample set the MSE was seen to reduce from

15 to ~ 13 , supporting the incorporation of this seed layer. However, the authors also noted a significant correlation between the thickness of the bulk and seed layer and the impurities within each layer, suggesting non-unique results with multiple combinations of fractions of the constituents and thicknesses could provide the same quality of fit [97]. In an attempt to validate the sp^2 content indicated by SE the authors performed micro-Raman. Taking into account the differing Raman scattering ratios of diamond and non-diamond content the authors estimate diamond contents of 92–97%, similar to the 84–93% obtained through SE [97, 125, 126].

Pinter *et al.* meanwhile performed SE between 1.9–4.1 eV on bias enhanced nucleation produced seeds at 730 °C and the resulting films produced at 820 °C while calculating sp^2 , H, and SiC contents through Rutherford Backscattering Spectrometry (RBS) in combination with Elastic Recoil Detection (ERD) [95]. After 8 minutes of H₂ plasma cleaning followed by 8 minutes of BEN the authors observed a 3.5 nm layer composed of 95% diamond/0.6% graphite/4.4% SiO₂ with ellipsometry. After an iterative process similar to that within Figure 4.4, SE performed after an hour of growth revealed a 21 nm seed layer of 50% graphite/43% void/7% SiC buried under a 189 nm bulk layer of 2% graphite content, in good agreement with a 3% graphite composition estimated by RBS-ERD. The hydrogen content obtained with ERD within the film was 2%, correlating with the graphitic content suggested with SE and suggesting coexistence within the grain boundaries grain boundaries. Lastly, on top of the bulk film a 17% graphite/83% void layer due to carbon condensation at the end of plasma deposition was identified with ERD estimating a correlating 18–20% H content [95].

Using the reference constants of diamond in combination with those of glassy carbon, Lohner *et al.* found a similarly absorptive seed layer for films grown with CH₄ diluted in varied H₂/Ar chemistries. For similarly produced BEN films grown under 1% CH₄/89% H₂/10% Ar conditions at 750 and 700 °C during nucleation and growth respectively, a seed layer of thickness 41 nm was found to contain 30.8% glassy-C in comparison to 0.13% within the 278 nm thick bulk layer. However with the spectral range used of 0.7–6.5 eV, extending further into the UV than previous studies, the authors observed a discrepancy in the measured and modelled spectra due to the loss of long range order of the diamond crystallites, and hence modelled the diamond component with a Tauc-Lorentz oscillator. With this revised model the fit suggested a seed

layer of 41 nm of 21.6% glassy-C under a 277 nm bulk of 0.77 % glassy-C, reiterating the existence of an inferior quality seed layer when more accurately modelling the changing dielectric function with loss of long range order of diamond [71]. As such, SE has demonstrated its ability to study the variation in optical constants with depth allowing the characterisation of the initial stages of diamond growth, with the results corroborating with techniques requiring more complex experimental apparatus and offering varying sensitivity to the constituent materials.

4.2.3 Microcrystalline Films

As the thickness of nanocrystalline diamond films increase, the extensive periods of van der Drift overgrowth of competing crystals can lead to peak to peak roughness values exceeding 100 nm. Should this roughness exceed $\sim 30\%$ of the probing wavelength, multiple scattering from the largest crystallite peaks will lead to a steady decrease in the degree of polarisation, p , of the reflected light [66, 127]. The first panel of Figure 4.5 demonstrates the steady reduction in polarisation below a probing wavelength of 413 nm (3 eV) obtained on a ~ 200 nm thick NCD film, obtained with a PSC_{RA} instrument capable of producing a depolarisation spectrum through the measurement of all Stokes parameters [128]. Thickness in-homogeneity of the film also acts to reduce p through introducing a probability density to the measured intensity of the S_1 , S_2 , and S_3 parameters at the detector, becoming most pronounced when each of the parameters reach a maximum in magnitude [129]. As the S_3 ellipsometry parameter detailed within Equation 3.5 is equal to $-p \sin 2\psi \sin \Delta$ it can be expected that at the zero crossing of Δ at 3.4 eV within the second panel of Figure 4.5 the value of S_3 will reach a minimum, producing the valley observed in the depolarisation spectrum. For instrument configurations incapable of measuring all four Stokes parameters however, such as P_RSA where the handedness of S_3 is indeterminate and PSMA where S_1 and S_2 cannot be measured in a single measurement, the assumption of perfectly polarised light can lead to misinterpretations of the acquired spectra. Such a misinterpretation is shown in the bottom 2 panels of Figure 4.5, where the Δ and ψ obtained with the PSC_{RA} instrument taking into account the depolarisation spectrum are plotted along with Δ and ψ obtained on the same film through the use of P_RSA instrument. As scattering becomes significant above 3.6 eV (344 nm) it can be seen that significant differences

in the spectra are observed, potentially leading to the incorrect determination of the ellipticity of reflected light for the P_RSA instrument [128]. The poor continuity in the spectra of the rotating polariser instrument at 0° crossings and ±180° transitions when the light is almost linearly polarised arise from the lack of measurement of S_3 . As such S_3 is only determinable from conversion from the \cos term within S_2 detailed in Equation 3.5 with the associated large errors around 0° and ±180° [68].

With regards to modelling, as the scale of the roughness exceeds 10% of the probing wavelength used, the mixing of diamond and void can no longer be considered homogenous, and thus unsuitable characterising with the effective medium approximation [69]. To account for the large pyramidal crystallites, smaller crystallites from secondary nucleation at grain boundaries, and the resulting concentration gradient Cella *et al.* successfully used a stack of two EMA layers of varying void fraction to model the roughness on micron thick polycrystalline diamond films [130]. Across a series of 0.6–2 µm thick films grown at varying temperature and methane admixture, the fitting procedure suggested a layer of ~38% void fraction placed on top of a denser ~9% void fraction layer, with average thicknesses across the sample set of 27 nm and 47 nm respectively [130].

As films approach micron thicknesses with lateral crystallite dimensions and roughness values of the order of microns, non-specular scattering can occur causing a reduction in the intensity at the detector [131–133]. Should SE be possible, the low signal to noise ratio will then drastically increase measurement errors [66, 107, 134]. Figure 4.6 demonstrates such a reduction in intensity in p and s polarised light reflected from MCD films grown at 1% CH₄/H₂ on 12 µm powder scratched silicon with increasing durations of 30 min. (○), 60 min. (□), and 90 min. (△) [134]. In combination with the E₁ transition visible at ~3.4 eV indicative of incomplete coverage of the substrate and inhomogeneity at the scale of the probing light (1.6–4.5 eV), fitting of the films with an EMA was then deemed impossible [134]. To facilitate ellipsometry, the wavelengths used can then be extended into the IR to provide immunity from significant light scattering and prevent potential breakdown of the effective medium approximation [106, 135, 136]. Using an IRSE ellipsometer between the range 3–12 µm (0.1–0.4 eV) using both the reference optical constants of diamond and on a wavelength by wavelength fitting basis, Fang *et al.* and Wang *et al.* were able to effectively characterise microcrystalline diamond films [106, 135]. The authors were able to successfully compare the optical constants of a

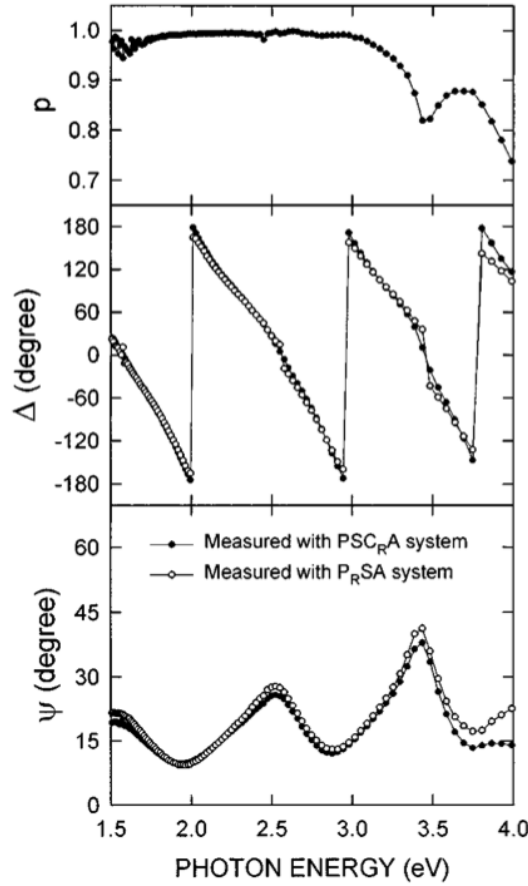


Figure 4.5: Depolarisation spectra obtained on a 200 nm thick NCD film obtained with a PSC_RA instrument and resulting p and Δ parameters, and Δ and ψ parameters obtained with a P_RSA instrument. Increasing scattering as the wavelength of probing light approaches the scale of surface roughness leads to a decrease in the degree of polarisation, p . As a result, misinterpretation of ellipticity for the P_RSA instrument, where perfectly polarised light is assumed, is seen as visible by the divergence of the two spectra above 3.7 eV. Discontinuities in Δ for the P_RSA instrument at 0° and $\pm 180^\circ$ are a result of instrument errors without the measurement of S_3 . Reprinted from [128], with the permission of AIP Publishing.

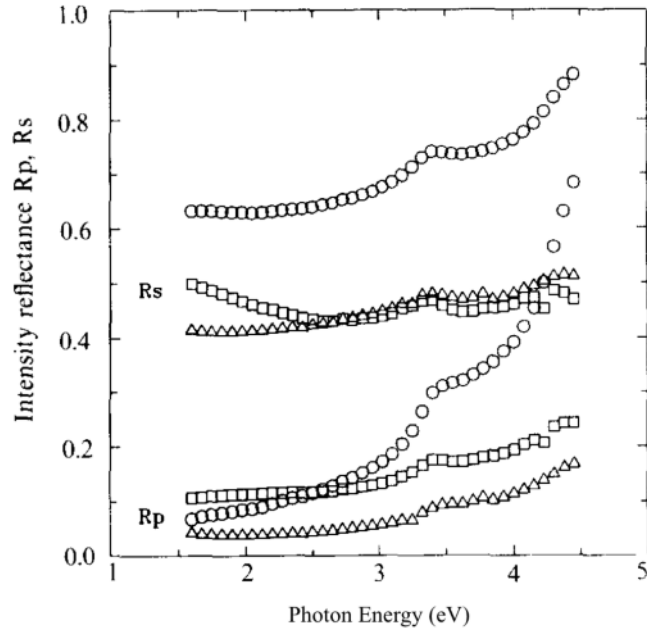


Figure 4.6: Reflectance intensity for R_p and R_s polarised light obtained for MCD samples after 30 min. (\circ), 60 min. (\square) and 90 min. (\triangle) of growth. As van der Drift growth continues the increased diffuse scattering attributable to roughness reduces the intensity of light at the detector. With ellipsometry determining the polarisation state from the intensity, such large scattering makes determination of the pseudo-dielectric function difficult and increases measurement errors. Reprinted from *Diamond and Related Materials*, **2**, J. Cifre *et al.*, "Spectroscopic ellipsometry measurements of the diamond-crystalline Si interface in chemically vapour-deposited polycrystalline diamond films", 728–731, Copyright (1993), with permission from Elsevier.

HFCVD film with a roughness of 879 nm on top of a 12 μm bulk layer to a smoother MPCVD produced film [135]. However, as a consequence of IRSE being only moderately sensitive for detection of the expected extremely thin interfacial layers, the addition of a 9 nm SiO_2 layers scarcely affects the quality of the fit preventing characterisation of the interfacial region [106, 135]. Alternatively, Cifre *et al.* embedded the surface of the polycrystalline diamond film within a polyester resin, followed by a chemical etch of the silicon substrate to reveal the smoother nucleation side of the diamond film more suitable for characterisation with ellipsometry [134]. As the surface roughness/polyester boundary lies below the film, the bulk layer can then be considered as a semi-infinite medium due to the significant roughness causing dispersion of incident light, preventing interference of reflected light. SE in combination with XRD was then able to identify a 25 nm seed layer of β -SiC, glassy-C, and air atop the $\sim 5 \mu\text{m}$ bulk layer [134].

Therefore it can be seen that the scattering that occurs with the substantial roughness present within diamond film prevents ellipsometry studies of thicker microcrystalline diamond films, and hampers ellipsometry of thicker nanocrystalline diamond films. As a result, ellipsometry is more suited to the initial stages of diamond growth before significant roughness has developed and in applications where the atomic scale sensitivity can be used.

4.2.4 *In-Situ* Spectroscopic Ellipsometry

As demonstrated, the non-diamond content contained within films varies significantly with both thickness and the process conditions used, with real time studies of the initial stages of growth therefore being advantageous to exert greater control over the production of high quality films [96, 128, 137]. However, the energetic and highly reactive plasmas used to produce diamond films rule out techniques utilising electrons or ions, leaving only the possibility of techniques reliant on photons [137, 138]. Of the possible choices, SE is advantageous due to its ability to provide the volume fractions of diamond, sp^2 , and void concentrations at equal sensitivity for films of 4 nm thickness, with the added benefit of being passive without the need for equipment to be placed within the reactor [96, 139–141].

With *in-situ* characterisation comes additional complexity due to the dynamic nature of data collection and the elevated temperatures of the sample. For instruments

that use rotating optical elements the spectral acquisition time is defined by the rotation rate, typically in the range 10–100 Hz [68]. *In-situ* studies previously carried out NCD make use of a polariser rotating at 15.6 Hz and a photo-diode array enabling simultaneous detection of the polarisation state across the spectral range at an acquisition time of 32 ms [128]. Upon averaging, measurement and subtraction of the background with the shutter closed, real-time analysis, and data storage the sampling time was increased to a minimum of 10 s [96]. Within this time deposition rates of the order of 0.1 nm s^{-1} will lead to an increase in thickness of the film of $\sim 1 \text{ nm}$, sufficient for the accurate monitoring of growth [96, 139].

To obtain the dielectric function of the substrate at the elevated temperatures used during growth an unseeded Si wafer was subjected to CVD conditions, with the low nucleation density of diamond on unseeded wafers expected to prevent diamond growth from altering the ellipsometry spectra before thermal equilibrium [96]. Temperature calibration of the silicon is then possible through the use of the position of the $E_0'-E_1$ critical point complex at 3.4 eV, at higher temperatures predominantly arising from the E_1 transitions along the Λ direction in the Si band structure [96, 128]. As the peak position is expected to decrease linearly with increasing temperature from 3.23 eV at $36 \text{ }^\circ\text{C}$ to 3.04 eV at $830 \text{ }^\circ\text{C}$, the true temperature of the Si surface can be calculated by extracting the position through performing critical point analysis [96]. With an absorption depth, α^{-1} , at the E_1 critical point of $\sim 20 \text{ nm}$, this surface temperature is likely indicative of the uppermost $3\alpha^{-1}$ or $\sim 60 \text{ nm}$ of the wafer [140]. While the thickness of the SiO_2 is expected to reduce however during subjection to plasma conditions due to chemical etching and replaced by low density silicon carbide during this equilibration period, the difference in surface temperature obtained with and without an assumed oxide is $10\text{--}15 \text{ }^\circ\text{C}$, placing a maximum error on the temperature obtained of $\pm 8 \text{ }^\circ\text{C}$, remaining smaller than the $15\text{--}30 \text{ }^\circ\text{C}$ error when deducing temperature through pyrometry [96, 141].

To investigate the impact of the initial stages of diamond growth on the Si substrate Collins *et al.* subjected unseeded wafers to growth conditions with and without CH_4 for between 2 and 60 mins; initiating before the 5 min. required for the temperature to stabilise and with the entire duration less than the nuclei induction time [138]. Before reaching growth temperatures a porous weakly absorbing layer of $\sim 7 \text{ nm}$ thickness with

63% void fraction was present on top of a ~ 10 nm damaged layer consisting of crystalline silicon, amorphous silicon, and void, presumably a remnant of wafer production. As durations exceed 5 min., annealing causes crystallisation of the damaged silicon layer with thicknesses remaining constant between 10–20 nm [137, 138]. The weakly absorbing top layer meanwhile became more dense with a reduced void fraction of 31% while remaining within the thickness range of 4–7 nm [138]. However, accurate determination of the composition of this thin absorbing layer is not possible with ellipsometry, with SiC/void, SiO₂, and diamond/void all fitting the acquired spectra equally well. After a K₃Fe(CN)₆/NaOH SiC etch, the thickness of the layer was reduced by 2 nm suggesting a defective carbide composition [138]. Determination of the structure of the carbide was not possible due to the similarity in refraction and extinction coefficients between the possible polytypes [138]. Attempts at characterisation of the diamond content on the substrate after mechanical scratching with diamond grit meanwhile were unable to resolve any residual diamond, with the spectra being sufficiently modelled by a heavily damaged rough amorphous layer and conformal native oxide [96, 137].

Proceeding to growth, Figure 4.7 details the fitting procedure upon subjecting a mechanically scratched seeded silicon substrate to similar growth conditions of 1% CH₄/(CH₄+H₂) at (a) 626 and (b) 841 °C performed by Hong *et al.* with a P_RSA configured ellipsometer [96]. The reference optical constants of diamond were adjusted for the temperatures during growth while the optical constants of a glassy carbon reference sample measured as a function of temperature and used to represent the non-diamond inclusions within the films. The thickness of the bulk (d_b) and surface roughness/seed (d_s) layers are displayed in the top panels, while the void fractions ($f_{v,s}$ and $f_{v,b}$) and sp² fractions ($f_{sp^2,s}$ and $f_{sp^2,b}$) for the seed and bulk layers respectively are represented in the bottom two panels. During the initial stages of growth of the seed, bulk and surface roughness layers the composition could not be determined due to parameter correlation with the horizontal lines indicate the fixing of values to ensure convergence. Such fixing of the composition then allows the thickness of the layers to be accurately determined. As visible from the plot, the isolated islands present during the initial stages of diamond growth are best modelled through the use of a porous EMA of diamond/void with minimal sp² contents of 8% and 0% for the films grown at 626 and 841 °C respectively [96, 139]. As growth proceeds the disk shaped nuclei evolve into hemispherical islands, with

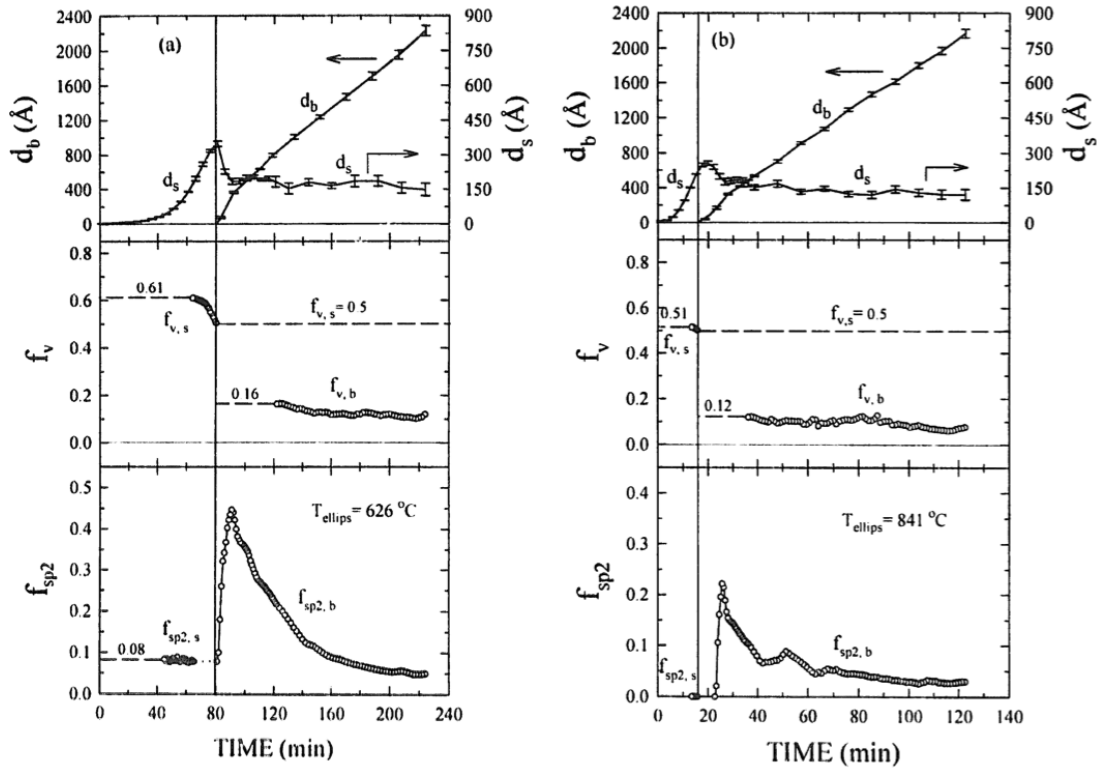


Figure 4.7: Evolution of structural parameters of NCD films prepared at (a) 626 and (b) 841 °C on micro scratched silicon substrates under 1% $\text{CH}_4/(\text{CH}_4+\text{H}_2)$ growth conditions. The thickness of the bulk (d_b) and seed layer/surface roughness (d_s) layers are plotted in the top panels while the void fractions ($f_{v,s}$ and $f_{v,b}$) and sp^2 fractions ($f_{\text{sp}^2,s}$ and $f_{\text{sp}^2,b}$) for the seed and bulk layers respectively are plotted in the bottom two panels. During the early stages of growth the isolated islands are best modelled with a single EMA while after coalescence a bilayer model of surface roughness/bulk is required to model the growth. Both nucleating and bulk layers are composed of diamond/void/ sp^2 , while the volume fractions of the surface roughness is fixed as 0.5 diamond/0.5 void. Dashed lines indicate the fixing of composition to prevent parameter correlation and allow the accurate determination of layer thicknesses. Reprinted from *Diamond and Related Materials*, **6**, B. Hong *et al.*, "Effects of processing conditions on the growth of nanocrystalline diamond thin films: real time spectroscopic ellipsometry studies", 55–80, Copyright (1997), with permission from Elsevier.

the parabolic decrease in the void content indicative of growth occurring much faster in the plane of the substrate than out of plane [96, 139]. Upon reaching thicknesses of 36 and 22 nm for the 626 and 841 °C samples respectively, the void content reaches 0.5, close to the 0.48 expected when modelling contacting hemispheres on a square grid and indicative of the formation of a complete film [141]. After this coalescence point a two layer model is required to model the data with the void content of this porous layer fixed at 0.5 to represent the surface roughness while a second, buried EMA layer consisting of diamond/void/sp² is added to represent the bulk [96, 139]. Simultaneously, the roughness saturates and relaxes by 10–20 nm as the diamond content is incorporated into the bulk layer with resulting stable roughness layers of 15 and 12 nm for the 626 and 841 °C growth films respectively, close to values obtained by AFM [96]. After coalescence and surface smoothing, the thickness of the bulk layers increase linearly as a function of time with rates of 14.4 and 1.9 nm min⁻¹ [96]. Meanwhile, the sp² increases rapidly till a thickness of ~250–300 nm before decreasing asymptotically to a value depending on growth temperature, with values of 5% and 3% for the 626 and 841 °C samples respectively [96]. However, as the mass thickness (volume fraction times by physical thickness) remains the same after peaking, the contribution from successive layers is minimal suggesting this sp² content lies predominantly within the grain boundaries, cementing the diamond crystallites [139, 141]. Simulations have demonstrated that the correct sp² mass thickness is attained for films with a concentration gradient when modelling with a single bulk layer, while neglecting the sp² content within the surface roughness results in the overestimation of the volume fraction within the bulk by the equivalent mass thickness, demonstrating that the model provides the total sp² within the film irrespective of location [96, 141]. Upon the development of the PSC_RA instrument capable of measuring the significant depolarisation created by nanocrystalline diamond films, similar trends were observed including the evolution of the nucleating and bulk layer thicknesses and the sp² content within the first 100 nm of growth, with the value of $p > 0.98$ between 1.5 and 3 eV [128]. For thicker films however the authors note significant deviation of p from 1 indicating depolarisation must be accounted for in the modelling of thicker films [128].

Additional growth runs carried out between the two extremes in temperature of 626 and 841 °C then allow the identification of trends in impurity content, deposition rate,

contact thickness, and steady state surface roughness [96]. At lower temperatures the value of void fraction within the nucleation layer and the thickness before coalescence is at a maximum due to low surface diffusion length of C-containing precursors and minimal thermal activation of the seeds [96, 140]. For hemispherical nuclei with an in plane size twice that of the out of plane size, or thickness, arranged on a square grid, a contact thickness of 36 nm is indicative of a nucleation at the lower end of $2 \times 10^{10} \text{ cm}^{-2}$ [96, 140]. As a result of this poor conversion from seed to nuclei and subsequent growth the low growth temperature films also exhibit a larger fraction of sp^2 within the nuclei layer, and a larger peak and slower rate of decay within the bulk. As growth temperatures increase to $\sim 750 \text{ }^\circ\text{C}$ growth of the nuclei become more efficient resulting in a decrease in the contact thickness, and void and sp^2 contents within the bulk and nuclei layer [96, 139]. The increased nucleation density of $6 \times 10^{10} \text{ cm}^{-2}$ then results in a smaller lateral crystallite size at coalescence and a corresponding decrease in the surface roughness [96]. Further increases in growth temperature to $841 \text{ }^\circ\text{C}$ reverses such trends in the composition due to enhanced etching of the nuclei from the hydrogen plasma, leading to a reduced calculated nucleation density of $5 \times 10^{10} \text{ cm}^{-2}$ [96].

The authors then postulate that the drastic increase in sp^2 content upon coalescence is attributed to the inability of differing orientation crystals to bond via sp^3 in combination with shadowing of sp^2 bonds present on crystallite facets from the etching effects of the hydrogen plasma [139]. Such a supposition is supported by the apparent correlation between the sp^2 and void fraction suggesting that sp^2 lines the void structures between incompletely coalesced nuclei [96, 139]. SEM studies of isolated micron sized diamond crystallites have meanwhile demonstrated the formation of sp^2 hybridised material on crystallite faces shadowed by the hydrogen plasma in conjunction with epitaxial diamond growth [96]. As the grain size increases and the surface/volume fraction reduces, the sp^2 content then decreases before plateauing at a value dependant on growth temperature and feed gas, with low growth temperatures and excess methane admixtures leading to the largest sp^2 contents [139]. A slight increase in contact thickness was meanwhile observed with increasing CH_4 content and attributed to poor reproducibility of the seeding through mechanical abrasion [96]. Furthering the studies, the authors also investigated the effect of the addition of up to 10% $\text{O}_2/(\text{O}_2 + \text{H}_2)$ to the feed supply while fixing the $\text{CH}_4/(\text{CH}_4 + \text{H}_2)$ at 6% and the growth temperature at $785 \text{ }^\circ\text{C}$. While

varying the oxygen content within the plasma the contact thickness was observed to remain the same along with a minor decrease in the sp^2 content within the seed layer from 27% to 34%. The sp^2 value within the bulk at a thickness of 200 nm was meanwhile seen to decrease linearly from 17% to 2% upon reaching an oxygen flow ratio of 10%. As a result the authors conclude that the nucleation is determined by carbon residing within the substrate after mechanical polishing; should nucleation be determined by carburisation or methyl radicals from within the plasma the contact thickness would decrease with decreasing oxygen content along with an associated increase in the sp^2 content within the seed layer [96].

As demonstrated, SE has been successfully used to characterise bulk films grown on top of abraded, nanoparticle, and BEN seeded wafers and the initial stages of growth on abrasion and BEN seeded silicon. Previous *in-situ* works utilising extrinsic seeding techniques have however been unable to identify the presence of diamond residue after seeding while also not accounting for the dynamic nature of the carbide thickness [96, 137]. It was therefore decided to use ellipsometry to characterise films grown on electrostatic based seeded silicon with nucleation densities of the order of 10^{11} cm^{-2} with the gentler, damage free technique potentially allowing the characterisation of the carbide interfacial region [14].

4.3 Spectroscopic Ellipsometry of Nanocrystalline Diamond Growth

4.3.1 Experimental Methods

For the study of the initial stages of diamond growth a series of films of varying growth duration were deposited onto 2" p-type $\langle 100 \rangle$ silicon wafers of 500 μm thickness. To increase the nucleation density as required to produce a coalesced film the substrates were first seeded with a hydrogen terminated mono-dispersed nano-diamond/DI H_2O colloid in an ultrasonic bath for 10 minutes, known to result in seeding densities $> 10^{11}$ cm^{-2} [39]. After seeding, each wafer was subjected to a DI H_2O rinse, spun dry, and then immediately placed inside a Seki AX6500 CVD reactor in preparation for growth. Growth was carried out with a methane flow rate of 20 SCCM diluted in 498 SCCM of hydrogen (3.86% CH_4) for the first 3 minutes to prevent etching of the diamond seeds,

and subsequently reduced to 3 SCCM (0.6% CH₄) for the remaining growth in an attempt to produce films of high sp³ content [14]. Throughout growth the pressure and power were maintained at 40 Torr and 3.5 kW respectively, resulting in growth temperatures of ~860 °C as determined by dual wavelength pyrometry. After 4–123 minutes of total growth the samples were cooled down in a purely H₂ fed plasma to prevent deposition of non-sp³ carbon. The films were then diced up with a diamond scribe and a ~1 by 1 cm² piece taken from the centre of each for all subsequent characterisation.

Spectroscopic ellipsometry was performed with a J.A. Woollam M-2000D PSC_{RA} type ellipsometer between the wavelength range 1.2–6.2 eV (200–1000 nm) with 506 sample points at an acquisition time of 1 second. Incidence angles of 65°, 70°, and 75° were chosen due to the Brewster angle of diamond, and hence the region of highest contrast between r_p and r_s , being at 67.5°. Due to the significant depolarisation observed, a 5 nm bandwidth of the photodiode array was accounted for in the N, C, and S parameters, with any residual depolarisation being accounted for by thickness non-uniformity. As depolarisation spectra are obtained from the DC component of the measured signal during the rotation of the compensator, the resulting offset from ambient light and electronic noise was corrected for during each measurement. Attempts were made at fitting the measured spectra with varying structural models with the iterative process discussed within subsection 4.3.5.

X-ray grazing incidence diffraction and reflection were carried out on beam line I07 at the Diamond Light Source synchrotron working with Professor Emyr Macdonald of Cardiff University, Thomas Dane, formally of Bristol University, and the staff of the beam line: Dr Chris Nicklin, Dr Jonathan Rawle, and Dr Tom Arnold. An energy of 12.5 keV was used through the use of a Si (111) double crystal monochromator, with the intensity captured with a Pilatus 100k area detector. During scattering the normal to the sample surface was orientated horizontally and held inside a helium flushed chamber to minimise background scatter, with the incident beam entering through a x-ray transparent window, represented by A and B within Figure 4.8. The detector (C) was meanwhile positioned 497 mm from the centre of the diffractometer and enshrouded in lead, aluminium, and mylar in an attempt to block scatter from objects other than the sample. Figure 4.9 details the inside of the sample chamber with the aluminium/mylar front removed highlighting the additional attempts to remove back-

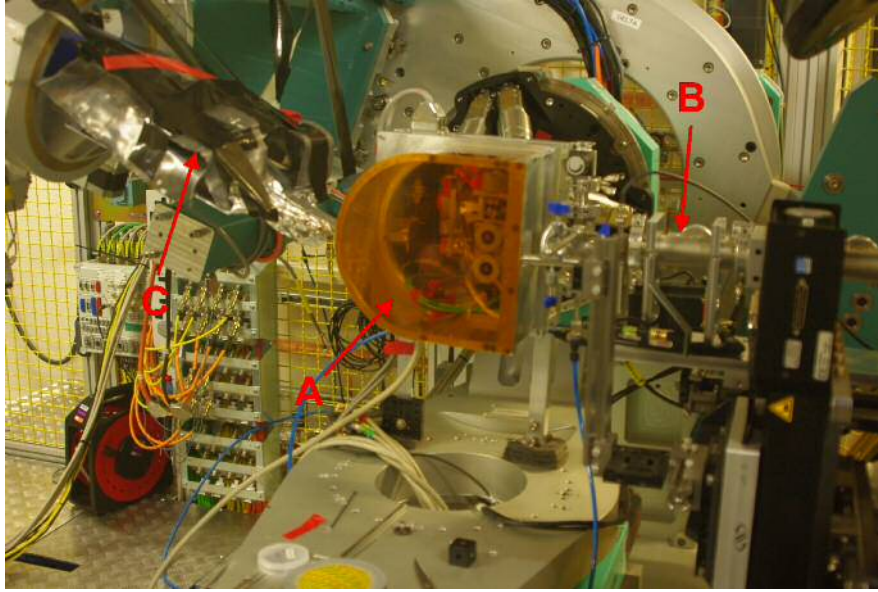


Figure 4.8: Setup of x-ray scattering experiments carried out at beam line I07 of the Diamond Light Source synchrotron. (A) Helium flushed chamber containing the sample with the normal to the surface orientated horizontally; (B) flight tube from the focusing optics and double crystal monochromator emitting 12.5 keV incident radiation; (C) detector shielded with lead, aluminium, and mylar to minimise scatter from objects other than the sample.

ground scatter through the further use of lead (C) and the 2 sets of independent shutters in the vertical and horizontal orientation closed around the incident beam (B). Also visible is a ~ 1 by 1 cm² sample (A) orientated with the $\langle 110 \rangle$ direction of the substrate roughly parallel to the incident beam, observed to minimise the interference of peaks attributable to Thermal Diffuse Scattering (TDS) of the silicon substrate with the Bragg peaks of diamond. Lastly, the lead foil (D) was used to shield the detector from the damaging high intensity of the main beam during specular reflectivity measurements. Variable filters within the beam line were meanwhile used to attenuate the reflected beam during reflectivity scans and varied as required with changing measured intensity.

During grazing incidence diffraction the angle of incidence (α_i) was fixed below the expected critical angle at 0.1° , forming an evanescent wave sampling only the NCD film and preventing the Bragg peaks of the film from being swamped by signal from the silicon substrate, and above the expected critical angle at 0.4° in an attempt to study the variation in diffraction with depth. The centre of the detector was tilted 2° away from the direction of propagation of the beam with the 33.5 mm high detection area

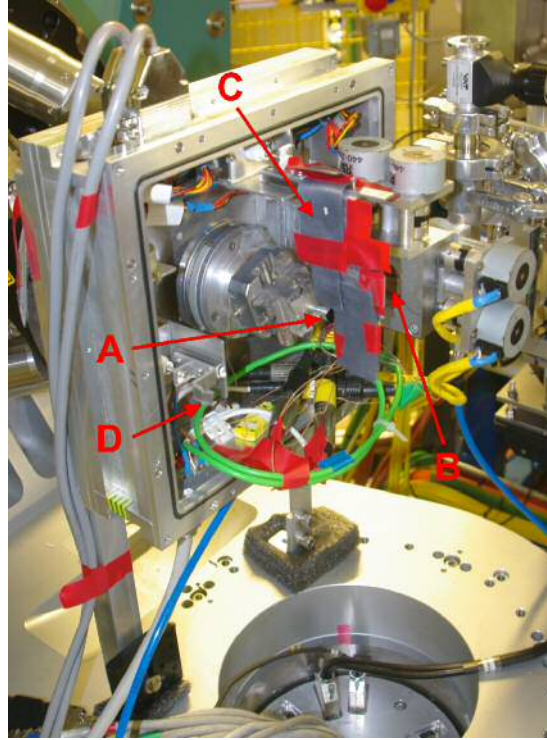


Figure 4.9: Details of x-ray scattering sample chamber. (A) Sample mounted with normal to the surface orientated horizontally and $\langle 110 \rangle$ orientation parallel to the direction of incident radiation, shown to reduce the effect of TDS from the silicon substrate; (B) incident radiation sample slits closed around the beam to minimise background scattering; (C) lead placed around the sample in a further attempt to minimise background scattering; (D) lead shield used to protect the detector from the full flux of the main beam upon carrying out reflectivity measurements.

then permitting angle of reflection (α_f) values from the shadow horizon cast upon the detector due to shielding from the sample to $\sim 5^\circ$. During the grazing incidence scans the detector moved in the vertical direction to maintain a constant sampling depth while scanning 2θ between 25° and 90° in 0.5° intervals with an acquisition time of 5 seconds for wide survey scans. Narrow scans were meanwhile taken between 26.8° and 28.8° , and 45.3° and 47.3° in 0.1° increments with an acquisition time of 20 seconds to scan the (111) and (220) Bragg peaks of diamond respectively. Expanding upon code provided by Jonathan Rawle at Diamond Light Source, a python script was written to import raw images taken at each increment of the scan, account for drift in the sample horizon due to misalignment, and create regions of interest at set values of α_f to allow analysis of the data.

Reflectivity scans were taken while varying α_i between 0.1° and 5° while rotating the detector at $2\alpha_i$ to track the specular beam, with 0.01° intervals for low α_i values and 0.05° for $\alpha_i \geq 1.9^\circ$, all at an acquisition time of 2 seconds. Analysis of the data was carried out with a modified python script based on code supplied by Jonathan Rawle at Diamond Light Source to track the reflected beam and then subtract the baseline intensity. Using a gaussian profile to the beam with a measured FWHM of $178 \mu\text{m}$, the cumulative distribution function can be used to calculate the footprint assuming the alignment procedure has correctly placed the axis of rotation of the sample in the middle of the beam, and correct for the amount of the beam the sample subtends as α_i varies [142]. Finally, the script stitches together a series of scans taking into account the reducing attenuation used to prevent saturation and damage from occurring to the detector with increasing α .

Raman Spectroscopy was carried out by Ashek Ahmed under the supervision of Professor Chia-Liang Cheng at National Dong Hwa University, Taiwan. Using a Witec Alpha scanning near-field optical microscope equipped with a 488 nm laser at a power of 0.5 mW and an acquisition time of 30 seconds, spectra were taken on the 6–123 min. samples. SEM images were taken with the SE2 detector of a Raith eLine system operating at 20 kV and a working distance of 10 mm, with particle size analysis being carried out with ImageJ. Finally, AFM was performed with a Park Systems XE-100 AFM operating in non-contact mode and equipped with TESPA silicon AFM tips (320 kHz resonant frequency, 42 N/m spring constant, and 8–12 nm tip radius). Multiple

areas of $1\ \mu\text{m}^2$ and $25\ \mu\text{m}^2$ were scanned around the middle of each sample for the seeds to 40 min. and 123 min. growth duration samples respectively, with particular care taken to tap lightly during imaging of the seeds to minimise tip wear. Post AFM analysis was then carried out with WSxM and Gwyddion SPM analysis software.

4.3.2 Morphology

A typical AFM scan of a nano-diamond seeded silicon wafer along with a 500 nm long height profile are shown within panels A and B of Figure 4.10 respectively. Due to the large zeta potential difference between the hydrogenated seeds and the native oxide at pH 7 the strong electrostatic attraction between the two results in the complete coverage of the Si substrate, reminiscent of the AFM images and line traces taken by Hees *et al.* under similar purification and dispersion methods [39]. The height profile reiterates this close packing while showing a maximum variation of ~ 2 nm, less than the 4–8 nm particle size and suggesting that the large magnitude of zeta potential of > 30 mV provides a large enough repulsion force to prevent agglomeration of the seeds [143]. The large ~ 40 nm lateral size is likely due to convolution of the features with the 10 nm nominal tip radius of the probe, compounded by tip wear due to the hardness of the diamond particles in comparison to the silicon probe [124]. As a result, seeding densities are likely of the order of $10^{11}\ \text{cm}^{-2}$ as required to produce thin, coalesced nanocrystalline diamond films [39, 124].

AFM images of the 4–123 min. growth duration films can be seen in panels A–H of Figure 4.11, while Figure 4.13 plots the average RMS roughness versus growth duration for the seeded silicon and 4–123 min. growth samples. As visible in Figure 4.11 A, upon 4 minutes of growth a large increase in the height variation appears with the formation of clusters of crystallites with height of ~ 20 nm above their surroundings. A corresponding increase in the roughness is also then observed from 0.5 to 3.3 nm RMS. Meanwhile, a relatively minor increase in the lateral size is also observed along with little reduction in the density of crystallites indicative of a large number of seeds withstanding the predominantly H^+ plasma, with previously estimated etch rates of the order of nm h^{-1} [116]. As growth proceeds, this trend in crystallite size and roughness continues with little change to the maximum height variation within the scans while reaching a roughness value of 4.6 nm RMS after 8 min. of growth. After this peak

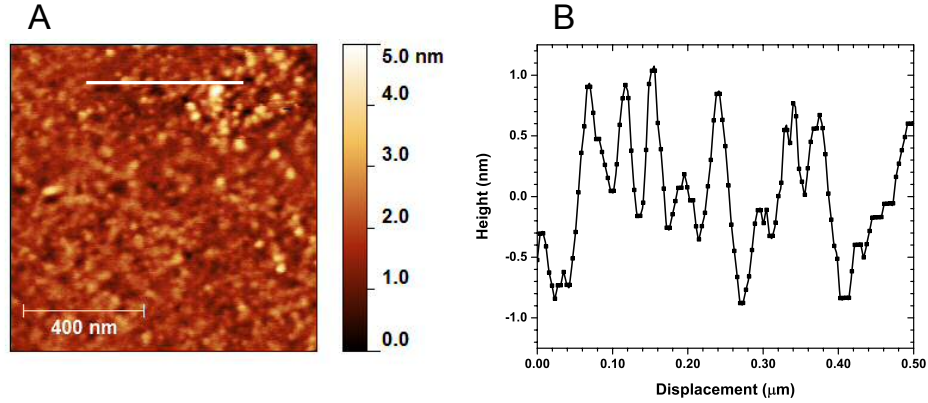


Figure 4.10: AFM image and 500 nm line trace of seeded silicon. The height profile with maximum deviation (~ 2 nm) less than the 4–8 nm particle size indicates a high seeding density and aggregate free surface, while the large ~ 40 nm lateral size is attributable to the convolution of the tip and features and exacerbated by tip wear due to the use of etched silicon AFM tips against the harder diamond.

the roughness relaxes to 3.7 nm RMS before rising linearly to 8.9 and 34.3 nm RMS after 40 and 123 min. of growth at a rate of approximately 0.3 nm min^{-1} . During this period the crystallite size continues to increase, with facets beginning to become resolvable with AFM after 20 minutes of growth. The SEM images of the samples within Figure 4.12 reiterate this trend of increasing particle size and crystallinity with growth duration, with the longer growth duration samples showing little evidence of poor nucleation attributable pin holes. The particle size analysis shown within Figure 4.14 quantitatively shows this trend with average diameter values of 20.1, 42.2, and 178.2 nm for the 4, 40, and 123 min. growth duration samples respectively while the differing growth rates of competing facets results in a sizeable distribution of crystallite size.

4.3.3 Raman

To characterise the changing forms of carbon present during the initial stages of growth Raman spectroscopy was performed, using an excitation of 488 nm to ensure the visibility of peaks associated with both sp^3 and sp^2 hybridised sites [144, 145]. Figure 4.15 plots the spectra obtained for the 6–40 min. samples normalised to the second order

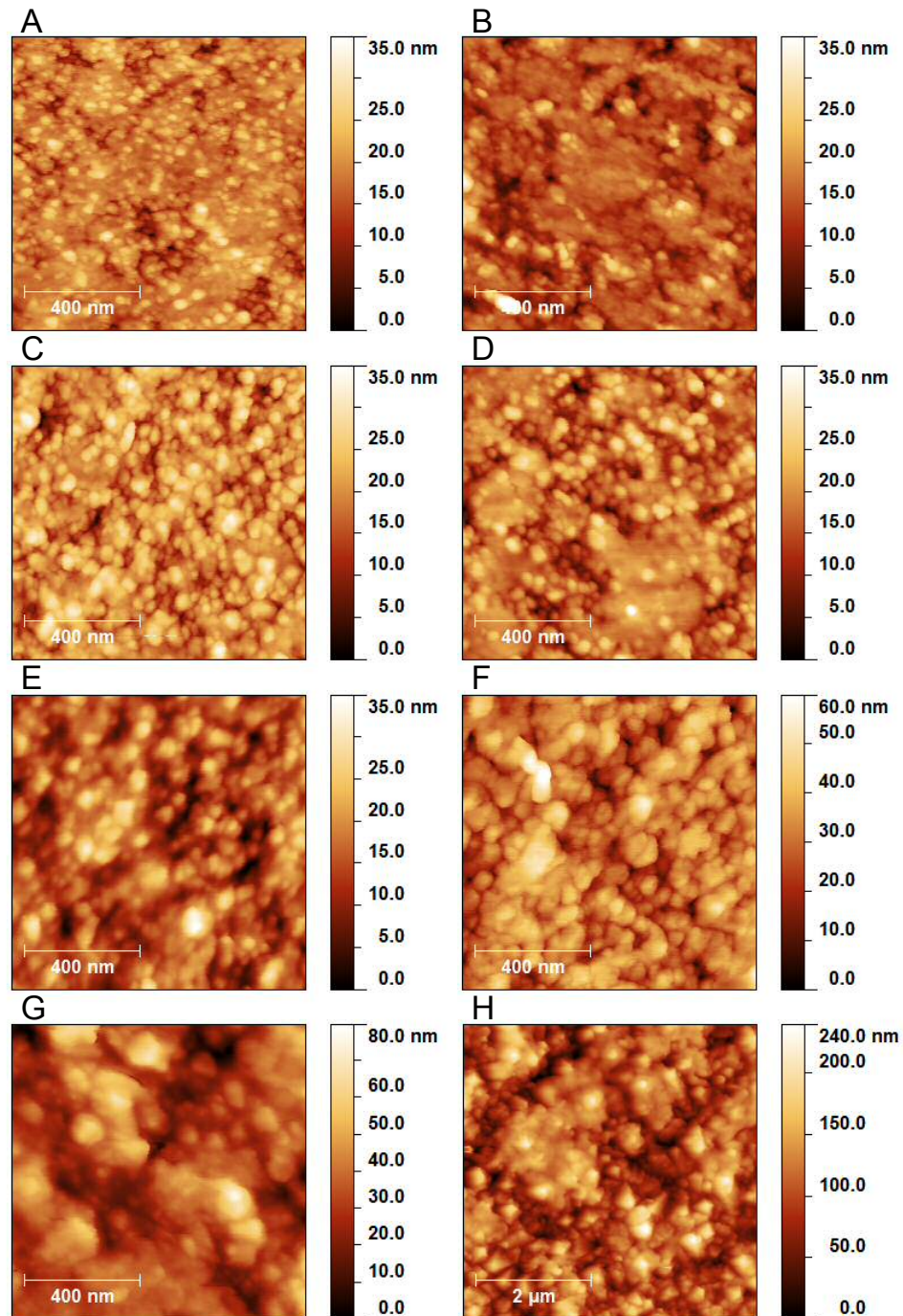


Figure 4.11: AFM images of the initial stages of nanocrystalline diamond film growth, with panels A–H representing the 4–123 min. growth duration films respectively. As indicated by the scale bar, a lower magnification image was taken for the 123 min. sample to obtain a more representative roughness value of the film. With longer growth durations comes an increase in the height variation and comparatively minor changes in the lateral size, indicative of a high nucleation density.

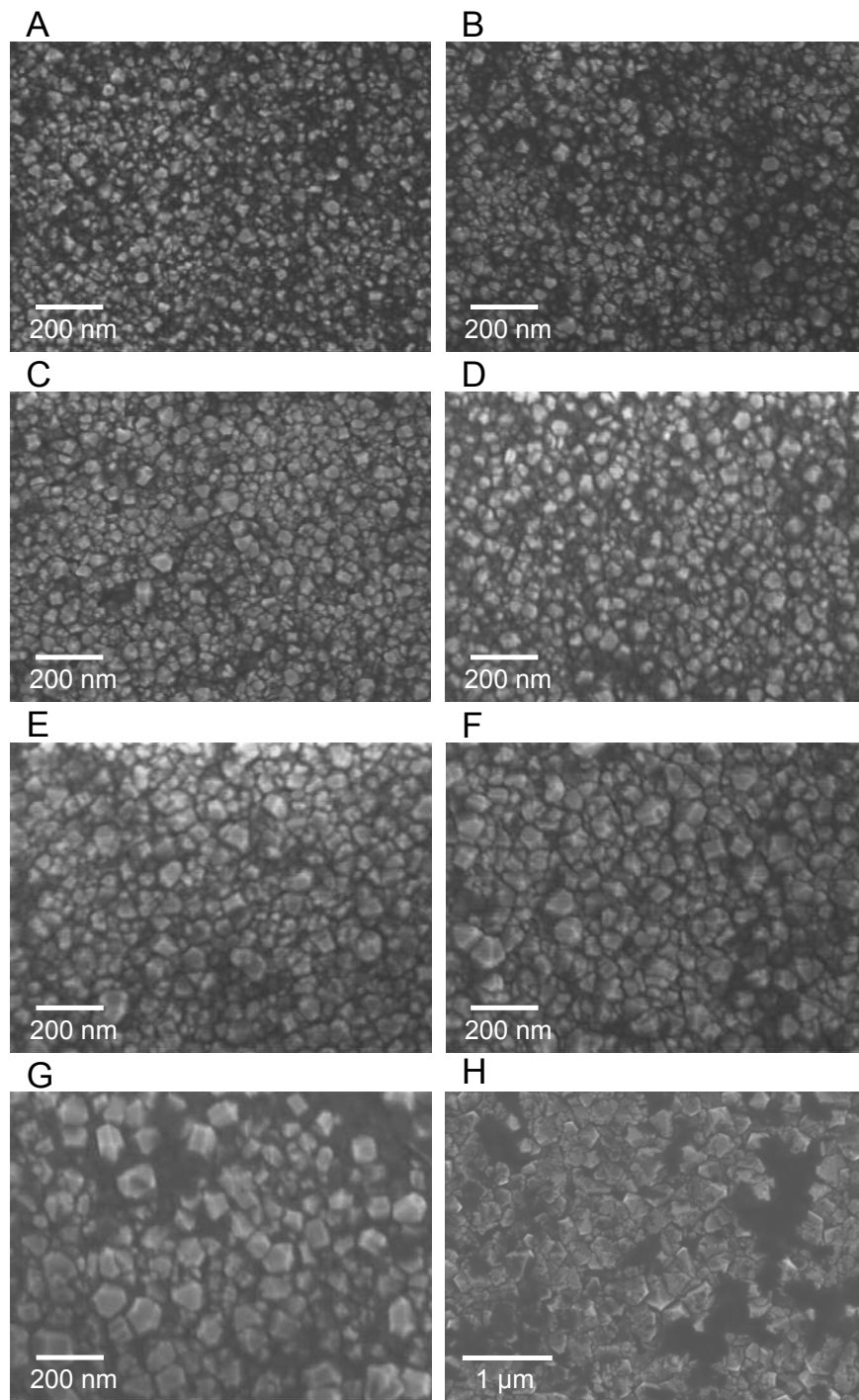


Figure 4.12: Corresponding SEM images of the initial stages of nanocrystalline diamond film growth, with panels A–H representing the 4–123 min. growth duration films respectively. Once again, as indicated by the scale bar a lower magnification was used for the 123 min. sample in order to gain a sufficiently large sample set for particle size analysis.

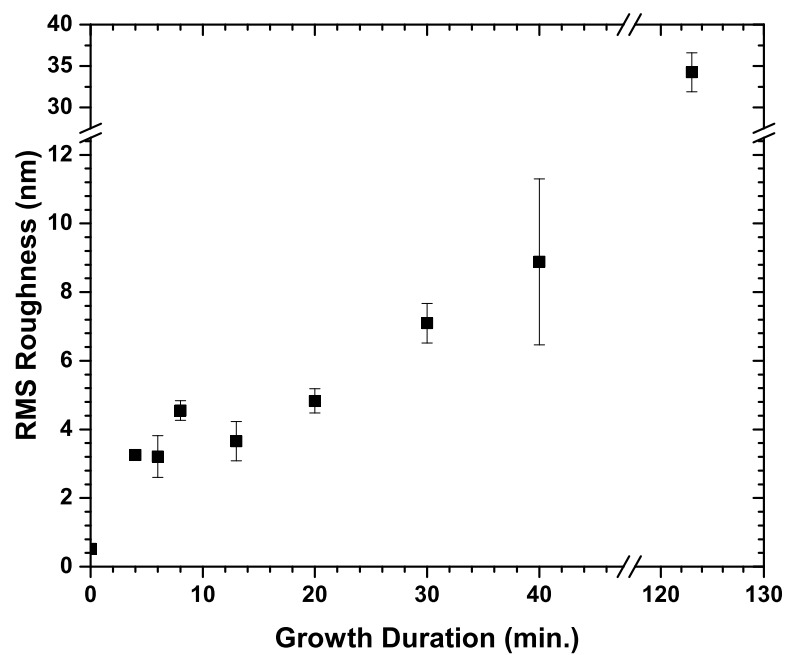


Figure 4.13: AFM obtained roughness against growth duration during the initial stages of NCD growth. Little change in the roughness during the initial 6 minutes of growth is seen to occur with values of ~ 3.2 – 3.3 nm RMS, followed by a sharp peak of 4.6 nm RMS at 8 minutes of growth at before relaxation and subsequent linear increase with growth duration for the 13 min. growth duration film onwards.

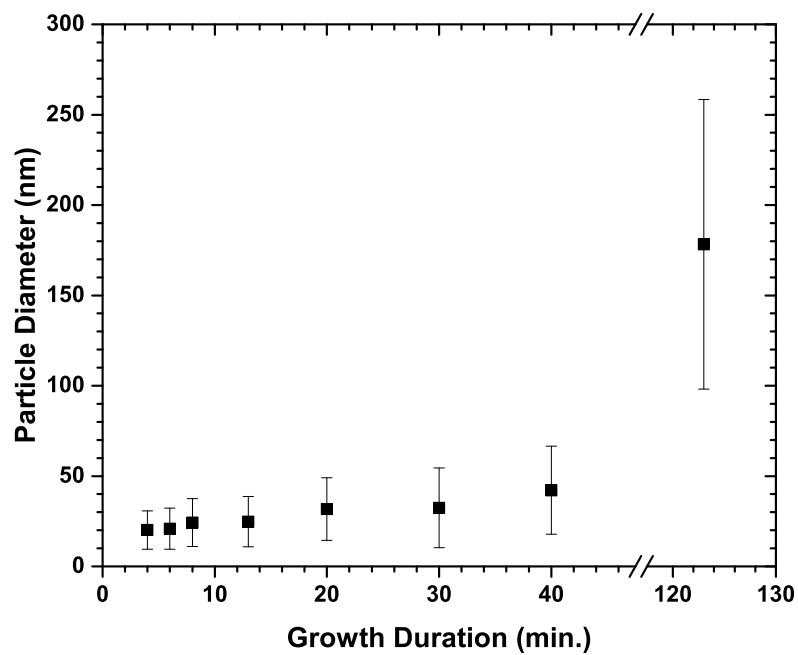


Figure 4.14: SEM obtained particle size against growth duration during the initial stages of NCD growth. The particle size is seen to increase from 20.1 to 42.2 nm at a linear rate between 4 and 40 minutes of growth before accelerating to 178.2 nm for the 123 min. growth duration sample, with the competing nature of crystallites of differing faceting and growth rate leading to a wide distribution in particle size.

TO peak of the silicon substrate at 980 cm^{-1} , along with the unadjusted spectra for the thicker 123 min. sample. As expected with the thicknesses of the films the most prominent peaks are the first order TO peak of the silicon substrate at 520 cm^{-1} , and the aforementioned second order peak at 950 cm^{-1} [146]. The features on the tail of the first order silicon peak are believed to be due to boron within the heavily doped (10^{19} cm^{-3}) substrate; doping concentrations exceeding 10^{18} cm^{-3} have been shown to lead to the superposition of two local modes onto the tail of the optical phonon of diamond at 620 cm^{-1} and 644 cm^{-1} for the B^{11} and B^{10} isotopes respectively [147, 148]. The relatively constant intensity peak at 830 cm^{-1} is tentatively attributed to amorphous SiC with a similar broad band peak positioned between $800\text{--}830\text{ cm}^{-1}$ observed in sputtered, pulsed laser deposition and CVD produced SiC films [149–152].

Figure 4.16 shows a magnified view of the spectra between the range 1050 and 1800 cm^{-1} normalised to the first order diamond line at 1332 cm^{-1} . As typical for NCD films, the diamond line at 1332 cm^{-1} exhibits peak broadening due to the reduced crystallite size and thickness of the film. Heavily convoluted with the diamond line is the disordered carbon peak at 1360 cm^{-1} arising from the breathing mode of graphitic rings [63, 153]. Meanwhile, the G band due to the in plane stretching mode of pairs of sp^2 sites, typically present at 1560 cm^{-1} at an excitation of 514 nm , can be seen at $\sim 1500\text{--}1510\text{ cm}^{-1}$ [63, 153]. Such a decrease in the G band position to $1450\text{--}1510\text{ cm}^{-1}$ is indicative of the introduction of disorder within carbon sheets and the transition from nanocrystalline graphite to amorphous carbon, with weaker bonds softening the sp^2 vibrational modes [144, 145, 154]. Combined with the low $I(D)/I(G)$ ratio, which has been shown to be linearly related to the particle size due to the loss of aromatic rings, it is then believed that the sp^2 sites within the samples are largely amorphous [63, 145]. Lastly, the peak at 1150 cm^{-1} is attributable to transpolyacetylene (TPA) present at the grain boundaries [154]. While always accompanied by a peak at 1450 cm^{-1} due to the pair representing the sum and difference of C=C and C-H modes within the TPA chain, this additional peak is shrouded by the relatively large G band peak [154].

From the magnified spectra of Figure 4.16 it can be seen that after 13 min. of growth an increase in the G band peak with respect to the diamond phonon line occurs. The G band then peaks at 20 min. and subsequently decreases for the longer growth duration films, reaching a minimum after 123 min. of growth. The TPA content meanwhile,

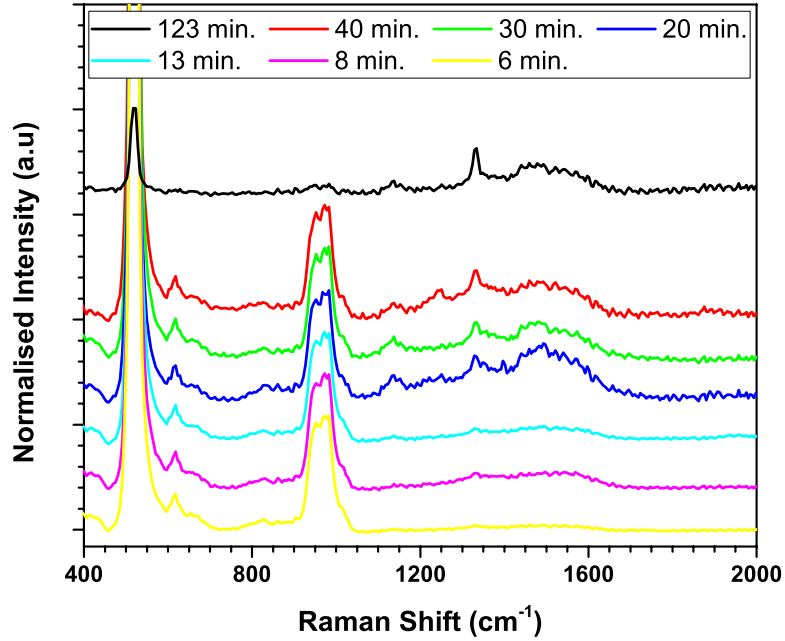


Figure 4.15: Raman spectra of the 6–40 min. growth duration samples normalised to the second order TO peak of silicon, and the unadjusted spectra of the 123 min. sample. The peaks visible are attributable to: silicon first order TO at 520 cm^{-1} , substitutional B^{11} and B^{10} at 620 cm^{-1} and 644 cm^{-1} respectively; amorphous silicon carbide at 830 cm^{-1} ; silicon second order TO at 950 cm^{-1} ; and finally, C–C, C=C, and C–H bonds of the NCD film within the range $1100\text{--}1700\text{ cm}^{-1}$. With increasing growth duration the peak tentatively attributed to SiC remains at roughly the same intensity while the peaks attributable to the nanocrystalline diamond film grow due to increasing thickness.

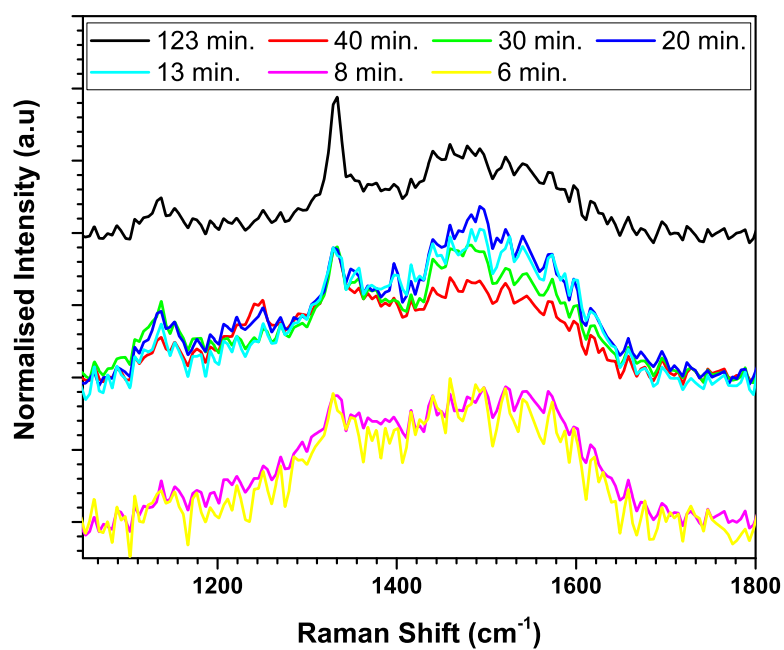


Figure 4.16: Magnified Raman spectra of the 6–40 min. growth duration samples normalised to the diamond peak. The peaks visible are attributable to: TPA at 1150 cm^{-1} ; diamond at 1332 cm^{-1} ; D band breathing modes of sp^2 aromatic rings at 1360 cm^{-1} ; and G band in plane stretching modes of sp^2 at $1500\text{--}1510\text{ cm}^{-1}$. An increase in the ordered carbon and TPA is visible after 13 mins of growth and then decreases with longer growth durations.

believed to lie predominantly within the grain boundaries, only becomes apparent after 13 minutes of growth, peaks at 20–30 minutes, and then decreases while still remaining present for the thicker film. Because of the composite nature of films with spectral features dependant on the distribution of the sp^2 bonded carbon, quantification of this impurity content is often difficult [94]. Furthermore, with the excitation wavelength being closer to the electronic transitions of sp^2 bonded sites than sp^3 bonds, coupled with their ease of polarisation, the scattering efficiency of sp^2 and sp^3 differ vastly [144, 153]. Resulting Raman cross sections of graphite and amorphous carbon are typically 50–250 times that of diamond at an excitation of 514 nm [63, 97, 144, 145]. Nevertheless, a scattering efficiency ratio of 75 has previously been used to compare the quality factor of films within a series through the definition [99, 125, 126, 155]:

$$f_q = \frac{75 \cdot I_d}{75 \cdot I_d + \sum_{nd} I_{nd}} \cdot 100 \quad (4.9)$$

Where f_q is the percentage of diamond content, I_d is the Raman diamond peak areas, and $\sum_{I_{nd}} I_{nd}$ is the sum of the Raman sp^2 phases peak area. De-convoluting the spectra within the range 800–2000 cm^{-1} to the peaks assigned previously, the 123 min. growth film yields sp^2 fractions of 13%. Deconvolution of the 40 and 20 min. growth duration samples meanwhile suggest sp^2 fractions of 27% and 23% respectively, reiterating the reduction in impurity content with increasing thickness. For the remainder of the samples the fit process did not converge due to the weak signal emanating from the thin films.

4.3.4 X-ray Scattering

To fully characterise the growth process X-ray reflectivity and X-ray diffraction were performed at Diamond Light Source, with the brilliance of synchrotron radiation potentially allowing the characterisation of seeded silicon and thin film samples. While grazing incidence scans were obtained above and below the expected critical angle at α_i values of 0.1 and 0.4° in an attempt to more definitively attribute signal to film and substrate, the various items placed in close proximity to the beam caused significant shadowing preventing the ‘below the critical angle’ scans from being used. To prevent swamping of the signal from the TDS arising from lattice vibrations within the substrate

when using the scan taken at α_i of 0.4° , the height of the region of interest was varied with the upper edge ranging between α_f of 0.05 and 0.3° above the sample horizon while the lower edge was fixed at 0.1° . A judgment was then made on the region of interest size that offered the best compromise between the intensity of the peaks attributable to the surface and the intensity of the background TDS, with a chosen region of interest of between -0.1 and 0.1° about the sample horizon. Due to time constraints at the end of the allocated beamtime, capturing finer resolution scans of the Bragg peaks of diamond were abandoned to allow scanning of the complete sample set. As such, additional code was written to move a region of interest within a single image with knowledge of the sample misalignment from the wider scans.

The resulting wide diffraction scans for the seeded silicon to 123 min. growth duration sample are plotted in Figure 4.17. As visible from the plot, the silicon substrate shows broad peaks wider than those expected from Bragg peaks and characteristic of TDS centred at 2θ values of 42 and 71° . To prevent the location of TDS peaks from coinciding with the diamond peaks the azimuthal angle was varied during the calibration procedure, with the best results observed with the $\langle 110 \rangle$ direction of the silicon placed parallel to the propagation direction of the beam. Upon drop seeding of the nano-diamond colloid on top of the silicon substrate a weak peak at $\sim 28^\circ$ attributable to the (111) peak of diamond becomes apparent. Merged with the (111) diamond peak is a peak at 28.6° not present on the silicon substrate and therefore attributable to either the seeds or scatter from the sample setup. With the peak lying reasonably close to the expected position of the (101) peak of graphite at 28.3° it could be conjectured that such a peak is attributable to onion like shells encapsulating the seeds. However, vacuum annealing studies have demonstrated that the structure of such shells are essentially turbostratic and lacking the stacking structure required to present the three dimensional Bragg peaks [156, 157]. The typically prominent (002) peak attributable to planes of stacked graphene meanwhile would lie at a 2θ value of 17° , outside of the measurement range used and preventing confirmation of the presence of onion like shells. Furthermore, powder XRD performed on purified and untreated diamond powder of the same origin as that within the present study by Williams *et al.* do not exhibit peaks attributable to non sp^3 carbon with only the Bragg peaks of diamond being visible, making the source of this peak difficult to determine [143].

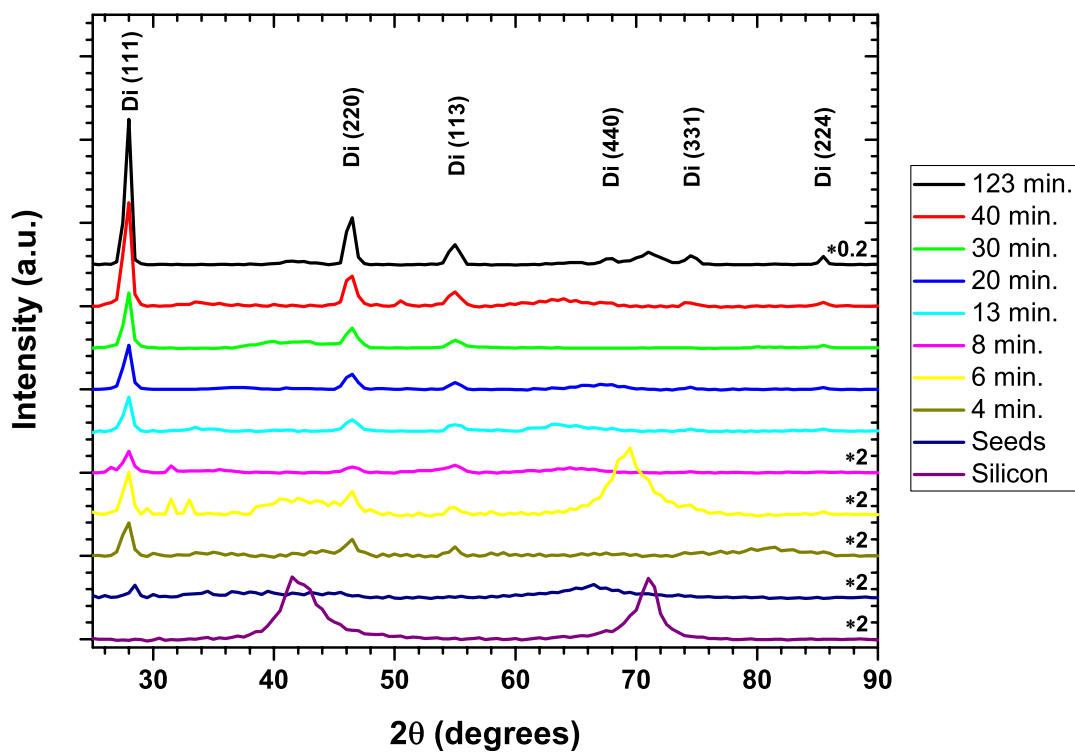


Figure 4.17: X-ray diffraction of a silicon substrate, seeded silicon, and 4–123 min. growth duration samples. After drop seeding with dispersed diamond seeds the (111) Bragg peak of diamond becomes visible, with growth bringing about an increase in intensity and reduction in FWHM. As growth proceeds and films become thicker peaks attributable to the (220), (113), (440), (331), and (224) plane groups become apparent. The broad peaks visible at 42 and 70° are attributable to lattice vibrations from the silicon substrate and their effect on the Bragg peaks of diamond minimised through careful choice of the azimuthal and reflection angles.

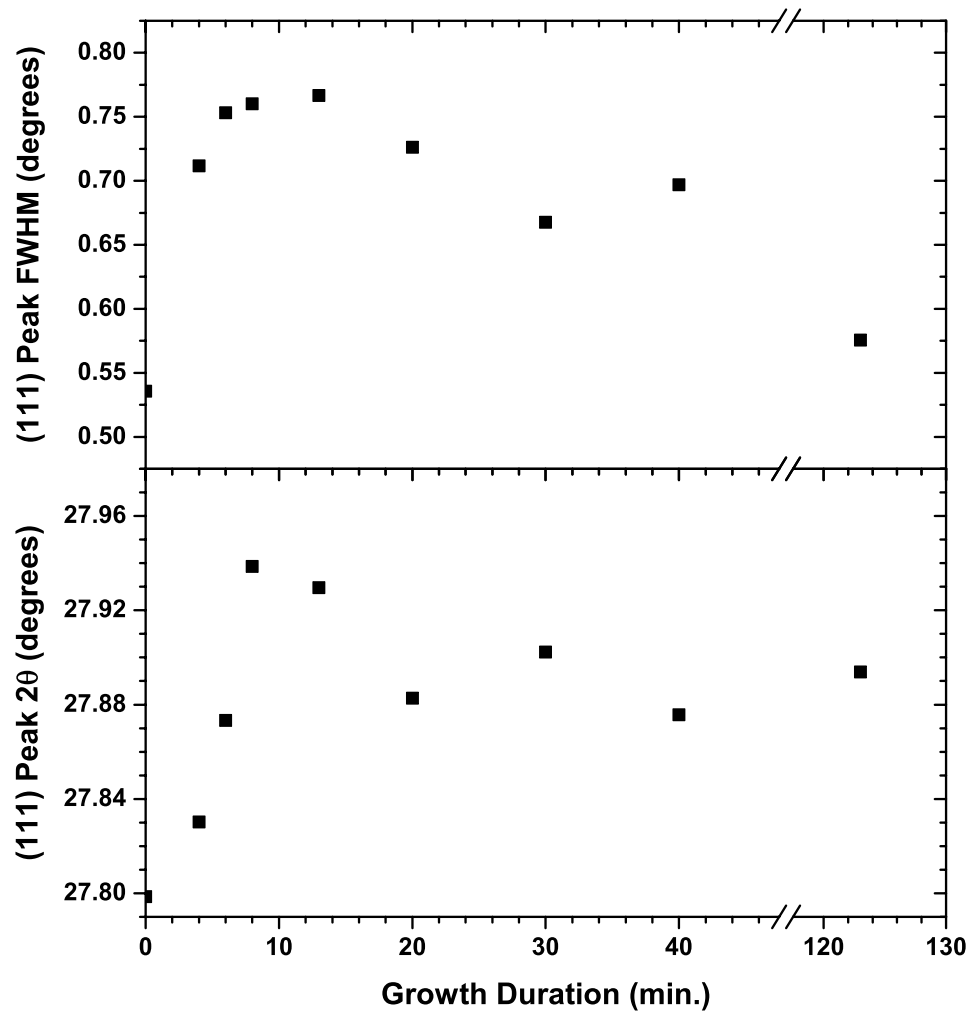


Figure 4.18: FWHM and peak position of the Gaussian line shapes fitted to the (111) diamond Bragg peaks of seeded silicon, and the 4–123 min. growth duration samples. After drop seeding with dispersed diamond seeds a Bragg peak appears at 27.8° appears, suggesting a lattice parameter of 3.576 \AA , 0.26% higher than that of bulk diamond at 3.5667 \AA . Upon subjecting to growth conditions the lattice then compresses closer to that of natural diamond, before reaching a final value of 3.5639 \AA for the 123 min. growth duration sample, 0.07% lower than that of natural diamond at 3.5667 \AA . Meanwhile, increases in growth duration leads to a reduction in the FWHM indicative of an increase in scattering domain size.

Upon growth the (111), (220), and (113) diamond Bragg peaks appear and rise in intensity for the 4–8 min. growth duration samples. Also present for the 6 and 8 min. samples is a peak at 26.4° , close to the expected location of the (200) Bragg peak of β -SiC. While the sole presence of the (200) peak could be indicative of the formation of a heteroepitaxial layer on the (100) orientated substrate, the peak shows considerable intensity below the horizon of the shadow cast on the detector by the $500\ \mu\text{m}$ thick Si substrate. As the $1\times 1\ \text{cm}^{-2}$ samples tilted at 0.4° project a height of $70\ \mu\text{m}$ in comparison to the $178\ \mu\text{m}$ FWHM height of the beam, it is therefore likely that the peak is instead attributable to material within the sample chamber and placed around the detector. Further peaks at 31.3 and 32.8° possess similar trends in intensity, while a peak present at 38.5° was observed to disappear during the 2 scan for the 6 min. growth duration reiterating the possibility of sample setup scattering. Increases in growth duration brings about the addition of Bragg peaks of the (440), (331), and (224) planes of diamond, while shadowing prevents the (331) peak for the 30 min. growth duration sample from being observed.

Towards the end of the scheduled beamtime it was deemed necessary to abandon the finer scans of the diamond Bragg peaks in order to investigate the complete sample set. As such, during analysis additional code was written to move a region of interest across an individual image, taking into account sample misalignment and the projection of radiation onto the flat detector. Fine resolution scans of the (111) diamond Bragg peak were then produced at increments of 0.05° in $2\ \theta$ with the upper and lower limits of the region of interest set to 0.1° above and below the sample horizon. The resulting (111) Bragg peaks were then fitted with a Gaussian line shape, with Figure 4.18 plotting the resulting FWHM and $2\ \theta$ positions.

Due to the presence of the aforementioned peak at 28.6° in combination with the large intensity variation observed when shifting the edge of the ROI from one pixel to another to account for sample misalignment, accurate determination of the FWHM of the (111) peak of the seeded substrate is not possible. The peak position is meanwhile tentatively deemed to be 27.8° suggesting a lattice parameter of $3.576\ \text{\AA}$, 0.26% higher than that of bulk diamond at $3.5667\ \text{\AA}$. Such an increase is in accordance with previous studies on XRD of diamond nanoparticles where strain of the surface, which constitutes a large fraction of the atoms within the particle, leads to the shifting of the apparent

lattice parameter [158]. Upon subjecting the seeded substrates to growth conditions the trend in FWHM reiterates the sharpening of the peaks seen within Figure 3.4 indicating an increase in size of the scattering domains. In addition the peak position shifts to higher 2θ indicating a reduction in lattice parameter before reaching a final position of 3.5639 \AA for the 123 min. growth duration sample, 0.07% lower than that of natural diamond at 3.5667 \AA .

In addition to X-ray diffraction, X-ray reflectivity scans were taken through varying the incidence angle and tracking the intensity of the specular beam with the aim of studying film thickness, density, and surface and interfacial roughness. At low angles of incidence the less than unity refractive index of materials at X-ray wavelengths lead to total external reflection of the incident beam and normalised reflectivity intensities of ~ 1 . Upon exceeding the critical angle of the multi layer stack, dependant on the electron densities of the constituent materials, the X-rays begin to penetrate the film leading to a reduction in intensity measured at the detector at a rate of 2^{-4} in the case of a perfectly smooth surface [159, 160]. Should the surface or interfacial region be rough at the atomic scale however, diffuse scattering will lead to a more rapid reduction in the measured intensity [159, 161]. Meanwhile, the constructive and destructive interference with reflections from the differing interfaces within the stack will lead to the superposition of Kiessig oscillations on top of this decay, with the angular period correlated to the thickness of the film as $\Delta 2\theta \approx \lambda / 2t$, where λ is the X-ray wavelength and t is the thickness of the layer [161].

Figure 4.19 details the X-ray specular reflectivity with increasing scattering vector for the silicon substrate to 123 min. growth duration sample. As visible within the plot, the silicon substrate appears free of over-layers with a constant decay after a critical scattering vector (q_c) of $\sim 0.045 \text{ \AA}^{-1}$. Upon the deposition of diamond, be it in the form of seeds, isolated islands or coalesced film, q_c then appears to decrease to with a value of $\sim 0.037 \text{ \AA}^{-1}$ for the 20 min. growth duration sample. For films consisting of a dense bulk layer sandwiched between thinner, less dense layers the critical angle is expected to be representative of the bulk, suggesting that for the substrate and thicker films in which a clear coalesced layer exists the critical angle are representative of silicon and diamond respectively [159, 160]. However, as the electron density of diamond is larger than that of silicon it is expected that the increased scatter will lead to a lower refractive

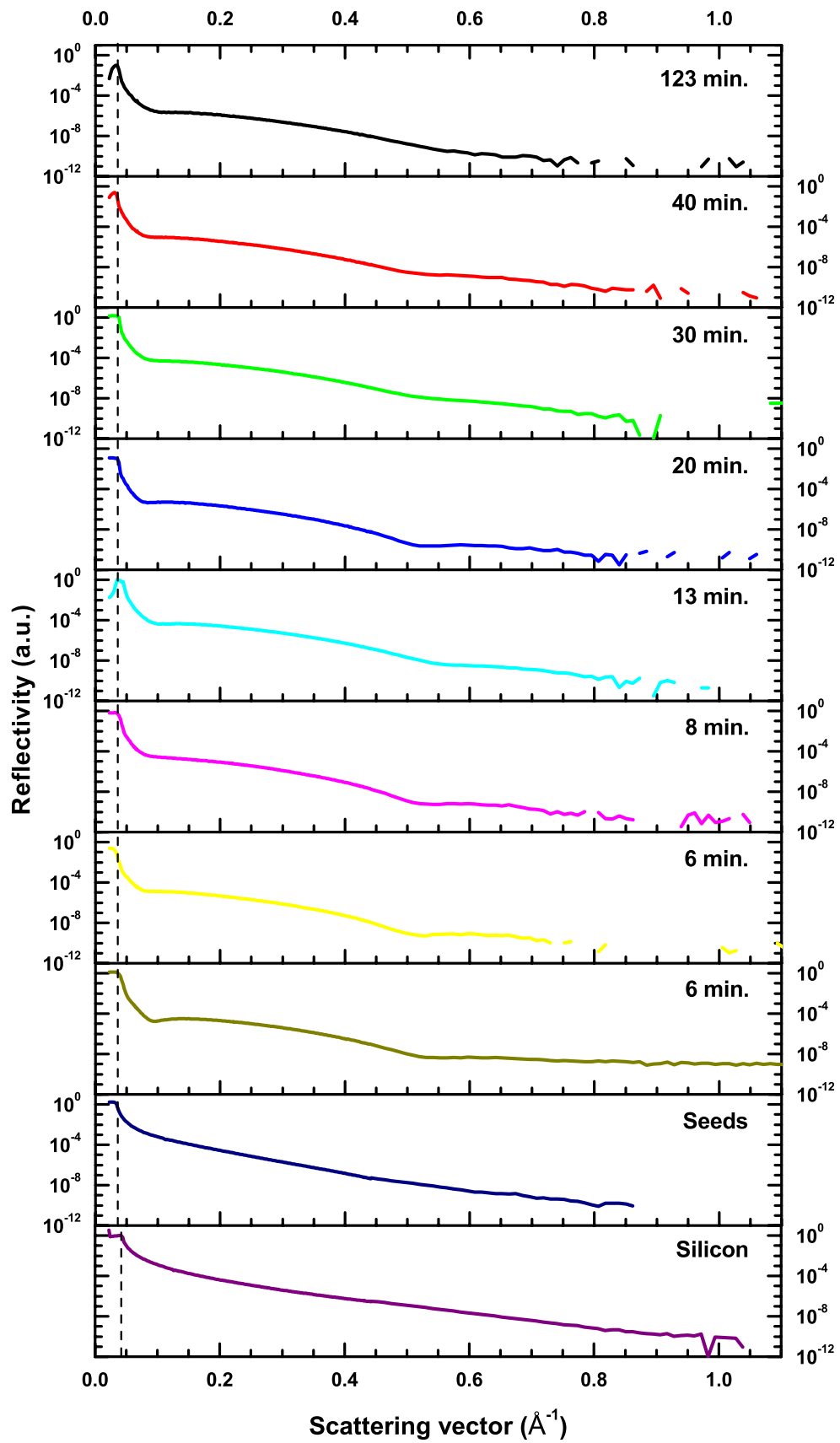


Figure 4.19: X-ray reflectivity of a silicon substrate, seeded silicon, and 4–123 min. growth duration samples.

index and hence larger critical angle, the reverse of the trend observed within the plot [160]. Meanwhile, the period of the oscillations remains largely the same throughout the series, suggesting layer thicknesses of ~ 1.5 nm. As this value is less than the diameter of the seeds it is therefore believed that the surface roughness of the films, as observed in Figure 4.13, along with the interfacial roughness at the diamond/substrate boundary prevent the constructive and destructive interference required to indicate the thickness of the bulk. Such roughness values are typically larger than the 0.4–2 nm typically observed on DLC films where thickness determination of up to 360 nm was possible with X-ray reflectivity [159–162]. In addition, at grazing incidence angles the footprint of the beam along the sample is typically of the order of cm resulting in the addition of the Kiessig fringes observed along sample illuminated by the beam [159]. As the inhomogeneity of the diamond samples is visible by eye over the 1 by 1 cm² pieces, such an addition will further reduce the amplitude of the peaks. As fitting of the reflectivity data requires the creation of a model with only the roughness being the only potential parameter to be gained, it was decided not to proceed with the analysis of the XRR data.

4.3.5 Spectroscopic Ellipsometry

To prevent problems with parameter correlation occurring upon fitting the nanocrystalline diamond films, the optical properties of the substrate and native oxide were first determined. On top of the silicon substrate, thick enough to prevent incoherent backside reflection affecting the acquired spectra, a preference for the optical constants of native oxide was observed, with refractive index between that of Si and bulk SiO₂ due to incomplete oxidation [163]. An additional two layers were then added for the modelling the NCD films creating a stack consisting of: a Bruggeman EMA surface roughness layer of 50% void and 50% bulk; a bulk layer of two oscillators matched to the optical constants of type Ia and IIa natural diamond from Edwards and Phillips; a 1.64 nm native oxide layer; and finally, the silicon substrate [163, 164]. As to be expected, the resulting fits were poor with an average Mean Squared Error (MSE) for the 4–40 min. samples of 78; believed to be due to inclusions and interface layers not accounted for by the optical properties of bulk diamond. Bar 1 of Figure 4.20 details the relatively poor fit of this model for the 13 min. growth duration film with an MSE

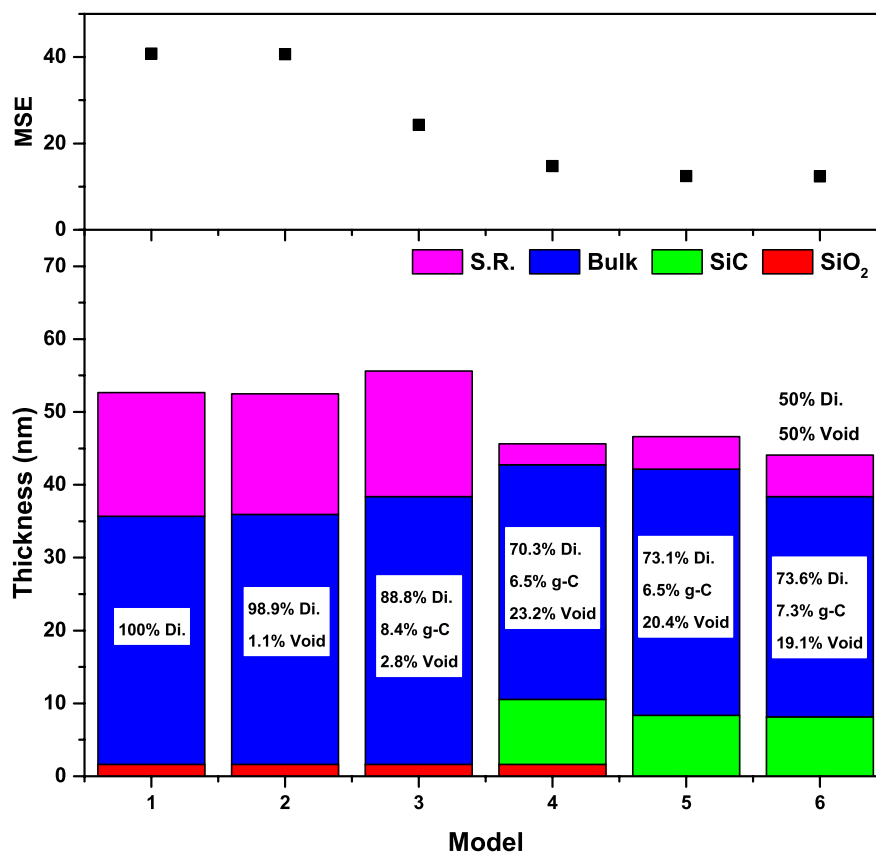


Figure 4.20: Progression of the ellipsometry model fitted to the 13 min. growth duration sample. With the incorporation of glassy carbon and void content the MSE is seen to reduce by half. More accurate modelling of the interface with the addition of β -SiC, removal of the native oxide, and removal of the glassy-carbon content within the surface roughness layers results in a reduction in MSE to 12 from the initial value of 41.

of 41. While the incorporation of nitrogen in the transition from type IIa to Ia natural diamond is known to cause a shift in the UV absorption edge of diamond, the use of the optical constants from a Tauc-Lorentz oscillator fitted to thicker polished films affected the trends in composition and absolute values little for the initial growth films [163]. Parameter correlation meanwhile excluded the direct parameterisation of the diamond content for the early growth films due to the low thickness and complicated structure of the samples, permitting the use of reference optical constants for the diamond content.

Accounting for the void content arising from the transition from Volmer-Weber to van der Drift type growth and non-diamond carbon hybridisations present, the optical constants of void, glassy carbon or tetrahedrally amorphous carbon were then mixed

with those of diamond through the use of the Bruggeman effective medium approximation [92, 165]. The addition of a void content alone did little to improve the fit, while the combination of glassy carbon and void lead to a reduction in average MSE to 52. The use of the optical constants of ta-C was meanwhile deemed unreasonable suggesting values of 67% ta-C for the 40 min. growth duration film and contradicting the crystallinity observed in the panel G of Figures 4.11 and 4.12, highlighting the need for the validation with non-model dependant characterisation methods [109]. This improvement in fit is visible in bar 3 of Figure 4.20 where the addition of 8% of glassy carbon accounts for the increased absorption in the film at grain boundaries with an associated minor increase in thickness due to a reduced refractive index of the effective medium.

Further reductions in the MSE were attained through more accurately modelling the interface between NCD and substrate; previous studies of growth exceeding 800 °C have indicated the presence of a < 10 nm amorphous SiC layer due to combined carburisation from CH₄ derived radicals within the plasma and direct reaction with nano-diamond particles [116, 119, 120]. Meanwhile, hydrogen plasmas have been shown to result in the etching of the native oxide of silicon with rates of approximately 0.3 nm min⁻¹ [117, 118, 120, 123, 166]. Using the optical constants of β -SiC a layer was placed atop the native oxide, with the linear regression procedure indicated a layer thickness of 4.68–8.93 decreasing with growth duration resulting in a MSE over the sample set of 39 [167]. Upon allowing the 1.64 nm thickness of the native oxide layer to vary the fitting procedure rejected the layer, further reducing the MSE to 37. Finally, the surface roughness layer consisting of 50% bulk/50% void is replaced with a Bruggeman EMA of 50% diamond/50% void with a further decrease in the average MSE to 26. As the samples were cooled down in a purely H₂ fed plasma to remove any adventitious carbon at the surface, such a result is in accordance with the sp²/amorphous sp³ content being predominantly present within the grain boundaries. The resulting fit of the 13 min. growth sample indicates a surface roughness of 6 nm on top of a 30 nm bulk layer (7% glassy-C, 19% void) and a 8 nm SiC interlayer, while providing a MSE of 12. The apparent reduction in the bulk thickness between model 5 and 6 of Figure 4.20 is attributable to the in built surface roughness acting as a ‘stealing’ layer in which half of its thickness is taken from the sub-layer, i.e. a bulk layer of 80 nm with a 20

	S.R. Thickness	Bulk Thickness	Bulk Glassy-C %	Bulk Void %	SiC Thickness
S.R. Thickness	1	-0.905	0.541	-0.951	-0.936
Bulk Thickness	-0.905	1	-0.279	0.879	0.738
Bulk Glassy-C %	0.541	-0.279	1	-0.527	-0.577
Bulk Void %	-0.951	0.879	-0.527	1	0.939
SiC Thickness	-0.936	0.738	-0.577	0.939	1

Table 4.1: Correlation matrix of the fitting parameters within model 6 when fitting for the 13 min. growth sample. Values close to ± 1 signify that the two parameters produce the same result and are not unique. Of note is the high correlation of the surface roughness thickness with the thickness of the bulk and SiC layers, and the void fraction within the bulk, warranting validation and preventing the addition of a further seed layer to account for the expected increase in sp^2 and void content before coalescence of the film. Meanwhile the glass carbon content is relatively free from correlation suggesting a unique value.

nm roughness using the inbuilt surface roughness is rather a 70 nm bulk layer with 20 nm roughness, making the bulk thickness values closer than it appears within Figure 4.20 at 32 and 30 nm respectively. Upon the removal of the glassy-C content from the surface roughness layer a correlated increase in the content within the bulk is observed to maintain a constant mass thickness of 2.2 nm, following behaviour observed in previous studies [141]. To investigate this correlation further the correlation matrix of model 6 fitted to the 13 min. growth sample is shown in Table 4.1, with values equal to ± 1 and 0 indicative of full correlation and no correlation respectively. Of note is the relatively low correlation of the bulk glassy-C content with the other fit parameters suggesting a unique value, whereas the surface roughness thickness is highly correlated to the thickness of the bulk and SiC layers, and the void fraction within the bulk, warranting validation with AFM. The resulting modelled and acquired and spectra for the 13 min. growth duration sample at an incidence angle of 70° are then plotted within Figure 4.21, with the close fitting of the spectra reiterating the suitability of the final model to the initial stages of NCD growth.

Once settled on the optimal structure the optical constants of the non-diamond content and carbide layer were varied using reference functions of ta-C, graphite, DLC pro-

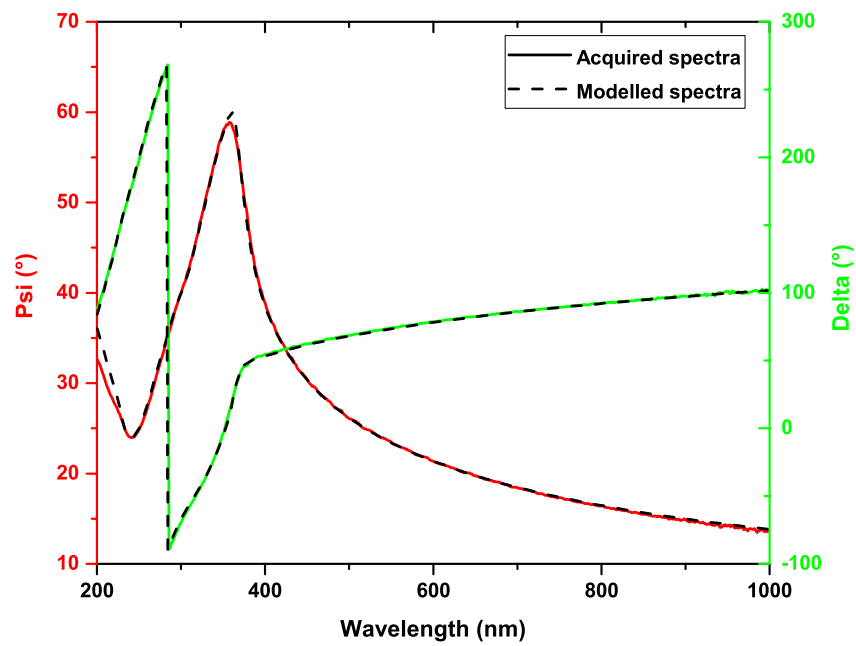


Figure 4.21: Acquired Ψ and Δ spectra for the 13 min. growth duration sample at an incidence angle of 70° along with the spectra resulting from model 6 within Figure 4.20. The close fitting reiterates the suitability of the model to the fitting of the initial stages of NCD film growth.

duced under various conditions, amorphous SiC, and α -SiC from the Woollam database and the literature [167–169]. In a similar result to Cella *et al.*, changing the optical constants of the non-diamond content results in a varying absolute value within the film while the trend with growth duration remains the same [130]. Meanwhile, minor changes in value are observed in the remaining fit parameters due to the relatively low correlation with the glassy-C fraction, and the MSE. Previous characterisation by Hong *et al.* demonstrate that while the dielectric function of glassy-C does not follow the shape of the sp^2 inclusions within a 200 nm thick NCD film, particularly the presence of a fundamental band gap of 0.77 eV, the average magnitudes are similar [96]. In combination with trends observed with Raman, it was decided to retain the optical constants modelled by glassy-C. Upon changing the optical constants of the carbide interface however, large deviations in the surface roughness and void in the bulk occur. All but the β -SiC optical constants demonstrate relatively consistent roughness values for the 4–30 min. growth duration films in the range 10–20 nm before increasing for the final 40 min. growth duration sample, contradicting the roughness values obtained with AFM in Figure 4.13. The use of the optical constants of β -SiC meanwhile rejects the surface roughness layer for the 4–8 min. growth samples then increases linearly for the growth duration, with the point of inclusion of this surface roughness layer coinciding with the peak in the roughness plot of Figure 4.13. Such a local maximum would be expected at the point of coalescence with the height of the islands reaching their peak while still being isolated crystals, and is similar to the trends observed by Collins and coworkers [96, 140, 141]. As such β -SiC, was chosen to represent the optical constants of the interfacial region.

The resulting trends in fitting parameters with growth duration are plotted in Figure 4.22. For the results reported further depolarisation was fitted manually to account for thickness non-uniformity, leading to minor improvements seen in the MSE and small modifications to the structural parameters reported above. As is visible from the plot, before growth the seed spectra are best modelled by a Bruggeman EMA layer of 4.38 nm thickness with 54.9% void content and 4.5% glassy-C, sitting on top of a 1.64 nm thick native oxide layer. Upon being subjected to CVD the thickness of the porous layer then increases to a relatively constant ~ 30 nm for the first 8 minutes of growth while steadily growing laterally as suggested by the decreasing void content to 28.8%

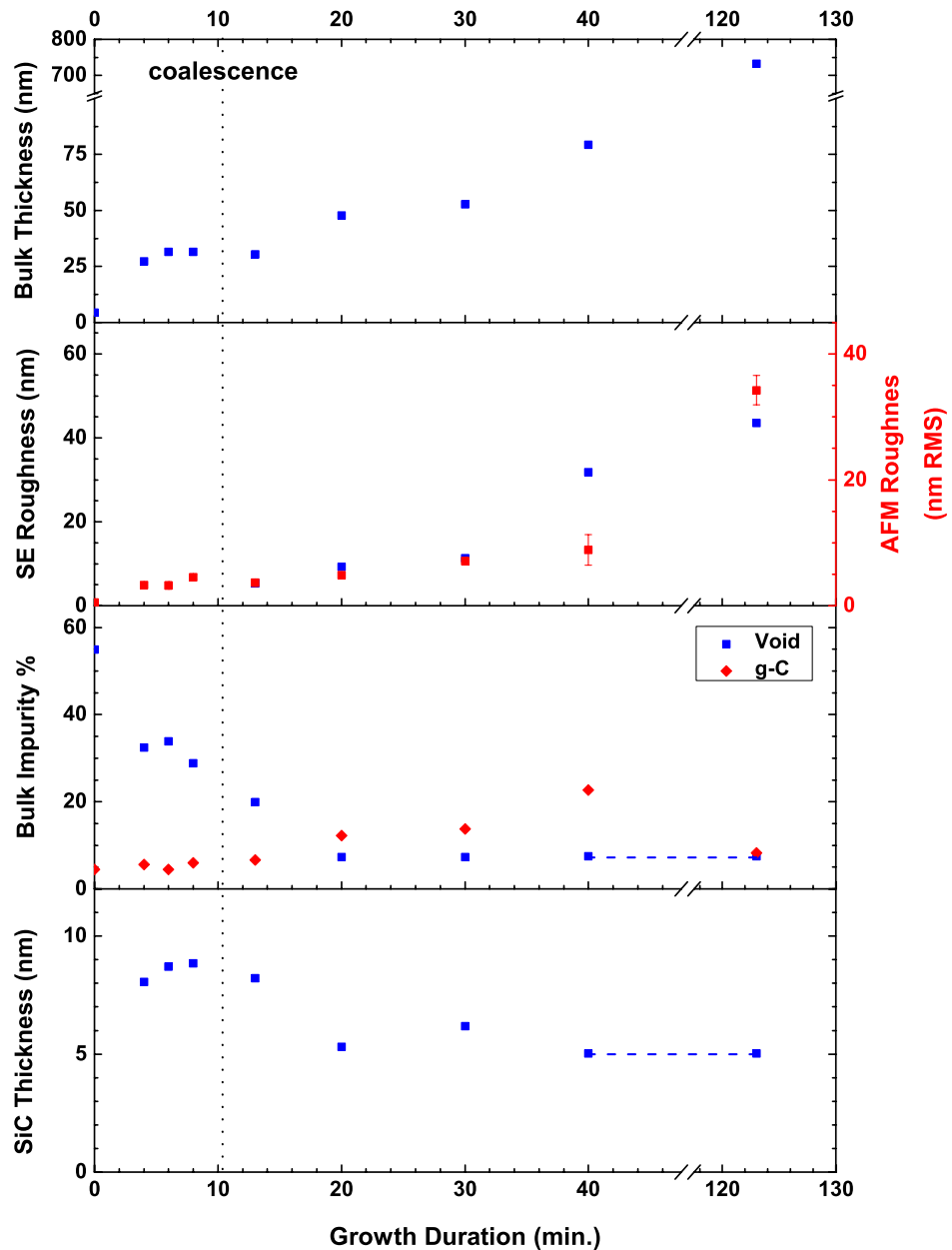


Figure 4.22: Fitting parameter trends with increasing growth duration during the initial stages of nanocrystalline diamond film growth detailing the trends in thickness of the surface roughness, bulk and SiC layers, and the glassy-C and void content within the bulk layer. The point of requirement of the surface roughness layer correspond to the local maximum in AFM roughness and the increase in bulk thickness, with the thickness of the layer correlating with AFM obtained RMS roughness. Meanwhile, the glassy-C content remains constant before this transition before increasing to 22.7% and subsequently dropping for the longer growth duration film, while the void content parabolically decreases with increasing thickness.

for the 8 min. growth duration sample. During this time the glassy-C to diamond ratio remains the same, while the thickness of the newly formed SiC layer peaks at 8.9 nm. After 13 min. of growth the requirement of a surface roughness layer to accurately model the spectra correlates with the peak in roughness obtained with AFM and the point at which the thickness begins to rapidly rise from ~ 30 nm to 79.3 nm for the 40 min. sample. Meanwhile, plotting the RMS roughness obtained through AFM with a multiplying factor of $2/3$ shows a coarse correlation with the thickness of this surface roughness layer. Along with this increase in thickness also comes an increase in the indicated glassy-C content, rising to 22.7% for the 40 min. growth sample while the void content falls parabolically before plateauing at 7.4%. Finally, the SiC layer thickness decreases and remains relatively constant at 5–6 nm. For the thicker and rougher 123 min. growth duration film the surface roughness is no longer homogenous within the wavelength range used, resulting in a breaking down of the EMA and an overestimation of the void content within the bulk at 22.1% should it be allowed to vary; therefore the value was fixed at 7.5%. Meanwhile the thickness of the film prevents fitting of the buried SiC layer, which was again set to 5.03 nm as per the films of shorter growth durations [94]. Should the parameters be allowed to vary, the low correlation results in minor changes to all but the bulk thickness value plotted within Figure 4.22, with values of 43.8 nm, 6.7%, 22.1%, and 12.46 nm for the surface roughness thickness, glassy-C and void contents within the bulk, and SiC layer thickness respectively, validating the trends observed in the glassy-C content and surface roughness.

4.3.6 Discussion

From the plot of the trends in fitting parameters with growth duration of Figure 4.22 a clear distinction can be observed between the nucleation period and bulk growth regime. For the 3–8 min. growth duration films the fitting procedure rejects the presence of a surface layer consisting of fixed composition of 50% diamond/50% void, instead fitting with a single EMA composed of diamond/void/glassy carbon. During this time minor increases in the thickness of the layer occur while the void content decreases sharply, indicating that growth occurs is occurring at a faster rate in the plane rather than normal to the plane. Reiterating this Volmer–Weber type growth the AFM images of panels A–C of Figure 4.11 show agglomerated islands with the displacement in height as deduced

by AFM larger than the thickness determined with SE. Meanwhile, the average particle diameter deduced from SEM as plotted in Figure 4.14 indicates a 20% increase in the particle diameter from 20 to 24 nm for the 3 and 8 min. growth duration samples, while the FWHM of the (111) diamond Bragg peak reduces. After the roughness provided by AFM, as shown in Figure 4.13, locally peaks at an SE indicated thickness of 31 nm a second layer is then required to model the surface roughness, indicative of the formation of a coalesced film. A similar peak in roughness indicating the requirement of a second EMA layer has been observed, and is visible in Figure 4.7, during *in-situ* studies of the growth of diamond and attributable to the size of the isolated islands reaching a maximum before making contact and forming a complete film [96, 128, 139–141, 170]. Through assuming hemispherical nuclei arranged on a square grid in which a void fraction of 0.48 indicates coalescence, *in-situ* studies previously carried out add a bulk layer upon the the void fraction within the nuclei dropping below 0.5 [141]. As a result, relatively constant thicknesses of 20–30 nm are attained upon the transition from nucleation to the bulk growth regime with nucleation densities of the order of 10^{10} cm⁻² [96]. Within the present study however SE estimates that the 4 nm thick seed layer prior to growth contains 55% void, which upon 3 minutes of growth and the formation of aggregated, less ordered nuclei reduces to 33%. Therefore, with the high packing density of the 4–8 nm DND seeds demonstrated by the low vertical displacement in Figure 4.10 reminiscent of that demonstrated by Hees *et al.* and the previously demonstrated stability of seeds under H₂ plasma conditions, it is likely the nucleation density is of the order of 10^{11} cm⁻² [39, 116]. For thicker NCD films modelled with a bilayer stack to account for the inferior quality diamond present at the interface with the substrate, similar thickness values of seed layer in the range 15–41 nm are achieved [71, 97].

The resulting surface roughness EMA thickness and the roughness obtained through the averaging of $1 \times 1 \mu\text{m}^2$ and $5 \times 5 \mu\text{m}^2$ AFM scans for the 4–40 min. and 123 min. growth duration samples respectively are plotted in the second panel of Figure 4.22. Due to the nature of the effective medium approximation, SE is most sensitive to roughness between the atomic scale and a tenth of the wavelength of the probing light, above which the EMA breaks down [69, 88]. AFM on the other hand offers greater sensitivity to larger undulations of the order of a micron, and reduces the texture down to a

single parameter (e.g. R_a or R_{RMS}) [88, 171]. SE and AFM studies on hydrogenated amorphous Si produced with PECVD have demonstrated a relationship between the thickness of the roughness layer deduced with SE (t_{SE}) and the RMS roughness obtained with AFM (R_{RMS}) of the form $t_{SE} \approx 1.5 \cdot R_{RMS} + 0.4$ nm for $1 \leq t_{SE} < 10$ nm [172]. The slope of the relationship suggests that the roughness deduced with SE lies between the peak to peak and RMS roughness obtained with AFM while the non-zero intercept is due to roughness with spatial period below the resolution of the AFM, proposed to be due to SiH_x and CH_x ($x = 2,3$) groups present at the surface from incomplete cross linking during growth [172]. Previous studies on NCD films have demonstrated a similar relationship between the two techniques, and as a result a multiplier of 1.5 was incorporated into the SE deduced roughness plotted in Figure 4.22 [71, 96]. As visible from the plot the 13–30 min. growth duration samples, the roughness obtained with SE are closely correlated with the AFM roughness. Upon the roughness approaching ~ 10 nm with increased growth duration however the homogenous mixing requirement of the Bruggeman EMA no longer holds and the fitting procedure is no longer able to accurately model the dielectric function of the surface roughness. Further difference in the roughness for the 40 min. growth duration sample are believed to be attributable to the increasing grain size with respect to the $1 \times 1 \mu m^2$ AFM scan size, leading to an underestimate of the R_{RMS} .

Of particular intrigue is the trend in glassy carbon content observed upon the formation of a coalesced film as plotted in the third panel of Figure 4.22; during the seed and nucleation phase of growth the ratio of diamond to glassy-carbon content remains constant at approximately 11.2, upon the transition to a complete film begins to increase to a peak of 3.1 for the 40 min. growth sample, and subsequently decreases to 10.1 for the 123 min. growth duration sample. With the low correlation observed in the matrix of Table 4.1 it is unlikely that this peculiar increase in the content is an artefact of the fitting procedure with such a low correlation being previously reported during *in-situ* NCD studies [141]. Should the previously fixed void content of the 123 min. growth duration sample be allowed to vary during the fitting procedure to 22.1%, a relatively minor increase in the diamond/glassy-C ratio to 10.6 is observed and remaining significantly larger than the peak value of 3.1. This trend is supported by the increase in the Raman G band at $1500\text{--}1500$ cm^{-1} with the D band at 1360 cm^{-1} remaining constant

observed after 20 min. of growth, indicative of an increase in the amorphous sp^2 content within the film. The intensity of the G peak then begins to decrease for the 30 min. growth sample before reaching a minimum for the 123 min. growth duration sample. Meanwhile, deconvolution of the 20, 40, and 123 min. growth durations and accounting for the areas of both D and G peaks reveal non-diamond contents of 23%, 27%, and 13%, reiterating this decrease in non-diamond content after 40 minutes of growth. The discrepancy between the apparent peak in amorphous sp^2 contents between SE and Raman is believed to be due to non-uniformity over the spot size of the ellipsometer. A clear colour change was visible by eye over the 1 by 1 cm^2 sized 40 min. growth duration sample which when coupled with the sharp increase in the glassy-carbon content from 13.8% to 22.7% within the 26 nm thickness difference between 30 and 40 min. growth samples could lead to a shift in the indicated peak of the glassy-C content.

To explain the trend in glassy-C content the Volmer-Weber and van der Drift growth models need to be considered; during NCD film growth the polycrystalline nature of competing crystals of random orientation will prevent the formation of sp^3 bonds between neighbouring crystallites, allowing the formation of hydrogenated amorphous sp^3 , sp^2 , and sp^1 sites [99, 100]. Therefore, it is to be expected that during the initial stages of production in which growth primarily consists of isolated islands that the non-diamond content will be minimal due to the lack of trapping of material between coalescing crystallites. Such a supposition is supported within the current study as the increased methane admixture of 3.86% for the first 3 minutes of growth before a reduction to 0.6% appears to have little effect on the glassy carbon content during the nucleation phase of growth, with the content remaining constant between 4.5 and 6 %; should the increased methane admixture result in the inclusion of non-diamond carbon within the film a parabolic decrease in the content would be observed for the 4 min. growth sample onwards. Previous *in-situ* studies have shown that upon varying the oxygen within the feed gas from $O_2/(O_2+H_2)$ concentrations of 0% to 10%, the sp^2 content within the nuclei remain near the detection limit of 1%. Meanwhile, the corresponding sp^2 content within the bulk linearly decreases from 15% to 2% due to the reduction in the lifetime of sp^2 sites with preferential etching by oxygen ions [96]. Upon coalescence the formation of grain boundaries then lead to an increase in the glassy-C content, which peaks while the surface/volume ratio of the crystallites is at a maximum and then followed by a

decrease as crystallite size increases. In addition, the large magnitude of the similar peaks in sp^2 content observed by Hong *et al.* in Figure 4.7 are additionally attributed to shadowing of crystallite facets. The sp^2 content then increases due to the inability of the atomic hydrogen to preferentially etch the sites away, with previous SEM studies showing the formation of sp^2 sites on the facets of micron-sized diamond particles [96]. The increase in signal assigned to grain boundary TPA at 1150 cm^{-1} after 13 minutes of growth then supports such an argument.

Lastly, previous *in-situ* studies performed during the subsection of unseeded silicon wafers to CVD growth conditions have revealed the formation of a 4–7 nm thick porous SiC layer, with longer growth durations increasing the density of the layer while leaving the thickness unchanged [138]. However, such studies did not extend to include a variable thickness interlayer upon diamond growth on seeded wafers, presumably due to the difficulty in distinguishing such a thin layer from scratching induced damage and recrystallisation at elevated temperatures, or near substrate diamond [94, 137, 141]. *In-situ* XPS studies on BEN and mechanically scratched seeded films have shown the removal of signal arising from silicon suboxides atop the substrate during the first 15 minutes and domination by a signal attributable to SiC, with overlayer calculations placing thicknesses at 2–9 nm [119–121, 123]. The source of such carbon can be either from CH_4 derived radicals within the plasma or through etching/direct interaction with diamond crystallites, with XPS studies on nano-diamond seeded silicon revealing the formation of SiC upon subsection to either H_2 or H_2/CH_4 plasmas [116]. While the thickness of this amorphous SiC layer is kinetically limited by silicon diffusion through the existing carbide, for thicker interfaces EELS has shown spectra identical to that of single crystal β -SiC [119, 173, 174]. After the formation of a diffusion layer preferential evaporation of Si and/or etching of SiC then occurs, hastened by the transition to a hydrogen rich plasma after the termination of bias enhanced seeding and the beginning of conventional growth [119, 175]. It is therefore believed that during the 3 minute period of increased methane admixture the growth of the SiC layer is enhanced leading to the peak thickness of 8.85 nm, less than the diffusion limited thickness of 9 nm indicated during *in-situ* XPS. Before coalescence this layer begins to reduce in thickness after 8 minutes, with the believed non-uniformity in growth of the samples allowing this reduction to continue past 13 mins when the entirety of the film sampled by ellipsometry

has coalesced. Stable thicknesses of ~ 5.5 are then observed for the 20–40 min. growth samples and fixed for the thicker 123 min. sample. Raman tentatively supports the presence of such a SiC layer with the constant appearance of a broad peak at 830 cm^{-1} for all but the thicker 123 min. growth sample indicative of the presence of amorphous SiC.

4.4 Conclusion

SE has been applied to the characterisation of the initial stages of growth of nanocrystalline diamond films from nano-diamond seeds, with the resulting trends in thickness, and void and non-diamond fractions corroborated with Raman, SEM, AFM, and XRD. Through the use of 2 Bruggeman EMA layers, SE has modelled the coalescence of isolated islands on top of a carbide layer into to a complete film, with the transition coinciding with a peak in AFM roughness and the introduction of the Raman trans-polyacetylene peak from the formation of grain boundaries. After coalescence the SE indicated peak in non-diamond content attributable to the surface/volume ratio is supported by Raman, while the thickness of the newly formed surface roughness layer is observed to correlate with AFM derived roughness values. Thus with its ease of measurement, ability to characterise the void, non-diamond and SiC content present within newly formed nanocrystalline films, SE is a powerful method for the characterisation of the early stages of nanocrystalline diamond film growth.

Chapter 5

Chemical Mechanical Polishing of Diamond

The polishing of gem stone diamond is believed to have been carried out since at least the 14th century with the technique changing little to this day. However, with the recent developments in the growth of high quality nanocrystalline diamond films and single crystal diamond, the material is being heralded as a future material in applications ranging from micro- and nano-electro-mechanical systems to thermal management coatings. These advanced technological applications require not only high quality diamond, but also efficient polishing techniques capable of uniformly polishing diamond to the required roughness whilst minimising damage. Within this chapter a brief overview is given of diamond polishing methods to date, leading to the adaptation of the IC fabrication technique of chemical mechanical polishing. With this method it is shown that mechanical polishing introduced damage can be removed from single crystal diamond and that nanocrystalline diamond can be polished to under 2 nms RMS, as required for the titular application of this thesis.

5.1 Why Polish?

For polycrystalline films grown under low CH_4/H_2 conditions, the formation of columnar grains leads to an increase in grain size and roughness with film thickness [14]. Meanwhile, growth hillocks, facets, and macroscopic steps are typically observed in the growth of single crystal diamond [176]. This considerable surface roughness hinders the use of both single crystal and polycrystalline diamond in a variety of applications. For example, in thermal management applications this surface roughness reduces the contact between the film and device limiting the heat transport. In applications utilising diamond's broadband transparency surface roughness leads to diffuse scattering at wavelengths below $10\ \mu\text{m}$, which after polishing can be reduced to $2\ \mu\text{m}$ [177]. Through reducing the H_2 /increasing the CH_4 content of the plasma the crystallite growth in polycrystalline films can be interrupted, leading to a reduction in the grain sizes and curtailing of the surface roughness. However, the inevitable increase in sp^2 at grain boundaries with reducing crystallite size increases phonon scattering, and absorption due to the increase in tail states and the presence of π and π^* states within the band gap [14, 178, 179].

For tribological applications unpolished diamond films have shown to present a high coefficient of friction due to ploughing of surface asperities into the mating tool along with abrasive wear [180]. Upon polishing, the formation of plateaus reduces the separation needed between diamond and counter-surface, allowing the transition to hydrodynamic lubrication to occur at lower sliding speeds. After this onset a corresponding reduction in coefficient of 0.25 to 0.02 was observed between polished polycrystalline diamond and stainless steel [180, 181].

Considering diamonds use in MEMS, polycrystalline films are frequently utilised in surface acoustic wave (SAW) devices due to diamond's unmatched acoustic velocity ($18\,000\ \text{m s}^{-1}$); such a PCD/aluminium nitride device operating at 10–14 GHz has demonstrated Q factors and out of band rejection ratios of 12 560 and 36 dB respectively, rivalling the largest reported values for SAW resonators [2, 7]. However, as the surface wave propagates up to a wavelength into the bulk, film thicknesses of the order of tens of microns are required to utilise diamonds high acoustic velocity [182]. For such thick films grown under low methane admixture conditions, the surface roughness can

preclude successful construction, while renucleation driven UNCD will not demonstrate such superlative acoustic properties [15, 101]. Figure 5.1 shows aluminium interdigital electrodes of a SAW device deposited onto (a) AlN/NCD/Si, and (b) AlN/PCD/Si structures. The aluminium digits are clearly defined on the smoother renucleation driven UNCD film with thickness and roughness of 2.4 μm and 23 nm RMS respectively. However, numerous breakages and shorts between sets of digits occur on those deposited onto the rougher columnar growth polycrystalline diamond film. In addition, in order to maximise the coupling coefficient of a thin film electro-acoustic device the *c*-axis of the piezoelectric must be uniformly orientated perpendicular to the diamond film. As the piezoelectric conforms to the topography of the substrate, rough films makes such tight control of the crystallographic orientation difficult. XRD studies have shown that a surface roughness below 4 nm RMS is required, otherwise a peak attributable to the (100) plane is visible in addition to the (002) peak suggesting a distribution of texture rather than uniform *c*-axis orientation [182, 183]. With the signal that is successfully transduced, the surface roughness will then cause scattering of the surface acoustic wave and conversion to bulk acoustic waves, increasing dissipation and lowering the *Q* factor of the resonator [184]. To work around this, previous reports have utilised the smoother nucleation side of freestanding diamond films through removing the silicon substrate and bonding to a support structure [185]. However the quality of this diamond is often inferior, while this process is complicated, time consuming, and incompatible with some of the applications mentioned previously and particular MEMS/NEMS geometries.

As discussed within Chapter 6 the reduction in volume upon the transition from MEMS to NEMS results in further sources of and more pronounced dissipation, with *Q* scaling to device volume (*V*) as $Q \propto V^{1/3}$ [6]. With continued miniaturisation to nano-scale dimensions the increased surface to volume ratio is expected to result in an enhanced contribution to loss from atoms and adsorbates, dangling bonds, and defects present at the surface [6, 16, 17]. The significant roughness inherent to NCD films is then expected to further increase the surface to volume ratio, enhancing this loss and spoiling the *Q* factor of resonators fabricated from such stock.

To utilise diamond films and single crystals without compromising on quality in the applications mentioned above, a polishing step is therefore required. The rest of this chapter details the progression of currently used diamond polishing methods, the

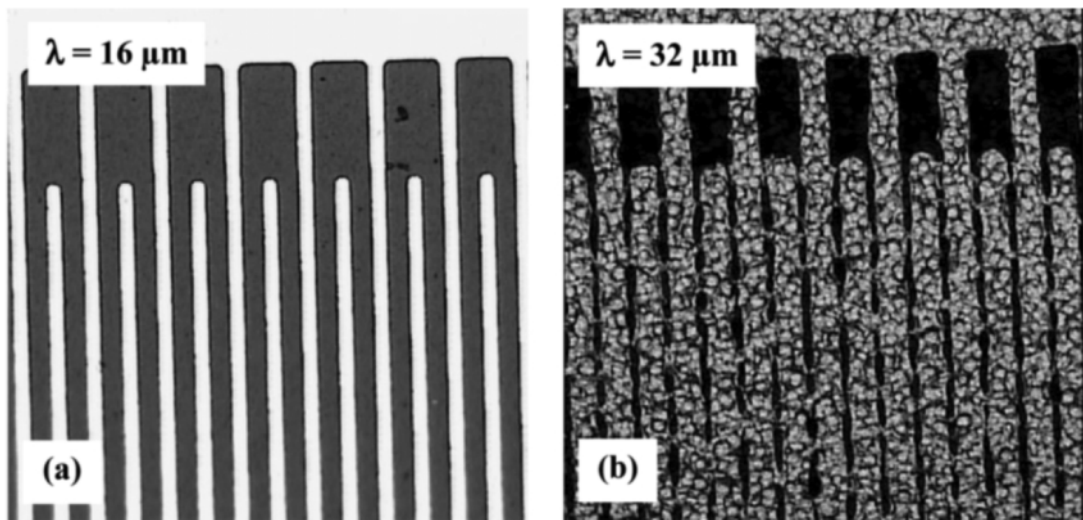


Figure 5.1: Surface acoustic wave devices created on (a) UNCD and (b) PCD films. The smooth surface of the renucleation driven film is more conducive to the formation of $1.5 \mu\text{m}$ thick interdigital transducers, while deposition on rougher columnar grown polycrystalline diamond films create open and short-circuited digits unable to create an efficient SAW device. Reprinted from *Diamond and Related Materials*, **13**, F. Bénédic *et al.*, "Surface acoustic wave devices based on nanocrystalline diamond and aluminium nitride", 347–353, Copyright (2004), with permission from Elsevier.

innate problems with each, and finally the adaptation and testing of chemical mechanical polishing to the polishing of nanocrystalline and single crystal diamond.

5.2 Mechanical Polishing

Due to diamond's extreme hardness, polishing has traditionally been carried out on the basis that 'diamond polishes diamond' with the technique of mechanical polishing [186]. During this process the sample to be polished is applied to a fast rotating (2500 rpm) cast iron or alumina scaife of approximately 300 mm in diameter, resulting in wear rates of up to $1 \mu\text{m s}^{-1}$ [187–189]. However, as much as an order of magnitude difference in the wear rate is known to occur between different polishing directions, while fracture induced micro fissures that are initiated at the surface propagate up to $2.5 \mu\text{m}$ into the bulk creating a highly damaged surface region [188, 190].

5.2.1 Polishing Process

Prior to use, approximately 1 to 2 carats (200–400 mg) of industrial diamond grit with an olive oil binder is dispensed onto the scaife and worked in by hand. After continued working leads to the particles becoming sufficiently embedded within sand-blasted pores or pre-machined radial grooves, the scaife turns matt grey. The scaife is then subjected to a process known as 'boarting', in which a piece of inferior diamond is held with the $\langle 100 \rangle$ direction parallel to the velocity of the scaife and swept across at polishing speeds and pressures. After the initial working by hand the grit is randomly orientated, however upon boarting these particles rotate to present flat topped crystals, also orientated along the cubic $\langle 100 \rangle$ direction due to the desire of two frictionally anisotropic particles to maximise the friction between them [189]. After continued boarting the scaife will turn a matt black, signifying that the process is complete and that polishing can begin. During polishing the diamond workpiece is held against the rotating scaife at pressures of 2.5–6.5 MPa for coarse material removal at rates of up to $1 \mu\text{m s}^{-1}$, or reduced pressures of 1–2.5 MPa for polishing [187]. While large grits work for bulk material removing during initial grinding, a finer grit is needed to produce a smoother surface. As such, the size of the grit is reduced from $20 \mu\text{m}$ to sub micron sizes as polishing progresses [189].

Since the advent of mechanical polishing it has been seen that the wear rate is highly dependant on both the crystallographic orientation of the diamond and the azimuthal angle of polishing [190]. There are three crystallographic plane groups of diamond; the cubic $\{100\}$, dodecahedral $\{110\}$, and octahedral $\{111\}$ typically referred to as the 4-point, 2-point, and 3-point planes respectively [188]. With each face comes ‘soft’ polishing directions in which the material removal rate is at a maximum and leads to rapid heating of the scaife, and ‘hard’ polishing directions in which damage to both the crystal and scaife occur, accompanied by an unpleasant grinding noise and excessive vibration [191]. For the $\{100\}$ and $\{110\}$ planes these soft polishing directions lie along the cubic $\langle 100 \rangle$ direction, while the hard polishing directions are along the $\langle 110 \rangle$ direction, as indicated in Figure 5.2 [189]. The $\{111\}$ surface meanwhile remains difficult to polishing along all directions with only slight three fold symmetry and a maximum wear rate 0.1 times that possible along the ‘soft’ direction of a $\{110\}$ face [187]. In terms of the wear rate, this anisotropy can be explained through the use of periodic bond chains (PBC), in which minimal wear is seen when the polishing direction is parallel to chains of bonded atoms or ‘growth units’. Along these PBC vectors the bonds are most resistant to compression or bending due to the supporting action of neighbouring bonds within the chain. Looking at the dodecahedral $\{110\}$ plane group lattice view of Figure 5.2 only one such PBC can be seen, linking the five lowermost black atoms along the $[110]$ direction [192, 193]. In comparison, the $\{111\}$ plane exhibits three such PBCs with three fold symmetry and a high planar density of atoms, leading to a higher wear resistance. From Figure 5.2 it can also be seen that a rotation or tilt in the crystallographic orientation of a few degrees can lead to drastic changes in the wear rate. Should the sample to be polished have a tilt in the face with respect to the the principle plane group the wear rate along along a supposedly ‘soft’ polishing direction can significantly increase, reducing the number of practical polishing directions [188, 194]. For example, the wear rate when polishing along the $\{111\}$ surface increases by a factor of 30 when the face of the sample has a misalignment angle with respect to the principle plane of as little as 5° [195]. Therefore, before polishing the sample is precisely orientated along the desired polishing direction with the use of Laue geometry XRD, adding complexity to the process and increasing the setup time required [191].

With the complicated three body mechanism to the polishing, the wear rate is a

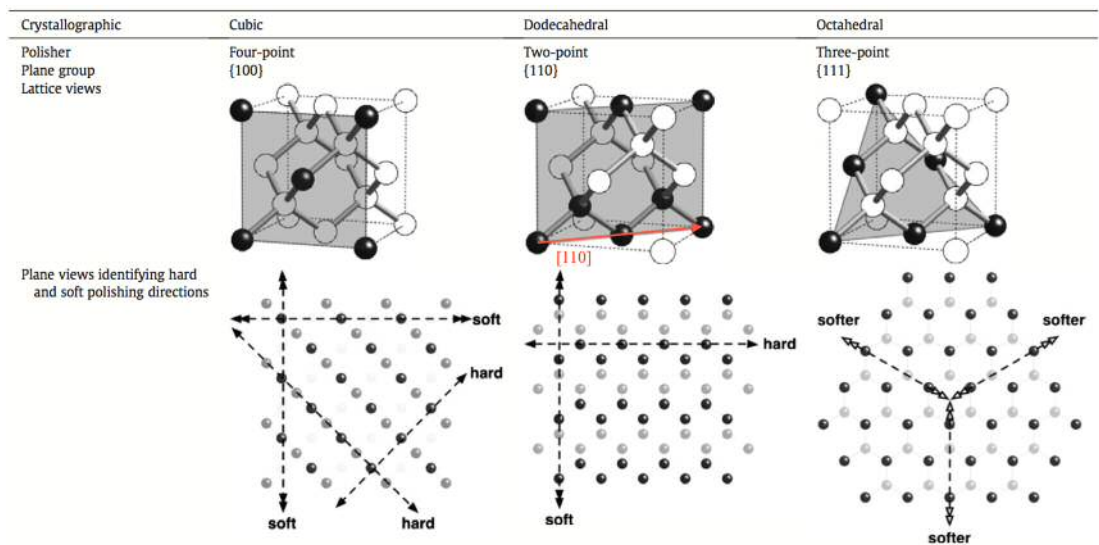


Figure 5.2: Unit cell of diamond indicating the cubic, dodecahedral, and octahedral diamond plane groups, along with their respective ‘hard’ and ‘soft’ polishing directions. Also indicated on the dodecahedral plane group unit cell is the [110] direction, highlighting 5 atoms that constitute the PBC responsible for the minimal wear rate seen along the ‘hard’ $\langle 110 \rangle$ direction. Reprinted from *Diamond and Related Materials*, **32**, T. Schuelke and T. A. Grotjohn, "Diamond polishing", 17–26, Copyright (2013), with permission from Elsevier.

function of the properties of the scaife, the diamond grit, the polishing debris, frictional heating, and finally the velocity and applied pressure [189]. Figure 5.3 shows the non-linear wear surface observed when polishing along the ‘soft’ $\langle 100 \rangle$ cube direction of a $\{100\}$ crystallographic face. Before the onset of polishing, low velocities and pressures lead to low grating noise and degradation of the scaife surface. The wear rate then suddenly increases with increasing pressure and velocity in a non-linear fashion. Increasing the contact pressure reduces the onset of wear, while increasing the velocity at a given pressure brings about a more substantial wear rate. Further increases in the velocity and pressure bring about a softening of the scaife due to frictional heating, allowing the diamond grit to submerge into the scaife reducing the amount of grit available for mechanical action and causing the wear rate to plateau off [191].

5.2.2 Removal Mechanism

Due to diamond being both brittle and hard it was initially postulated by Tolkowsky that wear was the result of micro-cleavage along the easy to fracture octahedral $\{111\}$ plane, with anisotropy being down to the orientation of this face with respect to the face being polished. Such directions in which the force applied by the grit is easily able to result in cleavage were then referred to as ‘soft’ [190]. This can be through having a large component of force along the cleavage plane, or because the topography of the workpiece surface allows for easy detachment of surface asperities [190]. However when a sample that has been polished along a ‘soft’ direction is observed with AFM, features are seen that cannot be explained by a wear model based on micro-fracture, while also being significantly different to those seen along a ‘hard’ direction. Along the ‘soft’ direction smooth nano-grooves are observed with widths of 20–1000 nm, typically smaller than the grit embedded within the scaife [196]. This is in stark contrast to the rough ‘hill and valley’ type structures seen along when polishing along ‘hard’ directions which are more consistent with a model based on fracture. Furthermore, it has been shown through electron-energy-loss spectroscopy (EELS) that the debris consists of less dense carbon with the density estimated to be 1.8 g cm^{-3} , a marked decrease from the density of diamond of 3.5 g cm^{-3} and similar to that of graphite [190, 197]. Meanwhile, diamond on diamond sliding experiments have also shown that the volume of debris produced is approximately 2 times that of the volume of the nano-grooves created [196].

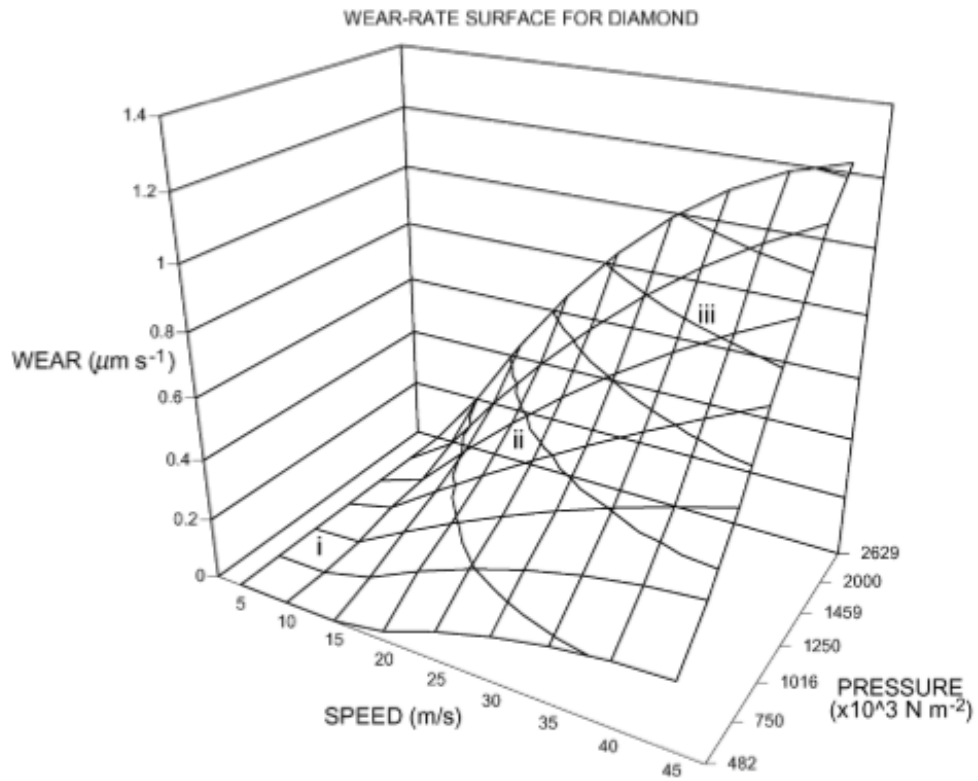


Figure 5.3: Wear surface detailing the relationship between velocity, pressure, and wear rate when polishing along the soft $\langle 100 \rangle$ direction of a $\{110\}$ plane group. Low velocities and pressures lead to damage of the scaife and minimal material removal. Increasing pressures and velocities lead to an enhanced removal rate until the point at which frictional heating causes diamond grit to embed within the scaife, reducing the particles available for mechanical action. Reprinted from *Wear*, **258**, Second International Conference on Erosive and Abrasive Wear, J. Hird and J. Field, "A wear mechanism map for the diamond polishing process", 18–25, Copyright (2005), with permission from Elsevier.

Instead, it has therefore been proposed that wear along ‘soft’ polishing directions is a result of a shear induced phase transformation from sp^3 diamond to sp^2 amorphous carbon [189]. As SEM studies of the workpiece and the grit embedded within the scaife both show nano-grooved features indicative of reciprocal wear and a lack of knife edges, it is believed that these flat grit particles act as anvils for smaller loose grit [189]. Through this process large forces are reached that would be unobtainable should the looser grit be directly pressed against the softer cast iron scaife. Estimates can be placed on the size of these particles through looking at the size at which a particle will begin to flow plastically rather than act as an indenter, known as the brittle-ductile transition. Values found of the order of tens of nms dependant on the load and orientation give credence to the idea that small grit particles contained within the black layer of the scaife are responsible for the nano-grooves observed [189]. Molecular dynamic simulations have further backed up this model, in which two diamond surfaces sliding against each other at pressures of 10 GPa has been shown to lead to gradual conversion of the diamond interface to an amorphous ad-layer [198]. Wear is then explained by the likelihood that a passing a-C atom can form a strong enough bond to a surface sp^3 hybridised atom to pull said atom into the ad-layer. Polishing along ‘hard’ directions require further bonds to be broken and at a higher energy than along ‘soft’ polishing directions explaining the anisotropy seen. This amorphous material is then removed through mechanical abrasion by a passing knife edge of a grit particle, or through the formation of CO and CO₂.

5.2.3 Surface Finish

With the difference in the wear resistance of the ‘hard’ and ‘soft’ polishing directions of the {100} and {110} plane groups comes a difference in the resulting surface topography. As touched upon earlier, polishing along the ‘soft’ cube direction of either the {100} or {110} plane group leads to the formation of nano-grooves due to passing grit drawing atoms into an amorphous ad-layer and subsequent abrasion. These striations are usually devoid of fracture and flat bottomed with widths of 20–1000 nm dependant on the size of the grit used, and depths of up to 7 nm [189, 199]. Meanwhile, polishing along ‘hard’ directions leads to ‘hill and valley’ type structures as a result of fracturing along the {111} plane. Figure 5.4 shows AFM scans taken of {100} and {111} orientated samples after being mechanically polished with 0.5 μm grit along both the $\langle 100 \rangle$ and $\langle 110 \rangle$

directions. As would be expected, for directions along which wear is readily seen the resulting width and depths of the features and the surface waviness is larger than that along the more wear resistant directions. This difference in the wear mechanism is then reflected in the roughness, where values of 3.5 nm Ra and 1.6 nm Ra were seen when polishing along the $\langle 100 \rangle$ and $\langle 110 \rangle$ direction of the $\{100\}$ surface, and 4.5 nm Ra and 2.9 nm Ra for the corresponding directions on the $\{110\}$ plane [200].

Due to nature of mechanical polishing with a certain amount of fracture occurring even when polishing along soft directions, cracks that are initiated on the surface often propagate into the bulk. Generally, the larger the particle the more subsurface damage that is created. Through oxygen plasma etching in which defects are preferentially etched, it has been seen that the etch pits created, and thus the depth of the cracks, are limited to below 1 μm deep [176]. Cathodoluminescence and photoluminescence carried out on a polished 65 μm thick diamond film have meanwhile shown an increase in defect bands attributable to considerable sub-surface micro cracks as a result of polishing, which subsequently disappear after etching of 4–5 μm of the surface away [201].

Applications requiring the use of highly polished defect free substrates are then affected by the presence of these newly created defects. With the inherent difficulties in controlling the point defect content of HPHT synthetic diamond as required for electronic and optical applications, HPHT seeds are often used as substrates for homoepitaxial CVD growth in which the boron, phosphorous, and nitrogen content can be controlled effectively in both doped and un-doped layers [202]. However, dislocation defects within the seed tend to propagate to the epitaxial layer, while new dislocations can nucleate at or close to the interface between the two materials. Part of this increase can be attributed to surface and subsurface damage arising from mechanical polishing. This increase in dislocations can then lead to plastic deformation and trapping of carriers, birefringence, and luminescence quenching defects when used in optical applications [176, 201].

Through the use of XRT it has been shown that careful polishing of HPHT substrates leads to a significant reduction in the dislocations attributable to mechanically introduced damage, with the remaining defects being randomly orientated rather than along lines of possible polishing damage, suggesting they originate within the bulk of the seed [176]. More definitively, it has also been shown through XRT that when com-

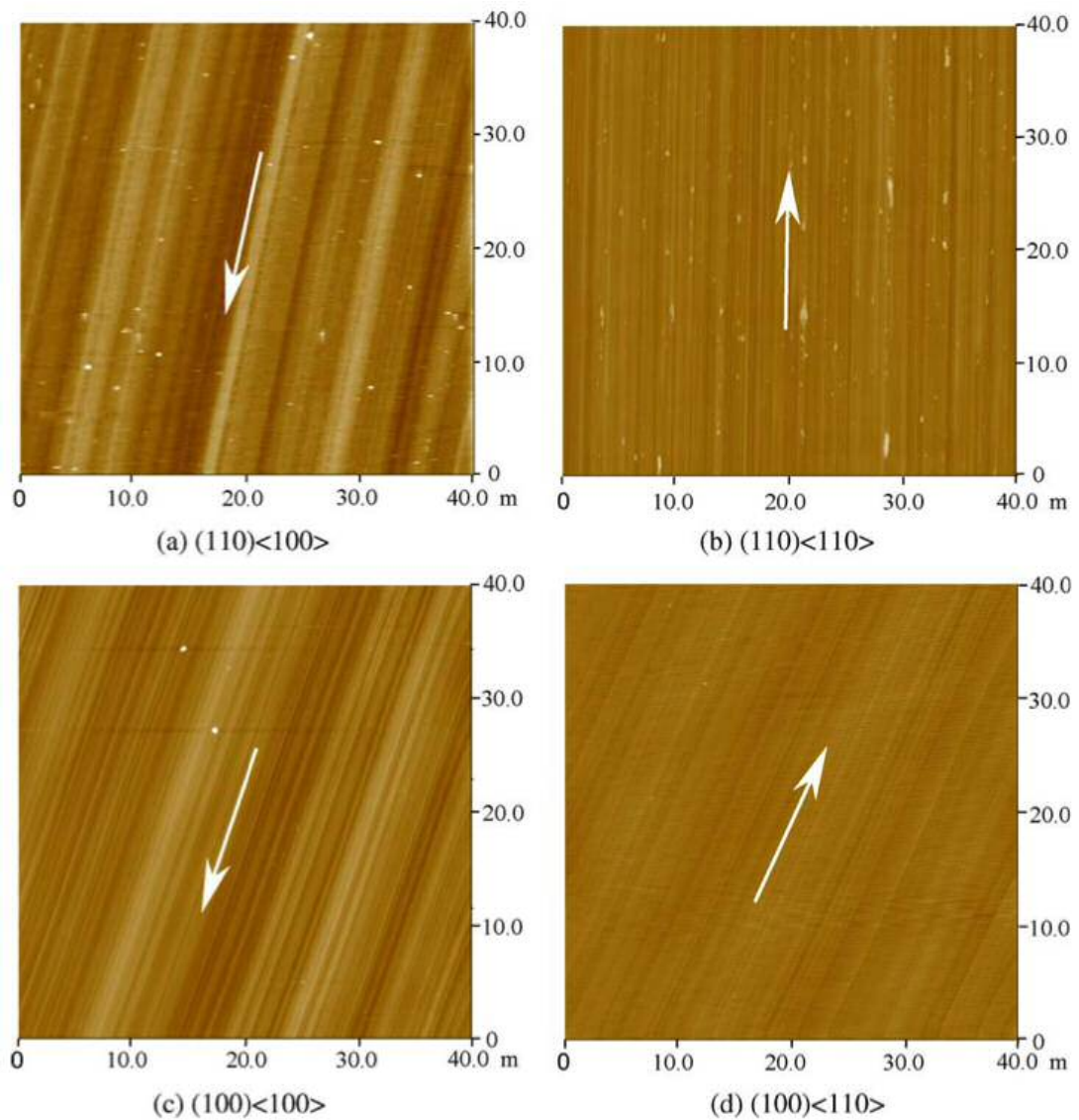


Figure 5.4: AFM scans of $\{100\}$ and $\{110\}$ diamond workpieces polished along the $\langle 100 \rangle$ and $\langle 110 \rangle$ directions. Polishing along the ‘soft’ $\langle 100 \rangle$ direction leads to flat bottomed nano-grooves and large surface waviness, in stark contrast to the smoother ‘hill and valley’ structures seen when polishing along the harder $\langle 110 \rangle$ direction. Reprinted from International Journal of Machine Tools and Manufacture, **45**, W. Zong *et al.*, "The material removal mechanism in mechanical lapping of diamond cutting tools", 783–788, Copyright (2005), with permission from Elsevier.

paring a homoepitaxial layer grown on a mechanically polished substrate to one that has been grown on the same substrate after UV-assisted polishing, a much gentler polishing technique, the formation of new dislocations at the interface was prevented [203]. Through the use of carefully polished substrates with low defect density, epitaxial layers have been grown with defect densities as low as 400 cm^{-2} resulting in high mobility values of 4500 and $3800 \text{ cm}^2 \text{ V}^{-1} \text{ s}^{-1}$ for electrons and holes respectively and ultra low birefringence (5×10^{-7}) crystals [51, 176]. To prevent these defects arising in homoepitaxial layers a subsequent, far gentler, polishing step is therefore required to remove mechanically introduced artefacts from the initial seeds.

5.2.4 Mechanical Polishing of Nanocrystalline Diamond

When mechanically polishing microcrystalline diamond films, the grit embedded within the scaife will see grains orientated in both the ‘hard’ and ‘soft’ directions due to the random texturing of the films. With each crystal having its own wear rate, the average over the entire film is then reduced to the order of tens of nm h^{-1} [204]. As a result, the ‘hard’ orientated grains will not only see considerable subsurface damage but will also leave protruding crystals, reducing the achievable roughness of the film [180]. As also mentioned previously, due to the van der Drift model of competing grains microcavities will be formed within the film. As polishing progresses these microcavities will then intersect with the surface, creating surface pits and placing a natural limit on the achievable roughness, with higher growth rate films having larger microcavities [205].

A large barrier to the mechanical polishing of polycrystalline, particularly nanocrystalline, films is the presence of stress after heteroepitaxial growth, being reported to be either compressive or tensile depending on the CVD technique and growth conditions used. For films grown on silicon substrates, there exists a considerable difference in the coefficient of expansion values between the diamond film and silicon substrate with values of $2.0 \times 10^{-6} \text{ K}^{-1}$ and $3.5 \times 10^{-6} \text{ K}^{-1}$ respectively [206]. Upon cooling from deposition temperatures the contraction of the substrate will be greater than that of the film, resulting in compressive stress typically of the order of -0.2 to -0.3 GPa for the film thickness and deposition temperatures of the films used within this thesis [207]. Meanwhile, the intrinsic stress of the diamond film is typically tensile and arising from two competing sources: graphitic inclusions with a corresponding specific volume larger

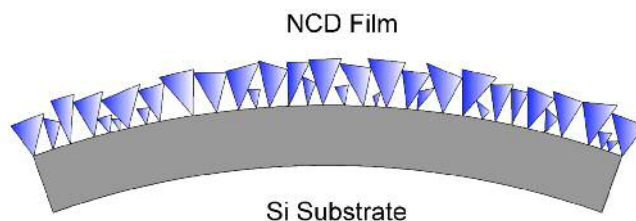


Figure 5.5: Exaggerated schematic detailing the wafer bow present due to high stress. Should such a wafer be applied to a hard scaife under pressure, uneven polishing will occur along with potential shattering. Reprinted from [210] under a Creative Commons license, <https://creativecommons.org/licenses/by/3.0/>.

than that of diamond causing compressive stress; and attractive atomic forces across grain boundaries and voids causing tensile stress [207]. For thin nanocrystalline diamond films the summation of the thermal and intrinsic stress typically yields values of between 0.8 GPa and -0.1 GPa, decreasing with increasing methane fraction and decreasing deposition temperature [8, 207, 208]. This considerable stress can cause considerable wafer bow of $20\ \mu\text{m}$ over a $525\ \mu\text{m}$ thick 100 mm dia. wafer, and cause the film to delaminate or peel off should the magnitude of stress be large enough [209]. Such a wafer bow is in addition to the already present wafer bow of several microns present with $500\ \mu\text{m}$ thick silicon wafers. A schematic, albeit exaggerated, is shown in Figure 5.5 where a large compressive stress results in a convex bow with respect to the surface of the NCD film. Should one of these highly stressed and bowed wafers then be subjected to the high pressures characteristic of mechanical polishing, uneven polishing will occur due to the bow being larger than the film thickness along with the potential of shatter [187]. Therefore, a polishing technique capable of producing polished surfaces at lower pressures is required for the successful polishing of thin nanocrystalline diamond samples.

5.3 Chemically Assisted Mechanical Polishing

In order to overcome the low wear rate and/or poor surface finish seen after subjecting single crystal and polycrystalline diamond films to mechanical polishing, the technique of chemically assisted mechanical polishing (CAMPP) was developed. First pioneered

by Thornton and Kühnle, it was observed that when KNO_3 and NaNO_3 salts were used in conjunction with a virgin scaife, i.e. one that had not come into contact with diamond powder, steady polishing occurred on both $\{100\}$ and $\{111\}$ orientated single crystal samples [132, 211]. Through this technique, the mechanical phase transformation/fracture of scaife polishing is used in conjunction with oxidiser driven conversion to CO and CO_2 to provide a gentle atom by atom removal of material. As a result, a superior surface finish is achievable with little indication of surface polishing introduced artefacts.

5.3.1 Polishing Process and Removal Mechanism

In a similar fashion to mechanical polishing, the sample to be polished is placed against a fast rotating (~ 80 rpm) cast iron, or more typically alumina, plate at reduced loads of the order of 1 MPa and 0.1 MPa for single crystal and polycrystalline diamond samples respectively [132, 205, 211, 212]. While high loads will increase the removal rate for single crystal samples, similar loads on polycrystalline samples are generally avoided to prevent shattering with the large stress present after CVD [133]. Polycrystalline alumina (Al_2O_3) plates are generally favoured with CAMPP due to ceramics typically being harder than metals and more conducive to cracking asperities and crystallite peaks without deforming [205]. The use of ceramics also reduces contamination of the sample from the scaife and minimises equipment corrosion within the heavily oxidising environment [132, 213]. During use the plate is fed with oxidisers, historically NaNO_3 , KNO_3 , or KOH , with melting points of 308, 324, and 360 °C respectively [180, 205, 211, 213]. The oxidiser is then heated to above their respective melting points either through direct contact with a heated scaife or through the use of infra-red lamps [180, 205, 211, 213]. Through using oxidisers with lower melting points higher reaction rates will occur at a given temperature, or equipment can be made simpler and more cost effective. As such H_2O_2 , HClO , HNO_3 , H_2SO_4 , AgO , Cr_2O_3 , MnO , BaO_2 , PdO_2 or combinations thereof have all been demonstrated [132]. For example, the combination of KNO_3 and LiNO_3 has a combined melting point of 130 °C, and as a result has been shown to have a higher fraction of ionised oxidising agents within the mix, increasing the removal rate [132].

Upon polishing, the high loads on the sample result in the creation of micro-cracks

and the removal of material from crystallite peaks or asperities that initially come into contact with the plate. Under the elevated pressures and temperatures created by the plate the molten oxidisers then enter these cracks and convert the material to CO and CO₂, further weakening the peaks/asperities and allowing further cracking to occur [205]. As the contact area increases for a given load the force at the asperities reduces, leading to a tailing off of the mechanical component to the polishing and a larger surface area available for chemical etching. With the propensity of the oxidisers to preferentially etch regions of high surface energy, such as vertices and edges, the asperities are concurrently etched away to produce smooth plateaus with little evidence of surface pitting [132]. Alternatively, with the still large shearing forces and temperatures present on the sample, a phase conversion to less dense forms of carbon can also occur. This material can then be abraded away by the polishing plate [132]. To further increase the removal rate diamond grit, Fe₂O₃, or Cr₂O₃ powder can also be added albeit at the expense of the surface finish [132, 177]. Once polishing is complete, the oxidisers are easily washable with water in contrast to the more difficult to remove polishing grit utilised with mechanical polishing [177].

5.3.2 Single Crystal Diamond CAMPP

Early studies on the use of CAMPP were more rudimentary than the presently used techniques described above and solely focused on the polishing of single crystal samples. Instead of using heated oxidisers, the salts were either dissolved in DI, dispensed onto the plate and left to evaporate, or pressed into sticks and abraded against the cast iron scaife. Frictional heating then cause temperature hotspots and melting of the oxidisers. Using the latter method with velocity and loads of 40 m s⁻¹ and 1 MPa respectively, Kühnle and Weis demonstrated that removal rates of 0.5 μm h⁻¹ are possible when polishing {100} single crystal samples with NaNO₃. A corresponding reduction in roughness from 1.7 nm to 0.19 nm RMS after 32 mins of CAMPP is observed along line traces perpendicular to scaife introduced nano-grooves of an initially mechanically polished sample. With the same apparatus and KNO₃ the polishing of a {111} face, typically difficult to polish without significant misalignment angles with mechanical polishing, has shown a reduction in roughness from 4.1 nm RMS to 185 pm RMS after 30 mins [211].

As detailed previously, one such application that benefits from an improvement in the polishing of single crystal diamond is homoepitaxial growth. As shown in Figure 5.6, subsequent homoepitaxial growth on CAMPP samples shows a considerable reduction in roughness in comparison to growth on a mechanically polished {100} substrate. For the growth on top of the as received sample it can be seen that the roughness closely resembles that of the substrate, with the mechanically introduced nano-grooves propagating through the growth, highlighting the effectiveness of a subsequent fine polish after an initial mechanical polish for single crystal samples [211].

5.3.3 Polycrystalline Diamond CAMPP

Due to the difficulties in the mechanical polishing of polycrystalline diamond films CAMPP has been more widely applied to the polishing of diamond films, where the variation of removal rate and surface finish with polishing parameters and oxidiser have also been studied. As would be expected given the still significant mechanical action to the technique, the removal rates of CAMPP are highly dependant on the applied load and relative velocity of the polishing plate. Larger loads increase the friction force and shear stress on the films leading to an increase in the number of micro-cracks [132]. As a result oxidation can occur at a faster rate due to the increased contact area between the diamond film and oxidising agents. However, too high a force can lead to shattering of the highly stressed polycrystalline film [133]. Meanwhile, an increase in the velocity of the plate will also increase the cracking and material available for oxidation due to the larger number of contact points between the plate and sample. However, too large a velocity will cause an uneven distribution and spin off and of the molten oxidisers due to the centrifugal force, resulting in a removal mechanism dominated by micro-chipping [132].

In order to investigate the achievable surface finish Tsai *et al.* mechanically and CAMP polished 20 μm thick polycrystalline diamond films for 5 hours while periodically checking the roughness with AFM [213]. Mechanical polishing was carried out with the use of diamond grit of unspecified size and a ceramic plate, with the addition of KOH and KNO_3 heated to 350 $^\circ\text{C}$ through the use of infrared lamps in the case of CAMPP. The resulting reduction in roughness of both films with time is detailed in Figure 5.7. Meanwhile, Figure 5.8 shows SEM images of (a) an as-grown film, (b) a film subjected

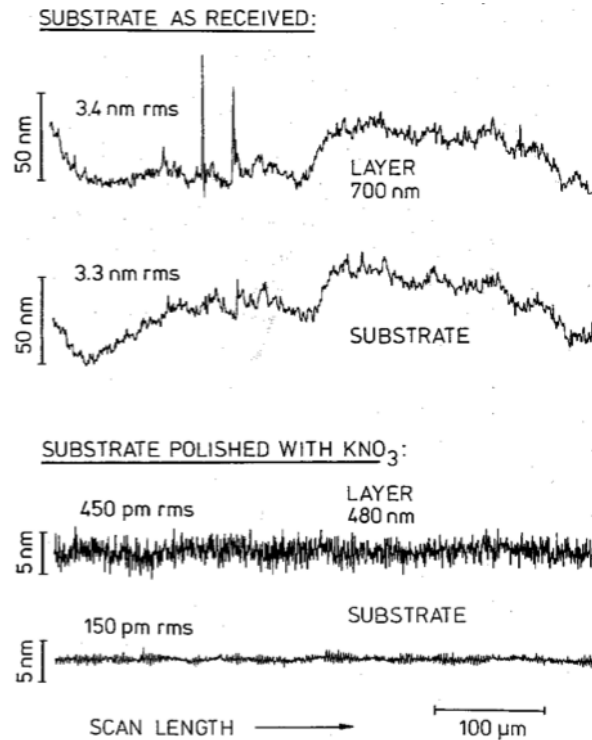


Figure 5.6: Homoepitaxial growth on an as received single crystal diamond polished with and without CAMPP. Line traces taken perpendicular to mechanical polishing introduced nano-grooves show a clear reduction in roughness from 3.4 nm RMS to 150 pm RMS after CAMPP polishing with KNO_3 on the $\{100\}$ orientated diamond sample. The surface roughness of the homoepitaxial growth closely resemble the roughness of the substrates, reiterating the benefit of a final CAMPP step on single crystal samples. Reprinted from Surface Science, **340**, J. Kühnle and O. Weis, "Mechanochemical superpolishing of diamond using NaNO_3 or KNO_3 as oxidizing agents", 16–22, Copyright (1995), with permission from Elsevier.

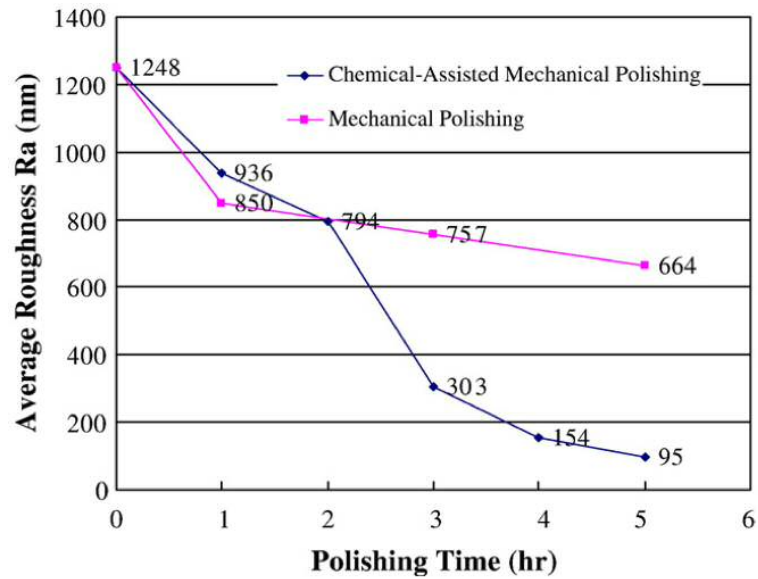


Figure 5.7: Reduction in roughness with time for mechanical polishing and CAMPP of 20 μm thick polycrystalline films. Roughness values are identical for the first two hours due to the largely fracture based removal mechanism. Upon the contact area increasing the combined mechanical and chemical action vastly improves the reduction in roughness achievable, with a decrease to 95 nm Ra after 5 hours. Reprinted from *Diamond and Related Materials*, **16**, H. Y. Tsai *et al.*, "Evaluation research of polishing methods for large area diamond films produced by chemical vapor deposition", 253–261, Copyright (2007), with permission from Elsevier.

to 5 hours of mechanical polishing, (c–e) films subjected to CAMPP for 1–5 hours, and (f) a close up view of the the 5 hour CAMPP film. As can be seen from Figure 5.7, for the first two hours the reduction in roughness is identical for both techniques with a reduction from 1248 nm to 794 nm Ra. Due to the load being applied solely to the crystal peaks the material removal is predominately through microchipping with little chemical etching [214]. As polishing progresses and the contact area increases, the contribution to polishing from the molten oxidisers is increased leading to a drastic reduction in roughness [132]. Further CAMPP then leads to the merging of the plateaus and the formation of a planar surface devoid of fracture or scratches as seen with mechanical polishing, as can be made out in the SEM images after 5 hours of CAMPP of Figure 5.8 e and f. At this point of polishing the addition of oxidisers has lead to a corresponding reduction in roughness from 1248 nm Ra to 95 nm Ra, far less than the 664 nm Ra achieved with diamond grit based mechanical polishing, demonstrating the superior polishing ability of CAMPP [213].

To improve the technique, other authors have focused on the reduction potential of oxidisers in order to increase the oxidative etching observed [133, 214]. Through mixing a variety of oxidisers with dilute sulphuric acid (H_2SO_4) to start the reduction reactions, it was seen that oxidisers with the largest reduction potentials show a greater reduction in the surface roughness [214]. However in order to optimise the process, the mechanical action must be matched closely to the chemical etching [133]. For example when polishing with potassium chlorate (KClO_3) and potassium permanganate (KMnO_4), oxidisers with lower reduction potentials, the load and speed must be reduced otherwise removal through micro-chipping will dominate resulting in an inferior surface. Conversely, when polishing with hydrogen peroxide (H_2O_2) and potassium persulfate ($\text{K}_2\text{S}_2\text{O}_8$), oxidisers with high reduction potentials, high loads and speeds must be used to best match the rate of mechanical polishing to chemical oxidation. Through the use of $\text{K}_2\text{S}_2\text{O}_8$ with a diamond grit of 4–8 μm at a load of 0.18 MPa, speed of 200 rpm at 90 °C it has been shown that the removal rate can be as large as 1.39 $\mu\text{m h}^{-1}$. The largest reduction in roughness from the as-grown 216 nm to 29 nm Ra after 4 hours polishing was meanwhile observed with KMnO_4 at a reduced rotational speed of 100 rpm and a finer grit of 0–0.5 μm [214].

As such, CAMPP has been demonstrated to be an effective method for the polish-

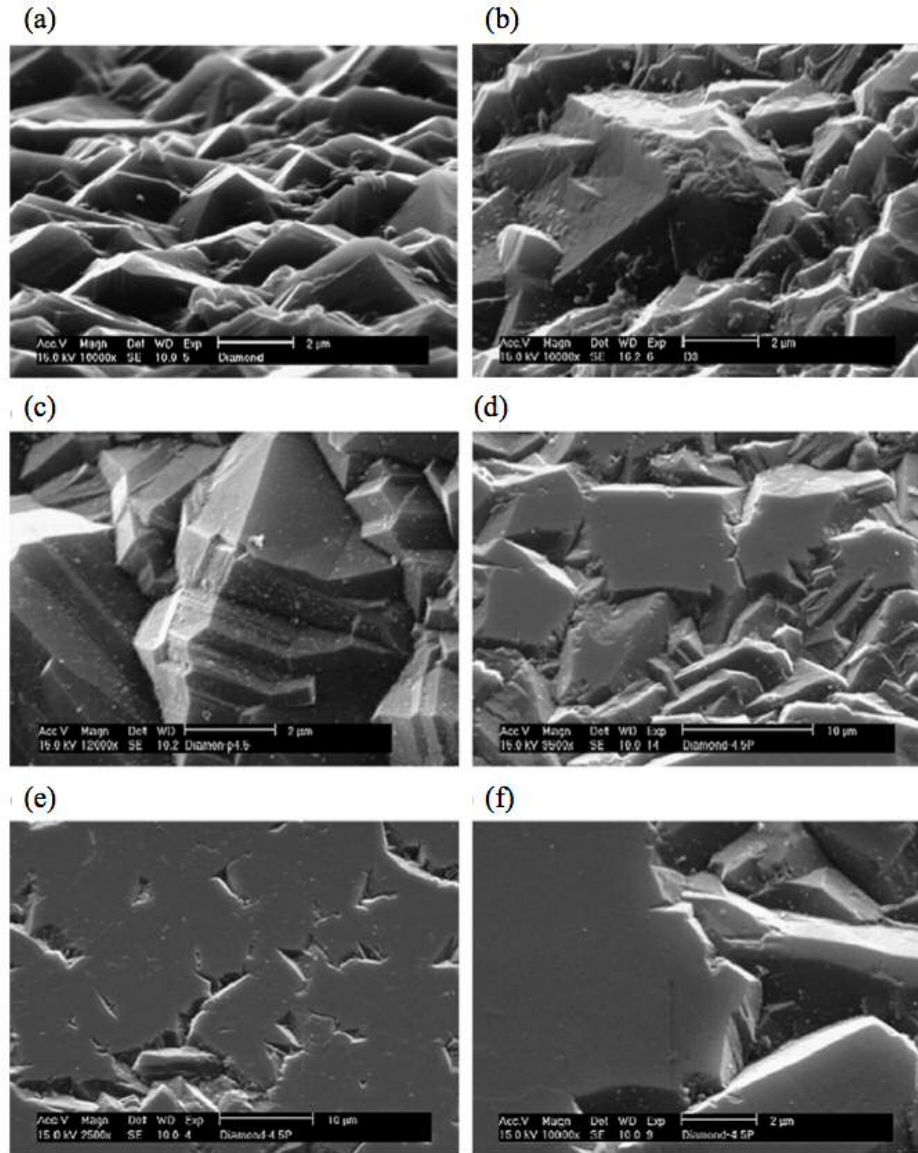


Figure 5.8: Comparison of chemically assisted mechanical polishing and mechanical polishing of polycrystalline diamond. (a) surface morphology of diamond film before polishing; (b) film subjected to 5 hours of mechanical polishing with characteristic fracture based removal of material; (c) sample polished with CAMPP for 1 hour; (d) sample polished for 3 hours indicating with smooth plateaus appearing; (e) sample polished for 5 hours; (f) close up of sample polished for 5 hours with CAMPP showing lack of surface damage or polishing related artefacts. Reprinted from *Diamond and Related Materials*, **16**, H. Y. Tsai *et al.*, "Evaluation research of polishing methods for large area diamond films produced by chemical vapor deposition", 253-261, Copyright (2007), with permission from Elsevier.

ing of polycrystalline diamond films to a smooth finish over a large area, and without significant contamination. However, with the presence of the hard cast iron or ceramic plate for thin and more fragile films in which the bow of the wafer is larger than the film thickness, uniform polishing cannot be achieved. While other techniques have been developed ranging from laser ablation to reactive ion etching, each have inherent foibles and difficulties achieving the roughness values required [177, 188, 213, 215, 216]: Thermochemical polishing relying on carbon diffusion into a metal plate under elevated temperatures presents the same problem of high loads and non-uniform polishing as CAMPP [213]; Laser ablation/oxidation with Nd-YAG or excimer lasers have pronounced differences in removal rates for crystallites and grain boundaries limiting the achievable surface finish, while the continual thermal shocks can cause cracks and adhesion problems for thinner films [177]; While ion beam etching with oxygen/argon ions and reactive ion etching with oxygen/hydrogen both require expensive high vacuum equipment limiting the dimensions of the samples that can be polished [177]. Therefore a technique widely used in the IC fabrication industry, chemical mechanical polishing (CMP), is to be trialled on thin film diamond with the aim to replicate the surface finish achievable with CAMPP on thinner highly bowed nanocrystalline wafers.

5.4 Chemical Mechanical Polishing

5.4.1 Polishing Process and Removal Mechanism

Since emerging in the 1980's, Chemical Mechanical Polishing (CMP) has become vital in the reduction of gate oxide thickness and channel length in the production of devices, and the planarisation of inter-level dielectrics and metal interconnects in the IC fabrication industry [217]. Adapted from the polishing of glass, the technique involves pressing samples against a rotating porous polymer pad (~ 40 rpm) at pressures of 1–10 psi (0.69–6.9 kPa) in the presence of a sub micron abrasive slurry [217, 218]. Typical materials for such pads are far softer than the cast iron or alumina plates used previously in the polishing of diamond, being made up of either a matrix of cast polyurethane foam with filler material to control the hardness, or polyurethane impregnated felts [217]. Meanwhile, the most commonly used slurry in the CMP industry consists of silica, fumed or precipitated, of size ~ 200 nm dispersed in DI water [217].

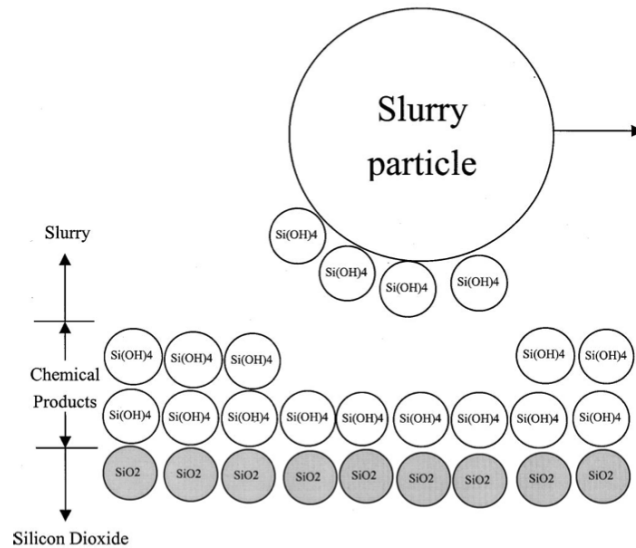


Figure 5.9: Schematic of the mechanism of chemical mechanical polishing of SiO_2 . OH^- ions within the alkaline polishing fluid react with the surface SiO_2 bonds, hydrating the bonds and creating a silanol, $\text{Si}(\text{OH})_4$, based surface layer. This soft ductile layer is then abraded away by silica particles within the fluid, removing material. Reproduced from [221] by permission of The Electrochemical Society.

Differing from the model used to describe CAMPP of diamond, CMP follows a true synergistic approach reliant on the formation of a ductile hydrous layer that is subsequently abraded away by passing slurry particles, as shown in Figure 5.9. During polishing the hydroxide ions within the fluid rupture the surface siloxane, hydrate the bonds, and create a silanol (SiOH_4) functional group based surface layer [219]. This ductile surface layer can then be abraded away through the mechanical interaction of silica particles within the slurry with kinetic energy supplied by pad asperities [220]. Spent slurry and abraded material is then transported through the pores within the pad and spun off through transport channels cut within the pad.

5.4.2 Removal Rate

In a similar fashion to CAMPP, the mechanical removal rate must be closely matched to the chemical etching to achieve global planarisation without sacrificing on removal rate. However, in order for material to be mechanically removed through abrasion, a soft ductile layer must first be created through chemical interaction. Should there be an

increase in the compressive stress, a reduction in the activation energy of the hydrate reaction of silica would be seen along with an acceleration in the rate of formation of silanol groups. However, an increase in the removal rate has been observed with increasing mass content within the slurry, unattributable to a change in the reaction rate [221, 222]. Therefore the bottleneck in the process is believed to be the subsequent mechanical abrasion [221]. Should the pad, slurry, and temperature then remain the same the relationship between the wear rate, velocity and removal rate can be approximated by Preston's equation (Equation 5.1), where MRR is the removal rate, P is the down pressure, v is the velocity, and K_p is a constant encompassing remaining polishing parameters [218, 222].

$$MRR = K_p \cdot P \cdot v \quad (5.1)$$

As shown in Equation 5.1, the removal rate is linearly proportional to the local pressure and the relative velocity between the pad and sample. For the polishing of SiO_2 with silica slurries, typical pressures and velocities are 1–10 psi (0.69–6.9 kPa) and 10–70 m min^{-1} , resulting in wear rates of 100–500 nm min^{-1} [221]. Pressures exceeding 10 psi (6.9 kPa) result in the wafer travelling unevenly over the pad leading to wafer breakage, while excessive speed leads to poor distribution of slurry and an associated tailing off of the wear rate [218]. However, given the complicated three-body nature to the process process, Preston's coefficient, K_p , encompasses a range of parameters from the composition of the slurry to the condition of the polishing pad that also need to be considered in order to optimise the wear rate and the achievable finish.

With the importance of abrasion to the technique, the size, morphology, and concentration of abrasive particles within the slurry all heavily dictate the wear rate and resulting surface finish. For fumed or colloidal silica based slurries, particles of 20 nm form roughly spherical aggregates with a distribution of sizes centred around 100–300 nm [223]. Particles exceeding 1 μm are likely to lead to mechanical damage through deep micro-scratching and non-uniformity due to differential polishing pressure [217, 224]. To prevent this agglomeration the zeta potential is typically controlled with the addition of acids, salts, ionic-surfactants or buffers. Increasing the pH of silica based slurries leads to hydroxylation and disassociation of silicic acid at the surface of silica

particles, increasing the magnitude of the surface charge and the repulsion forces of the particles [223]. For example, a fumed oxidised silica based slurry (12.5 %wt) with a pH of 11.45 through addition of KOH has demonstrated a zeta potential of -27 mV, suggesting incipient stability [225]. Surface damage is therefore minimised through preventing flocculation by maintaining a pH of 10–11, accomplished through the addition of KOH, NH_4OH , or NaOH. However, while NaOH is the best medium of OH^- , due to the mobility of the Na^+ there is a possibility of device contamination leaving KOH and NH_4OH as the preferred alkali additives [217]. Immediately before use ultrafiltration of the slurry is also carried out to remove larger particles of 1–3 μm [217, 226]. Meanwhile, solid content of the slurry is typically in the range 10–20 wt%, with the MRR being linearly dependant on the number of abrasives involved in polishing at low concentrations due to the increase in contact area [222]. For larger concentrations however, the MRR tails off due to changing removal mechanism, with a corresponding increase in the cost of slurry per litre [217].

Meanwhile, the pad, arguably the most important component of any CMP system, is typically constructed out of a cast polyurethane foam or a polyurethane impregnated felt. Such a foam combines polyurethanes superior properties of hardness, ability to withstand abrasion, chemical resistance to the harsh alkaline or acidic polishing slurries, and wettability with the flexibility required to conform to samples [227]. During polishing the pores within the pad collect consumed slurry and reaction products from the sample, and transport slurry uniformly across the pad. The inter-pore surface asperities are responsible for transmitting the shear forces required for polishing while ensuring uniform distribution of the applied pressure [227, 228]. During polishing the pores can become blocked with slurry particles and abraded pad material, while the radial sweeping of the carrier induces a surface flow and permanent closing; both affecting the pads ability to transport slurry and potentially modifying the nature of the polishing mechanism [228]. Concurrently, the micro-roughness of the surface decreases due to rolling and fatigue type wear reducing the number of surface asperities in a process called ‘glazing’ [229]. Such abrasion has been observed in the polishing of SiO_2 where micro-roughness decreased from 3.5 to 2.3 μm R_{pk} in 5–10 minutes, bringing about a corresponding reduction in removal rate from 2500 to 1700 $\text{\AA} \text{min}^{-1}$ [230]. In order to re-increase the micro-roughness and the porosity of the pad an electroplated or brazed

diamond grit ‘conditioner’ is used to abrade away the top damaged layer revealing the unused pad underneath [217].

5.4.3 Previous Attempts at CMP of Diamond

Previous attempts at CMP of diamond have used a combinational approach of the mechanical nature of scaife polishing with the chemical action from CMP. Haisma *et al.* added a limited fraction of diamond grit to a concentrated silica based polishing fluid (Syton). Upon becoming embedded within the pearlitic cast iron scaife, the grit became encapsulated by the silica through van der Waals’ interaction. The hardness of the diamond (Vickers hardness ~ 100 GPa) is then shielded by the silica (Vickers hardness ~ 7.4 GPa) preventing the formation of nano-grooved features [46]. During polishing of $\{100\}$ single crystal samples with the modified slurry, a reduction in roughness from the ~ 3 nm R_q achieved with traditional scaife polishing to 0.5 nm R_q at pressures of 100 kPa was observed, with Rutherford backscattering giving little indication of subsurface damage [46]. To explain this reduction in roughness, the authors postulate that hydroxyl groups bound to the surface of the silica particles react with surface carbonyl (C=O), ether (C–O–C), and hydroxyl (C–OH) groups present on the diamond sample. While bond breakages will likely occur between the carbon and oxygen atoms, occasionally a C–C bond will rupture and be replaced hydroxyl and carbonyl groups, gradually releasing the carbon atom from the diamond lattice. For silica polishing of oxides it has been estimated that 1 in 500 million collisions results in the extrication of a silanol group, with the rate likely far lower in the case of diamond polishing, explaining the 1 atomic layer per minute rate observed. When using unmodified silica polishing slurry without the diamond grit additive, the authors were not able to observe any polishing. Yuan *et al.* have meanwhile utilised a boron carbide (B_4C)/potassium ferrate (K_2FeO_4) slurry against a sandblasted glass plate at pressures of 266.7 kPa and temperatures of 50 °C to effectively polish microcrystalline diamond films. With the increased hardness of the B_4C grit, Vickers hardness of 38–40 GPa, scratching of the diamond surface occurs creating a higher surface energy. Oxidation due to the K_2FeO_4 then more readily occurs resulting in a step step by step release of carbon atoms, in a similar fashion to that proposed by Haisma *et al.* [46, 231]. With the techniques roughness values of 0.187 nm R_a were achieved over a $10 \times 10 \mu m$ area on top of a

crystal plateau.

While both of the techniques described above utilise softer than diamond abrasives to drive oxidation, it is believed that the rigid scaife used could be switched for the more commonly used polymer polishing pads, albeit at reduced removal rates, in the polishing of nanocrystalline diamond film. The relatively low pressures used will allow course adjustment of the wafer bow through the application of back pressure, leaving the flexible pad to conform to the residual bow to provide uniform polishing without the risk of shattering. With the lack of polishing related artefacts and subsurface damage observed with the techniques, and oxidation being the critical process in material removal, it is believed that true CMP will enable the production of uniformly polished nanocrystalline thin film diamond.

5.5 CMP of Nanocrystalline Diamond

5.5.1 Experimental Methods

For the purposes of polishing, a series of NCD films were grown on 2" p-type <100> silicon wafers of thickness 500 μm . Before use each wafer was given a standard SC-1 clean of 30% H_2O_2 : NH_4OH :Deionised H_2O (1:1:5) at 75 $^\circ\text{C}$ for 10 min., followed by a DI H_2O rinse, and finally spun dry. In order to gain a coalesced NCD film, the substrates were seeded in a hydrogen terminated mono-dispersed nano-diamond/DI H_2O colloid in a ultrasonic bath for 10 minutes, known to result in seeding densities $>10^{11}$ cm^{-2} . After seeding, each wafer was rinsed, spun dry, and then immediately placed inside the CVD reactor.

Film growth was carried out in a Seki AX6500 CVD reactor operating at 40 Torr chamber pressure, 3.5 kW power, and methane admixture of 3% CH_4/H_2 . Heating arose solely from the plasma, resulting in a temperature of ~ 840 $^\circ\text{C}$ as determined by dual wavelength pyrometry. Upon termination of growth, each film was cooled down in a pure H_2 fed plasma to prevent deposition of non- sp^3 carbon and provide a hydrogenated surface. Film thicknesses were judged to be ~ 380 nm through the use of *in-situ* interferometric pyrometry and confirmed *ex-situ* with the use of a Filmetrics F20 spectral reflectance system.

Polishing was carried out with a Logitech Tribo CMP system fitted with a Suba-X

polyurethane impregnated polyester polishing felt and a Logitech supplied Syton alkaline colloidal silica polishing fluid (15–50% SiO₂, 4–5% ethylene glycol, 9.2–10.1 pH). Radial grooves of ~4 mm were cut into the pad to allow for spend slurry to be effectively removed through centrifugal force. Before polishing, each pad was conditioned through sweeping a diamond grit embedded chuck at 4 psi across the wet pad for 30 minutes. Through this process the pad is roughened on the micro-scale, creating surface asperities necessary for polishing, while also opening up pores to allow for a more efficient distribution of slurry. In preparation for polishing samples were held in a puck, as shown in Figure 5.10, through capillary action and raised up with Kapton shims to ensure the film is protruding above the surrounding template by approximately 100–200 μm ; enough to observe uniform polishing of the film while preventing the edge of the sample digging into the pad and subsequent delamination of the film. During polishing the puck and polishing pad were kept rotating at 60 rpm in opposite directions, as shown in Figure 5.11, with a down load of 4 psi (27.6 kPa) and slurry feed rate of 40 ml min⁻¹ maintained throughout polishing. As shown in Figure 5.10, when polishing both sample and the larger area template come into contact with the polishing pad. With the inflation of an air pocket used to maintain this fixed down pressure the resulting load on the sample will then reach a maximum of 56 N, increasing as polishing progresses due to the larger contact area with removal of the crystallite peaks. To coarsely account for wafer bow a back pressure of 20 psi (138 kPa) was also applied, as determined through the use of a Logitech grazing incidence diffractometer. Three films were polished for durations of 1, 2, and 4 hours. After polishing each film was cleaned with the SC-1 process detailed previously in an attempt to remove the remaining slurry, following current CMP practice in IC fabrication [217].

SEM images were taken with the SE2 detector of a Raith eLine system operating at 20 kV and a working distance of 10 mm. AFM was carried out with a Veeco Dimension 3100 AFM operating in tapping mode and equipped with etched silicon TESPA tips of nominal radius of 8 nm, resonant frequency of 320 kHz, and spring constant of 42 N m⁻¹. 5 areas of 25 μm^2 were taken around the centre of each film, and analysed with WSxM and Gwyddion SPM analysis software. Removal rates were determined through measuring 13 points across the film with a Filmetrics F20 spectral reflectance system before and after polishing using a simple tri-layer model consisting of surface

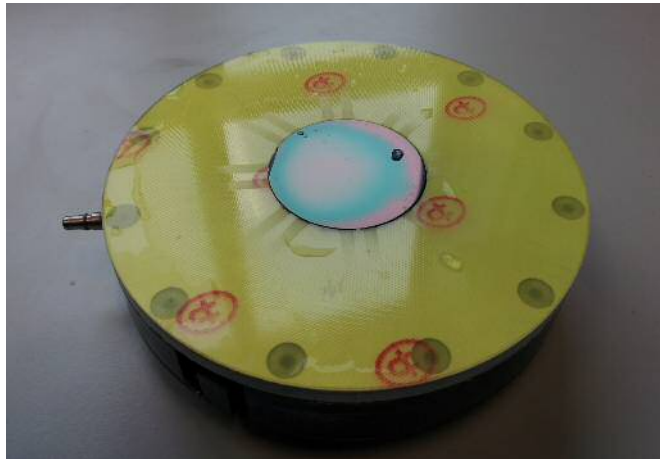


Figure 5.10: Example NCD wafer in puck. Kapton shims are used to ensure the surface of the NCD is protruding 100–200 μm above the surrounding template, with capillary action holding the shims and wafer in place when not in contact with the polishing pad. Positive back pressure is applied from the port on the left hand side to coarsely account for the stress induced wafer bow, with the soft pad conforming to the residual bow during polishing.

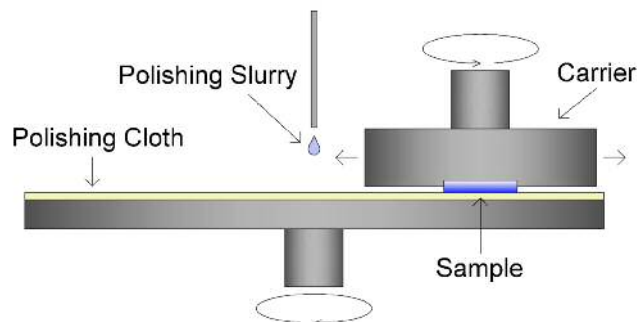


Figure 5.11: Schematic of the chemical mechanical polishing system. The puck is held in a rotating carrier and swept across the counter-rotating polishing pad. The pad is doused through the use of two slurry distribution pipes towards the front and rear of the polishing pad, while slurry distribution grooves are cut into the pad to allow for spent slurry to be spun off by centrifugal force. Reprinted from [210] under a Creative Commons license, <https://creativecommons.org/licenses/by/3.0/>.

Duration	Polishing Rate (nm h ⁻¹)	RMS Roughness (nm)
As-grown	-	18.3
1 hour	17.0	11
2 hours	15.5	4.5
4 hours	16.3	1.7

Table 5.1: Polishing rates and roughness values for the as-grown to 4 hour polished films. Reported polishing rates assumed to be linear and show an average of $\sim 16 \text{ nm h}^{-1}$, while roughness values show a steady decrease to close to optimal values of under 2 nm RMS over $25 \mu\text{m}^2$.

roughness/diamond/silicon with the inbuilt optical constants for bulk diamond and silicon.

XPS was carried out by Dr Geoffrey Nelson and Professor John Foord at the Chemistry Research Laboratory at Oxford University with a VG Scientific ESCALAB X-ray photoelectron spectrometer. An Al K α (1486.3 eV) radiation source was used at 10 kV potential, 10 mA emission current, and pressure of 1×10^{-9} Torr. Fixed analyser transmission mode was used, with pass energies set to 50 eV and 25 eV for wide ‘survey’ and ‘narrow’ scans, respectively. The binding energies given were calibrated with respect to the C1s peak at 284.6 eV, and have an error of ± 0.25 eV. Peak areas were normalised to the cross-section of the F1s peak through the use of atomic sensitivity factors. Elemental ratios were worked out from the normalised peak areas with an approximate error of 15–20%.

5.5.2 Morphology

SEM images of the as-grown and 1–4 hour polished films can be seen in Figure 5.12. As can be seen from the as-grown SEM image, the films show clear faceting reminiscent of films grown under high power density and low CH₄/H₂ growth conditions. This film also show a distribution of grain sizes between 100 nm and 250 nm with a random distribution of {111} and {100} texturing. Upon an hour of polishing a clear difference can be seen with the removal of the crystallite peaks that comes into contact with the polishing pad first, suggesting a significant mechanical nature to the polishing mechanism. This trend continues for the 2 and 4 hour polished films to the intersection point with neighbouring crystals with little to no pin holes opening up to the substrate, while the

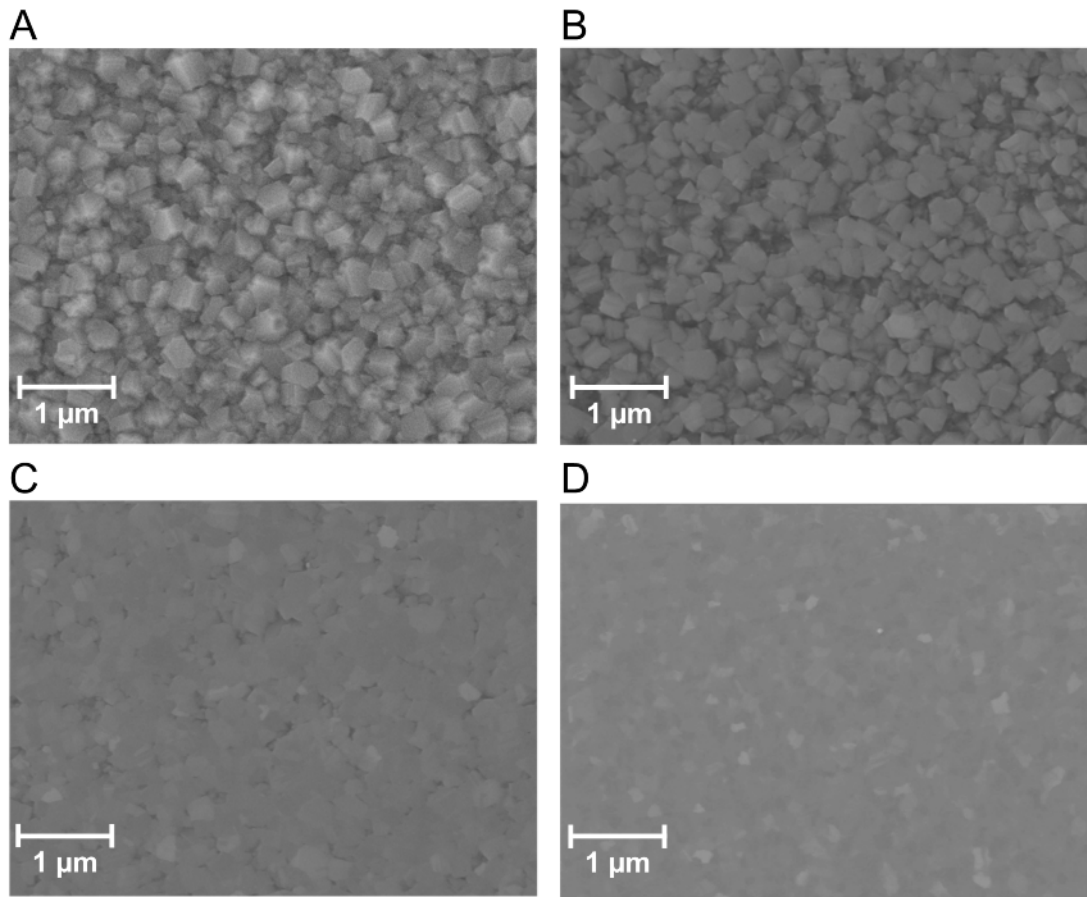


Figure 5.12: SEM images of the as-grown (A), 1 hour (B), 2 hour (C), and 4 hour polished films (D). Clear polishing can be observed with the removal of the tops of individual crystals progressing down to the point at which they intersect with neighbouring grains. No surface pits or pin holes can be made out suggesting close to optimal polishing and a high nucleation density. Reprinted from [210] under a Creative Commons license, <https://creativecommons.org/licenses/by/3.0/>.

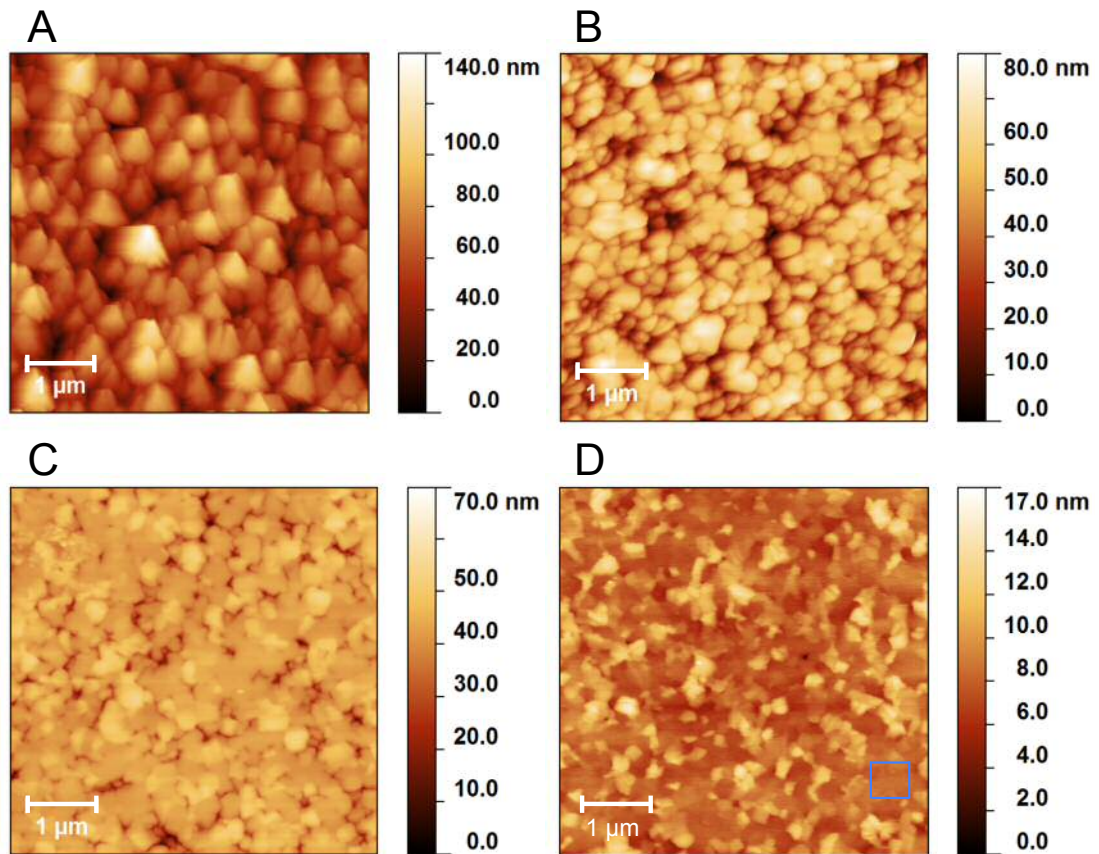


Figure 5.13: Corresponding AFM images of the as-grown (A), 1 hour (B), 2 hour (C), and 4 hour polished films (D). The clear polishing trend is reiterated over the $25 \mu\text{m}^2$ scan areas with little indication of fracture or damage occurring to the polished samples. Also shown in panel D is a reduced area of $\sim 0.25 \mu\text{m}^2$ with a roughness value of 0.42 nm RMS, highlighting the near atomic level smoothness attainable over an area close to the grain size.

resulting plateaus also appear to be smooth and fracture free. Also evident from these images is the lack of polishing debris, be it slurry or removed material, initially suggesting that an SC-1 clean is suitable for post CMP cleaning. This clear polishing trend is reiterated by the AFM images for the as-grown to 4 hour polished films in Figure 5.13 and the average roughness values over $25\ \mu\text{m}^2$ in Table 5.1. After 4 hours of polishing the RMS roughness has been reduced from 18.3 nm to 1.7 nm. Also visible in Figure 5.13D is a smaller area of $\sim 0.25\ \mu\text{m}^2$ in which the roughness has been reduced to 0.42 nm RMS, indicating close to atomic flatness levels are observed on the plateaus formed. The average linear polishing rate for the three films is $\sim 16\ \text{nm h}^{-1}$, of similar orders of magnitude to the possible rates achievable with mechanical polishing of polycrystalline diamond [188].

5.5.3 X-ray Photoelectron Spectroscopy

In order to investigate the mechanism responsible for polishing, Shell Isolated Nanoparticle Enhanced Raman Spectroscopy (SHINERS) was attempted. In this technique a silica coated ($\sim 2\ \text{nm}$ thick) gold nano-particle ($\sim 55\ \text{nm}$ dia.) containing colloid is dropped onto the surface and left to evaporate. In a similar fashion to tip enhanced Raman spectroscopy, upon excitation with a suitable laser the electromagnetic field is enhanced in the region surrounding the metallic nano-particles. With the joint signal from the multitude of enhancing particles, the Raman signal from the surface is enhanced providing an ultra-surface sensitive technique capable of characterisation to a single molecular level [232]. However, the difference in heights and areas of the D and G bands were greater for differing areas probed of each sample in comparison to that between polished and unpolished samples, preventing any inferences from being made on the mechanism of polishing.

As surface enhanced Raman failed to explain the polishing mechanism, XPS was performed to study the functional groups present on the surface of the polished and unpolished NCD films. The resulting wide energy survey spectra can be seen in Figure 5.14A with the pertinent photoelectron and Auger signals labelled, while the inset figure shows a magnified view at low binding energies. Top to bottom the traces are of the 4 hours CMP, 2 hours, 1 hour, and as-grown NCD films. From the traces it can be seen that all four films have significant peaks at 285 eV and 531 eV representa-

tive of the C1s and O1s binding energies respectively. Also visible from the scans are the general increase or appearance in features arising from fluorine, chlorine, sulphur, sodium, and silicon, suggesting that the polishing process results in contamination of the samples. However, it is believed that this contamination is not substantial enough to be detrimental to the use of such films and preferable to the contamination and damage observed when using techniques reliant on micro-fracture. For the removal of silicon a hydrofluoric acid etch could be performed, while for the other traces it is likely that current post CMP cleaning process used in the IC fabrication industry such as a polyvinyl alcohol brush or $\text{NH}_4\text{OH}/\text{HF}$ acid could be adapted for use with NCD given the general chemical resistance of diamond [217].

To study the changes in concentrations of graphite, diamond and carbon bound surface species, an attempt can be made to de-convolute the C1s peak into its constituents before and after polishing. However, distinguishing between the distinct species, in particular the alcoholic and etheric groups, is often made difficult due to the overlapping peaks [233]. Figure 5.14Bi and Bii show such peaks and de-convolutions of the as-grown and a typical polished film respectively, with peaks attributable to: diamond (C–C 285.0 eV), hydrocarbon(C–H 285.5 eV), alcohol/ether (C–O 286.5 eV), and carbonyl (C=O 287.5 eV). As typical of polycrystalline diamond films after CVD and without surface modification, the predominant feature is the hydrocarbon peak arising from the largely hydrogenated surface and grain boundaries. Meanwhile, it is believed that the C–O feature is more likely attributable to hydroxyl terminated carbon rather than the less energetically favourable bridge like etheric groups [234]. Further slight oxidation can then occur once the samples are removed from the growth reactor bringing about a further increase in singly bonded oxygen component in the form of alcoholic/etheric groups [235]. Lastly, traces of carbonyl are also present, while no evidence of carboxyl (C=O)OH 285.5 eV) was observed. Comparing the two de-convoluted spectra it can be seen that polishing does not significantly alter the surface termination, but instead brings about subtle changes with the increase in the relative concentrations of carbonyl character and a minor increase in the C1s binding energy due to the larger electronegativity of oxygen. It is well known that wet chemical oxidation with sulphochromic and piranha lead to increases in the oxygen content on the surface of diamond films that can be ascribed to carbonyl and/or alcoholic/etheric functional groups [234, 236–238].

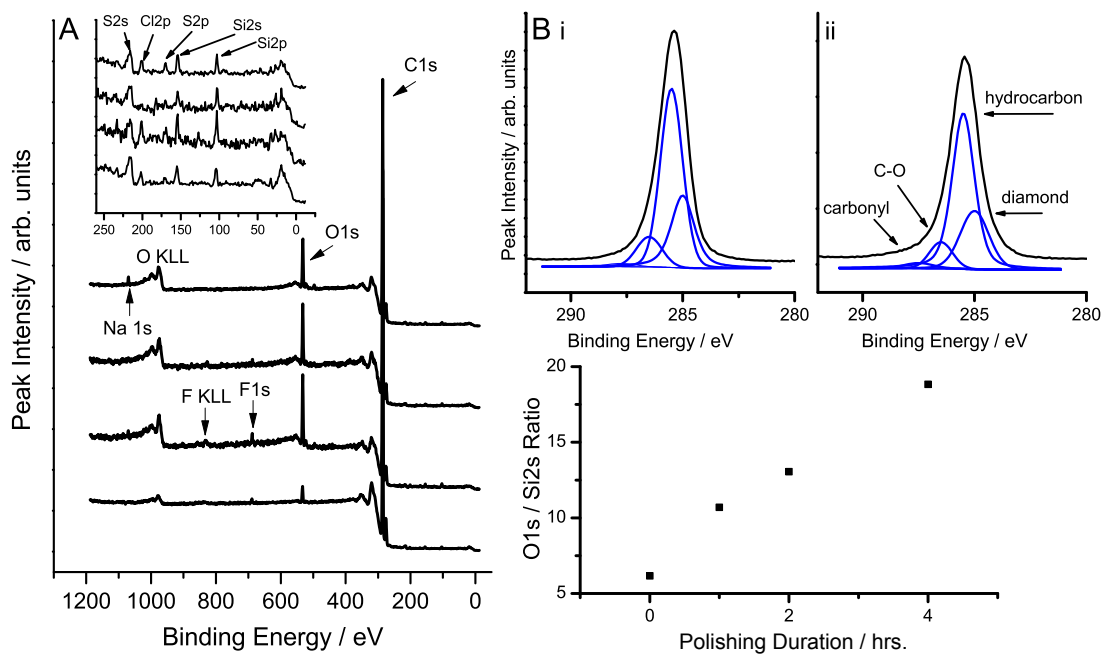


Figure 5.14: XPS of the as-grown to 4 hour polished films. (A) Wide energy survey spectra for the as-grown to 4 hour polished film (bottom to top), with the pertinent photoelectron and Auger signals labelled. The inset shows a magnified view of the lower binding energy region to highlight contamination arising from the polishing process. (B) De-convoluted O1s spectra before (i) and after (ii) polishing with carbonyl, single bonded oxygen, hydrocarbon and diamond peaks resolved, highlighting the subtle changes in the surface termination and lack of sp^2 attributable peak. (C) O1s/Si2s ratio plotted as a function of polishing duration indicating silica is not the main component of oxygen present on the film surface.

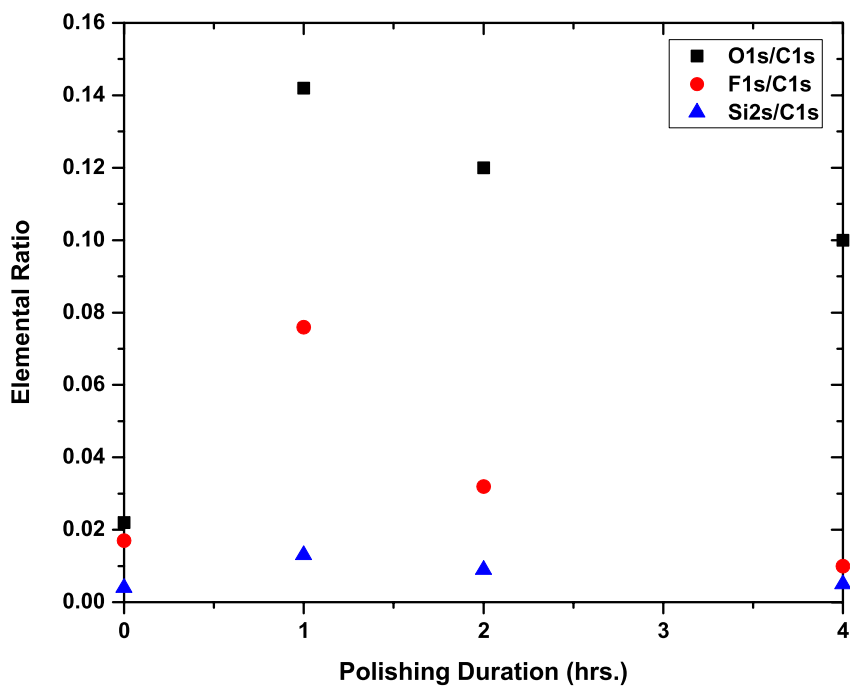


Figure 5.15: Elemental ratios of O1s, F1s, and Si2s with respect to C1s for the as-grown to 4 hour polished films. The drastic increase in the O1s/C1s indicates oxidation of the film after polishing corresponding to a monolayer of oxygen on the diamond surface, while the rise in the Si2s/C1s suggests bound silica particles remaining after SC-1 cleaning.

However, the most important aspect of the deconvolution is that after polishing there are no peaks attributable to graphite or sp^2 related defects, highlighting the gentle nature of the CMP technique. Such defects have been shown to present peaks shifted by ~ 1 eV to lower binding energies from the C-C peak upon Argon or Carbon ion bombardment, and electrochemical anodisation studies of single crystal and polycrystalline diamond [239, 240]. In contrast to the C1s peak, due to the close packing of C-O, C=O and Si-O environments, de-convolution of the O1s peak was not as successful with at most one or two peaks being able to be adequately resolved [236].

With the significant increase in the O1s peak and the mechanisms currently used to explain silica based CMP, further investigation into its origin and variation with respect to the C1s peak is required. Figure 5.15 details the elemental ratios of the O1s, F1s, and Si2s signals with respect to the C1s core level peak. After 1 hour of polishing it can be seen that the O1s/C1s peak area ratio drastically increases by ~ 0.1 and stays permanently oxidised after continued polishing. Given the large inelastic

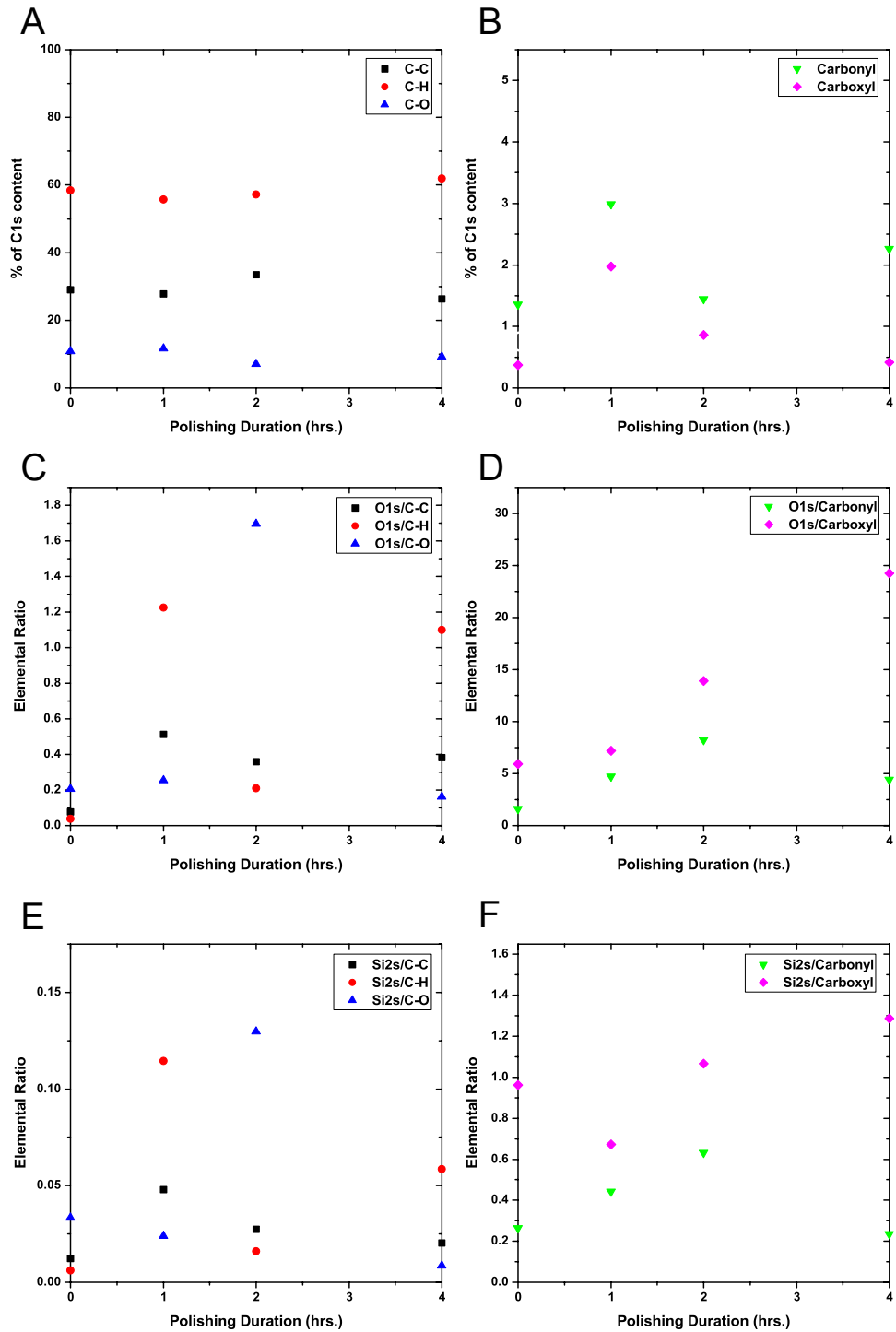


Figure 5.16: (A–B) De-convoluted C1s components, and (C–D) elemental ratios of O1s and Si2s with respect to de-convoluted C1s components for the as-grown to 4 hour polished films. Subtle changes occur in the carbon bonding present after polishing, with the variation in the large C1s components preventing inferences from the elemental ratios as to the nature of carbon bonding required for polishing.

mean free path of the C1s peak (> 1 nm) the sampling depth is likely to be up to 10 C layers [236, 241]. As a result, such an increase represents approximately a monolayer of oxygen forming on the surface after polishing. However, the increase in the carbon oxidation from the de-convoluted C1s were more subtle suggesting that the oxygen arises predominantly from other sources. With regards to the silicon character, previous XPS studies have shown an increase in the silicon signal for NCD films when approaching grazing incidence angles suggesting diffusion of silicon through the grain boundaries as a result of the high growth temperature [233]. This is believed to be the source of silicon observed on the as-grown NCD film, while the subsequent increase in the Si2s/C1s ratio is likely caused by silica slurry tightly bound to the surface and resisting the SC-1 clean. Figure 5.14 C meanwhile plots the non constant O1s/Si2s ratio against polishing duration, highlighting that the oxygen also cannot be solely from the silica; had it been the main source the ratio would remain constant throughout polishing. The increase in the F1s/C1s ratio also shown in Figure 5.15 was also unexpected given the polishing set-up, and is likely to arise from either the Teflon holders used in the post CMP cleaning process, the polymer based pads, or surfactants in the slurry. The ratio can be seen to rise by ~ 4 times after an hour of polishing before dropping down to pre-polishing levels after 4 hours.

In an attempt to investigate further, the contributing species of the C1s peak are plotted within panels A and B of Figure 5.16, while elemental ratios of the O1s and Si2s signals to the species are shown within panels C–F. Reiterating the subtle changes visible within Figure 3.6Bi and ii, minor changes are observed in the C–C, C–H, and C–O contents upon polishing along with increases in the already minor carbonyl and carboxyl species. The O1s and Si2s peak areas with respect to the de-convoluted C1s peaks can all be seen to increase upon polishing, while minor changes in the comparatively large C1s denominator then lead to large shifts in the elemental ratio. For example, the decrease in the C–O content after 2 hours of polishing leads to drastic increase in both the O1s/C–O and Si2s/C–O elemental ratios, preventing any inferences into whether a particular carbon environment is responsible for polishing. Given the rise in oxygen content cannot then fully be attributed to alteration of the functional groups of the diamond surface or the bound silica, it is possible that the rise in oxygen is generally correlated with polishing contamination as indicated by the presence of F, Cl, S peaks

in the survey spectra, which remain tightly bound after cleaning. The most likely sources of such molecular species are the polymer based pads, slurry surfactants, or post-polishing remaining silica.

5.5.4 Discussion

As visible in Figure 5.12, polishing begins at crystallite peaks initially in contact with the pad, and then progresses down to the point at which the crystals intersect. The fact that polishing occurs at areas only in contact with the pad suggest a significant mechanical action, whereas the resulting smooth plateaus devoid of fracture conversely indicate a considerable chemical action. Coupled with the fact that polishing attempts solely with DI water showed no material removal, a true chemical-mechanical synergy to the polishing is suggested. This steady polishing is reiterated with the AFM images of Figure 5.13, in which the roughness reduces from the as-grown roughness of 18.3 nm RMS to 1.7 nm RMS over $25 \mu\text{m}^2$ after 4 hours. On top of one of the polished plateaus of area $\sim 0.25 \mu\text{m}^2$ the roughness meanwhile can be as low as 0.42 nm RMS signifying uniformity down to several atomic layers on individual grains, values unobtainable with diamond grit mechanical polishing. With regards to removal rate, the $\sim 16 \text{ nm h}^{-1}$ value achieved is of similar order of magnitude to that achievable with mechanical polishing, and significantly less than the $\mu\text{m h}^{-1}$ rates achievable with CAMPP [188, 214]. However, due to the use of a flexible polymer based pad rather than a hard alumina or cast iron scaife, far thinner films on highly bowed substrates can be polished with uniform polishing and with little risk of cracking.

With regards to the means of material removal, contact polishing can be divided into three mechanisms: micro-chipping, conversion to graphite/amorphous sp^2 , and chemical reaction [177]. As described earlier, when two moving surfaces come into contact with each other frictional forces are generated. Should these frictional forces surpass the atomic binding energy of the diamond surface, material at surface asperities will be chipped away along the $\{111\}$ cleavage planes. During mechanical polishing loose grit is responsible for causing fracture when polishing along ‘hard’ directions, while CAMPP utilises alumina plates with Vickers hardness of $\sim 19 \text{ GPa}$ to fracture crystalline peaks [242]. Comparing this value to hardness values of 30–100 MPa and $\sim 7.4 \text{ GPa}$ for the polishing pad and colloidal silica respectively, it is unlikely that the pad can cause

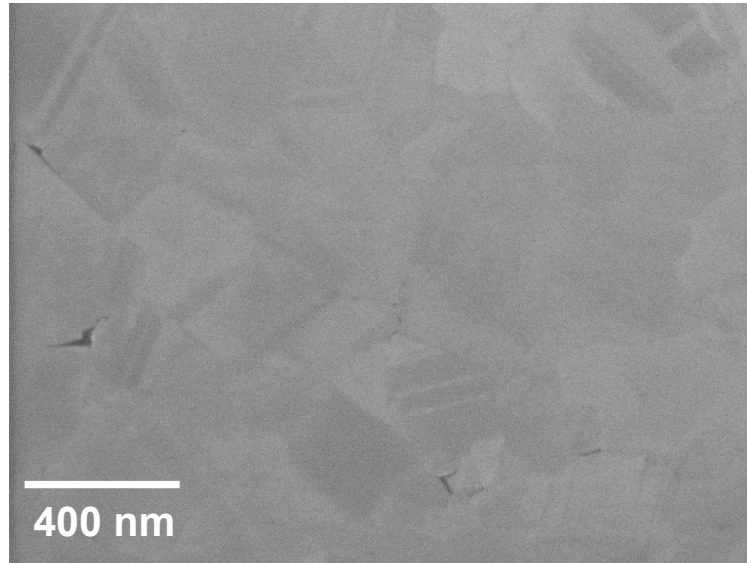


Figure 5.17: Magnified SEM image of a CMP film detailing the lack of steps or etch pits attributable to chemical oxidative etching. The pits that can be resolved are at the boundary between individual grains, suggesting insufficient polishing for this particular sample.

a significant frictional force against NCD with hardness of 63–95 GPa [46, 222, 243, 244]. This is supported by the fact that the conditioner used to initially abrade the pad, and those used in the IC-fabrication industry, are typically electroplated or brazed diamond grit [217, 245]. More recently, CVD grown polycrystalline diamond coatings on a ceramic plate have also been used successfully in the conditioning of CMP pads, reiterating the unlikelihood of fracture [246].

Given the movement of diamond against polymer it is also unlikely that the friction can give rise to a large enough shear force to drive a phase transformation to less dense sp^2 forms of carbon. In order to surmount the large activation energy required to convert diamond to graphite, a transition metal such as Fe, Ni or Co can be used to reduce the temperatures required to 700 °C. However this is still significantly higher than the pad temperatures of 30–50 °C seen after extended polishing [25, 177]. Coupled with the lack of a photoelectron peak attributable to sp^2 carbon after polishing it is also unlikely that conversion to graphite/amorphous carbon could be responsible for material removal.

Lastly, solely chemical based etching with KOH and KNO_3 while either open to atmosphere or with water vapour has also been demonstrated with etch rates of the order of tens of $\mu m h^{-1}$ [247–249]. During heating the etchant decomposes to atomic

oxygen and monovalent species such as $-\text{OH}$ and $-\text{H}$; the atomic oxygen either converts material to CO and CO_2 , while the hydroxyl ions stabilise the surface through the saturation of dangling bonds dependant on crystal orientation. As a result of this stabilisation, etching proceeds in a stepwise fashion with surface defects and/or dislocations bringing about pitting, with geometries and inclinations dependant on the crystallographic orientation and etching temperature [248]. While KOH , NaOH , or NH_4OH are added to maintain a pH of the slurry of ~ 10 , temperatures of $600\text{--}1100\text{ }^\circ\text{C}$ are typically used for conversion to CO and CO_2 due to diamond only becoming soluble in KNO_3 at $300\text{ }^\circ\text{C}$. Meanwhile polishing only occurs at the areas in contact with the pad suggesting a mechanical contribution to the polishing observed, while high magnification images of resulting CMP surfaces, as shown in Figure 5.17, show no indication of pitting or stepwise etching. Previous attempts at the use of Syton with a KNO_3 additive against a cast iron scaife, with a likely far higher shear force, have also been unsuccessful suggesting that direct conversion to CO and CO_2 is unlikely to be responsible for the polishing seen.

Given that the mechanisms usually used to describe the polishing of diamond cannot be adapted to explain the polishing observed, it is believed that the material removal is instead attributable to the increase in the oxygenated functional groups/general oxidation and the silicon present on the surface. As visible from the de-convoluted spectra of Figure 5.14B, polishing brings about subtle changes in the high binding energy region of the $\text{C}1\text{s}$ peak, with slight increases in the carbonyl and ether character of the NCD surface. Meanwhile, as detailed in Figure 5.15, the $\text{Si}2\text{s}/\text{C}1\text{s}$ ratio increases after 1 hour of CMP suggests silica remains tightly bound after the post polishing SC-1 clean. The ratio then decreases due to the surface becoming smoother and more of the bulk of the NCD being sampled by XPS.

It is therefore proposed that the polishing mechanism mirrors that used to describe removal of silicon dioxide with silica based CMP. In oxide polishing, hydroxide ions within the alkaline polishing fluid convert the surface siloxane (Si-O-Si) bonds to silanol $\text{Si}(\text{OH})_4$ groups, which in turn facilitate the binding of silica particles to the surface of the wafer. Should a pad asperity then provide a shearing force to the particle larger than the binding energy of the silanol group, both particle and silanol group will be removed. For diamond it is believed that the alkaline slurry converts the largely hy-

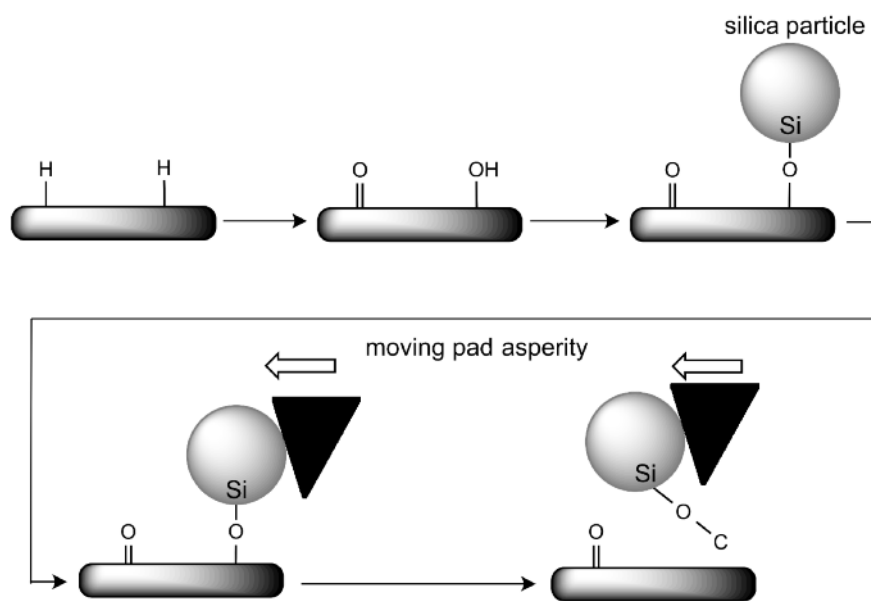


Figure 5.18: Wet oxidation of the NCD surface occurs, increasing the proportion of carbonyl and hydroxyl bound surface groups and facilitating the binding of silica particles within the slurry. Should an asperity of the polishing pad then provide a shearing energy larger than the binding energy of carbon atoms on the surface, the atom will be removed. Reprinted from [210] under a Creative Commons license, <https://creativecommons.org/licenses/by/3.0/>.

drophobic hydrogen terminated surface to a partly hydrophilic surface rich in carbonyl and hydroxyl character. Silica particles within the slurry then bind to the surface creating an Si–O–C bridge, which when faced with a sufficient shearing force will remove carbon from the surface, as shown in Figure 5.18. Given the bond strengths of Si–O, O–C, and C–C are 800, 1077, and 610 kJ mol⁻¹ respectively, it is believed that upon the application of this force the C–C bond will break first [250]. Alternatively, an already hydroxylated silica particle can directly bond to the NCD surface. Post polishing DLS was attempted to study the change in slurry with polishing, however this was hampered by the high concentration of the slurry and the relatively minor changes these bound silanol groups bring about in scattering.

Recently Peguiron *et al.* have performed density functional theory calculations on the degradation of the diamond surface when in contact with silica and silicon, mirroring those carried out to describe the mechanisms responsible for mechanical polishing. The authors observed that while shearing studies of the silicon/diamond system resulted in plastic deformation of silicon, occasional C–C bond breakage was observed in the silica/diamond case. With the polar nature of silica, the formation of strong C–O or C–Si bonds between silica particles and the diamond surface can occur, with strengths rivaling diamond like C–C bonds present on the reconstructed surface. Therefore, should a passing Si or O atom bond with a C atom within a zigzag chain on a {110} surface and exert a force, a previously weakened C–C bond can be broken. Such weakening can occur when an ad-atom or species such as H, Si(OH)₃, or SiH₃ binds to a neighbouring atom within the zig-zag chain converting a σ bond to a π bond and breaking the aromaticity [19]. Given the bond weakening is dependant on the location of the ad species rather than the atomic species present within it, presumably the hydroxyl radicals within the alkaline slurry could facilitate the weakening of the C–C chain, following the model proposed in Figure 5.18.

With the successful demonstration of the polishing of nanocrystalline diamond, chemical mechanical polishing could be used to remove the scaife introduced surface features observed on single crystal diamond samples, beneficial to applications ranging from MEMS/NEMS to homoepitaxial growth. Through the use of crystals with different orientation, the polishing rates of differing plane groups can be investigated and correlation to periodic bond theory validated.

5.6 CMP of Single Crystal Diamond

5.6.1 Experimental Methods

For the study of single crystal CMP, high pressure high temperature {100} and {111} orientated single crystal samples were obtained from Daniel Twitchen at Element 6, with dimensions of approximately $2 \times 2 \times 0.5$ mm high and $3 \times 3 \times 0.7$ mm high respectively. Misalignment angles were stated to be less than 2° , insignificant enough to prevent any considerable reductions in the wear resistance from the {100} and {111} plane groups [195]. Before use both crystals were given a standard SC-1 clean as detailed previously for 10 mins., followed by an ultrasonic DI H₂O bath for 10 mins.. Initial attempts to bond the samples directly to 2-inch silicon wafers were unsuccessful with the shear forces during polishing proving to be too large and removing the sample upon contact with the pad. Therefore, to facilitate polishing the samples were bonded within a recess of a 2-inch dia. polymer plastic holder with cyanoacrylate, as shown in Figure 5.19. The recess was then filled and the sample capped with Crystalbond 509 to prevent excessive shearing forces on crystal edges from dislodging the sample. Upon polishing the top of the cap is then immediately removed leaving only the face to be polished protruding. The template was then placed into the puck, as shown in Figure 5.10, in a similar fashion to the NCD films used in the previous section, and the puck then placed into a carrier within the polishing system.

CMP was carried out with a Logitech Tribo CMP tool equipped with a SUBA-X polyester/polyurethane polishing pad and Logitech supplied Syton alkaline colloidal silica polishing fluid. Unlike the pad used to polish the NCD samples, the pad did not have radial drainage channels due to the risk of the small single crystal samples dropping between pad sections and coming loose from the template. Before being used the pad was roughened up, or conditioned, with the use of an electroplated diamond grit plate to provide asperities for polishing and maximise slurry distribution. During polishing both puck and pad were kept rotating at 60 rpm in opposite directions, while the holder was swept across the pad. Down pressure on the sample was held at 4 psi (27.6 kPa), while a backing pressure of 20 psi (138 kPa) was applied to ensure contact between the sample and pad. To keep the pad sufficiently rough during polishing, the conditioner was placed in a second carrier and applied to the pad at a pressure of 1 psi

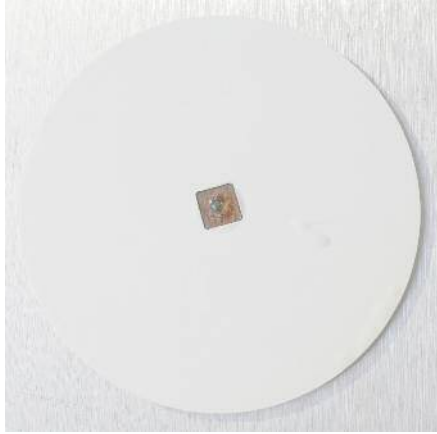


Figure 5.19: Sample mounted within CMP holder. Sample is bonded with cyanoacrylate within recess and capped with Crystalbond 509. After being pressed against the pad, the Crystalbond cap is removed leaving only the surface to be polished protruding.

(6.9 kPa) while rotating at 60 rpm. After initial wetting of the plate, the slurry feed rate was kept at 40 ml min^{-1} . Polishing durations were 3 and 7 hours for the $\{100\}$ and $\{111\}$ samples respectively, judged to be the point at which sufficient removal of the mechanical polishing introduced nano-grooves was seen. After polishing, the samples were cleaned with SC-1 and hydrofluoric acid to remove bound silica and any remaining polishing introduced contamination.

AFM was carried out with a Park Systems XE-100 AFM operating in non-contact mode and equipped with NT-MDT NSG30 silicon AFM tips (320 kHz resonant frequency, 40 N m^{-1} spring constant, 10 nm tip radius). Multiple areas of $25 \mu\text{m}^2$ were scanned before and after polishing, with analysis being carried out with WSxM and Gwyddion SPM analysis software. Swatches of a fresh pad, a conditioned pad, and a pad subjected to 7 hours of single crystal polishing were imaged with the SE2 detector of a Raith eLine SEM operating at 10 kV acceleration voltage and 9 mm working distance.

5.6.2 AFM of Polished $\{100\}$ and $\{111\}$ Single Crystal Samples

Typical AFM scans of the $\{100\}$ polished face are shown in panels A and B of Figure 5.20 respectively, with line traces taken perpendicular (1) and parallel (2) to the scaife introduced nano-grooves plotted in panels C and D. From the AFM image of

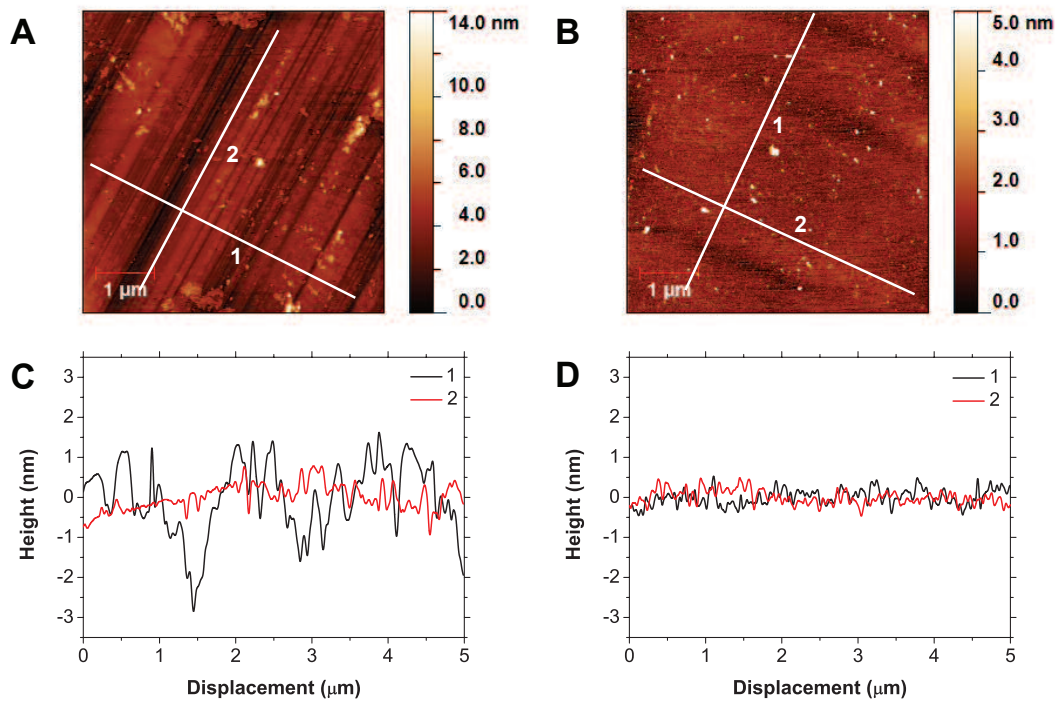


Figure 5.20: AFM images of the $\{100\}$ orientated single crystal sample before (A) and after CMP (B). Line traces taken perpendicular and parallel to the mechanical polishing introduced scribe marks before and after polishing are shown in panels C and D. Clear removal of the grooved features can be seen with the roughness of the perpendicular to the nano-grooves being reduced from 0.92 to 0.23 nm RMS. Reprinted from [251] under a Creative Commons license, <https://creativecommons.org/licenses/by/3.0/>.

the sample prior to polishing, the nano-grooved features as a result of polishing along the soft $\langle 100 \rangle$ direction can clearly be observed. The perpendicular to the polishing direction line trace meanwhile indicates groove widths of between 100 and 500 nm and an average depth of 3 nm. The trace taken along the polishing direction meanwhile shows far less variation due to the role of passing diamond grit particles; removal proceeds via an induced phase transformation and abrasion producing a level trough, rather than brittle fracture along the $\{111\}$ plane. Resulting roughness values are 0.92 nm RMS and 0.34 nm RMS for line traces taken perpendicular and parallel to the grooved features. Upon polishing for 3 hours a clear difference can be seen in the AFM scan of Figure 5.20B, with the removal of the nano-grooved features to the point at which deduction of the original polishing direction is difficult. This clear removal is also demonstrated by the two line traces being in close agreement with each other while the large undulations present in the perpendicular to the original polishing direction have disappeared. As a result the roughness values for the perpendicular and parallel to the mechanical polishing direction are now 0.23 and 0.19 nm RMS respectively.

In a similar fashion to the $\{100\}$ orientated sample, AFM scans before and after polishing of the $\{111\}$ face are shown in panels A and B of Figure 5.21, with line traces taken perpendicular and parallel to the assumed original mechanical polishing direction shown in panels C and D. From the pre-polishing AFM scan and the associated line traces it can be seen that the grooved features are far shallower than those present on the $\{100\}$ crystal due to the superior wear resistance of the $\{111\}$ plane group and material removal being largely fracture based. Heights of the features are approximately 1.2 nm with widths similar to those seen for the $\{100\}$ orientated sample of between 100 and 500 nm, while roughness values are 0.31 nm RMS and 0.23 nm RMS for the line traces taken perpendicular and parallel to the mechanical polishing direction. Once again, after polishing for 7 hours it is difficult to resolve the original polishing direction with only the deeper grooves remaining. Both line traces meanwhile give roughness values of 0.09 nm RMS, reiterating this clear removal.

5.6.3 Polishing Pad

Given the tentative model used to describe the polishing of diamond, the polishing pad is arguably the most important aspect of CMP with its mechanical properties heavily

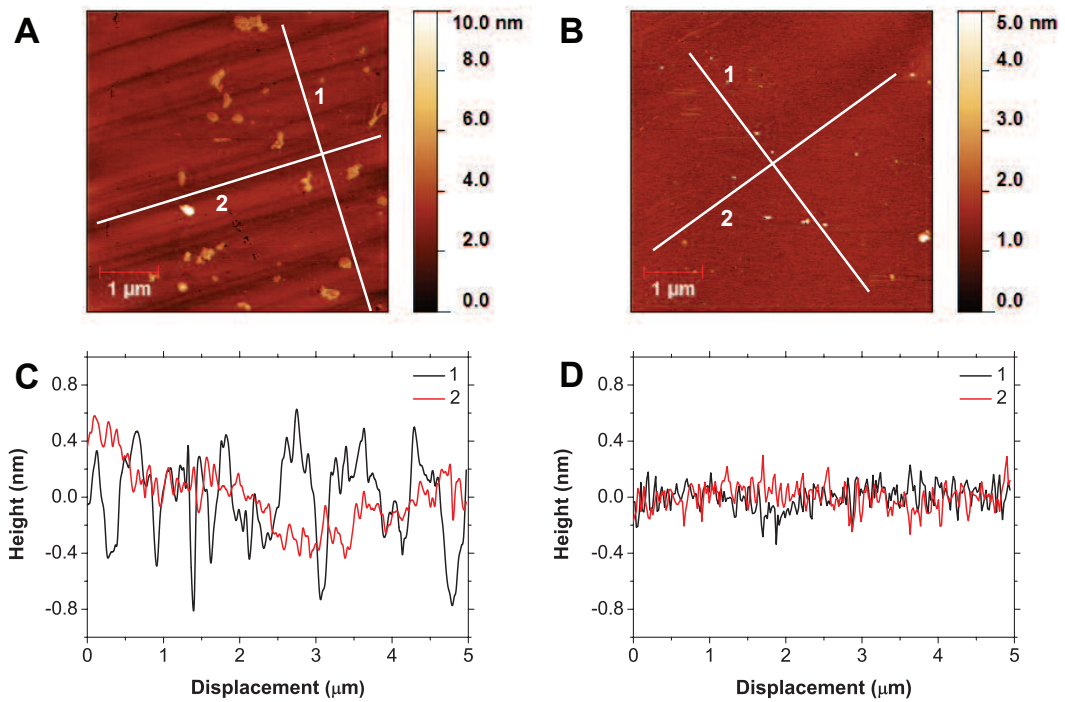


Figure 5.21: AFM images of the $\{111\}$ orientated single crystal sample before (A) and after CMP (B). Line traces taken perpendicular and parallel to the mechanical polishing introduced scaife marks before and after polishing are shown in panels C and D. Once again, clear removal of the scaife introduced damage can be seen with reduction in roughness from 0.32 to 0.09 nm RMS for the line trace perpendicular to the original polishing direction. Reprinted from [251] under a Creative Commons license, <https://creativecommons.org/licenses/by/3.0/>.

determining the wear rate and uniformity possible [252]. As stated earlier, before use pads are typically ‘run in’ or ‘conditioned’ with the use of an electroplated or brazed diamond grit to roughen the surface, creating the asperities required for mechanical action while also opening up pores to enhance slurry distribution [229]. Should the pad then be used without further conditioning, shear forces will induce plastic deformation reducing the roughness of the pad [230]. As a result the pad will appear ‘glazed’, with the reduction in surface asperities causing a tailing off in the polishing rate in as little as 5–10 minutes [229]. Meanwhile, the pores will reduce in diameter due to trapped slurry, polishing debris and abraded pad material, reducing the pads ability to transport slurry [228]. Given the bulk of the pad remains unchanged, further conditioning to abrade away the damaged surface layer will increase the removal rate back to that of a fresh run-in pad [229].

Plan view SEM images of (A) an as received pad, (B) a pad subjected to conditioning for 1 hour, and (C) a pad subjected to 7 hours of single crystal polishing are shown in Figure 5.22 along with side view schematics at corresponding times of the pad’s life. As visible in panel A the as received pad consists of randomly orientated, intact polyester strands bound together with a polyurethane foam. The pores within the foam appear relatively small with little variation in the surface roughness across the image. Upon abrading with the diamond grit conditioner the polyester strands have been severed, while the underlying polyurethane binder has roughened up and become more porous. Such a structure will then be more capable of providing the shear forces necessary for the removal of material, while also being more efficient at transporting slurry and debris throughout the pad. After 7 hours it can be seen that the pad is heavily worn with all the polyester strands being truncated down to polyurethane, while the binder has become smoother and pores have closed up. At this stage a narrow wear track was visible by eye suggesting a significant change in pad thickness due to abrasive wear by the passing diamond samples. Therefore, the pad has lost its ability to provide the forces required even with continued conditioning, and has reached the end of its usable life.

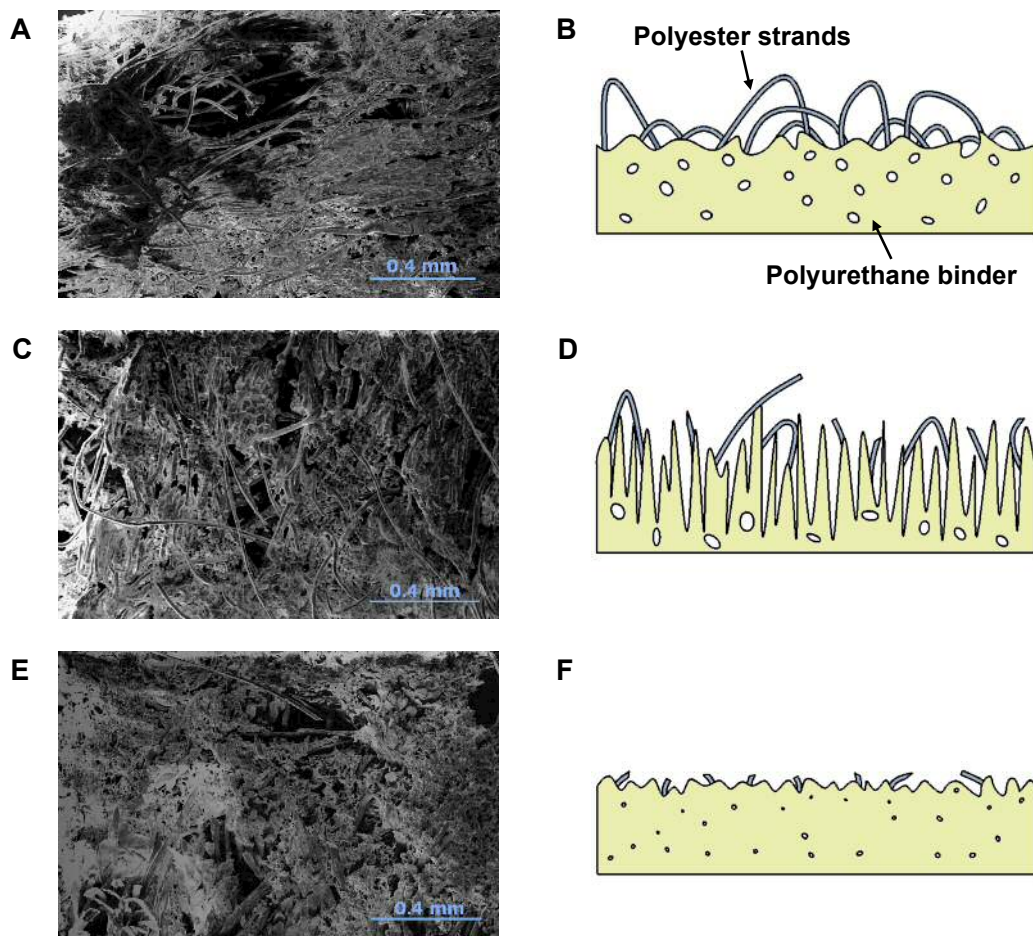


Figure 5.22: Plan view SEM images of the SUBA-X pad (A) as received, (C) after conditioning, and (E) after being subjected to 7 hours of single crystal CMP. Shown in panels (B), (D), and (F) are corresponding side view schematics at the different stages of use. After conditioning the polyester strands have become partly severed, while the polyurethane binder has become rougher and more porous. At this point the pad will be at its optimum for applying shear to silica particles and transporting slurry and debris through the pores. After 7 hours of use all of the polyurethane strands have been truncated to the surface of the pad, while the polyurethane binder has become smoother and less porous signifying the pad has reached the end of its usable life. Reprinted from [251] under a Creative Commons license, <https://creativecommons.org/licenses/by/3.0/>.

5.6.4 Discussion

From the AFM images of Figures 5.20 and 5.21 a clear removal of the mechanically induced nano-grooved features can be seen to the point at which it is difficult to resolve the direction in which the samples were mechanically polished. This reduction is again shown in the 5 μm line traces taken perpendicular to these nano-grooves with the samples prior to polishing showing groove depths of 3 nm and 1 nm for the $\{100\}$ and $\{111\}$ samples respectively and widths of 100–500 nm. After polishing the grooved features disappear and the line traces taken parallel and perpendicular to the marks appear very similar with roughness values of the line traces taken perpendicular to the original mechanical polishing direction being 0.23 and 0.09 nm RMS respectively. Such roughness values are on par with those achieved with the fracture based technique of CAMPP, with presumably no further subsurface damage occurring [211, 212]. With regards to the polishing rate it can tentatively be stated that the reduction in roughness rate is larger for the $\{100\}$ sample due to the shorter duration required to see removal of the scaife marks, in agreement with periodic bond chain theory and following results observed with mechanical polishing.

It is worth noting that no attempt was made to polish along the ‘soft’ $\langle 100 \rangle$ of the $\{100\}$ sample or any of the ‘softer’ directions of the $\{111\}$ face, with the samples continually rotating against the pad. Therefore, equal time was spent along the hard and soft directions of the sample with no indication of the fracture typically observed when mechanically polishing along ‘hard’ directions. As a result it can be safely assumed that the subsurface region is free from any additional micro-cracks as is often seen up to 5 μm deep with mechanical polishing [201]. The samples also show little indication of surface pitting or atomic steps as a result of being subjected to a highly oxidising environment, with all the material removal being seen from the points in contact with the polishing pad. Therefore, while not able to confirm the mechanism proposed for silica polishing of diamond, the removal seen follows the model presented during the polishing of NCD in Figure 5.18. Little evidence of polishing introduced contamination such as removed material, bound silica or abraded pad are also observed on the samples suggesting that the cleaning process of SC-1 followed by a HF etch is sufficient. This is in sharp contrast to the traditionally difficult to remove diamond grit from mechanically polished samples.

Due to the long durations seen when polishing diamond *in-situ* conditioning is required to maintain the roughness and porosity of the pad. The diamond sample itself contributes substantially to pad wear with wear tracks visible by eye after 7 hours of polishing, placing the pad lifetime seen here at the lower end of that observed with more traditional CMP [229]. This significant abrasion is highlighted in panels E and F of Figure 5.22, suggesting further optimisation of the pad is required in order to increase the removal rates of diamond and the cost effectiveness of the technique.

5.7 Further Polishing Experiments

Further attempts in the polishing of nanocrystalline diamond films have highlighted that the limiting step is often adhesion between the substrate and film, or lack thereof. In order to successfully polish films with minimal loss, the adhesion needs to be accounted for in two ways; careful mounting of the wafer to prevent digging in and excessive shear forces on the sample edges, and the trade off between polishing rate and sample loss. As mentioned previously, and as shown in Figure 5.10, the protrusion of the wafer above the surrounding template is set with the use of Kapton shims adhered to each other with capillary action. Should the wafer protrude too far above the surrounding template, the edge of the sample can dig into the pad leading to excessive shear forces and subsequent delamination. Therefore it must be ensured that the protrusion is no more than 100–200 μm , with as little protrusion as possible with the available shims the better.

Also believed to be responsible for delamination is the condition of the polishing pad; should samples be applied to the pad at pressures of 4 psi (27.6 kPa) immediately after the initial conditioning stage the sample will begin to delaminate. Should such high pressures be sustained delamination will continue inwards till the entire film has been removed. It is believed that the fresh pad is able to conform well to the bow of the wafer, and if the pressures applied are too large, large areas will simultaneously be subjected to shear. As the pad is abraded with further use and the pores filled up, the pad becomes less flexible and larger pressures are required to maintain sufficient contact with the wafer to maintain polishing. Therefore, there is a trade off between the removal rate and the loss of the wafer, with polishing conditions needing to be tailored to both

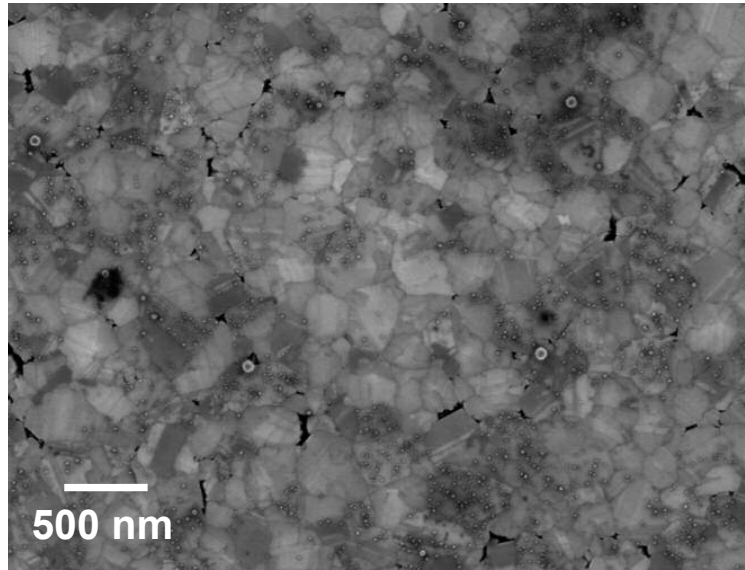


Figure 5.23: NCD film polished with recycled SF-1 showing large SC-1 resistant slurry particles. The coarse method of filtering and reuse of polishing slurry prevents sedimentation of larger and aggregated fumed silica particles from occurring and results in larger particles bound to the surface. Due to the gentle polishing mechanism no increase in the surface damage can be made out, with attainable roughness values remaining the same as with fresh slurry.

the condition of the pad and the interfacial adhesion between film and substrate. At Cardiff Diamond Foundry polishing is generally begun at pressures of 2 psi (27.6 kPa) and then increased in stages of 0.5 psi (2.45 kPa) as the pad condition deteriorates with resulting removal rates in the range 10–30 nm h⁻¹.

With the cost of SF-1 (~£11 GBP l⁻¹) and the difficulties in the disposal of alkalines, dissolved silicates, and buffer salts along with the silica within the polishing fluid, trials were conducted into the reuse of the fluid [225, 253]. Previous studies have shown that as much as 90% of the slurry is not consumed during polishing suggesting that the slurry can be reused without a decrease in the removal rate or worsening of surface finish [226, 254]. While it has been seen that particles exceeding 1 µm have lead to an increase in the surface scratches in oxide polishing, with the lack of abrasion in the mechanism proposed for polishing of diamond it is believed that such damage is unlikely to occur with diamond [224, 226]. However, care is warranted to prevent a reduction in the solid content within the fluid; when diluted with DI and in the presence of CO₂ the pH can decrease, causing precipitation due to the reduced dissolution rate of silica [225].

Care was taken not to add excessive amounts of DI when cleaning the apparatus and the slurry was coarsely filtered to remove larger aggregates and abraded pad material before reuse. Upon polishing the wear rate was seen to be in the range $10\text{--}30\text{ nm h}^{-1}$, the same as before dilution and with no change in surface quality as seen in Figure 5.23. Also present on the surface are dispersed $\sim 50\text{ nm}$ silica particles as well as larger $\sim 200\text{ nm}$ particles, lacking in the SEM and AFM images of films polished with fresh SF-1 of Figures 5.12 and 5.13. It is postulated that these larger particles are present due to the coarse filtering re-dispersing the larger particles, with the slurry being reused before the time required for adequate settlement of larger particles (of the order of weeks) [224]. Alternatively, aggregation can also occur due the reduction in pH with addition of DI and the presence of CO_2 leading to a reduction in the stability of silica, or from a change in the zeta potential with additional carbon [217, 225]. Such particles are presumably more difficult to remove by the passing pad due to the increased number of bonds to the NCD with larger particle diameter.

5.8 Conclusion

CMP has been adapted to the polishing of nanocrystalline and single crystal samples to remove the columnar growth and mechanically introduced surface roughness respectively. For the diamond films a reduction in roughness from the as-grown 18.3 nm to 1.7 nm RMS over $25\text{ }\mu\text{m}^2$ was observed, with values as low as 0.42 nm RMS over the area of a grain size ($\sim 0.25\text{ }\mu\text{m}^2$). Meanwhile, scribe marks present after mechanical polishing of $\{100\}$ and $\{111\}$ orientated single crystals have been removed, with $5\text{ }\mu\text{m}$ line traces taken perpendicular to the scribe marks reducing from 0.92 to 0.23 nm RMS and 0.31 to 0.09 nm RMS for the samples respectively. Finally, through performing XPS a model of general oxidation of the diamond surface, binding of the silica particles within the slurry, and subsequent shearing has been postulated as the removal mechanism. Thus with its relatively low cost of operation, simplicity, ability to polish highly bowed wafers, and the similarities to current practice in the IC fabrication industry CMP is a promising mechanism for the polishing of both polycrystalline and single crystal diamond.

Chapter 6

Nanocrystalline Diamond

Nano-Electro-Mechanical Systems

With the ability to possess resonant frequencies (f) in the GHz while maintaining quality factors (Q) far in excess of their electrical counterparts, Micro and Nano-Electro-Mechanical Systems resonators incorporating micro- and nano-scale mechanical elements into electronic circuits are of increased interest in both technological and fundamental physics applications. As the frequency of such a device is proportional to the acoustic velocity of the constituent material, $\sqrt{E/\rho}$, diamond with a Young's Modulus of 1200 GPa is the ideal material for attaining GHz resonators with minimal loss. While previous NCD resonators have displayed fQ products rivalling those of more complex designs constructed from the conventionally used Si, their performance has been limited by the considerable surface roughness arising from the columnar nature of NCD films. Therefore, this chapter details the fabrication and initial testing of NEMS structures from 'smooth' CMP polished NCD films with the aim to study the effect of roughness on the Q factor and produce high fQ product NCD resonant structures.

6.1 Micro and Nano-Electro-Mechanical Systems

Micro and Nano-Electro-Mechanical Systems (MEMS/NEMS) incorporating the actuating, controlling, and sensing of micro- and nano-scale mechanical element into an electrical circuit are increasingly being utilised in both technological applications and the study of fundamental physics [6, 9, 17]. Typically fabricated from Si, AlN, GaAs, or SiC a series of such doubly clamped resonant NEMS, the most basic of resonator structure, constructed from 259 nm thick SiC are shown in Figure 6.1 [7, 9, 255]. Employing the magneto-motive transduction technique, upon being placed in a static magnetic field while supplying a sinusoidal AC signal the resulting Lorentz force will cause the bridge to flex at a resonant frequency f_n . Mechanical energy is then lost from the bridge due to intrinsic material and extrinsic circuit losses with the ratio of the energy lost per oscillation to the energy stored within the cantilever termed dissipation, Q^{-1} , the inverse of the quality factor [6]. The actuation of MEMS/NEMS devices have then been used for the filtering of RF signals, while perturbation of the resonant frequency has been used for low cost gravimeters, single virus detectors and atomic-resolution mass spectrometers [1, 2, 4, 256]. In addition, through cooling a piezoelectric resonator to its quantum ground state and coupling with a quantum bit the transfer of quantum excitations have been observed, demonstrating the applicability of quantum mechanics to macroscopic mechanical objects [257]. To improve the sensitivity in these applications, minimise the effect of the mechanical noise background, and facilitate use in RF and IF filtering, resonant frequencies in the high MHz to GHz range are required [4, 5]. Low dissipation meanwhile reduces the frequency domain response width of the device, maximising sensitivity to external perturbations, reducing power consumption allowing the cascading of devices, and in the case of filtering allowing the selection of individual channels at RF frequencies [4, 5, 17, 258]. Current NEMS devices offer Q factors in the range 10^3 – 10^5 , greatly in excess of those provided by electrical oscillators and cementing their current use [17].

To calculate the resonant frequency of the nano-scale bridges within Figure 6.1, the Euler-Bernoulli beam equation can be used with boundary conditions to account for account for zero displacement and diminishing slope at the anchor points either side of

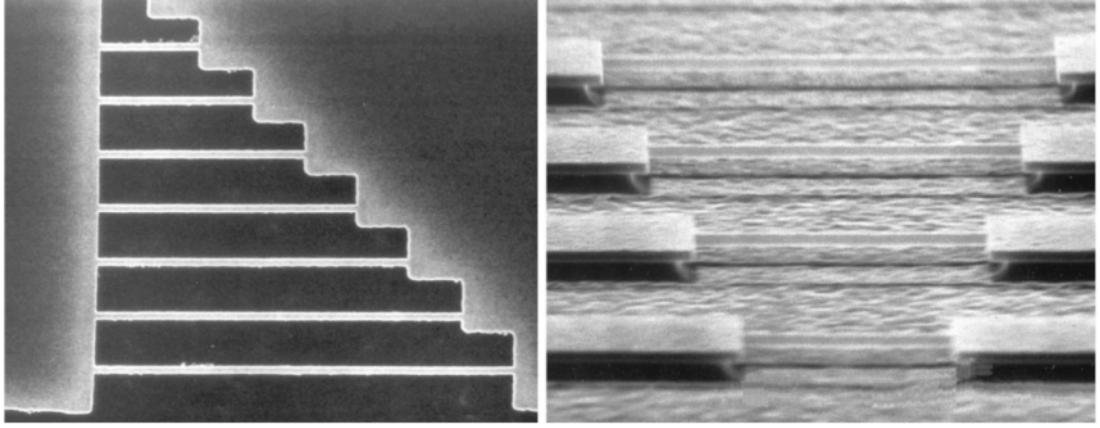


Figure 6.1: Doubly clamped NEMS resonators constructed from 259 nm thick SiC patterned with e-beam lithography and electron cyclotron resonance (ECR). Upon placing in a magnetic field and sweeping an applied AC signal the resulting Lorentz force will cause the resonators to flex at a resonant frequency f_n between 6.8 and 134 MHz while dissipating energy at Q^{-1} . Reprinted from [255], with the permission of AIP Publishing.

the beam [6, 9];

$$f_n = \eta_n \sqrt{\frac{E W}{L^2}} \quad (6.1)$$

Where: η_n is the mode number, equal to 1.028 for the fundamental mode of a doubly clamped beam; $\sqrt{E/\rho}$ is the acoustic velocity composed of the Young's Modulus of the material E , and the mass density ρ ; and W/L^2 is the geometric factor composed of the width of the beam W , and the length of the beam L . With widths of between 150–600 nm, thickness of 259 nm, and lengths of 2–17 μm the nano-scale SiC beams within Figure 6.1 are then designed to resonate at frequencies between 6.8 and 134 MHz [255]. From the relationship it can then be seen that the resonant frequency can be increased through shortening L or increasing W within the geometrical term, or through selection of a stiffer material with a larger acoustic velocity term. Therefore, replacing the commonly used Si with SiC with acoustic velocities of 7500 and 11 400 m s^{-1} respectively increases the resonant frequency by a factor of 1.5 for a structure of identical dimensions, or allows a larger structure to attain the same resonant frequency [7, 17]. Use of stiffer diamond however with a high Young's Modulus of 1200 GPa leading to the high acoustic velocity of 18 000 m s^{-1} will result in an increase in resonant frequency by a factor of 2.4, allowing

relatively large micron-long diamond NEMS devices to achieve GHz frequencies while placing less demand on nano-machining processes [7, 15, 17]. Coupled with diamonds superior thermal conductivity in comparison to SiC (2000 to 114 W m⁻¹ K⁻¹), superior Vickers hardness (~100 to 31–34 GPa), and the ability to be doped from an insulator to superconductor at cryogenic temperatures through the incorporation of boron makes diamond an attractive material for NEMS devices operating at high frequency in harsh environments [6, 9, 46, 259].

With the use of diamond allowing larger scale devices, dissipation upon reaching sub-micron levels from sources intrinsic to the material and from the construction of the resonator, observed to scale with device volume at $Q \propto V^{1/3}$, are minimised [6]. Should the set of bridges within Figure 6.1 be actuated, the significant undercut formed from isotropic etching of the Si substrate will result in the displacement of the anchor. As the strain is at a maximum at the node points for the fundamental mode of a flexural beam, elastic waves will then propagate into the anchor increasing the dissipation and scaling at $\alpha w^3/L^3$ and $\beta t/L$ for in plane and out of plane actuation respectively [6, 17, 18]. While this dissipation can be minimised through increasing the aspect ratio, such a change to the geometry requires a reduction in length of the device to obtain an identical resonant frequency, placing more stress on machining, making actuation more difficult and enhancing scaling induced loss [6]. As a result, doubly clamped beams typically possess quality factors below 10^4 or 10^3 upon an increase in frequency from 10^7 to 10^9 Hz [6, 9]. Therefore to more effectively reduce this clamping loss geometries that minimise strain at the anchor supports can be employed [8, 18, 260, 261]. Huang *et al.* constructed SiC free-free beams, as shown in Figure 6.2A, consisting of a fundamental beam free at either end and supported by 4 flexural supports positioned at motional nodal points to minimise the strain at the anchors [18, 260]. Comparing to doubly clamped resonators the authors noted an increase in Q upon using the free-free design from 4500 to 11 000 for beams with resonant frequencies of ~170 MHz [18]. Meanwhile Gaidarzhy *et al.* demonstrated a design consisting of the collective mode of a series of short paddles positioned along a central beam, as shown in Figure 6.2, constructed from a 600 nm thick intrinsic NCD film with gold conductive layer. With the design the authors obtained Q factors of 23 200 while resonating at 631 MHz with fQ products among the highest reported value for NEMS devices at 1.46×10^{13} , surpassing more

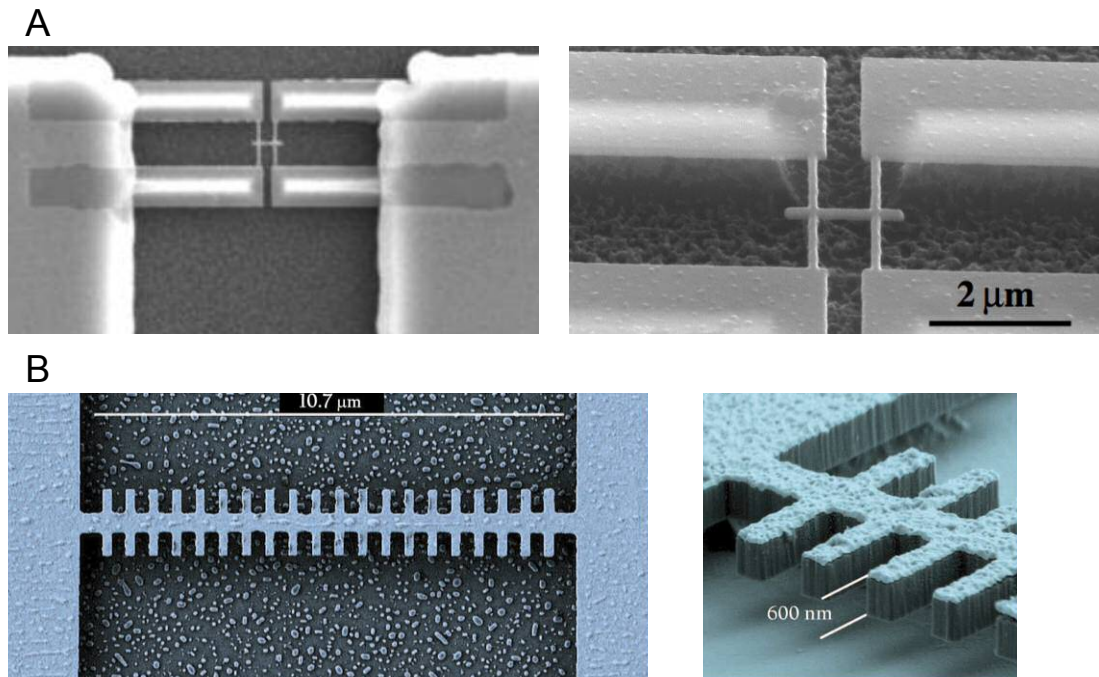


Figure 6.2: (A) Free-free and (B) paddle resonator geometries designed to reduce the propagation of strain into the anchors and associated dissipation. Upon resonance of the free-free beam in the plane of the sample the 4 support structures positioned at the motional nodal points of the cantilever are designed to resonate flexurally, minimising strain at the anchor supports and the associated dissipation. In comparison, the order of magnitude smaller cantilevers within the paddle design fabricated from NCD collectively resonate to focus strain at the attachment points to the central beam, producing fQ products rivalling more complex geometries constructed out of Si. (A) reprinted from [18] under a Creative Commons license, <https://creativecommons.org/licenses/by-nc-sa/3.0/>. (B) reprinted from [8], with the permission of AIP Publishing.

complicated geometries constructed from Si and highlighting the benefits of using a material with high acoustic velocity [5, 8].

Heteroepitaxial growth of diamond however is limited to iridium substrates, precluding the growth and processing of wafer scale sized single crystal films atop a sacrificial layer [9–11]. To work around this limitation, FIB milling, the selective etching of a ~ 200 nm deep ion irradiated layer, and angled anisotropic etching have all been used to create free-standing structures within thick single crystal diamond [9–11]. Alternatively, 10–40 μm diamond plates have been ‘sandwiched’ between two quartz plates and bonded to a Si substrate through the use of a hydrogen silsesquioxane layer that converts to silicon dioxide under thermal annealing to create freestanding resonators [10, 11]. However, upon irradiation the high energy ions (MeV) traversing through the diamond device lead to the formation of defects degrading the performance of the resulting device, while the use of a carrier requires extensive polishing of the diamond plate to remove the large wedge shapes prevalent with CVD samples (>10 μm over a plate) and careful monitoring during plasma thinning to sub-micron thicknesses [10, 11]. With the ability to be grown on a range of foreign substrates at wafer scale and the retention of the Young’s Modulus of bulk diamond in films as thin as 140 nm, NCD then offers a thin film form of diamond atop a sacrificial layer and processable with standard NEMS fabrication techniques [9, 15].

As miniaturisation continues to sub-micron levels, the surface to volume ratio increases leading to a larger contribution to dissipation from atoms and adsorbates, dangling bonds and defects present at the surface [6, 16, 17]. Upon annealing SCD cantilevers created through Ar/Cl plasma in air at 450 °C, the conversion from H, O, and Cl covalently bonded termination to an oxygen terminated hydrophilic surface was observed to increase Q by a factor greater than 10 when operating under high vacuum [10]. Subsequent exposure to CF_4 plasma and the creation of a fluorinated hydrophobic and oleophobic surface with minor molecular absorption reduced the Q factor between that of the as processed and oxygen terminated cantilevers. As such it is hypothesised that surface loss is dominated by the terminating atoms and their ability to couple to the strain and relax energy [6, 10]. The significant roughness seen within the previous chapter (~ 20 nm RMS for a ~ 380 nm thick film) arising from the columnar nature of NCD growth is therefore not only expected to hamper the construction but also re-

duce the Q factor from an increased surface to volume ratio. Demonstrating this effect, doubly clamped SiC beams with roughness of 7.1 nm RMS were only operational to VHF frequencies in vacuum suggesting a quality factor of below 100, while smoother beams with roughness < 2 nm RMS were operational in the UHF/microwave regime [18]. Similarly, in Si nano-wires with 45 nm beam-widths and 380 MHz frequencies, the Q factor was reduced from 3000 to 500 by an increment of the surface area volume ratio from 0.02 to 0.07 [184]. To definitively attribute this change in Q factor to surface topography, Erginçan *et al.* FIB milled commercially available cantilevers with a variety of surface texture and tested between the free molecular ($P < \sim 10$ Pa for a 100 μm long cantilever) to viscous regime ($P < \sim 10^3$ Pa). Over the entire pressure range it was observed an order of magnitude decrease in the Q factor can be correlated to the increasing surface area with milling, with etching perpendicular to the direction of wave propagation (along the width of the cantilever) causing less of a decrease than that along it (along the length of the cantilever) [184]. The authors attribute such a decrease to defect dissipation within the effective surface layer, and the differing loss with etching direction due to the scattering of surface acoustic waves into the bulk [184]. In addition, at larger pressures mechanical resonators generate a flow in the fluid medium, which becomes amplified with increasing surface roughness, adding to the dissipation and the reduction in sensitivity of the cantilever to external perturbations [184, 262].

Therefore the use of smooth CMP polished films are expected to be advantageous to the construction and Q factor of NEMS with the low roughness and high Young's Modulus of single crystal retained, while being in thin film form and the ability to be grown atop a suitable sacrificial layer. Within this chapter doubly clamped resonators are to be built from CMP polished 'smooth' and as grown 'rough' NCD films to facilitate the study of the effect of the surface roughness on NCD NEMS devices, with the eventual aim to realise more complex geometries to minimise clamping losses. The following sections detail the development of a recipe for the construction of such devices and the initial attempts at testing doubly clamped beams constructed from 'smooth' NCD stock.

6.2 NEMS Fabrication

For the purposes of NEMS fabrication, a series of films were deposited onto 2" 500 μm thick intrinsic FZ $\langle 100 \rangle$ silicon wafers of resistivity $> 10\,000\ \Omega\text{cm}$, with a 500 nm thermal oxide on both sides. Before use each wafer was subjected to a standard SC-1 clean of 30% H_2O_2 : NH_4OH : DI H_2O (1:1:5) for 10 minutes at 75 $^\circ\text{C}$, rinsed with DI H_2O and spun dry. To improve the nucleation density the substrates were seeded through the use of a hydrogen terminated mono-dispersed nano-diamond/DI H_2O colloid for 10 minutes in an ultrasonic bath, known to produce seeding densities $> 10^{11}\ \text{cm}^{-2}$ [39]. After seeding each wafer was again rinsed, spun dry, and then placed inside the CVD reactor.

Film growth was carried out in a Seki AX6500 series CVD reactor operating at 4100 W power and pressure of 45 Torr, resulting in temperatures of 730 $^\circ\text{C}$ as indicated by dual wavelength pyrometry. To prevent etching of the seeds and produce low sp^2 content films a methane flow rate of 25 SCCM diluted in 475 SCCM of hydrogen was maintained for the first 5 minutes (5% CH_4), and then subsequently dropped to 3 SCCM of methane in 497 SCCM of hydrogen (0.6% CH_4) for the remainder of the growth duration. Two films were grown to thicknesses of $\sim 460\ \text{nm}$ and $\sim 350\ \text{nm}$ as determined by *in-situ* laser interferometry, and then ramped down in a purely H_2 fed plasma to prevent the deposition of non- sp^3 bonded carbon. The thicker of the two films was then subjected to colloidal silica CMP, as detailed within the previous chapter, for 3.5 hours and subsequently treated with HF acid to remove any residual silica present after the post CMP SC-1 clean. Resulting thicknesses at the centre of each wafer were then deduced with spectroscopic ellipsometry as 327 and 353 nm for the 'rough' and 'polished' films respectively through the use of a four phase model consisting of surface roughness/bulk/500 nm SiO_2 /Si between the spectral range 500 and 1000 nm and with the optical constants of the bulk composed of that of natural diamond mixed with glassy carbon. The thicknesses of the SE surface roughness layer were 29 and 1 nm for the 'rough' and 'polished' films respectively, in close agreement with values AFM deduced roughness values obtained over multiple areas of 5 by 5 μm of 35 and 2.3 nm RMS, allowing the study of the effect of surface roughness on the Q factor of NCD NEMS devices.

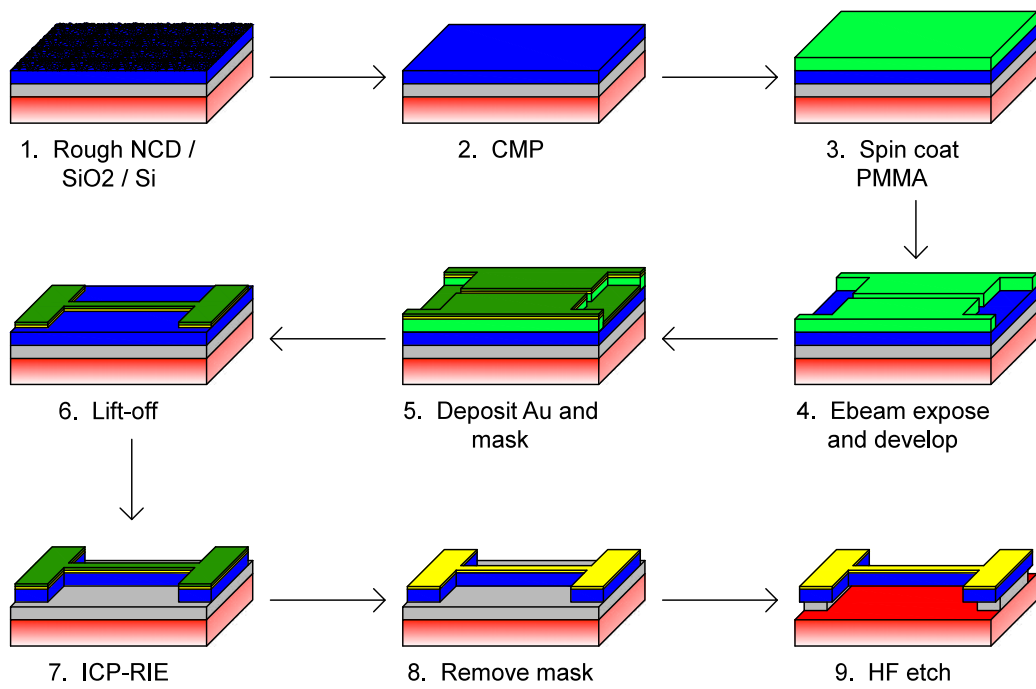


Figure 6.3: Overview of the fabrication process used to construct doubly clamped resonant beams from CMP polished films, detailing the steps taken from a rough NCD film on top of an intrinsic FZ silicon wafer with 500 nm buffered oxide layer to the production of free standing structures.

Figure 6.3 details the subsequent steps involved in the construction of resonating beams from the NCD wafers. Briefly, after the ‘thicker’ of the two wafers is first CMP polished both films are then diced up to 1 by 1 cm² square pieces, with the most uniform pieces within the central 1" used for device construction. To remove debris and organic residue after dicing the selected pieces are then cleaned with methanol, acetone and IsoPropyl Alcohol (IPA). The samples are then spun coat with PMMA resist and subjected to electron beam lithography to define a series of bridges with resonant frequencies between 10 MHz and 1 GHz suspended between sizeable anchor supports. An Au conductive layer is then subsequently deposited onto the patterned photoresist and capped by a hard metal mask. After liftoff to remove excess metal, the pattern is transferred to the underlying diamond through a highly anisotropic oxygen plasma etch followed by removal of the etch mask. Finally, the relatively narrow bridges are released from the SiO₂ buffer layer with an isotropic HF vapour etch leaving free standing resonators capped with a gold conductor suitable for wire-bonding to. The following subsections detail the optimisation of the process parameters for e-beam, metallisation, ICP, and HF etching culminating in the final recipe used to construct the initial test device.

6.2.1 Surface Termination

As the bridges are to be actuated magneto-motively at room temperature, a ~50 nm gold layer is required on top of the intrinsic NCD films to conduct the current required to achieve resonance. However, the adhesive properties of such an interface depend on the surface energies of the respective materials, and hence the surface termination, as well as the carbide formation enthalpy of the metal [263–265]. Elucidating on the adhesion between metal and diamond, Guo *et al.* carried out Density Functional Theory (DFT) studies between the unreconstructed diamond (111)–1×1 surface with Cu(111), Al(111), and Ti(111) [265]. Between Cu(111) and the unreconstructed diamond (111)–1×1 surface with the orientation between the respective surfaces chosen to minimise strain and registry of atomic positions to minimise energy, relatively weak covalent bonding was observed with the lone valence electrons of Cu surface atoms largely required to maintain the metallic bonding within the Cu bulk [265]. Without the presence of strong covalent, ionic, or metallic bonds van der Waals interactions lead to weak dis-

persive adhesion with the work required to separate the metal from the diamond equal to 3.36 J m^{-1} [264, 265]. In contrast, the carbide forming metals Al(111) and Ti(111) with 3 and 4 valence electrons respectively and a registry of 3 metal atoms to 2 carbon atoms permit the formation of strong interfacial covalent bonds, leading to increased work of separation values of 4.08 and 5.77 J m^{-1} for Al/diamond and Ti/diamond interfaces respectively [265]. With the increased work of separation with carbide formation ability, metals with a low formation enthalpy of the carbide phase such as Ti, Zr, V, Nb, Ta, or Cr are therefore required to provide highly adhered contacts [264–266].

However, with a large surface energy of 5.66 J m^{-1} , the clean (111) surface reconstructs to the Pandey (111)– 2×1 surface composed of $\text{C}-\text{C}$ bonded chains with a reduced surface energy of 3.35 J m^{-1} [267, 268]. For CVD produced films, mono-hydrogenation of the single dangling bonds of the unreconstructed (111) surface is instead expected to occur with a corresponding drastic reduction in the surface energy to 0.04 J m^{-1} [267–269]. DFT studies extended to both the reconstructed Al(111)/C(111)– 2×1 and hydrogenated Al(111)/C(111)– $1 \times 1:\text{H}$ interfaces observed that the strong covalent bonds at the hydrogenated diamond surface repel the Al atoms, preventing the formation of covalent, metallic, or ionic bond between C and Al atoms [267]. As a result of the reduction in surface energy coupled with passivation of the hydrogenated surface, work of separation values of 0.33 and 0.02 J m^{-1} are obtained for the Al(111)/C(111)– 2×1 and Al(111)/C(111)– $1 \times 1:\text{H}$ respectively [267]. Meanwhile single crystal diamond subjected to either Ar:O plasma or $\text{HNO}_3/\text{H}_2\text{SO}_4$ acid treatment oxidation demonstrate an increase in the thermal boundary conductance, shown to be correlated to the work of separation, above that of untreated and hydrogen plasma treated single crystals upon aluminium deposition [270, 271]. To maximise the adhesion between metal and diamond within the current study a fully oxidised surface is therefore desired, while a consistent surface termination is required to enable the comparison of NEMS constructed with both hydrogenated as-grown NCD and smoother, partially oxidised CMP polished films. Furthermore, with the weak dispersive adhesion expected between Au and diamond, a carbide forming interface is required to form strong covalent metal-diamond bonds. With the third largest smallest enthalpy of the carbon phase, behind only Hf and Zr, and ease of deposition with the equipment available, a Ti interlayer will then be deposited between the NCD surface and Au layer [265].

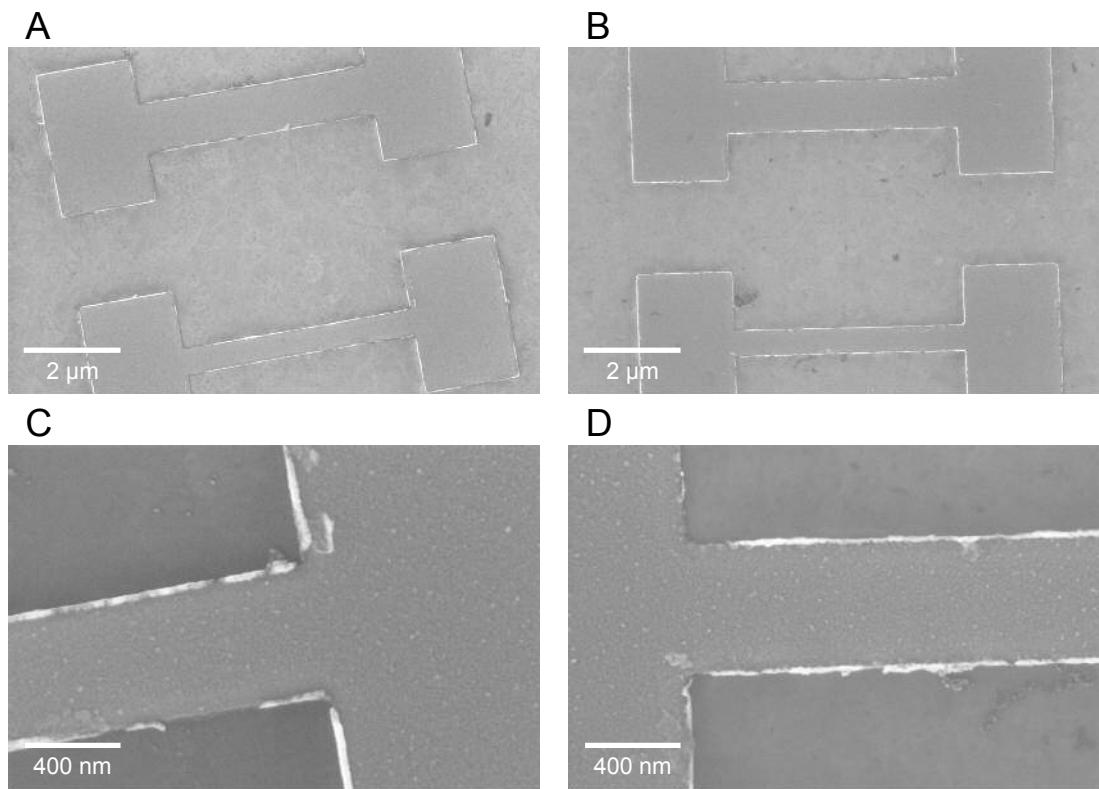


Figure 6.4: 50 nm Au/Al bilayer dose test deposited onto as-polished (A) and piranha treated (B) NCD samples, with magnified views of the 500 nm wide beams on the respective samples within panels (C) and (D). A minor improvement in the quality of lift off is observed after piranha treatment, presumably due to increased work of adhesion with further ketone groups present on the surface, with cleaner edges to the Au/Al bilayer.

To oxidise the diamond surface techniques from wet chemical to oxygen plasma subjection have been demonstrated to be capable of producing similar oxidation levels, primarily through the creation of singly oxidised carbon in the form of ether and epoxy like bridging groups with minor amounts of carbonyl and hydroxyl dependant on the technique used [235–237]. Upon comparing NCD subjected to a 150 W RF oxygen plasma, sulfochromic acid at 230–250 °C, and photochemical oxidation with a UV light source under atmospheric conditions, Klauser *et al.* demonstrated that a saturated oxidation level is achieved within 10–20 minutes, while the temperatures of 700 °C required to obtain similar levels of oxidation upon air annealing result in burning of the majority of the 2 µm thick film [235, 236]. Meanwhile, Speranza *et al.* have demonstrated that immersion in a piranha solution at 110 °C for 5 hours yields sample oxidations greater than that achievable with an oxygen plasma treatment at 50 W for 10 seconds and UV irradiation [237].

With difficulties in comparing the efficacies of oxidation methods trials were therefore carried out through the deposition of a 50 nm bilayer of Au/Al dose test on top of surplus as-polished, piranha treated, and O₂ plasma ashed CMP NCD samples in tandem with optimisation of e-beam exposure as detailed in the next subsection. Piranha treatment was carried out pre-electron beam processing with a 40 ml solution of H₂O₂:H₂SO₄ (1:3) for 5 minutes, with the strongly exothermic solution exceeding 100 °C before significant self-decomposition of the peroxide content within the treatment time. Plasma ashing was meanwhile carried out post electron beam processing in an attempt to oxidise the surface, ‘de-scum’ the resist from the bottom of exposed areas, and ensure vertical walls to the patterned features. As access to a dedicated plasma asher was limited, samples were subjected to an oxygen plasma within a SPTS Inductively Coupled Plasma-Reactive Ion Etcher (ICP-RIE) at Swansea University operating at 800 W ICP power, 25 W RIE power, 20 mTorr pressure, 20 °C carrier temperature, and 100 SCCM O₂ for 7 seconds, with the plasma striking and stabilising within the first 2 seconds. Dektak profilometry after development of the exposed PMMA and oxidation revealed step thicknesses of 193 and 85 nm respectively for the piranha treated and plasma ashed samples in comparison to the 197 nm thickness atop the as-polished sample, suggesting significant etching at a rate of approximately 22 nm s⁻¹ of the PMMA resist upon being subjected to the highly energetic oxygen ions within the ICP. As a result, upon metal

deposition and subsequent 1165 remover removal much of the metal remained on the plasma etched sample due to similarities in thickness between the ~ 85 nm PMMA and 50 nm metal bilayer. SEM images of the 1 μm and 500 nm wide beams deposited on top of the as-polished and piranha treated samples are shown within panels A and B of Figure 6.4, with magnified images of the 500 nm wide beams of the respective samples shown within panels C and D. As visible from the figures, upon piranha treatment a minor improvement in the quality of lift off is observed with sharper edges to the metal deposition, potentially attributable to an increase in the work of adhesion between Al and NCD. Therefore to improve adhesion and obtain a consistent surface termination between as-grown and polished NCD all subsequent NEMS samples were piranha treated, with an additional Ti interlayer to further improve the adhesion between metal and diamond.

6.2.2 E-beam Processing

Prior to e-beam patterning, the selected 1 by 1 by 1 cm pieces are first cleaned to remove organic residue and dicing debris for 5 minutes each in methanol, acetone, and IPA heated to 75 °C before being blown dry with N₂. Building upon a recipe used by Soumen Mandal at Institut Néel, Grenoble to construct the resonators within Bautze *et al.*, the NCD samples are then spun coated with PolyMethyl MethAcrylate (PMMA) 950 A4 at 4000 rpm for 30 seconds, 4000 rpm s⁻¹ acceleration, and baked on a hotplate set to 180 °C for 5 minutes, yielding a thickness of ~ 200 nm as determined through Dektak profilometry [272]. To obtain the optimum dose for the selected resist and spin parameters the dose test shown within Figure 6.5 was created and written to a spare CMP NCD sample. Consisting of a series of bridges of 5 μm length and widths of 50 nm–1 μm within a 50 μm area, the dose test replicates the resonating beams without the time intensive wide anchor supports and contact pads. Using a Raith eLine electron beam system at Swansea University a matrix of 5 \times 5 dose tests were written with incremental dose between 100–580 $\mu\text{A s cm}^{-2}$ with the ~ 40 pA current from the 10 μm aperture while operating at 20 kV acceleration voltage. The default deflection distance between spots, or beam step size, of 0.02 μm was initially deemed to large with the straight edges of the pattern composed of arcs from the circular beam so the step size was reduced to 0.006 μm for all subsequent writes carried out with the 10 μm aperture. The exposed

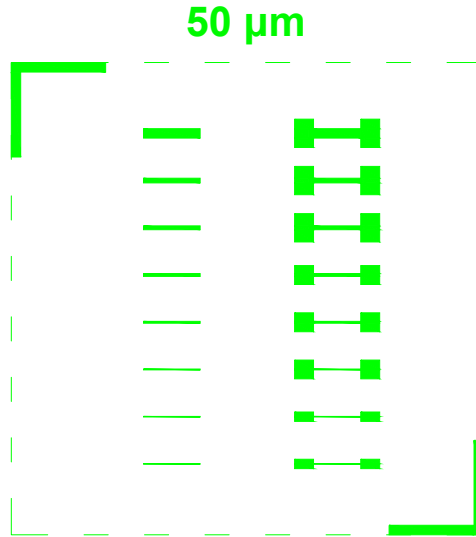


Figure 6.5: E-beam lithography dose test used to reach the optimal exposure dose for resist and spin parameters. Composed of a series of beams $5\ \mu\text{m}$ long and $50\ \text{nm}$ – $1\ \mu\text{m}$ wide with and without anchors supports within a $50\ \mu\text{m}$ area, such a dose test allows the rapid exposure of the resonant bridges at a variety of doses without the time intensive contact structures.

samples were then developed through immersion and gentle agitation in a 20 ml 1:3 Methyl Isobutyl Ketone (MIBK):IPA developer for 60 seconds, and then rinsed in IPA for 60 seconds and N_2 blown dry. Brief trials with developing and IPA rinsing periods of 45 seconds meanwhile yielded poor lift off upon subsequent metal deposition with the formation of ‘ears’ from metal covering the sidewalls, indicating a poor profile to the resist. As such development times were kept at 60 seconds for all further fabrication.

Figure 6.6 details the result of such a dose test on Piranha oxidised NCD after physical vapour deposition of a $50\ \text{nm}$ Au/Al bilayer with a Kurt Lesker PVD at Swansea University, and subsequent acetone based lift off. At the lower end of the dose scale the SEM image within panel A details the dose test resulting from a dose of $180\ \mu\text{A s cm}^{-2}$. Visible from the image is the poor replication of the dose test with the relatively few impinging electrons unable to produce a sufficient number of scissions to the long polymer chains of the $950\ \text{kDa}$ molecular mass PMMA, making it largely insoluble within the MIBK:IPA developer with only the thicker bridges being present [273]. For the dose test produced with a dose of $580\ \mu\text{A s cm}^{-2}$ shown in panel B meanwhile, overexposure of the features occur at the points of overlapping rectangles leading to bridges of non-

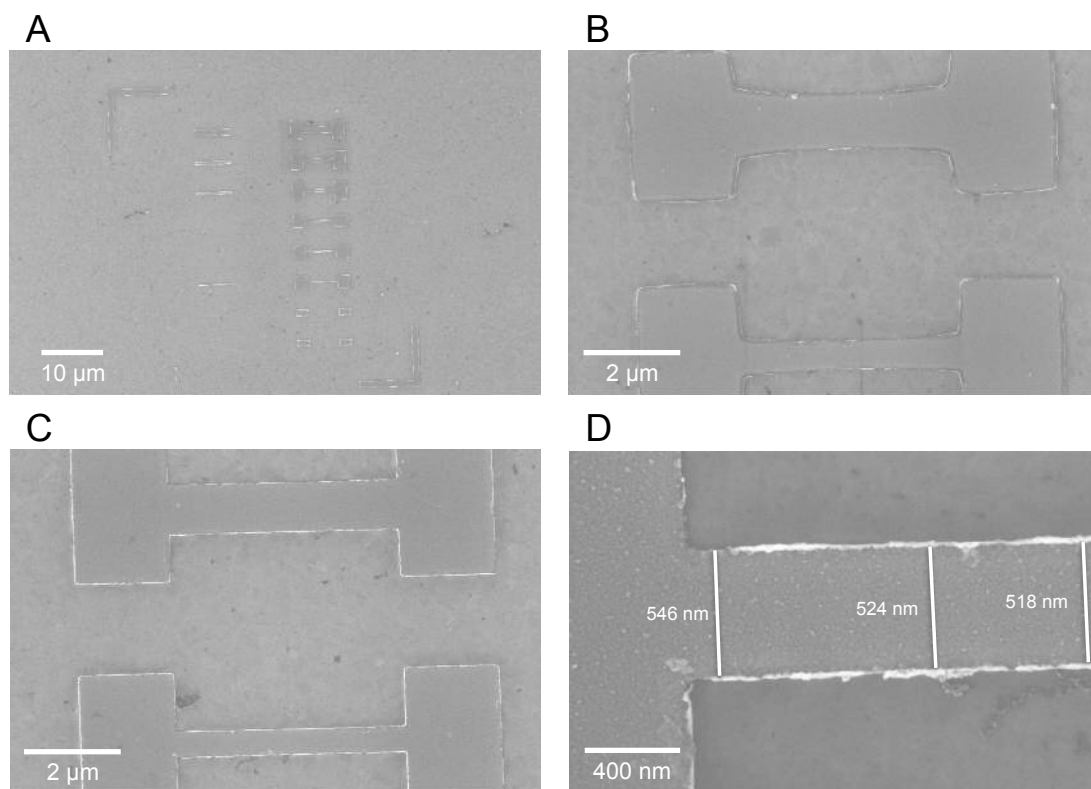


Figure 6.6: 50 nm Au/Al bilayer deposited onto dose test structures written at doses of (A) $180 \mu\text{A s cm}^{-2}$, (B) $580 \mu\text{A s cm}^{-2}$, and (C) $240 \mu\text{A s cm}^{-2}$. Underexposure prevents the pattern within the relatively high molecular weight PMMA from becoming soluble within the MIBK:IPA developer, while overexposure leads to the bowing of features at the point of overlap between neighbouring rectangles. A compromise between the two extremes occurs at a dose of $240 \mu\text{A s cm}^{-2}$, with the magnified view of the 500 nm wide bridge visible within panel (D) replicating the intended pattern while possessing a relatively uniform width.

uniform widths. Panel C represents a dose between the two extremes of $240 \mu\text{A s cm}^{-2}$, with panel D showing magnified view of the 500 nm wide bridge within the dose test. As visible from panels C and D the dose test shows little evidence of the overexposure with a uniform beam width with all of the features from the exposed dose test being replicated in the metal bilayer deposited. With the most accurate replication of the intended pattern, a dose of $240 \mu\text{A s cm}^{-2}$ was used for all subsequent writes performed with the $10 \mu\text{m}$ aperture.

To create structures suitable for releasing from the sacrificial SiO_2 layer and testing as resonators, the pattern within Figure 6.7 was created. Within the innermost $100 \mu\text{m}$ area exist a series of beams of 500 nm width and lengths of 2.9–29 μm between large squares of 10 by 10 μm . Taking a Young's Modulus of 950 GPa as found with superconducting resonators within Bautze *et al.* and a density of 3.52 g cm^{-3} , such geometries are designed to give in plane resonant frequencies of 10, 20, 50, 100, 200, 500, and 1000 MHz for the longest to shortest beams respectively [272]. These structures are then overlaid with 2 stages of large area contact strips as shown in panels B and C leading to large 100 by 100 μm^2 contact pads suitable for wire-bonding to, with the final structure being shown within panel D of Figure 6.7. In the interests of time, only the critical cantilevers were written with the $\sim 40 \text{ pA}$ current of the $10 \mu\text{m}$ aperture at a reduced step size of 0.006 μm . As the write-field increases to 200 μm the larger $\sim 170 \text{ pA}$ current of the 30 μm aperture was used at a beam step size of 0.01 μm , before increasing to the 6 nA current provided by the 120 μm aperture at a beam step size of 0.04 μm for the final 1000 μm write-field. For the final two non dimension-critical stages of this process an increased dose of $380 \mu\text{A s cm}^{-2}$ was observed to aid lift off. Write times for the 3 stages of writes are typically 2.5, 8.5, and 12 min. for the 100, 200, and 1000 μm write-fields respectively, reiterating the need for a significant current to write the large contacts in a reasonable time.

6.2.3 ICP

With the chemical inertness of diamond making it largely insusceptible to wet chemical etching, dry etching techniques utilising radical species activated by plasma discharge are typically utilised for device processing [274–277]. Upon the ionisation of oxygen or oxygen/argon chemistries, the combined effects of ion bombardment and the chemical

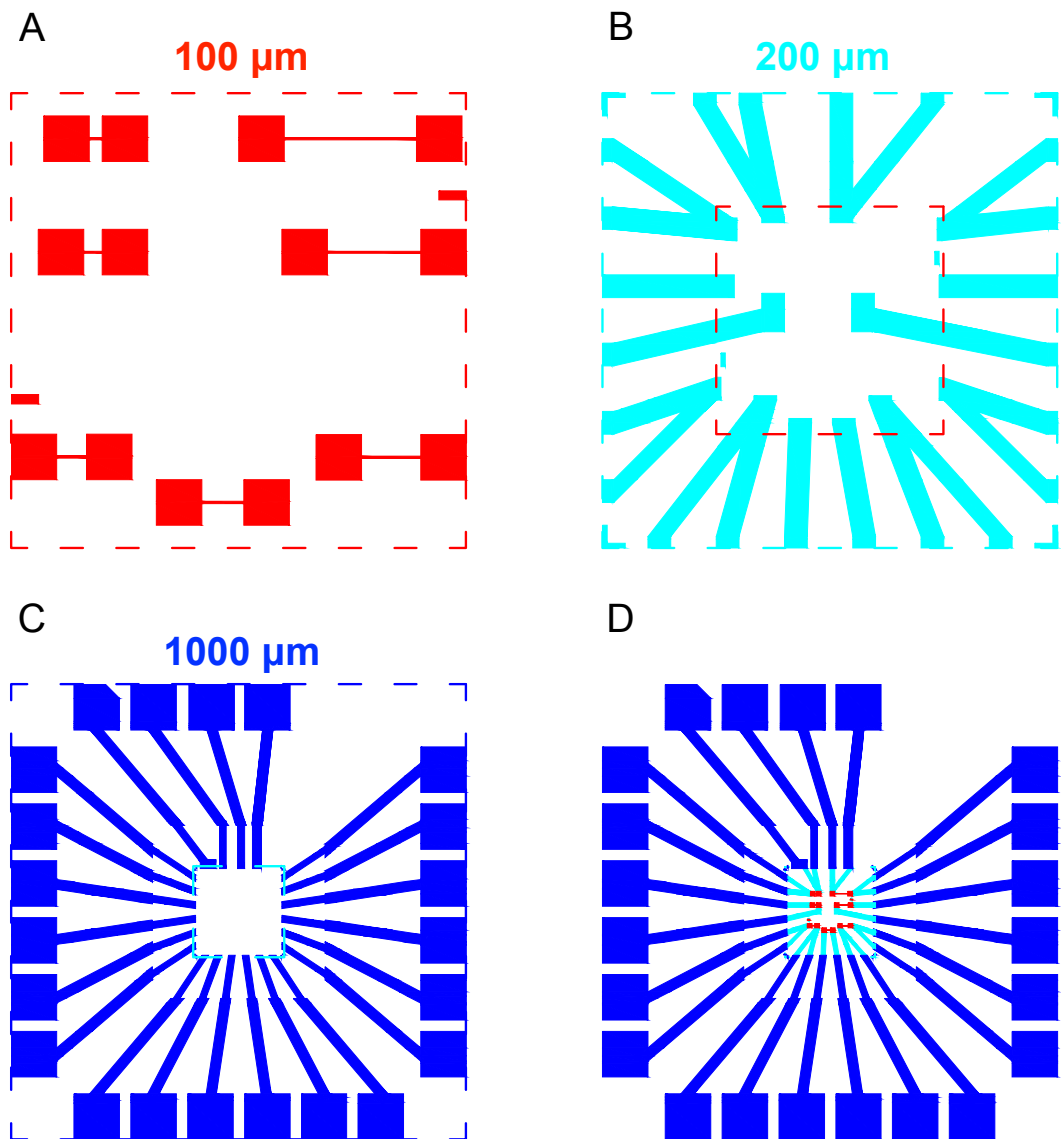


Figure 6.7: NEMS e-beam pattern consisting of (A) 100 μm , (B) 200 μm , (C) 1000 μm write-fields, all overlaid to result in the complete pattern within (D). The use of 3 differing sized write-fields allows the dimension critical bridges to be written with the relatively small ~ 40 pA current of the 10 μm aperture, before using the larger currents of the 20 and 120 pA apertures to write the high tolerance large area tracks and contact pads while minimising the duration of the write.

etching by reactive oxygen species lead to removal of carbon atoms from the diamond surface [274, 275, 278]. To produce smooth surfaces while etching at a sufficient rate diamond is typically etched at high plasma density, reasonably high substrate bias, and low pressure (< 10 mTorr) to prevent ion-ion and electron-ion recombination and ensure a strong ion bombardment [274, 278, 279]. Of such plasma assisted techniques including Electron Cyclotron Resonance (ECR) and Reactive Ion Etching (RIE), Inductively Coupled Plasma-Reactive Ion Etching (ICP RIE) is therefore typically favoured due to its ability to generate a high density plasma while allowing independent control the ion flux and energy allowing for anisotropic pattern transfer [277, 279–281].

When etching diamond with purely oxygen or oxygen/argon chemistries the significant physical etching component can result in the sputtering and redeposition of the hard mask material, which in combination with crystal defects can lead to masking with the formation of spire-like ‘whiskers’ and an increase in the surface roughness [276, 282, 283]. The columnar structure of polycrystalline film aids the formation of such features with dense ‘whisker’ formation observed along grain boundaries and attributed to non-diamond content acting as defects upon O_2/CF_4 etching [280, 281]. In contrast, H_2/Ar RIE has demonstrated preferential etching of grain boundary region believed to be due to the conductive sp^2 phase acting to locally enhance the local electric field and hence the mean energy of impinging ions [284]. To prevent the formation of such features and produce smooth diamond surfaces a small amount of fluorine containing gas is typically added to the etching process such as SF_6 , CHF_3 , or CF_4 [278, 281, 282]. As the aim of etching within the current work is to completely remove all uncovered diamond however, the resulting quality of the diamond surface is unimportant with the primary concerns the profile and smoothness of the sidewalls and the replication of the metallised pattern, allowing the trial of solely O_2 plasma etching.

Building upon the ICP-RIE recipe used by Soumen Mandal to create freestanding resonators within Bautze *et al.*, trial etches with a series of nickel etch masked NCD samples patterned with both photolithography and e-beam were first performed working with Georgina Klemencic of the Cardiff Diamond Foundry [272]. While not one of the more commonly used mask materials such as Al, Au, Si, and SiO_2 , Ni was initially chosen as an etch mask due to its use within Bautze *et al.* and it being the preferred etch mask within the ICP-RIE at Cardiff University [272, 278–280]. In preparation for

etching the samples were attached to 4" carrier wafers with fomblin oil to ensure good thermal contact between carrier and sample. Using an Oxford Instruments Plasmalab 100 ICP-RIE while maintaining an oxygen flow rate of 40 SCCM, pressure of 10 mTorr, 25 °C table temperature, and 30 mm table height the RIE and ICP powers were varied with the highest aspect ratio and smoothest sidewalls gained with a RIE power of 100 W and an ICP power of 1500 W. A reduced RIE power of 50 W was observed to lead to shallow sidewall profiles due to the more random nature of the ionic radicals with lower sample bias, while the suppression of physical sputtering increases the effect of the differing chemical etching rates of the randomly orientated crystals, increasing the sidewall roughness [277, 282, 285]. Meanwhile, increasing ion energies at a power of 300 W was observed to cause increased sputtering of the edges of the nickel mask due to the larger physical component to the etch, reducing the selectivity between mask and diamond and leading to worsening replication of the evaporated features [277]. Similarly, etch durations significantly longer (5 min.) than required to remove the uncovered diamond as suggested by *in-situ* 677 nm laser interferometry leads to increased concavity of the sidewalls due to sustained etching from randomly moving radicals [277]. As such RIE powers of 50 and 100 W were used for the etching of NEMS structures while ensuring that the plasma is extinguished soon after indication of the complete etching of the film.

To create NEMS patterns suitable for etching with ICP-RIE a metallic trilayer of 5 nm Ti/50 nm Au/10 nm Ni was deposited onto Piranha treated 'smooth' films using the pattern detailed within the previous subsection. The samples were lifted off with N-Methyl-2-Pyrrolidone (NMP) based 1165 remover on a hotplate at 75 °C and careful use of an ultrasonic bath, rinsed in acetone and IPA to remove traces of 1165 remover, and then left to evaporate naturally rather than N₂ blown try to protect the adhered metal. Careful use of Kapton tape was then used to fully remove stubborn excess metal. The samples were then once again attached to 4" carrier wafers through the use of Fomblin oil in preparation for O₂ plasma etching. Two samples were etched at 50 and 100 W RIE power, 1500 W ICP power, 40 SCCM O₂, 10 mTorr, 25 °C table temperature, and table height of 30 mm. Complete removal of the ~350 nm thick film occurred after 4 minutes 40 seconds and 3 minutes 40 seconds for the 50 and 100 W RIE power samples indicating etch rates of ~75 and ~95 nm min⁻¹ respectively, with

the plasma extinguished after a further 20 seconds to ensure complete etching over the entire sample while minimising lateral etching of the remaining features. The samples were then removed from the carrier and rinsed with IPA to remove traces of oil and left to dry naturally. Plan view SEM images of the 2.9 μm by 500 nm bridge within the 50 and 100 W RIE etched samples are shown in panels A and B of Figure 6.8, while panels C–F show tilted views of the respective etched structures.

For both samples it can be seen that the exposed pattern has been replicated well to first the metal, and then the underlying NCD upon etching due to the CMP polishing step. With the length of the beam being equal to the gap between two large contact pads the length of the bridge within panel A is shorter than intended by approximately 70 nm, while the width is 30 nm larger than designed. However, the uncertainties in the Young's Modulus of both the diamond and the resulting NCD/metal stack make such deviations from the designed dimensions tolerable. With the resonant frequency of bridge proportional to the width of the beam when resonating in the plane of the film the aspect ratio and sidewall roughness of the etch is of greater importance. For the 50 W RIE etched sample an average sidewall width of 61 nm is obtained, suggesting an aspect ratio to the etch of $\sim 6:1$. In comparison, the use of a higher 100 W RIE power leads to a larger flow of ionic radicals normal to the sample and a more physical component to the etching yielding a steeper etch with an average sidewall width of 39 nm as shown in panel B, suggesting an aspect ratio of $\sim 9:1$ [277, 285]. This difference in anisotropy is reiterated within the tilted views of panels C–F with both a steeper and smoother sidewall obtained upon minimising the affect of the differing etch rates of the diamond crystallographic planes through etching at increased RIE powers, with panel E highlighting one such difficult to etch grain remaining after etching through the majority of the film [282, 286]. As such, an RIE powers of 100 W was deemed the most suitable for further device construction.

Upon completing the etching process the Ni mask was then removed while leaving the gold intact through immersion and gentle agitation in a 60% w/v ferric chloride solution (FeCl_3) for 2 minutes [287]. Following 1 minute of gentle agitation in DI H_2O and an IPA rinse the samples were then left to dry naturally. Trials performed on etched diamond with a photolithography defined 70 nm Ni mask indicated complete removal of the Ni mask as visible by optical micrography after 1 minute, indicating

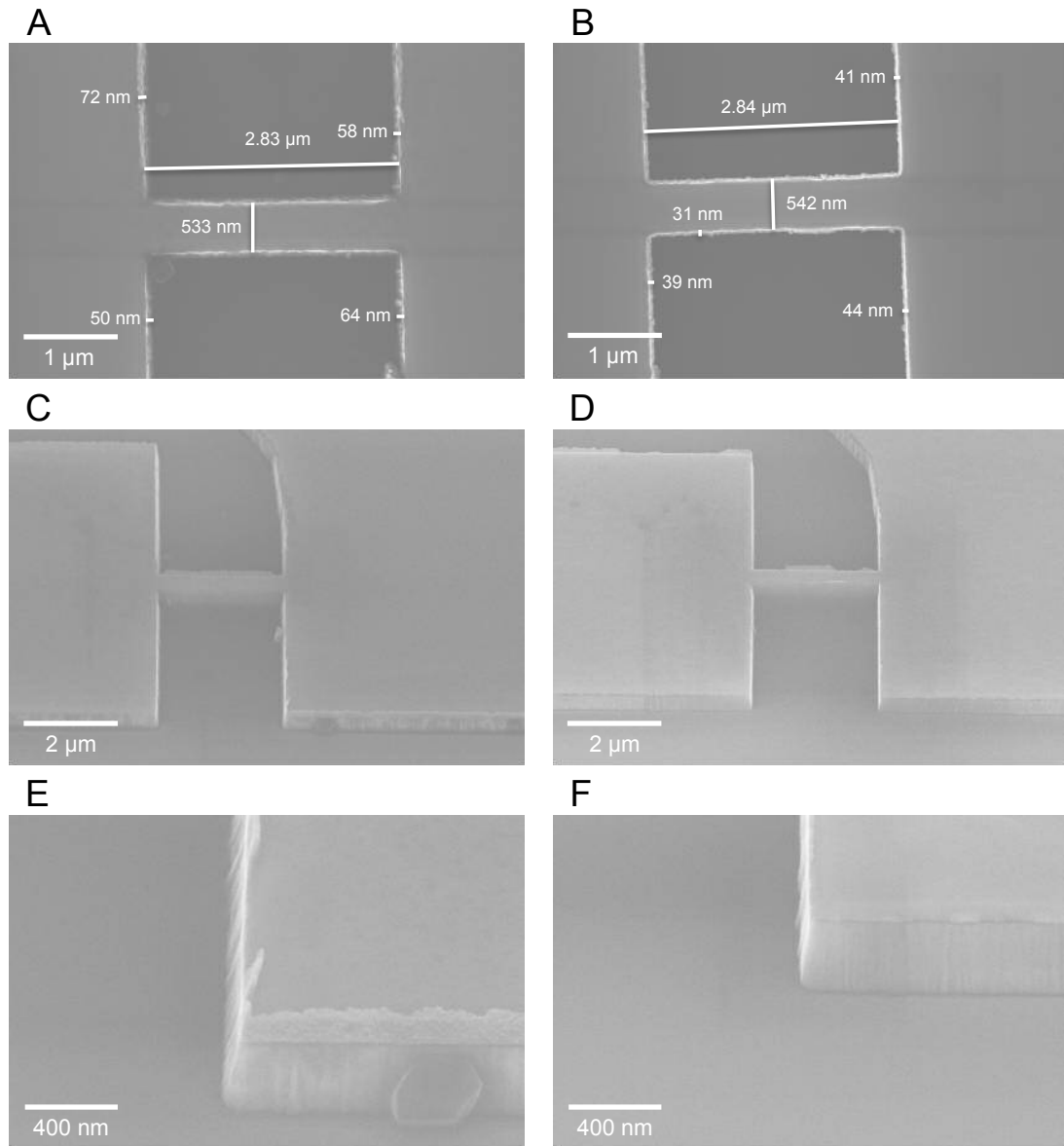


Figure 6.8: Metallised NEMS samples etched with ICP-RIE at (A) 50 W and (B) 100 W RIE power, with panels (C–D) showing tilted views of the respective features and panels (E–F) showing magnified views of the sidewall profile. Upon an increase in the bias the reduction in randomly moving ionic radicals and stronger bombardment lead to a higher aspect ratio of $\sim 9:1$ with smoother sidewall profiles. The reduced physical component to the etching for the 50 W RIE power sample is reiterated by the visibility of a crystal of difficult to etch orientation within panel E.

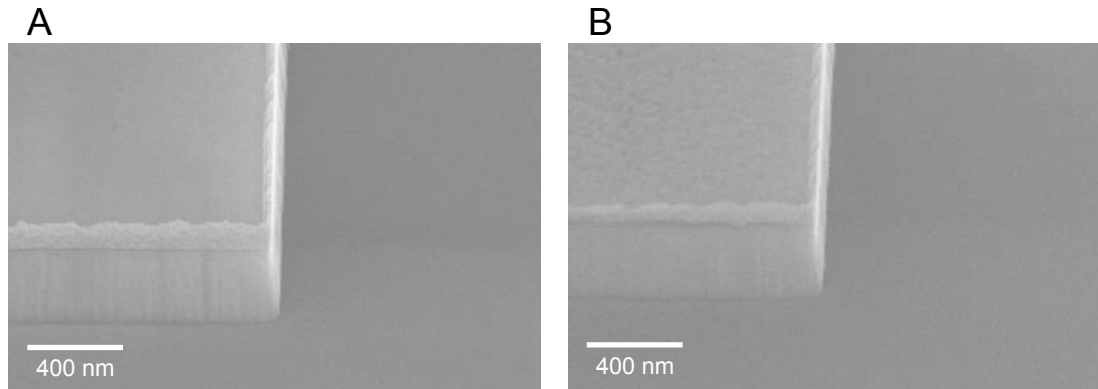


Figure 6.9: Sample etched at 100 W RIE power (A) before, and (B) after FeCl_3 immersion to remove nickel etch mask. Smooth surface of the deposited nickel mask results in the appearance of the granular gold conductor, with a noticeable reduction in thickness as indicated by the less prominent ‘ears’ remaining from the lift-off of excess metal.

2 minutes should be sufficient for the thinner 20 nm Ni mask used for the etching of NEMS structures. Figure 6.9 shows the NEMS sample etched at 100 W RIE power before (A), and (B) after removal of the Ni etch mask. As visible within the figure the smooth surface of the deposited Ni mask is replaced by the granular gold surface, along with a thickness reduction noticeable by the smaller ‘ears’ remaining from lift-off.

6.2.4 HF

The final stage of construction is to under-etch the 500 nm SiO_2 with hydrofluoric acid to leave freestanding narrow bridges between the wider support anchors. However, should the samples be immersed in hydrofluoric acid liquid the large surface tension of the subsequent DI rinse will pull the bridges down to the Si substrate, with static friction or ‘stiction’ then preventing separation and free movement upon drying [288]. To prevent the need for additional process steps to mitigate the effects of surface tension or removal of the rinse in a non-liquid state, HF vapour allows the quasi-dry etching of SiO_2 without the requirement of a rinsing step [289].

For SiO_2 held in close proximity above hydrofluoric acid it has been observed that the rate of etching is close to that within the acid [290]. The hydrofluoric acid will naturally evaporate and if the combination of the partial pressures of the Hydrogen Fluoride (HF), H_2O , and reaction product constituents be sufficiently large that the

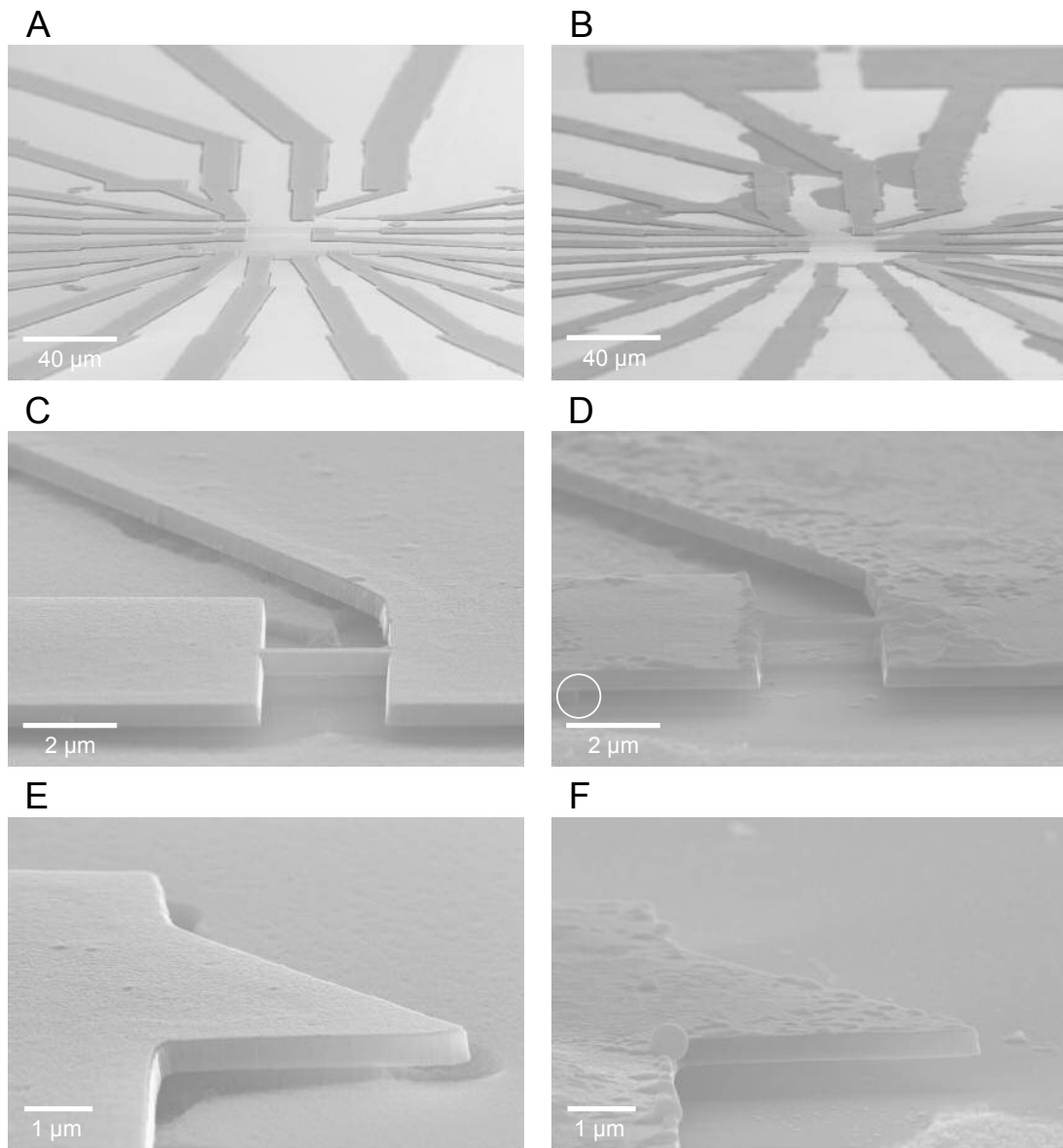


Figure 6.10: Hydrofluoric acid etching of SiO_2 to release NEMS bridges with durations of (A) 20 minutes and (B) 30 minutes, with panels (C–D) showing views of one resonating bridge, and panels (E–F) showing magnified views of the undercut. Etching initiates at the diamond structures and progresses outwards with increasing duration. Both samples show over-etching with the SiO_2 only visible within the circle in panel D to the far left of the leftmost anchor support, reiterated by the overhanging features of panels E and F.

rate of condensation is larger than the rate of evaporation, a condensed layer will form on the SiO₂ surface [290]. In an identical mechanism to that of liquid hydrofluoric acid, hydration of the SiO₂ surface by absorbed water occurs leading to each surface Si atom being attached to two hydroxyl groups and to the bulk through two O–SiH₃ siloxane groups [288, 290, 291]. Upon etching the Si–O bonds within the hydroxyl groups are then attacked with the transfer of a H atom from a H₂O molecule to the surface hydroxyl to form water, followed by subsequent H transfer from the HF to the H₂O molecule and the formation of a Si–F bond. This Si–O dissociation process continues for the remaining three Si–O bonds with H₂O acting as the catalyst until the liberation of a SiF₄ species from the surface [291]. With water therefore acting as the medium, initiator, catalyst, as well as byproduct for the reaction the rate of etching can then be controlled through varying the temperature of the SiO₂ and hence the absorbed water, with higher temperatures leading to a decrease in the absorbed water and a corresponding reduction in the etch rate [288]. As a result etch rates are expected to peak at 20–30 °C before rapidly falling to zero at temperatures of ~40 °C dependant on the production method of the SiO₂ [290].

Using an Idonus hydrogen fluoride Vapour Phase Etcher (VPE) a series of samples were etched by Soumen Mandal and Georgina Klemencic of the Cardiff Diamond Foundry. After attaching to a 4" carrier wafer with double sided Kapton tape, samples were suspended upside down above a 30% HF solution for 20, 25, and 30 minutes while maintaining a carrier temperature of 35 °C. Tilted SEM overviews of the 20 and 30 minute etched samples are then shown in panels A and B of Figure 6.10, with panels C and D showing views of the 2.9 μm by 500 nm bridges within the respective etches, and finally panels E and F showing magnified views of the under-etching. As visible from panels A and B it can be seen that etching initiates at the edges of the diamond structures and proceeds outwards with continued exposure to hydrofluoric acid vapour, presumably due to the comparatively rough diamond structures acting as nucleation sites for condensate formation over the smoother SiO₂ surface [290]. Both structures appear to be severely over-etched with the sidewall of the SiO₂ not visible underneath the anchor support of the resonator within panel C, and visible within the circle to the very far left of the anchor within panel D. Should such devices be used a significant dampening can be expected due to resonance of a sizeable portion of the anchors,

hampering the study of the effect on the surface roughness on the Q factor. This over-etching is reiterated in panels E and F with the overhanging features left completely unsupported. Therefore shorter etch durations are required to release the structure and maintain adequate support of the anchor, while increasing the temperature of the carrier will facilitate finer reproducibility due to the expected reduction in etch rate.

6.2.5 Condensed Recipe

With the successful manufacturing of NEMS devices the condensed recipe beginning after the growth of a ~ 350 nm thick NCD film upon a 2" FZ Si wafer with 500 nm thick sacrificial SiO_2 layer is as follows;

1. CMP polish to < 3 nm RMS, immediately SC-1 30% H_2O_2 : NH_4OH : DI H_2O (1:1:5) clean for 10 minutes at 75 °C to remove slurry, rinse with DI H_2O , and spin dry.
2. 30% hydrofluoric acid etch to remove remaining tightly bound silica slurry and DI rinse.
3. Piranha H_2O_2 : H_2SO_4 (1:3) oxidise for 10 minutes while leaving the exothermic solution to self-heat, and DI rinse.
4. Dice up wafer to 1 by 1 cm^2 pieces and select most uniform pieces from central 1" for device fabrication.
5. Clean organic residue and dicing debris for 5 minutes each in methanol, acetone, and IPA, all heated to 75 °C, and N_2 blow dry.
6. Spin coat sample with PMMA 950 A4 at 4000 rpm for 30 seconds, 4000 rpm s^{-1} acceleration, and bake on hotplate at 180 °C for 5 minutes. Results in resist thickness of ~ 200 nm.
7. E-beam expose sequence of 3 patterns within Figure 6.7 using;
 - (a) $100 \times 100 \mu\text{m}$ write field, $10 \mu\text{m}$ aperture, $\sim 40 \mu\text{A}$ current, $240 \mu\text{A s cm}^{-2}$ dose, $0.006 \mu\text{m}$ step size.
 - (b) $200 \times 200 \mu\text{m}$ write field, $30 \mu\text{m}$ aperture, $\sim 170 \mu\text{A}$ current, $380 \mu\text{A s cm}^{-2}$ dose, $0.01 \mu\text{m}$ step size.

(c) $1000 \times 1000 \mu\text{m}$ write field, $120 \mu\text{m}$ aperture, $\sim 6 \text{ nA}$ current, $380 \mu\text{A s cm}^{-2}$ dose, $0.04 \mu\text{m}$ step size.

8. Develop with MIBK:IPA (1:3) for 60 seconds, rinse in IPA for 60 seconds, and N_2 blow dry.
9. PVD deposit $5 \text{ nm Ti}/50 \text{ nm Au}/10 \text{ nm Ni}$ trilayer, Ti to improve adhesion, Au to conduct current, and Ni to act as hard metal mask upon oxygen etching.
10. Lift off with 1165 Remover heated to $75 \text{ }^\circ\text{C}$, short durations in ultrasonic bath for more stubborn metal, and rinse with acetone and IPA before leaving to dry naturally to prevent damage to adhered metal. Use of double sided kapton tape may be required to completely remove all excess metal.
11. Use Fomblin oil to attach sample to carrier wafer and ICP-RIE etch at 1500 W ICP power, 100 W RIE power, 40 SCCM O_2 , 10 mTorr pressure, $25 \text{ }^\circ\text{C}$ table temperature, and 30 mm table height. Once laser interferometry has indicated complete removal of NCD continue for 20 seconds to ensure complete etching across non-uniform sample.
12. Rinse with IPA to remove traces of Fomblin oil and leave to dry naturally.
13. Agitate in 60% w/v ferric chloride solution (FeCl_3) for 2 minutes to remove Ni mask, gently agitate in 1 minute of DI H_2O , and IPA rinse. Leave to dry naturally.
14. Attach to 4" carrier wafer with kapton tape and hydrofluoric acid isotropic vapour etch for 20 minutes at a carrier temp of $35 \text{ }^\circ\text{C}$ to etch SiO_2 under bridges.

6.3 NEMS Testing

To test the resulting NEMS structures the sample subjected to hydrofluoric acid vapour etching for 20 minutes was attached to the aluminium plate sample holder shown in panel B of Figure 6.11 with GE varnish. Aluminium wire-bonds were then made between contact pads of the $20.5 \mu\text{m}$ by 500 nm resonator, shown in Figure 6.11A, and the gold coated launch pads connected to the SMA jacks at the edge of aluminium plate. Assuming a reduced Young's Modulus of 950 GPa and a density of 3.52 g cm^{-3} a resonant frequency of 20.1 MHz is expected for the device when resonating in the

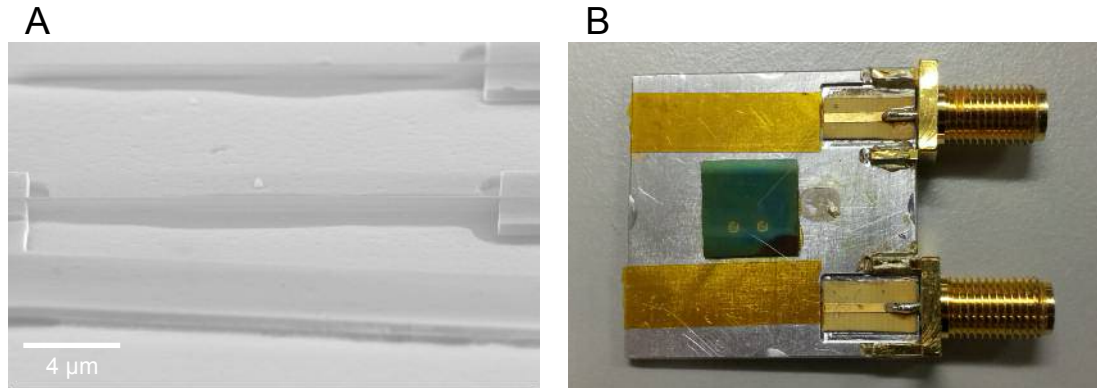
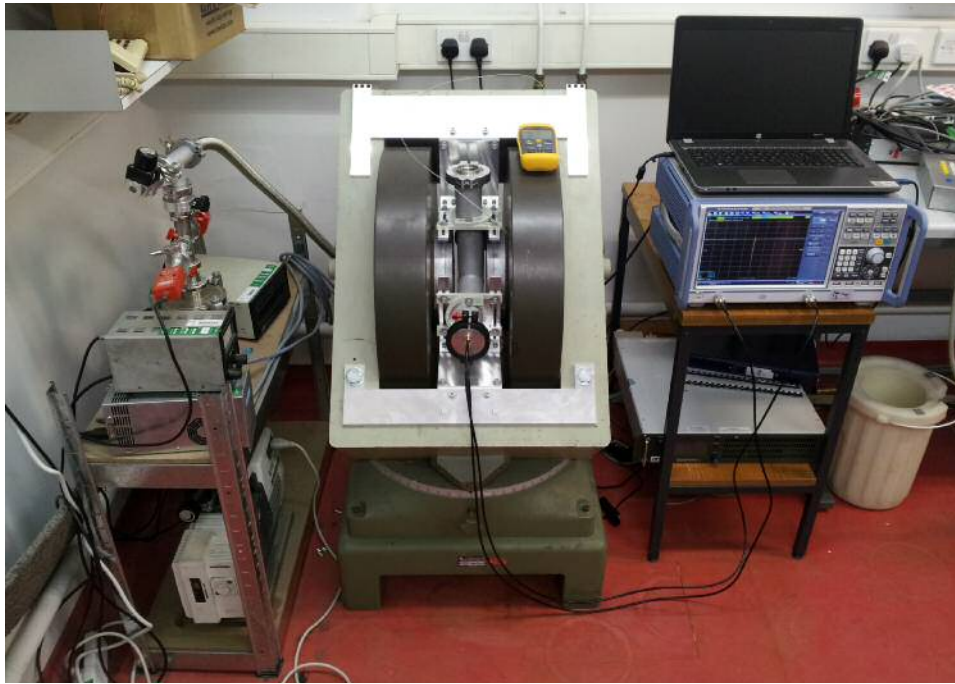


Figure 6.11: (A) Tested resonator and (B) NEMS sample holder. Sample bonded to aluminium plate with GE varnish with aluminium wire-bonds made between selected resonator and gold coated launch pads at edge of holder. Kapton tape used to prevent grounding of wire-bonds to aluminium plate when covering distance between launch pads and sample.

plane of the film. With size constraints limiting the separation between SMA jacks and preventing the placement of the sample between launch pads, kapton tape was used to ensure the relatively long wire-bonds covering the distance between sample and launch pad were not grounded to the aluminium plate. A resistance between the two launch pads was then measured to be $\sim 160 \Omega$ in comparison to the $\sim 150 \Omega$ measured from contact pad to contact pad for each of the resonators.

For the purposes of actuating the NEMS resonators magneto-motively, a custom made aluminium vacuum chamber was manufactured and placed within a Varian V7800 magnet equipped with 9" poles through the use of adjustable aluminium mounts, as shown in panels A and B of Figure 6.12. Upon being powered by a Adaptive Power Systems APS DDP 70-75 power supply a magnetic field of 0.81 T was achievable with a maximum deliverable current of 70 A. The sample holder was then attached to a KF50 flange with SMA feedthroughs through the use of two lengths of non-magnet RG402 rigid coaxial cable and fed into the middle of the vacuum chamber, as shown in the section view of Figure 6.12B, with the normal to the sample aligned perpendicular to the magnetic field to resonate the device in plane and minimise clamping losses. The chamber was then sealed with a Viton o-ring trapped within a polymer carrier and polymer clamp to prevent ground loops between the SMA feedthroughs and the vacuum chamber/magnet setup, and evacuated to pressures of 10^{-5} mbar through the

A



B

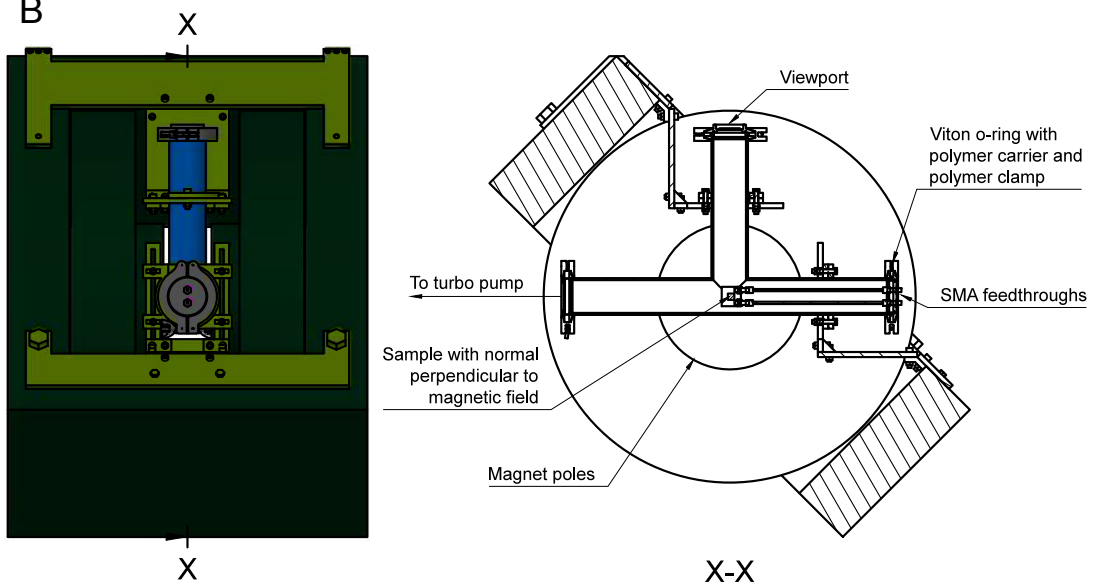


Figure 6.12: (A) NEMS magneto-motive testing setup and (B) cross section of magnet detailing sample positioning. Setup consists of a custom-made vacuum chamber positioned within the poles of a magnet, and evacuated through the use of the turbo-molecular pump and rotary pump to the left of the image. To the right of the image is the laptop and VNA automating the S_{21} measurement. Panel B shows the sample with normal orientated perpendicular to the magnetic field through the use of rigid coaxial, with SMA feedthroughs used to connect sample to VNA and Viton o-rings with polymer carrier and clamp used to isolate the feedthroughs from the magnet/chamber.

use of a turbo-molecular pump to minimise hydrodynamic loading and hence maximise contributions to loss from the surface roughness [6]. Finally, a Rohde & Schwarz ZND Vector Network Analyser (VNA) was calibrated and connected to the SMA feedthroughs with a laptop running a Python script within the R&S Forum scripting tool written to allow the automation of the measurement of the transmission or forward voltage gain, S_{21} . Upon reaching resonance a drop in transmission is expected due to the device dissipating energy from clamping losses and surface roughness effects.

Setting the static magnetic field to an initial value of 0.58 T the AC signal was swept between 15 and 25 MHz at bandwidth of 1000 Hz, 10 Hz resolution, and power of -20 dBm, with no clear dip in S_{21} observed. With Bautze *et al.* reporting fQ products of 4×10^{11} Hz at 10 MHz for similarly constructed resonators, albeit on rough NCD, a similar fQ product for the device constructed above would yield a width of resonance, f , of 1010 Hz [272]. Meanwhile, fQ products of 10^{12} and 10^{13} Hz would yield f values of 404 and 40.4 Hz respectively, greater than the resolution of the VNA frequency sweeps. Scans were then repeated at 0.81 T and -10 dBm with no discernible peak from resonance visible above the noise of the setup and an average loss in transmission of 8.29 dB.

With the VNA used during these initial trials the input power was limited to no less than -20 dBm, producing currents of 250 μ A for a cantilever resistance of 160 Ω . Upon the application of a 1 T field such a current would then result in a Lorentz force of 145 μ N m^{-1} along the 20.5 μ m long beam for a total force of 3 nN. Comparing to the similarly sized, albeit superconducting, resonators constructed within Bautze *et al.*, the authors observed the change in resonant amplitude upon increasing the input power past the critical current, J_c , of the boron doped material [272]. Taking a value of J_c of the order of 1×10^7 A m^{-2} as measured from superconducting films at the Cardiff Diamond Foundry, a width of 480 nm, and a thickness of 300 nm currents of the order of μ As are suggested. Combining with a field of 1 T as used by the authors, force per unit lengths of μ N m^{-1} are attained to provide a total force on the 30 μ m long beam of tens of pN. Such values are less than the forces generated on the beams within this thesis, tentatively suggesting that actuation may not be the reason for the lack of resonance observed. Subsequent trials with input powers of -20 dBm and -10 dBm at kHz frequencies due to the use of copper wire however caused peeling off of the 50 nm

Au layer from the NCD beam, suggesting that such currents are unsuitable for all but short measurements and require attenuation.

As superconducting magnets capable of reaching the magnetic fields of 1–16 T typically required to provide an adequate Lorentz force for mechanical actuation the magneto-motive technique is typically used for small devices operating at high frequencies and/or cryogenic temperatures [6, 9]. With this use of cryogenic temperatures, attenuators and amplifiers at successive temperature stages are typically used to reduce the noise temperature and amplify the signal from the sample [8, 18, 272, 292]. For superconducting double clamped NCD resonators Bautze *et al.* utilised two stages for a total 40 dB of attenuation and an amplifier of 50 dB gain resulting in 0.5 dB of loss in transmission upon resonance at a 1 T magnetic field [272]. Similarly Huang *et al.* utilised a combined 75 dB of amplification while using magnetic fields of 2–8 T and sitting at 4.2 K, with further increases in sensitivity gained through driving two balanced parallel SiC cantilevers 180° out of phase minimising the background and stray coupling between ports [18, 293]. However, time constraints limited the use of such techniques to improve the sensitivity within the current study. Tilted SEM imaging would reveal if the device is still intact or whether it had been destroyed from the relatively large applied powers, and hence whether the problem is the transduction or sensing of resonance. Should the device have collapsed from being excessively driven, amplification stages can then be investigated to improve the sensitivity of the measurement technique, whereas an intact device would warrant the use of superconducting magnets to increase the applied field and hence Lorentz force on resonator. Once a dip in transmission is observed from resonance the recipe developed could be used to construct similar bridges out of rough NCD films, permitting the completion of the study of the effect of roughness on the Q factor.

6.4 Conclusion

A process has been developed to create free-standing 500 nm wide and 2.9–29 μm resonant bridges from CMP polished NCD, with the low roughness surface allowing close replication of the desired pattern with smooth sidewalls. Consisting of e-beam lithography, metallisation, ICP-RIE etching, and HF vapour etching, attempts have been

made to drive the resulting structures magneto-motively within a custom made vacuum chamber to no avail. The incorporation of amplification stages and the use of the balanced bridge technique should facilitate the sensing of resonance, while the use of superconducting magnets should increase the amplitude of resonance and ease detection. Once resonance has been detected the developed recipe can be used to construct a similar series of bridges from ‘rough’ as-grown NCD allowing the study of the effect of the surface roughness on the Q factor of NCD NEMS.

Chapter 7

Conclusions and Future Work

Within this thesis two aspects of the use of NCD for NEMS has been studied, namely the characterisation of the initial stages of film growth and the removal of the considerable roughness, culminating in the construction of resonating structures from smooth NCD films. Chapter 4 details the modelling of the initial stages of the growth of NCD from seeds to coalesced film with the technique of Spectroscopic Ellipsometry (SE). Unlike previous attempts at SE of seeded Si in which the level of damage from mechanical scratching prevented the observance of residual diamond, spectra of the mono-dispersed diamond seeded Si indicated a 4 nm porous diamond layer atop a thin native oxide layer as a result of incomplete oxidation of the Si surface [137]. Upon being subjected to growth conditions the fitting procedure indicated the removal of the native oxide layer and the formation of a carbide layer 5–9 nm in thickness in agreement with *in-situ* XPS studies, along with a parabolic reduction in the void content of the diamond layer indicative of lateral growth of the Volmer-Weber islands [119–121]. After ~10 minutes of growth the thickness of the bulk layer begins to increase with a surface roughness layer required to adequately model the spectra indicative of the coalescence of the individual islands. Continued growth then leads to an increasing surface roughness as a result of the columnar nature of NCD growth, with the indicated thickness of the surface layer correlating well with AFM deduced RMS roughness values when corrected using a factor of 1.5 as reported for SE and AFM studies on hydrogenated amorphous Si [172]. Raman spectra meanwhile indicate the presence of amorphous SiC along with the appearance of a peak attributable to transpolyacetylene after coalescence and the formation of grain boundaries between crystallites. Peaks in both the SE indicated non-diamond carbon

content and G band Raman peak follow shortly, albeit slightly shifted from one another due to sample non-uniformity, reiterating the significant increase in the non-diamond carbon content shortly after coalescence and the formation of grain boundaries. Similar peaks have been reported previously by *in-situ* SE studies of growth from Si micro-scratched with diamond grit, with height and final value dependant on the temperature during deposition and the methane content of the feed gas [96]. Thus SE has been demonstrated to be a powerful technique in the characterisation of NCD from mono-dispersed diamond seeds, capable of quantitative estimation of the non-diamond carbon content from seeds to coalesced film.

As SE measures the change in polarisation between two perpendicular components of light, the technique is capable of *in-situ* studies of CVD growth through the highly energetic and reactive plasma without the requirement for internally mounted equipment. The next stage of the work is to therefore install the tool upon a CVD reactor at the Cardiff Diamond Foundry. Such measurements would allow the near continuous capture of spectra over an entire growth run, preventing the need to create multiple samples with differing growth duration and producing a number of sample points unfeasible with *ex-situ* characterisation. The peak observed in the non-diamond carbon content within Figure 4.22 could then be more conclusively attributed to material within grain boundaries, while the short duration between igniting the plasma and coalesce could be more accurately studied. In addition, critical point analysis of the $E_0'-E_1$ feature of Si would allow for determination of the true surface temperature of the substrate and comparison to pyrometry measured values [96]. Initial attempts at installing the M2000-D SE upon the Seki AX6500 reactor within Figure 3.7 however were unsuccessful, with the angle of incidence (28°) too far away from the Brewster angle to obtain a sufficient distinction between r_p and r_s [66]. The recent installation of a Carat Systems CTS6U at the Foundry with viewports at a $65-70^\circ$ angle of incidence should be more conducive to ellipsometry and allow a more comprehensive study of the initial stages of NCD film growth.

Progressing onto post growth processing, Chapter 5 sought to reduce the significant roughness of NCD films arising from the competitive overgrowth of crystallites. Through adaption of the IC fabrication technique of Chemical Mechanical Polishing (CMP) with an alkaline colloidal silica polishing fluid and polymer polishing pad, the large and

potentially shattering pressures of mechanical polishing are avoided while the flexible pad is able to conform to the bow of the sample and polish the film uniformly. As a result, a reduction in roughness from 18.3 nm RMS to 1.7 nm RMS over a $25 \mu\text{m}^2$ area was observed after 4 hours for ~ 380 nm thick films. Through performing XPS a model was then proposed consisting of alkaline oxidation and binding of silica particles within the slurry, followed by shearing away of the particle and attached carbon atom due to a passing asperity of the roughened polishing pad. Extending to single crystal samples, scribe marks present after mechanical polishing of $\{100\}$ and $\{111\}$ orientated samples have been removed, with roughness values along $5 \mu\text{m}$ line traces perpendicular to the grooves reduced from 0.92 to 0.23 nm RMS and 0.31 and 0.09 nm RMS respectively.

With the chemical/mechanical synergy to the polishing mechanism, variation of the properties of the abrasive particles, slurry chemistry, pad and processing parameters are all expected to affect the removal rate and surface finish attainable. While silica based CMP was initially predominantly used for the planarisation of SiO_2 , the technique has been extended to the polishing of metal interconnects, ceramics, and insulators [217]. With this extension came the development of additional slurries utilising abrasives including ceria (cerium oxide) and alumina (aluminium oxide) of differing hardness and with different atomic interaction between abrasive and wafer surface. The next stage in the adaption of the technique to diamond is to therefore attempt polishing with other commonly used slurries within the industry, initially without modification from the likely optimised pH to prevent agglomeration of the abrasive particles. Dependant on the findings the chemical makeup of the slurry can then be altered to counteract the oxidant in an attempt to elucidate on and either confirm or deny the polishing mechanism proposed within this thesis and by molecular dynamic simulations, while alterations in the particle size will then reveal the significance of the mechanical component of removal [19, 217]. With the importance of the condition and stage of life of the pad however, unless significant and conclusive differences are observed between slurries their effect on the polishing rate and surface finish cannot be attributed to the slurry alone [229]. The polishing pad can then be altered in an attempt to further optimise polishing and minimise delamination to improve the yield of polished NCD films.

Using the adapted polishing technique a series of doubly clamped NEMS structures were then created within Chapter 6 from smooth NCD stock. The optimisation of the

steps involved in the process of e-beam lithography, metallisation, ICP-RIE etching, and HF vapour etching are discussed, with the smooth films leading to the high aspect ratio, free-standing 500 nm wide bridges shown within Figure 6.10. Testing of a device with an expected resonant frequency of 20.1 MHz however was inconclusive, with the low 0.7 T magnetic field or the lack of amplification of the signal from the device believed to be responsible for the lack of observable resonance. To investigate whether the issue is with resonance or detection the sample should first be imaged: should the large -20 dBm input powers have caused stiction between the bridge and substrate or destruction, amplification stages could be used to increase the signal from subsequent samples. Alternatively, an intact device could suggest poor actuation and warrant the use of a higher magnetic field. Once resonance is observed similar structures can be made from unpolished diamond to study the effect of surface roughness on the Q factor, and hence the fQ product. Further increases in Q factor can then be gained through implementing geometries such as the ‘free-free’ beam as described within Section 6.1 in which 4 flexural supports are placed at nodal points along the beam to prevent the loss of strain to the anchor supports [260].

It is therefore hoped that the work presented within Chapter 4 of this thesis will pave the way for a more comprehensive *in-situ* spectroscopic ellipsometry study of the initial stages of diamond growth to optimise deposition and the quality of the resulting films. The benefits of the adaption of CMP are more immediately apparent, with the processing of previously difficult to polish highly bowed thin film samples beneficial in applications from thermal management to tribological coatings, and shown to aid nano-fabrication of devices within Figure 6.10. In tandem, both aspects of the work should aid in the increasing of the fQ product of diamond NEMS, with the creation of the nano-fabrication recipe within Chapter 6 suggesting that devices constructed from smooth NCD films will be created at Cardiff Diamond Foundry within the near future.

Bibliography

- ¹A. Gupta, D. Akin, and R. Bashir, “Single virus particle mass detection using microresonators with nanoscale thickness”, *Applied Physics Letters* **84**, 1976–1978 (2004).
- ²J. G. Rodriguez-Madrid, G. F. Iriarte, J. Pedros, O. A. Williams, D. Brink, and F. Calle, “Super-high-frequency SAW resonators on AlN/diamond”, *IEEE Electron Device Letters* **33**, 495–497 (2012).
- ³D. Scansen, *How MEMS enable smartphone features*, <http://www.engineering.com/ElectronicsDesign/ElectronicsDesignArticles/ArticleID/6124/How-MEMS-Enable-Smartphone-Features.aspx>, Accessed: 16/09/2016.
- ⁴J. K., K. Kim, and Z. A., “An atomic-resolution nanomechanical mass sensor”, *Nat Nano* **3**, 533–537 (2008).
- ⁵C. T. C. Nguyen, “MEMS technology for timing and frequency control”, *IEEE Transactions on Ultrasonics, Ferroelectrics, and Frequency Control* **54**, 251–270 (2007).
- ⁶M. Imboden and P. Mohanty, “Dissipation in nanoelectromechanical systems”, *Physics Reports* **534**, 89–146 (2014).
- ⁷L. Sekaric, J. M. Parpia, H. G. Craighead, T. Feygelson, B. H. Houston, and J. E. Butler, “Nanomechanical resonant structures in nanocrystalline diamond”, *Applied Physics Letters* **81**, 4455–4457 (2002).
- ⁸A. Gaidarzhy, M. Imboden, P. Mohanty, J. Rankin, and B. W. Sheldon, “High quality factor gigahertz frequencies in nanomechanical diamond resonators”, *Applied Physics Letters* **91**, 203503 (2007) 10.1063/1.2804573.
- ⁹P. Mohanty and M. Imboden, “Diamond nano-electromechanical systems”, in *Nanodiamond*, edited by O. A. Williams (The Royal Society of Chemistry, 2014) Chap. 17, pp. 411–447.
- ¹⁰Y. Tao, J. M. Boss, B. A. Moores, and C. L. Degen, “Single-crystal diamond nanomechanical resonators with quality factors exceeding one million”, *Nat Commun* **5** (2014).
- ¹¹Y. Tao and C. Degen, “Facile fabrication of single-crystal-diamond nanostructures with ultrahigh aspect ratio”, *Advanced Materials* **25**, 3962–3967 (2013).
- ¹²M. J. Verstraete and J.-C. Charlier, “Why is iridium the best substrate for single crystal diamond growth?”, *Applied Physics Letters* **86**, 191917 (2005) 10.1063/1.1922571.
- ¹³X. Jiang, K. Schiffmann, and C.-P. Klages, “Nucleation and initial growth phase of diamond thin films on (100) silicon”, *Phys. Rev. B* **50**, 8402–8410 (1994).
- ¹⁴O. A. Williams, “Nanocrystalline diamond”, *Diamond and Related Materials* **20**, 621–640 (2011).
- ¹⁵O. A. Williams, A. Kriele, J. Hees, M. Wolfer, W. Müller-Sebert, and C. E. Nebel, “High Young’s modulus in ultra thin nanocrystalline diamond”, *Chemical Physics Letters* **495**, 84–89 (2010).

- ¹⁶M. Imboden, P. Mohanty, A. Gaidarzhy, J. Rankin, and B. W. Sheldon, “Scaling of dissipation in megahertz-range micromechanical diamond oscillators”, *Applied Physics Letters* **90**, 173502 (2007).
- ¹⁷K. L. Ekinici and M. L. Roukes, “Nanoelectromechanical systems”, *Review of Scientific Instruments* **76**, 061101 (2005) 10.1063/1.1927327.
- ¹⁸X. M. H. Huang, X. L. Feng, C. A. Zorman, M. Mehregany, and M. L. Roukes, “VHF, UHF and microwave frequency nanomechanical resonators”, *New Journal of Physics* **7**, 247 (2005).
- ¹⁹A. Peguiron, G. Moras, M. Walter, H. Uetsuka, L. Pastewka, and M. Moseler, “Activation and mechanochemical breaking of C–C bonds initiate wear of diamond (110) surfaces in contact with silica”, *Carbon* **98**, 474–483 (2016).
- ²⁰H. O. Pierson, “The element carbon”, in *Handbook of carbon, graphite, diamonds and fullerenes* (William Andrew Publishing, Oxford, 1993) Chap. 2, pp. 11–42.
- ²¹*Hybridization*, <http://www.chemistrysources.com/2013/11/hybridization/>, Accessed: 04/09/2016.
- ²²G. Davies, “Basic properties of diamond: phonon spectra, thermal properties, band structure”, in *CVD diamond for electronic devices and sensors* (John Wiley & Sons, Ltd, 2009), pp. 1–28.
- ²³A. Ramdas, “Raman, brillouin and infrared spectroscopy of phonons in conventional diamond”, in *Properties, growth and applications of diamond*, edited by A. Neves and M. Nazaré, EMIS datareviews series (Institution of Electrical Engineers, 2001) Chap. A1.1, pp. 3–13.
- ²⁴M. A. Quiroz and E. R. Bandala, “Types of conducting diamond materials and their properties”, in *Synthetic diamond films* (John Wiley & Sons, Inc., 2011), pp. 57–75.
- ²⁵Y. Chen and L. Zhang, “Understanding the material removal mechanisms”, in *Polishing of diamond materials* (Springer, London, 2013), pp. 11–23.
- ²⁶V. V. S. S. Srikanth and X. Jiang, “Synthesis of diamond films”, in *Synthetic diamond films* (John Wiley & Sons, Inc., 2011), pp. 21–55.
- ²⁷C. Klein and B. Dutrow, *Manual of mineral science*, Manual of Mineralogy (John Wiley & Sons, 2007).
- ²⁸A. Collins, “Diamonds in modern technology: synthesis and applications”, in *The nature of diamonds*, edited by G. Harlow (Cambridge University Press, 1998) Chap. 13.
- ²⁹V. N. Mochalin, O. Shenderova, D. Ho, and Y. Gogotsi, “The properties and applications of nanodiamonds”, *Nat Nano* **7**, 11–23 (2012).
- ³⁰P. W. May, “Diamond thin films: a 21st-century material”, *Philosophical Transactions of the Royal Society of London A: Mathematical, Physical and Engineering Sciences* **358**, 473–495 (2000).
- ³¹H. O. Pierson, “Natural and high-pressure synthetic diamond”, in *Handbook of carbon, graphite, diamonds and fullerenes* (William Andrew Publishing, Oxford, 1993) Chap. 12, pp. 278–301.
- ³²H. Sumiya and S. Satoh, “High-pressure synthesis of high-purity diamond crystal”, *Diamond and Related Materials* **5**, 1359–1365 (1996).
- ³³J. B. Donnet, E. Fousson, T. K. Wang, M. Samirant, C. Baras, and M. Pontier Johnson, “Dynamic synthesis of diamonds”, *Diamond and Related Materials* **9**, 887–892 (2000).

- ³⁴A. Krueger, “The structure and reactivity of nanoscale diamond”, *J. Mater. Chem.* **18**, 1485–1492 (2008).
- ³⁵V. V. Danilenko, “On the history of the discovery of nanodiamond synthesis”, *Physics of the Solid State* **46**, 595–599 (2004).
- ³⁶N. R. Greiner, D. S. Phillips, J. D. Johnson, and F. Volk, “Diamonds in detonation soot”, *Nature* **333**, 440–442 (1988).
- ³⁷O. A. Shenderova, V. V. Zhirnov, and D. W. Brenner, “Carbon nanostructures”, *Critical Reviews in Solid State and Materials Sciences* **27**, 227–356 (2002).
- ³⁸A. Krüger, F. Kataoka, M. Ozawa, T. Fujino, Y. Suzuki, A. E. Aleksenskii, A. Y. Vul’, and E. Osawa, “Unusually tight aggregation in detonation nanodiamond: identification and disintegration”, *Carbon* **43**, 1722–1730 (2005).
- ³⁹J. Hees, A. Kriele, and O. A. Williams, “Electrostatic self-assembly of diamond nanoparticles”, *Chemical Physics Letters* **509**, 12–15 (2011).
- ⁴⁰J. C. Angus, A. Argoitia, R. Gat, Z. Li, M. Sunkara, L. Wang, and Y. Wang, “Chemical vapour deposition of diamond”, *Philosophical Transactions of the Royal Society of London A: Mathematical, Physical and Engineering Sciences* **342**, 195–208 (1993).
- ⁴¹J. C. Angus, “Development of low-pressure diamond growth in the united states”, in *Synthetic diamond: emerging CVD science and technology*. Edited by K. E. Spear and J. P. Dismukes (John Wiley & Sons, Inc., 1994) Chap. 2, pp. 21–40.
- ⁴²“Chemical vapour deposition synthetic diamond: materials, technology and applications”, *Journal of Physics: Condensed Matter* **21**, 364221 (2009).
- ⁴³M. N. R. Ashfold, P. W. May, J. R. Petherbridge, K. N. Rosser, J. A. Smith, Y. A. Mankelevich, and N. V. Suetin, “Unravelling aspects of the gas phase chemistry involved in diamond chemical vapour deposition”, *Phys. Chem. Chem. Phys.* **3**, 3471–3485 (2001).
- ⁴⁴F. Silva, K. Hassouni, X. Bonnin, and A. Gicquel, “Microwave engineering of plasma-assisted CVD reactors for diamond deposition”, *Journal of Physics: Condensed Matter* **21**, 364202 (2009).
- ⁴⁵M. N. R. Ashfold, P. W. May, C. A. Rego, and N. M. Everitt, “Thin film diamond by chemical vapour deposition methods”, *Chem. Soc. Rev.* **23**, 21–30 (1994).
- ⁴⁶J. Haisma, F. J. H. M. van der Kruis, B. A. C. M. Spierings, J. M. Oomen, and F. M. J. G. Fey, “Damage-free tribochemical polishing of diamond at room temperature: a finishing technology”, *Precision Engineering* **14**, 20–27 (1992).
- ⁴⁷J. Asmussen and D. Reinhard, “Introduction”, in *Diamond films handbook*, edited by J. Asmussen and D. Reinhard (Taylor & Francis, 2002) Chap. 1.
- ⁴⁸B. Streetman and S. Banerjee, *Solid state electronic devices*, 5th ed. (Prentice Hall, 2000).
- ⁴⁹P. K. Bachmann, “Diamonds from the vapour phase”, *Physics World* **4**, 32 (1991).
- ⁵⁰C. J. H. Wort and R. S. Balmer, “Diamond as an electronic material”, *Materials Today* **11**, 22–28 (2008).
- ⁵¹J. Isberg, J. Hammersberg, E. Johansson, T. Wikström, D. J. Twitchen, A. J. Whitehead, S. E. Coe, and G. A. Scarsbrook, “High carrier mobility in single-crystal plasma-deposited diamond”, *Science* **297**, 1670–1672 (2002).
- ⁵²R. P. Mildren, “Intrinsic optical properties of diamond”, in *Optical engineering of diamond* (Wiley-VCH Verlag GmbH & Co. KGaA, 2013), pp. 1–34.

- ⁵³D. C. Joy, “Scanning beam methods”, in *Electron microscopy*, edited by S. Amelinckx (Wiley-VCH Verlag GmbH, 2007) Chap. 2, pp. 305–497.
- ⁵⁴D. C. Bell and N. Erdman, “Introduction to the theory and advantages of low voltage electron microscopy”, in *Low voltage electron microscopy* (John Wiley & Sons, Ltd, 2012), pp. 1–30.
- ⁵⁵J. B. Bindell, “2.2 - SEM: scanning electron microscopy”, in *Encyclopedia of materials characterization*, edited by S. W. C. Richard Brundle, Charles A. Evans Jr. (Butterworth-Heinemann, Boston, 1992), pp. 70–84.
- ⁵⁶V. V. Tsukruk and S. Singamaneni, “Scanning probe microscopy basics”, in *Scanning probe microscopy of soft matter* (Wiley-VCH Verlag GmbH & Co. KGaA, 2011), pp. 9–33.
- ⁵⁷R. S. Howland and M. D. Kirk, “2.3 - STM and SFM: scanning tunneling microscopy and scanning force microscopy”, in *Encyclopedia of materials characterization* (Butterworth-Heinemann, Boston, 1992), pp. 85–98.
- ⁵⁸Y. Seo and W. Jhe, “Atomic force microscopy and spectroscopy”, *Reports on Progress in Physics* **71**, 016101 (2008).
- ⁵⁹S. N. Magonov and M.-H. Whangbo, “Scanning probe microscopes”, in *Surface analysis with STM and AFM* (Wiley-VCH Verlag GmbH, 2007), pp. 21–46.
- ⁶⁰W. B. White, “8.2 - Raman spectroscopy”, in *Encyclopedia of materials characterization* (Butterworth-Heinemann, Boston, 1992), pp. 428–441.
- ⁶¹P. Vandenabeele, “Theoretical aspects”, in *Practical Raman spectroscopy – an introduction* (John Wiley & Sons, Ltd, 2013), pp. 1–38.
- ⁶²J. Robertson, “Diamond-like amorphous carbon”, *Materials Science and Engineering: R: Reports* **37**, 129–281 (2002).
- ⁶³A. C. Ferrari and J. Robertson, “Raman spectroscopy of amorphous, nanostructured, diamond-like carbon, and nanodiamond”, *Philosophical Transactions of the Royal Society of London A: Mathematical, Physical and Engineering Sciences* **362**, 2477–2512 (2004).
- ⁶⁴B. B. He, “Introduction”, in *Two-dimensional x-ray diffraction* (John Wiley & Sons, Inc., 2009), pp. 1–27.
- ⁶⁵M. F. Toney, “4.1 - XRD: X-Ray diffraction”, in *Encyclopedia of materials characterization* (Butterworth-Heinemann, Boston, 1992), pp. 198–213.
- ⁶⁶H. Fujiwara, “Principles of optics”, in *Spectroscopic ellipsometry* (John Wiley & Sons, Ltd, 2007), pp. 13–48.
- ⁶⁷S.-i. Ohkoshi, T. Nuida, T. Matsuda, H. Tokoro, and K. Hashimoto, “The dielectric constant in a thermal phase transition magnetic material composed of rubidium manganese hexacyanoferrate observed by spectroscopic ellipsometry”, *J. Mater. Chem.* **15**, 3291–3295 (2005).
- ⁶⁸H. Fujiwara, “Principles of spectroscopic ellipsometry”, in *Spectroscopic ellipsometry* (John Wiley & Sons, Ltd, 2007), pp. 81–146.
- ⁶⁹H. Fujiwara, “Data analysis”, in *Spectroscopic ellipsometry* (John Wiley & Sons, Ltd, 2007), pp. 147–207.
- ⁷⁰H. Fujiwara, “Polarization of light”, in *Spectroscopic ellipsometry* (John Wiley & Sons, Ltd, 2007), pp. 49–79.
- ⁷¹T. Lohner, P. Csíkvári, N. Q. Khánh, S. Dávid, Z. E. Horváth, P. Petrik, and G. Hárs, “Spectroellipsometric and ion beam analytical investigation of nanocrystalline diamond layers”, *Thin Solid Films* **519**, 2806–2810 (2011).

- ⁷²C. R. Brundle, “5.1 - XPS: x-ray photoelectron spectroscopy”, in *Encyclopedia of materials characterization* (Butterworth-Heinemann, Boston, 1992), pp. 282–299.
- ⁷³J. F. Watts and J. Wolstenholme, “Electron spectroscopy: some basic concepts”, in *An introduction to surface analysis by XPS and AES* (John Wiley & Sons, Ltd, 2005), pp. 1–15.
- ⁷⁴P. van der Heide, “XPS instrumentation”, in *X-ray photoelectron spectroscopy* (John Wiley & Sons, Inc., 2011), pp. 27–60.
- ⁷⁵M. Besen, E. Sevillano, and D. Smith, *Microwave plasma reactor*, US Patent 5,556,475, Sept. 1996.
- ⁷⁶E. Sevillano and B. Williams, “Reactor development for microwave plasma deposition of diamond”, *Diamond Films and Technology* **8**, 73–91 (1998).
- ⁷⁷S. Logothetidis, M. Gioti, S. Lousinian, and S. Fotiadou, “Haemocompatibility studies on carbon-based thin films by ellipsometry”, *Thin Solid Films* **482**, 126–132 (2005).
- ⁷⁸Y. Lifshitz, “Diamond-like carbon — present status”, *Diamond and Related Materials* **8**, 1659–1676 (1999).
- ⁷⁹K. B. K. Teo, A. C. Ferrari, G. Fanchini, S. E. Rodil, J. Yuan, J. T. H. Tsai, E. Laurenti, A. Tagliaferro, J. Robertson, and W. I. Milne, “Highest optical gap tetrahedral amorphous carbon”, *Diamond and Related Materials* **11**, 1086–1090 (2002).
- ⁸⁰G. Fedosenko, D. Korzec, J. Engemann, D. Lyebyedyev, and H. C. Scheer, “Investigation of diamond-like carbon films synthesized by multi-jet hollow cathode rf plasma source”, *Thin Solid Films* **406**, 275–281 (2002).
- ⁸¹N. Savvides and T. J. Bell, “Microhardness and Young’s modulus of diamond and diamondlike carbon films”, *Journal of Applied Physics* **72**, 2791–2796 (1992).
- ⁸²M. Shamsa, W. L. Liu, A. A. Balandin, C. Casiraghi, W. I. Milne, and A. C. Ferrari, “Thermal conductivity of diamond-like carbon films”, *Applied Physics Letters* **89**, 161921 (2006).
- ⁸³W. I. Milne, “Field emission from tetrahedrally bonded amorphous carbon”, *Applied Surface Science* **146**, 262–268 (1999).
- ⁸⁴A. Canillas, M. C. Polo, J. L. Andújar, J. Sancho, S. Bosch, J. Robertson, and W. I. Milne, “Spectroscopic ellipsometric study of tetrahedral amorphous carbon films: optical properties and modelling”, *Diamond and Related Materials* **10**, 1132–1136 (2001).
- ⁸⁵D. Franta, L. Zajíčková, I. Ohlídal, J. Janča, and K. Veltruská, “Optical characterization of diamond-like carbon films using multi-sample modification of variable angle spectroscopic ellipsometry”, *Diamond and Related Materials* **11**, 105–117 (2002).
- ⁸⁶M. Gioti, D. Papadimitriou, and S. Logothetidis, “Optical properties and new vibrational modes in carbon films”, *Diamond and Related Materials* **9**, 741–745 (2000).
- ⁸⁷M. Gioti and S. Logothetidis, “Dielectric function, electronic properties and optical constants of amorphous carbon and carbon nitride films”, *Diamond and Related Materials* **12**, 957–962 (2003).
- ⁸⁸S. Gupta, A. Dudipala, O. A. Williams, K. Haenen, and E. Bohannan, “Ex situ variable angle spectroscopic ellipsometry studies on chemical vapor deposited boron-doped diamond films: layered structure and modeling aspects”, *Journal of Applied Physics* **104**, 073514 (2008) 10.1063/1.2990058.

- ⁸⁹N. Laidani, R. Bartali, G. Gottardi, M. Anderle, and P. Cheyssac, “Optical absorption parameters of amorphous carbon films from Forouhi–Bloomer and Tauc–Lorentz models: a comparative study”, *Journal of Physics: Condensed Matter* **20**, 015216 (2008).
- ⁹⁰A. R. Forouhi and I. Bloomer, “Optical dispersion relations for amorphous semiconductors and amorphous dielectrics”, *Physical Review B* **34**, 7018–7026 (1986).
- ⁹¹G. E. Jellison and F. A. Modine, “Parameterization of the optical functions of amorphous materials in the interband region”, *Applied Physics Letters* **69**, 371–373 (1996).
- ⁹²M. Williams and E. Arakawa, “Optical properties of glassy carbon from 0 to 82 eV”, *Journal of Applied Physics* **43**, 3460–3463 (1972).
- ⁹³D. L. Greenaway, G. Harbeke, F. Bassani, and E. Tosatti, “Anisotropy of the optical constants and the band structure of graphite”, *Physical Review* **178**, 1340–1348 (1969).
- ⁹⁴Y. Cong, R. W. Collins, G. F. Epps, and H. Windischmann, “Spectroellipsometry characterization of optical quality vapor-deposited diamond thin films”, *Applied Physics Letters* **58**, 819–821 (1991).
- ⁹⁵I. Pintér, P. Petrik, E. Szilágyi, S. Kátai, and P. Deák, “Characterization of nucleation and growth of MW-CVD diamond films by spectroscopic ellipsometry and ion beam analysis methods”, *Diamond and Related Materials* **6**, 1633–1637 (1997).
- ⁹⁶B. Hong, J. Lee, R. W. Collins, Y. Kuang, W. Drawl, R. Messier, T. T. Tsong, and Y. E. Strausser, “Effects of processing conditions on the growth of nanocrystalline diamond thin films: real time spectroscopic ellipsometry studies”, *Diamond and Related Materials* **6**, 55–80 (1997).
- ⁹⁷J. Mistrik, P. Janicek, A. Taylor, F. Fendrych, L. Fekete, A. Jager, and M. Nesladek, “Spectroscopic ellipsometry characterization of nano-crystalline diamond films prepared at various substrate temperatures and pulsed plasma frequencies using microwave plasma enhanced chemical vapor deposition apparatus with linear antenna delivery”, *Thin Solid Films* **571**, Part 1, 230–237 (2014).
- ⁹⁸J. Bousquet, G. Chicot, D. Eon, and E. Bustarret, “Spectroscopic ellipsometry of homoepitaxial diamond multilayers and delta-doped structures”, *Applied Physics Letters* **104**, 021905 (2014) 10.1063/1.4861860.
- ⁹⁹D. Ballutaud, F. Jomard, T. Kociniewski, E. Rzepka, H. Girard, and S. Saada, “Sp³/sp² character of the carbon and hydrogen configuration in micro- and nanocrystalline diamond”, *Diamond and Related Materials* **17**, 451–456 (2008).
- ¹⁰⁰S. Michaelson, O. Ternyak, A. Hoffman, and Y. Lifshitz, “Correlation between diamond grain size and hydrogen retention in diamond films studied by scanning electron microscopy and secondary ion mass spectroscopy”, *Applied Physics Letters* **90**, 031914 (2007).
- ¹⁰¹O. A. Williams, M. Nesladek, M. Daenen, S. Michaelson, A. Hoffman, E. Osawa, K. Haenen, and R. B. Jackman, “Growth, electronic properties and applications of nanodiamond”, *Diamond and Related Materials* **17**, 1080–1088 (2008).
- ¹⁰²O. A. Williams and M. Nesládek, “Growth and properties of nanocrystalline diamond films”, *physica status solidi (a)* **203**, 3375–3386 (2006).
- ¹⁰³M. Wiora, K. Brühne, A. Flöter, P. Gluche, T. M. Willey, S. O. Kucheyev, A. W. Van Buuren, A. V. Hamza, J. Biener, and H. J. Fecht, “Grain size dependent mechanical properties of nanocrystalline diamond films grown by hot-filament CVD”, *Diamond and Related Materials* **18**, 927–930 (2009).

- ¹⁰⁴D. E. Aspnes, J. B. Theeten, and F. Hottier, “Investigation of effective-medium models of microscopic surface roughness by spectroscopic ellipsometry”, *Physical Review B* **20**, 3292–3302 (1979).
- ¹⁰⁵S. Xu, L. K. Cheah, and B. K. Tay, “Spectroscopic ellipsometry studies of tetrahedral amorphous carbon prepared by filtered cathodic vacuum arc technique”, *Thin Solid Films* **312**, 160–169 (1998).
- ¹⁰⁶Z. Fang, Y. Xia, L. Wang, W. Zhang, Z. Ma, and M. Zhang, “An ellipsometric analysis of CVD-diamond films at infrared wavelengths”, *Carbon* **41**, 967–972 (2003).
- ¹⁰⁷S. Boycheva, C. Popov, W. Kulisch, J. Bulir, and A. Piegari, “Optical properties of nanocrystalline diamond/amorphous carbon composite films”, *Fullerenes, Nanotubes and Carbon Nanostructures* **13**, 457–469 (2005).
- ¹⁰⁸Z. G. Hu, P. Prunici, P. Hess, and K. H. Chen, “Optical properties of nanocrystalline diamond films from mid-infrared to ultraviolet using reflectometry and ellipsometry”, *Journal of Materials Science: Materials in Electronics* **18**, 37–41 (2007).
- ¹⁰⁹A. Zimmer, O. A. Williams, K. Haenen, and H. Terryn, “Optical properties of heavily boron-doped nanocrystalline diamond films studied by spectroscopic ellipsometry”, *Applied Physics Letters* **93**, 131910 (2008) 10.1063/1.2990679.
- ¹¹⁰S. Gupta, B. R. Weiner, and G. Morell, “Spectroscopic ellipsometry studies of nanocrystalline carbon thin films deposited by HFCVD”, *Diamond and Related Materials* **10**, 1968–1972 (2001).
- ¹¹¹L.-j. Wang, L.-w. Jiang, L. Ren, J.-m. Liu, Q.-f. Su, R. Xu, H.-y. Peng, W.-m. Shi, and Y.-b. Xia, “Ellipsometric analysis and optical absorption characterization of nanocrystalline diamond film”, *Transactions of Nonferrous Metals Society of China* **16**, **Supplement 1**, s289–s292 (2006).
- ¹¹²B. K. Tay, X. Shi, L. K. Cheah, and D. I. Flynn, “Optical properties of tetrahedral amorphous carbon films determined by spectroscopic ellipsometry”, *Thin Solid Films* **308–309**, 268–272 (1997).
- ¹¹³X. Jiang, K. Schiffmann, A. Westphal, and C. P. Klages, “Atomic force microscopic study of heteroepitaxial diamond nucleation on (100) silicon”, *Applied Physics Letters* **63**, 1203–1205 (1993).
- ¹¹⁴S. Iijima, Y. Aikawa, and K. Baba, “Early formation of chemical vapor deposition diamond films”, *Applied Physics Letters* **57**, 2646–2648 (1990).
- ¹¹⁵H. A. Girard, S. Perruchas, C. Gesset, M. Chaigneau, L. Vieille, J.-C. Arnault, P. Bergonzo, J.-P. Boilot, and T. Gacoin, “Electrostatic grafting of diamond nanoparticles: a versatile route to nanocrystalline diamond thin films”, *ACS Applied Materials & Interfaces* **1**, PMID: 20356151, 2738–2746 (2009).
- ¹¹⁶J. C. Arnault, S. Saada, M. Nesladek, O. A. Williams, K. Haenen, P. Bergonzo, and E. Osawa, “Diamond nanoseeding on silicon: stability under H₂ MPCVD exposures and early stages of growth”, *Diamond and Related Materials* **17**, 1143–1149 (2008).
- ¹¹⁷S. Qin, J. D. Bernstein, and C. Chan, “Hydrogen etching for semiconductor materials in plasma doping experiments”, *Journal of Electronic Materials* **25**, 507–511 (1996).
- ¹¹⁸C. P. Chang, D. L. Flamm, D. E. Ibbotson, and J. A. Mucha, “Diamond crystal growth by plasma chemical vapor deposition”, *Journal of Applied Physics* **63**, 1744–1748 (1988).
- ¹¹⁹B. R. Stoner, G. H. M. Ma, S. D. Wolter, and J. T. Glass, “Characterization of bias-enhanced nucleation of diamond on silicon by *invacuo* surface analysis and transmission electron microscopy”, *Physical Review B* **45**, 11067–11084 (1992).

- ¹²⁰D. N. Belton, S. J. Harris, S. J. Schmieg, A. M. Weiner, and T. A. Perry, “*In situ* characterization of diamond nucleation and growth”, *Applied Physics Letters* **54**, 416–417 (1989).
- ¹²¹R. Stöckel, K. Janischowsky, S. Rohmfeld, J. Ristein, M. Hundhausen, and L. Ley, “Growth of diamond on silicon during the bias pretreatment in chemical vapor deposition of polycrystalline diamond films”, *Journal of Applied Physics* **79**, 768–775 (1996).
- ¹²²R. Meilunas, M. S. Wong, K. C. Sheng, R. P. H. Chang, and R. P. Van Duyne, “Early stages of plasma synthesis of diamond films”, *Applied Physics Letters* **54**, 2204–2206 (1989).
- ¹²³S. Saada, J. C. Arnault, N. Tranchant, M. Bonnauron, and P. Bergonzo, “Study of the CVD process sequences for an improved control of the bias enhanced nucleation step on silicon”, *physica status solidi (a)* **204**, 2854–2859 (2007).
- ¹²⁴O. A. Williams, O. Douhéret, M. Daenen, K. Haenen, E. Osawa, and M. Takahashi, “Enhanced diamond nucleation on monodispersed nanocrystalline diamond”, *Chemical Physics Letters* **445**, 255–258 (2007).
- ¹²⁵A. Taylor, F. Fendrych, L. Fekete, J. Vlček, V. Řezáčová, V. Petrák, J. Krucký, M. Nesládek, and M. Liehr, “Novel high frequency pulsed MW-linear antenna plasma-chemistry: routes towards large area, low pressure nanodiamond growth”, *Diamond and Related Materials* **20**, 613–615 (2011).
- ¹²⁶W. Fortunato, A. J. Chiquito, J. C. Galzerani, and J. R. Moro, “Crystalline quality and phase purity of CVD diamond films studied by Raman spectroscopy”, *Journal of Materials Science* **42**, 7331–7336 (2007).
- ¹²⁷Z. Pápa, J. Budai, I. Hanyecz, J. Csontos, and Z. Toth, “Depolarization correction method for ellipsometric measurements of large grain size zinc-oxide films”, *Thin Solid Films* **571**, Part 3, 562–566 (2014).
- ¹²⁸J. Lee, P. I. Rovira, I. An, and R. W. Collins, “Rotating-compensator multichannel ellipsometry: applications for real time Stokes vector spectroscopy of thin film growth”, *Review of Scientific Instruments* **69**, 1800–1810 (1998).
- ¹²⁹G. E. Jellison and J. W. McCamy, “Sample depolarization effects from thin films of ZnS on GaAs as measured by spectroscopic ellipsometry”, *Applied Physics Letters* **61**, 512–514 (1992).
- ¹³⁰N. Cella, H. El Rhaleb, J. P. Roger, D. Fournier, E. Anger, and A. Gicquel, “Ex-situ spectroscopic ellipsometry studies of micron thick CVD diamond films”, *Diamond and Related Materials* **5**, 1424–1432 (1996).
- ¹³¹K. H. Chen, D. M. Bhusari, J. R. Yang, S. T. Lin, T. Y. Wang, and L. C. Chen, “Highly transparent nano-crystalline diamond films via substrate pretreatment and methane fraction optimization”, *Thin Solid Films* **332**, 34–39 (1998).
- ¹³²C. Y. Wang, F. L. Zhang, T. C. Kuang, and C. L. Chen, “Chemical/mechanical polishing of diamond films assisted by molten mixture of LiNO₃ and KNO₃”, *Thin Solid Films* **496**, 698–702 (2006).
- ¹³³C. Y. Cheng, H. Y. Tsai, C. H. Wu, P. Y. Liu, C. H. Hsieh, and Y. Y. Chang, “An oxidation enhanced mechanical polishing technique for CVD diamond films”, *Diamond and Related Materials* **14**, 622–625 (2005).
- ¹³⁴J. Cifre, J. Campmany, E. Bertran, and J. Esteve, “Spectroscopic ellipsometry measurements of the diamond-crystalline Si interface in chemically vapour-deposited polycrystalline diamond films”, *Diamond and Related Materials* **2**, 728–731 (1993).

- ¹³⁵L. Wang, Y. Xia, M. Zhang, H. Shen, Q. Su, B. Gu, and Y. Lou, “Spectroscopic ellipsometric study of CVD diamond films: modelling and optical properties in the energy range of 0.1–0.4 eV”, *Journal of Physics D: Applied Physics* **37**, 1976 (2004).
- ¹³⁶Y. Hayashi, W. Drawl, R. W. Collins, and R. Messier, “In-process ellipsometric monitoring of diamond film growth by microwave plasma enhanced chemical vapor deposition”, *Applied Physics Letters* **60**, 2868–2870 (1992).
- ¹³⁷R. W. Collins, Y. Cong, H. V. Nguyen, I. An, K. Vedam, T. Badzian, and R. Messier, “Real time spectroscopic ellipsometry characterization of the nucleation of diamond by filament-assisted chemical vapor deposition”, *Journal of Applied Physics* **71**, 5287–5289 (1992).
- ¹³⁸R. W. Collins, Y. Cong, Y. T. Kim, K. Vedam, Y. Liou, A. Inspektor, and R. Messier, “Real-time and spectroscopic ellipsometry characterization of diamond and diamond-like carbon”, *Thin Solid Films* **181**, 565–578 (1989).
- ¹³⁹B. Hong, M. Wakagi, W. Drawl, R. Messier, and R. W. Collins, “Real time spectroellipsometry study of the evolution of bonding in diamond thin films during nucleation and growth”, *Phys. Rev. Lett.* **75**, 1122–1125 (1995).
- ¹⁴⁰J. Lee, B. Hong, R. Messier, and R. W. Collins, “Real time spectroellipsometry for optimization of diamond film growth by microwave plasma-enhanced chemical vapor deposition from CO/H₂ mixtures”, *Journal of Applied Physics* **80**, 6489–6495 (1996).
- ¹⁴¹B. Hong, M. Wakagi, R. Collins, I. An, N. Engdahl, W. Drawl, and R. Messier, “Real-time spectroscopic ellipsometry studies of diamond film growth by microwave plasma-enhanced chemical vapour deposition”, *Diamond and Related Materials* **3**, 431–437 (1994).
- ¹⁴²A. Gibaud, G. Vignaud, and S. K. Sinha, “The correction of geometrical factors in the analysis of X-ray reflectivity”, *Acta Crystallographica Section A* **49**, 642–648 (1993).
- ¹⁴³O. A. Williams, J. Hees, C. Dieker, W. Jäger, L. Kirste, and C. E. Nebel, “Size-dependent reactivity of diamond nanoparticles”, *ACS Nano* **4**, 4824–4830 (2010).
- ¹⁴⁴S. M. Leeds, T. J. Davis, P. W. May, C. D. O. Pickard, and M. N. R. Ashfold, “Use of different excitation wavelengths for the analysis of CVD diamond by laser Raman spectroscopy”, *Diamond and Related Materials* **7**, 233–237 (1998).
- ¹⁴⁵D. Knight and W. White, “Characterization of diamond films by Raman spectroscopy”, *Journal of Materials Research* **4**, 385–393 (1989).
- ¹⁴⁶J. H. Parker, D. W. Feldman, and M. Ashkin, “Raman scattering by silicon and germanium”, *Physical Review* **155**, 712–714 (1967).
- ¹⁴⁷F. Cerdeira, T. A. Fjeldly, and M. Cardona, “Raman study of the interaction between localized vibrations and electronic excitations in boron-doped silicon”, *Phys. Rev. B* **9**, 4344–4350 (1974).
- ¹⁴⁸M. Chandrasekhar, H. R. Chandrasekhar, M. Grimsditch, and M. Cardona, “Study of the localized vibrations of boron in heavily doped Si”, *Phys. Rev. B* **22**, 4825–4833 (1980).
- ¹⁴⁹F. Neri, S. Trusso, C. Vasi, F. Barreca, and P. Valisa, “Raman microscopy study of pulsed laser ablation deposited silicon carbide films”, *Thin Solid Films* **332**, 290–294 (1998).
- ¹⁵⁰M. Lattemann, E. Nold, S. Ulrich, H. Leiste, and H. Holleck, “Investigation and characterisation of silicon nitride and silicon carbide thin films”, *Surface and Coatings Technology* **174–175**, 365–369 (2003).

- ¹⁵¹M. A. Fraga, M. Massi, I. C. Oliveira, H. S. Maciel, S. G. dos Santos Filho, and R. D. Mansano, “Nitrogen doping of SiC thin films deposited by RF magnetron sputtering”, *Journal of Materials Science: Materials in Electronics* **19**, 835–840 (2007).
- ¹⁵²E. Pascual, J. L. Andújar, J. L. Fernández, and E. Bertran, “Optical and structural characterization of hydrogenated amorphous silicon carbide thin films prepared by r.f. plasma chemical vapour deposition”, *Diamond and Related Materials* **4**, 1205–1209 (1995).
- ¹⁵³J. Filik, “Raman spectroscopy: a simple, non-destructive way to characterise diamond and diamond-like materials”, *Spectroscopy Europe* **17**, 10–17 (2005).
- ¹⁵⁴A. C. Ferrari and J. Robertson, “Origin of the 1150-cm⁻¹ Raman mode in nanocrystalline diamond”, *Physical Review B* **63**, 121405 (2001).
- ¹⁵⁵F. Silva, A. Gicquel, A. Tardieu, P. Cledat, and T. Chauveau, “Control of an MPACVD reactor for polycrystalline textured diamond films synthesis: role of microwave power density”, *Diamond and Related Materials* **5**, 338–344 (1996).
- ¹⁵⁶O. O. Mykhaylyk, Y. M. Solonin, D. N. Batchelder, and R. Brydson, “Transformation of nanodiamond into carbon onions: a comparative study by high-resolution transmission electron microscopy, electron energy-loss spectroscopy, x-ray diffraction, small-angle x-ray scattering, and ultraviolet Raman spectroscopy”, *Journal of Applied Physics* **97**, 074302 (2005).
- ¹⁵⁷Z. Q. Li, C. J. Lu, Z. P. Xia, Y. Zhou, and Z. Luo, “X-ray diffraction patterns of graphite and turbostratic carbon”, *Carbon* **45**, 1686–1695 (2007).
- ¹⁵⁸B. Palosz, E. Grzanka, S. Gierlotka, S. Stel’makh, R. Pielaszek, U. Bismayer, J. Neufeind, H. P. Weber, T. Proffen, R. Von Dreele, and W. Palosz, “Analysis of short and long range atomic order in nanocrystalline diamonds with application of powder diffractometry”, *Zeitschrift fur Kristallographie* **217**, 497–509 (2002).
- ¹⁵⁹A. C. Ferrari, A. Libassi, B. K. Tanner, V. Stolojan, J. Yuan, L. M. Brown, S. E. Rodil, B. Kleinsorge, and J. Robertson, “Density, sp³ fraction, and cross-sectional structure of amorphous carbon films determined by x-ray reflectivity and electron energy-loss spectroscopy”, *Phys. Rev. B* **62**, 11089–11103 (2000).
- ¹⁶⁰A. Libassi, A. C. Ferrari, V. Stolojan, B. K. Tanner, J. Robertson, and L. M. Brown, “Density and sp³ content in diamond-like carbon films by x-ray reflectivity and electron energy loss spectroscopy”, *MRS Online Proceedings Library Archive* **593**, 293–298 (1999).
- ¹⁶¹A. LiBassi, A. C. Ferrari, V. Stolojan, B. K. Tanner, J. Robertson, and L. M. Brown, “Density, sp³ content and internal layering of DLC films by X-ray reflectivity and electron energy loss spectroscopy”, *Diamond and Related Materials* **9**, 771–776 (2000).
- ¹⁶²R. M. Dey, S. K. Deshpande, S. B. Singh, N. Chand, D. S. Patil, and S. K. Kulkarni, “X-ray reflectivity study of bias graded diamond like carbon film synthesized by ECR plasma”, *Bulletin of Materials Science* **36**, 9–14 (2013).
- ¹⁶³C. M. Herzinger, B. Johs, W. A. McGahan, J. A. Woollam, and W. Paulson, “Ellipsometric determination of optical constants for silicon and thermally grown silicon dioxide via a multi-sample, multi-wavelength, multi-angle investigation”, *Journal of Applied Physics* **83**, 3323–3336 (1998).
- ¹⁶⁴D. F. Edwards and H. R. Philipp, “Cubic carbon (diamond)”, in *Handbook of optical constants of solids* (Academic Press, Boston, 1985), pp. 665–673.
- ¹⁶⁵J. I. Larruquert, L. V. Rodríguez-de Marcos, J. A. Méndez, P. J. Martin, and A. Bendavid, “High reflectance ta-C coatings in the extreme ultraviolet”, *Optics Express* **21**, 27537–27549 (2013).

- ¹⁶⁶M. Ishii, K. Nakashima, I. Tajima, and M. Yamamoto, “Properties of silicon surface cleaned by hydrogen plasma”, *Applied Physics Letters* **58**, 1378–1380 (1991).
- ¹⁶⁷S. A. Alterovitz and J. A. Woollam, “Cubic silicon carbide”, in *Handbook of optical constants of solids* (Academic Press, Burlington, 1997), pp. 705–707.
- ¹⁶⁸J. I. Larruquert, A. P. Pérez-Marín, S. García-Cortés, L. R.-d. Marcos, J. A. Aznárez, and J. A. Méndez, “Self-consistent optical constants of SiC thin films”, *J. Opt. Soc. Am. A* **28**, 2340–2345 (2011).
- ¹⁶⁹A. Borghesi and G. Guizzetti, “Graphite (C)”, in *Handbook of optical constants of solids*, edited by E. D. Palik (Academic Press, Burlington, 1997), pp. 449–460.
- ¹⁷⁰J. Lee, B. Hong, R. Messier, and R. W. Collins, “Application of real-time spectroscopic ellipsometry for the development of low-temperature diamond film growth processes”, *Thin Solid Films* **313–314**, 506–510 (1998).
- ¹⁷¹P. Petrik, M. Fried, T. Lohner, R. Berger, L. P. Biró, C. Schneider, J. Gyulai, and H. Ryssel, “Comparative study of polysilicon-on-oxide using spectroscopic ellipsometry, atomic force microscopy, and transmission electron microscopy”, *Thin Solid Films* **313–314**, 259–263 (1998).
- ¹⁷²J. Koh, Y. Lu, C. R. Wronski, Y. Kuang, R. W. Collins, T. T. Tsong, and Y. E. Strausser, “Correlation of real time spectroellipsometry and atomic force microscopy measurements of surface roughness on amorphous semiconductor thin films”, *Applied Physics Letters* **69**, 1297–1299 (1996).
- ¹⁷³A. A. Morrish and P. E. Pehrsson, “Effects of surface pretreatments on nucleation and growth of diamond films on a variety of substrates”, *Applied Physics Letters* **59**, 417–419 (1991).
- ¹⁷⁴Y. Hayashi, X. Li, and S. Nishino, “Ellipsometric monitoring of an oriented diamond nucleation process in bias-enhanced chemical vapor deposition”, *Applied Physics Letters* **71**, 2913–2915 (1997).
- ¹⁷⁵X. Li, Y. Hayashi, and S. Nishino, “In-situ ellipsometry study of initial stage of bias-enhanced nucleation and heteroepitaxy of diamond on silicon(100) by hot filament chemical vapor deposition”, *Diamond and Related Materials* **6**, 1117–1123 (1997).
- ¹⁷⁶I. Friel, S. Clewes, H. Dhillon, N. Perkins, D. Twitchen, and G. Scarsbrook, “Control of surface and bulk crystalline quality in single crystal diamond grown by chemical vapour deposition”, *Diamond and Related Materials* **18**, Proceedings of Diamond 2008, the 19th European Conference on Diamond, Diamond-Like Materials, Carbon Nanotubes, Nitrides and Silicon Carbide, 808–815 (2009).
- ¹⁷⁷A. P. Malshe, B. S. Park, W. D. Brown, and H. A. Naseem, “A review of techniques for polishing and planarizing chemically vapor-deposited (CVD) diamond films and substrates”, *Diamond and Related Materials* **8**, 1198–1213 (1999).
- ¹⁷⁸W. L. Liu, M. Shamsa, I. Calizo, A. A. Balandin, V. Ralchenko, A. Popovich, and A. Saveliev, “Thermal conduction in nanocrystalline diamond films: effects of the grain boundary scattering and nitrogen doping”, *Applied Physics Letters* **89**, 171915 (2006) 10.1063/1.2364130.
- ¹⁷⁹D. M. Bhusari, J. R. Yang, T. Y. Wang, S. T. Lin, K. H. Chen, and L. C. Chen, “Highly transparent nano-crystalline diamond films grown by microwave CVD”, *Solid State Communications* **107**, 301–305 (1998).
- ¹⁸⁰B. Bhushan, V. V. Subramaniam, A. Malshe, B. K. Gupta, and J. Ruan, “Tribological properties of polished diamond films”, *Journal of Applied Physics* **74**, 4174–4180 (1993).

- ¹⁸¹H. Miki, A. Tsutsui, T. Takeno, and T. Takagi, “Friction properties of partially polished CVD diamond films at different sliding speeds”, *Diamond and Related Materials* **24**, 167–170 (2012).
- ¹⁸²F. Bénédic, M. B. Assouar, F. Mohasseb, O. Elmazria, P. Alnot, and A. Gicquel, “Surface acoustic wave devices based on nanocrystalline diamond and aluminium nitride”, *Diamond and Related Materials* **13**, 347–353 (2004).
- ¹⁸³G. F. Iriarte, J. G. Rodríguez, and F. Calle, “Synthesis of c-axis oriented AlN thin films on different substrates: a review”, *Materials Research Bulletin* **45**, 1039–1045 (2010).
- ¹⁸⁴O. Ergincan, G. Palasantzas, and B. J. Kooi, “Influence of surface modification on the quality factor of microresonators”, *Physical Review B* **85**, 205420 (2012).
- ¹⁸⁵J. G. Rodríguez-Madrid, G. F. Iriarte, O. A. Williams, and F. Calle, “High precision pressure sensors based on SAW devices in the GHz range”, *Sensors and Actuators A: Physical* **189**, 364–369 (2013).
- ¹⁸⁶Y. Chen and L. Zhang, “Introduction”, in *Polishing of diamond materials* (Springer, London, 2013), pp. 1–10.
- ¹⁸⁷Y. Chen and L. Zhang, “Mechanical polishing”, in *Polishing of diamond materials* (Springer, London, 2013), pp. 25–44.
- ¹⁸⁸T. Schuelke and T. A. Grotjohn, “Diamond polishing”, *Diamond and Related Materials* **32**, 17–26 (2013).
- ¹⁸⁹J. Hird and J. Field, “Diamond polishing”, *Proc. R. Soc. Lond. A.* **460**, 3547–3568 (2004).
- ¹⁹⁰S. E. Grillo and J. E. Field, “The polishing of diamond”, *Journal of Physics D: Applied Physics* **30**, 202 (1997).
- ¹⁹¹J. Hird and J. Field, “A wear mechanism map for the diamond polishing process”, *Wear* **258**, Second International Conference on Erosive and Abrasive Wear, 18–25 (2005).
- ¹⁹²B. S. El-Dasher, J. J. Gray, J. W. Tringe, J. Biener, A. V. Hamza, C. Wild, E. Wörner, and P. Koidl, “Crystallographic anisotropy of wear on a polycrystalline diamond surface”, *Applied Physics Letters* **88**, 241915 (2006) 10.1063/1.2213180.
- ¹⁹³F. van Bouwelen and W. van Enckevort, “A simple model to describe the anisotropy of diamond polishing”, *Diamond and Related Materials* **8**, 840–844 (1999).
- ¹⁹⁴E. M. Wilks and J. Wilks, “The resistance of diamond to abrasion”, *Journal of Physics D: Applied Physics* **5**, 1902 (1972).
- ¹⁹⁵S. E. Grillo, J. E. Field, and F. M. van Bouwelen, “Diamond polishing: the dependency of friction and wear on load and crystal orientation”, *Journal of Physics D: Applied Physics* **33**, 985 (2000).
- ¹⁹⁶M. Couto, W. van Enckevort, and M. Seal, “Friction tracks on diamond surfaces imaged by atomic force microscopy”, *Diamond and Related Materials* **6**, 975–982 (1997).
- ¹⁹⁷F. M. van Bouwelen, “Polishing: mechanically induced degradation of diamond”, *physica status solidi (a)* **172**, 91–96 (1999).
- ¹⁹⁸L. Pastewka, S. Moser, P. Gumbsch, and M. Moseler, “Anisotropic mechanical amorphization drives wear in diamond”, *Nat Mater* **10**, 34–38 (2011).
- ¹⁹⁹T. Derry, N. van der Berg, and N. Makau, “Diamond surfaces polished both mechanically and manually; an atomic force microscopy (AFM) study”, *Diamond and Related Materials* **17**, 127–136 (2008).

- ²⁰⁰W. Zong, D. Li, K. Cheng, T. Sun, H. Wang, and Y. Liang, “The material removal mechanism in mechanical lapping of diamond cutting tools”, *International Journal of Machine Tools and Manufacture* **45**, 783–788 (2005).
- ²⁰¹P.-N. Volpe, P. Muret, F. Omnes, J. Achard, F. Silva, O. Brinza, and A. Gicquel, “Defect analysis and excitons diffusion in undoped homoepitaxial diamond films after polishing and oxygen plasma etching”, *Diamond and Related Materials* **18**, 1205–1210 (2009).
- ²⁰²P. M. Martineau, M. P. Gaukroger, K. B. Guy, S. C. Lawson, D. J. Twitchen, I. Friel, J. O. Hansen, G. C. Summerton, T. P. G. Addison, and R. Burns, “High crystalline quality single crystal chemical vapour deposition diamond”, *Journal of Physics: Condensed Matter* **21**, 364205 (2009).
- ²⁰³Y. Kato, H. Umezawa, S.-i. Shikata, and M. Touge, “Effect of an ultraflat substrate on the epitaxial growth of chemical-vapor-deposited diamond”, *Applied Physics Express* **6**, 025506 (2013).
- ²⁰⁴Y. Chen, L. C. Zhang, J. A. Arsecularatne, and C. Montross, “Polishing of polycrystalline diamond by the technique of dynamic friction, part 1: prediction of the interface temperature rise”, *International Journal of Machine Tools and Manufacture* **46**, 580–587 (2006).
- ²⁰⁵C. D. Ollison, W. D. Brown, A. P. Malshe, H. A. Naseem, and S. S. Ang, “A comparison of mechanical lapping versus chemical-assisted mechanical polishing and planarization of chemical vapor deposited (CVD) diamond”, *Diamond and Related Materials* **8**, 1083–1090 (1999).
- ²⁰⁶Q. H. Fan, J. Grácio, and E. Pereira, “Residual stresses in chemical vapour deposited diamond films”, *Diamond and Related Materials* **9**, 1739–1743 (2000).
- ²⁰⁷H. Windischmann, G. F. Epps, Y. Cong, and R. W. Collins, “Intrinsic stress in diamond films prepared by microwave plasma CVD”, *Journal of Applied Physics* **69**, 2231–2237 (1991).
- ²⁰⁸A. Kriele, O. A. Williams, M. Wolfer, D. Brink, W. Müller-Sebert, and C. E. Nebel, “Tuneable optical lenses from diamond thin films”, *Applied Physics Letters* **95**, 031905 (2009) [10.1063/1.3183534](https://doi.org/10.1063/1.3183534).
- ²⁰⁹M. J. Edwards, C. R. Bowen, D. W. E. Allsopp, and A. C. E. Dent, “Modelling wafer bow in silicon–polycrystalline CVD diamond substrates for GaN-based devices”, *Journal of Physics D: Applied Physics* **43**, 385502 (2010).
- ²¹⁰E. L. H. Thomas, G. W. Nelson, S. Mandal, J. S. Foord, and O. A. Williams, “Chemical mechanical polishing of thin film diamond”, *Carbon* **68**, 473–479 (2014).
- ²¹¹J. Kühnle and O. Weis, “Mechanochemical superpolishing of diamond using NaNO_3 or KNO_3 as oxidizing agents”, *Surface Science* **340**, 16–22 (1995).
- ²¹²A. Kubota, S. Fukuyama, Y. Ichimori, and M. Touge, “Surface smoothing of single-crystal diamond (100) substrate by polishing technique”, *Diamond and Related Materials* **24**, 59–62 (2012).
- ²¹³H. Y. Tsai, C. J. Ting, and C. P. Chou, “Evaluation research of polishing methods for large area diamond films produced by chemical vapor deposition”, *Diamond and Related Materials* **16**, 253–261 (2007).
- ²¹⁴H. Hocheng and C. C. Chen, “Chemical-assisted mechanical polishing of diamond film on wafer”, *Materials Science Forum* **505–507**, 1225–1230 (2006).
- ²¹⁵A. Hirata, H. Tokura, and M. Yoshikawa, “Smoothing of chemically vapour deposited diamond films by ion beam irradiation”, *Thin Solid Films* **212**, 43–48 (1992).

- ²¹⁶A. M. Ozkan, A. P. Malshe, and W. D. Brown, “Sequential multiple-laser-assisted polishing of free-standing CVD diamond substrates”, *Diamond and Related Materials* **6**, 1789–1798 (1997).
- ²¹⁷P. B. Zantye, A. Kumar, and A. K. Sikder, “Chemical mechanical planarization for microelectronics applications”, *Materials Science and Engineering: R: Reports* **45**, 89–220 (2004).
- ²¹⁸M. R. Oliver, “CMP technology”, in *Chemical-mechanical planarization of semiconductor materials*, Vol. 69, edited by M. R. Oliver (Springer, 2004) Chap. 2, pp. 7–40.
- ²¹⁹M. Krishnan, J. W. Nalaskowski, and L. M. Cook, “Chemical mechanical planarization: slurry chemistry, materials, and mechanisms”, *Chemical Reviews* **110**, 178–204 (2010).
- ²²⁰R. K. Singh and R. Bajaj, “Advances in chemical-mechanical planarization”, *MRS Bulletin* **27**, 743–751 (2002).
- ²²¹H. Hocheng, H. Y. Tsai, and Y. T. Su, “Modeling and experimental analysis of the material removal rate in the chemical mechanical planarization of dielectric films and bare silicon wafers”, *Journal of The Electrochemical Society* **148**, G581–G586 (2001).
- ²²²J. Luo and D. A. Dornfeld, “Material removal mechanism in chemical mechanical polishing: theory and modeling”, *Semiconductor Manufacturing, IEEE Transactions on* **14**, 112–133 (2001).
- ²²³K. Robinson, “Fundamentals of CMP slurry”, in *Chemical-mechanical planarization of semiconductor materials*, Vol. 69, edited by M. R. Oliver (Springer, 2004) Chap. 7, pp. 215–249.
- ²²⁴S. Haba, K. Fukuda, Y. Ohta, Y. Koubuchi, and T. Katouda, “Fumed silica slurry stabilizing methods for chemical mechanical polishing”, *Japanese Journal of Applied Physics* **42**, 418 (2003).
- ²²⁵H.-J. Kim, D.-H. Eom, and J.-G. Park, “Physical and chemical characterization of reused oxide chemical mechanical planarization slurry”, *Japanese Journal of Applied Physics* **40**, 1236 (2001).
- ²²⁶M.-S. Kim, S.-W. Woo, and J.-G. Park, “Point of use regeneration of oxide chemical mechanical planarization slurry by filtrations”, *Japanese Journal of Applied Physics* **41**, 6342 (2002).
- ²²⁷D. B. James, “CMP polishing pads”, in *Chemical-mechanical planarization of semiconductor materials*, Vol. 69, edited by M. R. Oliver (Springer, 2004) Chap. 6, pp. 167–213.
- ²²⁸H. Lu, B. Fookes, Y. Obeng, S. Machinski, and K. A. Richardson, “Quantitative analysis of physical and chemical changes in CMP polyurethane pad surfaces”, *Materials Characterization* **49**, 35–44 (2002).
- ²²⁹J. McGrath and C. Davis, “Polishing pad surface characterisation in chemical mechanical planarisation”, *Journal of Materials Processing Technology* **153–154**, 666–673 (2004).
- ²³⁰K. H. Park, H. J. Kim, O. M. Chang, and H. D. Jeong, “Effects of pad properties on material removal in chemical mechanical polishing”, *Journal of Materials Processing Technology* **187–188**, 73–76 (2007).
- ²³¹V. Domnich, S. Reynaud, R. A. Haber, and M. Chhowalla, “Boron carbide: structure, properties, and stability under stress”, *Journal of the American Ceramic Society* **94**, 3605–3628 (2011).

- ²³²J. F. Li, Y. F. Huang, Y. Ding, Z. L. Yang, S. B. Li, X. S. Zhou, F. R. Fan, W. Zhang, Z. Y. Zhou, W. Yin, B. Ren, Z. L. Wang, and Z. Q. Tian, “Shell-isolated nanoparticle-enhanced Raman spectroscopy”, *Nature* **464**, 392–395 (2010).
- ²³³S. Ferro, M. D. Colle, and A. D. Battisti, “Chemical surface characterization of electrochemically and thermally oxidized boron-doped diamond film electrodes”, *Carbon* **43**, 1191–1203 (2005).
- ²³⁴S. Torrenzo, R. Canteri, R. Dell’Anna, L. Minati, A. Pasquarelli, and G. Speranza, “XPS and ToF-SIMS investigation of nanocrystalline diamond oxidized surfaces”, *Applied Surface Science* **276**, 101–111 (2013).
- ²³⁵S. Ghodbane, D. Ballutaud, F. Omnès, and C. Agnès, “Comparison of the XPS spectra from homoepitaxial {111}, {100} and polycrystalline boron-doped diamond films”, *Diamond and Related Materials* **19**, 630–636 (2010).
- ²³⁶F. Klauser, S. Ghodbane, R. Boukherroub, S. Szunerits, D. Steinmüller-Nethl, E. Bertel, and N. Memmel, “Comparison of different oxidation techniques on single-crystal and nanocrystalline diamond surfaces”, *Diamond and Related Materials* **19**, 474–478 (2010).
- ²³⁷G. Speranza, S. Torrenzo, A. Miotello, L. Minati, I. Bernagozzi, M. Ferrari, M. Dipalo, and E. Kohn, “XPS and UPS in situ study of oxygen thermal desorption from nanocrystalline diamond surface oxidized by different process”, *Diamond and Related Materials* **20**, 560–563 (2011).
- ²³⁸S. Ghodbane, T. Haensel, Y. Coffinier, S. Szunerits, D. Steinmüller-Nethl, R. Boukherroub, S. I.-U. Ahmed, and J. A. Schaefer, “HREELS investigation of the surfaces of nanocrystalline diamond films oxidized by different processes”, *Langmuir* **26**, 18798–18805 (2010).
- ²³⁹W. M. Lau, L. J. Huang, I. Bello, Y. M. Yiu, and S. Lee, “Modification of surface band bending of diamond by low energy argon and carbon ion bombardment”, *Journal of Applied Physics* **75**, 3385–3391 (1994).
- ²⁴⁰J. Foord and J. P. Hu, “Electrochemical oxidation and reduction processes at diamond electrodes of varying phase purity”, *physica status solidi (a)* **203**, 3121–3127 (2006).
- ²⁴¹T. Haensel, J. Uhlig, R. J. Koch, S. I.-U. Ahmed, J. A. Garrido, D. Steinmüller-Nethl, M. Stutzmann, and J. A. Schaefer, “Influence of hydrogen on nanocrystalline diamond surfaces investigated with HREELS and XPS”, *physica status solidi (a)* **206**, 2022–2027 (2009).
- ²⁴²P. Rao, M. Iwasa, and I. Kondoh, “Properties of low-temperature-sintered high purity α -alumina ceramics”, *Journal of Materials Science Letters* **19**, 543–545 (2000).
- ²⁴³W. B. Yang, F. X. Lü, and Z. X. Cao, “Growth of nanocrystalline diamond protective coatings on quartz glass”, *Journal of Applied Physics* **91**, 10068–10073 (2002).
- ²⁴⁴P. Hess, “The mechanical properties of various chemical vapor deposition diamond structures compared to the ideal single crystal”, *Journal of Applied Physics* **111**, 051101 (2012) 10.1063/1.3683544.
- ²⁴⁵M.-Y. Tsai, S.-T. Chen, Y.-S. Liao, and J. Sung, “Novel diamond conditioner dressing characteristics of CMP polishing pad”, *International Journal of Machine Tools and Manufacture* **49**, 722–729 (2009).
- ²⁴⁶Y.-C. Kim and S.-J. L. Kang, “Novel CVD diamond-coated conditioner for improved performance in CMP processes”, *International Journal of Machine Tools and Manufacture* **51**, 565–568 (2011).

- ²⁴⁷Y. Yao, Y. Ishikawa, Y. Sugawara, H. Yamada, A. Chayahara, and Y. Mokuno, “Fast removal of surface damage layer from single crystal diamond by using chemical etching in molten KCl + KOH solution”, *Diamond and Related Materials* **63**, 86–90 (2016).
- ²⁴⁸F. K. de Theije, O. Roy, N. J. van der Laag, and W. J. P. van Enckevort, “Oxidative etching of diamond”, *Diamond and Related Materials* **9**, 929–934 (2000).
- ²⁴⁹F. K. de Theije, E. van Veenendaal, W. J. P. van Enckevort, and E. Vlieg, “Oxidative etching of cleaved synthetic diamond {111} surfaces”, *Surface Science* **492**, 91–105 (2001).
- ²⁵⁰D. R. Lide, ed., *CRC handbook of chemistry and physics*, 86th ed. (CRC Press, June 2005).
- ²⁵¹E. L. H. Thomas, S. Mandal, E. B. Brousseau, and O. A. Williams, “Silica based polishing of {100} and {111} single crystal diamond”, *Science and Technology of Advanced Materials* **15**, 035013 (2014).
- ²⁵²B. J. Hooper, G. Byrne, and S. Galligan, “Pad conditioning in chemical mechanical polishing”, *Journal of Materials Processing Technology* **123**, 107–113 (2002).
- ²⁵³Logitech, *Polishing suspensions*, <http://www.logitech.uk.com/products-solutions/products-and-accessories/consumables/polishing-suspensions.aspx>, Accessed: 25/11/2015.
- ²⁵⁴F. Testa, C. Coetsier, E. Carretier, M. Ennahali, B. Laborie, C. Serafino, F. Bulgarelli, and P. Moulin, “Retreatment of silicon slurry by membrane processes”, *Journal of Hazardous Materials* **192**, 440–450 (2011).
- ²⁵⁵Y. T. Yang, K. L. Ekinici, X. M. H. Huang, L. M. Schiavone, M. L. Roukes, C. A. Zorman, and M. Mehregany, “Monocrystalline silicon carbide nanoelectromechanical systems”, *Applied Physics Letters* **78**, 162–164 (2001).
- ²⁵⁶R. P. Middlemiss, A. Samarelli, D. J. Paul, J. Hough, S. Rowan, and G. D. Hammond, “Measurement of the Earth tides with a MEMS gravimeter”, *Nature* **531**, 614–617 (2016).
- ²⁵⁷A. D. O’Connell, M. Hofheinz, M. Ansmann, R. C. Bialczak, M. Lenander, E. Lucero, M. Neeley, D. Sank, H. Wang, M. Weides, J. Wenner, J. M. Martinis, and A. N. Cleland, “Quantum ground state and single-phonon control of a mechanical resonator”, *Nature* **464**, 697–703 (2010).
- ²⁵⁸N. Sepulveda, D. Aslam, and J. P. Sullivan, “Polycrystalline diamond MEMS resonator technology for sensor applications”, *Diamond and Related Materials* **15**, 398–403 (2006).
- ²⁵⁹J. D. Reddy, A. A. Volinsky, C. L. Frewin, C. Locke, and S. E. Sadow, “Mechanical properties of 3C-SiC films for MEMS applications”, *MRS Online Proceedings Library Archive* **1049** (2007).
- ²⁶⁰W. T. Hsu, J. R. Clark, and C. T. C. Nguyen, “Q-optimized lateral free-free beam micromechanical resonators”, English, in (2001), pp. 1110–1113.
- ²⁶¹K. Wang, A.-C. Wong, and C. T. C. Nguyen, “VHF free-free beam high-Q micromechanical resonators”, *Journal of Microelectromechanical Systems* **9**, 347–360 (2000).
- ²⁶²G. Palasantzas, “Random surface roughness influence on gas damped nanoresonators”, *Applied Physics Letters* **90**, 041914 (2007) 10.1063/1.2435328.

- ²⁶³P. L. Piotrowski, R. J. Cannara, G. Gao, J. J. Urban, R. W. Carpick, and J. A. Harrison, “Atomistic factors governing adhesion between diamond, amorphous carbon and model diamond nanocomposite surfaces”, in *Adhesion aspects in MEMS/NEMS* (CRC Press, 2011), pp. 135–161.
- ²⁶⁴J. Kusterer and E. Kohn, “CVD diamond MEMS”, in *CVD diamond for electronic devices and sensors* (John Wiley & Sons, Ltd, 2009), pp. 467–544.
- ²⁶⁵H. Guo, Y. Qi, and X. Li, “Adhesion at diamond/metal interfaces: a density functional theory study”, *Journal of Applied Physics* **107**, 033722 (2010).
- ²⁶⁶X. C. Tong, “Advanced materials for thermal management of electronic packaging”, in *Monolithic carbonaceous materials and carbon matrix composites* (Springer New York, New York, NY, 2011) Chap. 4, pp. 169–200.
- ²⁶⁷Y. Qi and L. G. Hector, “Adhesion and adhesive transfer at aluminum/diamond interfaces: a first-principles study”, *Phys. Rev. B* **69**, 235401 (2004).
- ²⁶⁸S. J. Sque, R. Jones, and P. R. Briddon, “Structure, electronics, and interaction of hydrogen and oxygen on diamond surfaces”, *Phys. Rev. B* **73**, 085313 (2006).
- ²⁶⁹X.-G. Wang and J. R. Smith, “Copper/diamond adhesion and hydrogen termination”, *Phys. Rev. Lett.* **87**, 186103 (2001).
- ²⁷⁰C. Monachon and L. Weber, “Effect of diamond surface orientation on the thermal boundary conductance between diamond and aluminum”, *Diamond and Related Materials* **39**, 8–13 (2013).
- ²⁷¹C. Monachon, G. Schusteritsch, E. Kaxiras, and L. Weber, “Qualitative link between work of adhesion and thermal conductance of metal/diamond interfaces”, *Journal of Applied Physics* **115**, 123509 (2014) 10.1063/1.4869668.
- ²⁷²T. Bautze, S. Mandal, O. A. Williams, P. Rodière, T. Meunier, and C. Bäuerle, “Superconducting nano-mechanical diamond resonators”, *Carbon* **72**, 100–105 (2014).
- ²⁷³M. A. Mohammad, M. Muhammad, S. K. Dew, and M. Stepanova, “Fundamentals of electron beam exposure and development”, in *Nanofabrication: techniques and principles*, edited by M. Stepanova and S. Dew (Springer Vienna, Vienna, 2012), pp. 11–41.
- ²⁷⁴C. Lee, H. Choi, E. Gu, M. Dawson, and H. Murphy, “Fabrication and characterization of diamond micro-optics”, *Diamond and Related Materials* **15**, Proceedings of Diamond 2005, the 16th European Conference on Diamond, Diamond-Like Materials, Carbon Nanotubes, Nitrides and Silicon Carbide, 725–728 (2006).
- ²⁷⁵J. Evtimova, W. Kulisch, C. Petkov, E. Petkov, F. Schnabel, J. Reithmaier, and C. Popov, “Reactive ion etching of nanocrystalline diamond for the fabrication of one-dimensional nanopillars”, *Diamond and Related Materials* **36**, 58–63 (2013).
- ²⁷⁶D. Tran, C. Fansler, T. Grotjohn, D. Reinhard, and J. Asmussen, “Investigation of mask selectivities and diamond etching using microwave plasma-assisted etching”, *Diamond and Related Materials* **19**, Proceedings of Diamond 2009, The 20th European Conference on Diamond, Diamond-Like Materials, Carbon Nanotubes and Nitrides, Part 2, 778–782 (2010).
- ²⁷⁷H.-a. Mehedi, V. Mille, J. Achard, O. Brinza, and A. Gicquel, “Effect of the process parameters of inductively coupled plasma reactive ion etching on the fabrication of diamond nanotips”, *physica status solidi (a)* **211**, 2343–2346 (2014).
- ²⁷⁸P. Forsberg and M. Karlsson, “High aspect ratio optical gratings in diamond”, *Diamond and Related Materials* **34**, 19–24 (2013).

- ²⁷⁹E. V. Catalan, P. Forsberg, O. Absil, and M. Karlsson, “Controlling the profile of high aspect ratio gratings in diamond”, *Diamond and Related Materials* **63**, 9th International Conference on New Diamond and Nano Carbons – NDNC 2015, 60–68 (2016).
- ²⁸⁰H. Uetsuka, T. Yamada, and S. Shikata, “ICP etching of polycrystalline diamonds: fabrication of diamond nano-tips for AFM cantilevers”, *Diamond and Related Materials* **17**, Proceedings of the International Conference on New Diamond and Nano Carbons 2007, 728–731 (2008).
- ²⁸¹T. Izak, A. Kromka, O. Babchenko, M. Ledinsky, K. Hruska, and E. Verveniotis, “Comparative study on dry etching of polycrystalline diamond thin films”, *Vacuum* **86**, 13th Joint Vacuum Conference, Štrbské Pleso, Slovakia, June 20-24, 2010 organized by the Slovak Vacuum Society in collaboration with the Vacuum Societies of Austria, Croatia, Czech Republic, Hungary and Slovenia, 799–802 (2012).
- ²⁸²M. P. Hiscocks, C. J. Kaalund, F. Ladouceur, S. T. Huntington, B. C. Gibson, S. Trpkovski, D. Simpson, E. Ampem-Lassen, S. Prawer, and J. E. Butler, “Reactive ion etching of waveguide structures in diamond”, *Diamond and Related Materials* **17**, 1831–1834 (2008).
- ²⁸³D. Tran, T. Grotjohn, D. Reinhard, and J. Asmussen, “Microwave plasma-assisted etching of diamond”, *Diamond and Related Materials* **17**, NDNC 2007 Proceedings of the International Conference on New Diamond and Nano Carbons 2007, 717–721 (2008).
- ²⁸⁴Y. S. Zou, Y. Yang, W. J. Zhang, Y. M. Chong, B. He, I. Bello, and S. T. Lee, “Fabrication of diamond nanopillars and their arrays”, *Applied Physics Letters* **92**, 053105 (2008) 10.1063/1.2841822.
- ²⁸⁵D. Hwang, T. Saito, and N. Fujimori, “New etching process for device fabrication using diamond”, *Diamond and Related Materials* **13**, Proceedings of the 9th International Conference on New Diamond Science and Technology (ICNDST-9), 2207–2210 (2004).
- ²⁸⁶S. Kiyohara, Y. Yagi, and K. Mori, “Plasma etching of CVD diamond films using an ECR-type oxygen source”, *Nanotechnology* **10**, 385 (1999).
- ²⁸⁷“Thin film processes”, in *Hybrid microcircuit technology handbook*, edited by J. J. Licari and L. R. Enlow, Second Edition (William Andrew Publishing, Westwood, NJ, 1998), pp. 63–103.
- ²⁸⁸T. Overstolz, P. A. Clerc, W. Noell, M. Zickar, and N. F. de Rooij, “A clean wafer-scale chip-release process without dicing based on vapor phase etching”, *Micro Electro Mechanical Systems*, 2004. 17th IEEE International Conference on. (MEMS), 717–720 (2004).
- ²⁸⁹D. W. Burns, “MEMS wet-etch processes and procedures”, in *MEMS materials and processes handbook*, edited by R. Ghodssi and P. Lin (Springer US, Boston, MA, 2011), pp. 457–665.
- ²⁹⁰C. R. Helms and B. E. Deal, “Mechanisms of the HF/H₂O vapor phase etching of SiO₂”, *Journal of Vacuum Science and Technology A* **10**, 806–811 (1992).
- ²⁹¹J. K. Kang and C. B. Musgrave, “The mechanism of HF/H₂O chemical etching of SiO₂”, *The Journal of Chemical Physics* **116**, 275–280 (2002).
- ²⁹²M. Imboden, O. Williams, and P. Mohanty, “Nonlinear dissipation in diamond nano-electromechanical resonators”, *Applied Physics Letters* **102**, 103502 (2013) 10.1063/1.4794907.

²⁹³K. L. Ekinici, Y. T. Yang, X. M. H. Huang, and M. L. Roukes, “Balanced electronic detection of displacement in nanoelectromechanical systems”, *Applied Physics Letters* **81**, 2253–2255 (2002).